UNIVERSITÀ DEGLI STUDI DI TRIESTE
Dipartimento di Fisica

XXII CICLO DEL DOTTORATO DI RICERCA IN FISICA
(I CICLO DELLE SCUOLE DI DOTTORATO)

The effect of star formation and feedback on the X–ray properties of simulated galaxy clusters

Settore scientifico disciplinare FIS/05

DOTTORANDA
Dunja Fabjan

COORDINATORE DEL COLLEGIO DEI DOCENTI
Chiar.mo Prof. Gaetano Senatore
Università degli Studi di Trieste
Firma:_____

RELATORE
Chiar.mo Prof. Stefano Borgani
Università degli Studi di Trieste
Firma:_____

TUTORE
Chiar.mo Prof. Stefano Borgani
Università degli Studi di Trieste
Firma:_____

Anno Accademico 2008/2009

Contents

List of Figures

List of Figures

List of Tables

List of Tables

INTRODUCTION

An important milestone in cosmology was reached in the past years, when all the observed cosmological phenomena to date were interpreted by a simple coherent model. This so–called *concordance model* is consistent with a flat geometry for the observable Universe and implies a total energy density very close to the critical one. Within this model a number of observations, such as the cosmic microwave background radiation (Komatsu et al., 2009), the large scale structure properties (e.g. Borgani, 2006) and the accelerating expansion measured with high–redshift supernovae (Kowalski et al., 2008) can be explained. The two dominant components of the Universe are a non–baryonic form of dark matter ($\sim 23\%$) that is responsible with its gravity for the formation of the observed structures, and a mysterious form of energy, called 'dark energy' ($\sim 72\%$), whose pressure causes the accelerating expansion of the Universe. The rest of the Universe is build up by baryonic matter, that amounts to $\sim 5\%$ of the total matter–energy content. This is however the only component of the Universe that we can directly measure and detect trough electromagnetic radiation emitted at different wavelengths. The *concordance model* explains many features of the observable Universe, but is not entirely satisfying because the nature of the dark matter and the origin of the dark energy remain unknown.

In this framework clusters of galaxies have a particular position, since they sit on the top of the hierarchy of non–linear structures (see Appendix 5.5) and, as such, they are sensitive tracers of cosmic evolution. They arise from the collapse of initial perturbations having a typical comoving scale of about 10 h^{-1} Mpc and are the largest structures in dynamical equilibrium nowadays. They played a key role in astrophysics: observing the velocity dispersion of cluster galaxies F. Zwicky (Zwicky, 1937) unveiled for first time the presence of dark matter, while the theory of gravitational instability was first developed in order to understand them. According to the standard model of cosmic structure formation, the Universe is dominated by gravitational dynamics in the linear or weakly nonlinear regime. In this case, the description of cosmic structure formation is relatively simple since gas dynamical effects are thought to play a minor role, while the dominating gravitational dynamics still preserves memory of initial conditions. On smaller scales, instead, the complex

astrophysical processes, related to galaxy formation and evolution, become relevant. Gas cooling, star formation, feedback from supernovae (SN) and active galactic nuclei (AGN) significantly change the evolution of cosmic baryons and, therefore, the observational properties of the structures. Since clusters of galaxies mark the transition between these two regimes, *they have been studied for decades both as cosmological tools and as astrophysical laboratories.*

Galaxy clusters are laboratories to study in detail the cosmic evolution of the intergalactic medium and the cluster galaxy population. In fact, most of the baryons in clusters are in the form of a hot, ionized gas, the so–called intra–cluster medium (ICM), which emits by thermal bremsstrahlung in the X–ray band, so that clusters can be detected as extended X–ray sources at large redshift. Present satellites allow the detection of clusters out to $z \sim 1.4$ and the detailed study of gas properties (density, temperature and metal abundance) out to $z \sim 1$ in fairly large samples. These observations provide most of the present knowledge on the thermodynamic structure of galaxy clusters. At the same time, these data show that the thermodynamical processes acting in galaxy clusters are much more complex than previously thought. The thermal content of the ICM contains the imprint of the cluster evolution and assembly, as well as the fingerprint of the energy released by sources like the Active Galactic Nuclei (AGN) and supernovae (SN). These sources of feedback are able not only to transport energy in the ICM but also to pollute it with the metals released during the evolution of stars in the galaxy. Metals are traced by the X–ray spectrum emission lines and their amount and spatial distribution represent a very important property of the ICM, due to the direct connection with the star formation process.

Clusters are used also as cosmological tools, placing important constraints on cosmological. The mass function of nearby galaxy clusters provides constraints on the amplitude of the power spectrum at the cluster scale (see Appendix 5.5). At the same time, its evolution provides constraints on the linear growth rate of density perturbations, which translate into dynamical constraints on the matter and Dark Energy density parameters. The baryon fraction in nearby clusters provides constraints on the matter density parameter, once the cosmic baryon density parameter is known, under the assumption that clusters are fair containers of baryons (e.g. Ettori et al., 2009). Furthermore, the baryon fraction of distant clusters provide a geometrical constraint on the DE content and equation of state, under the additional assumption that the baryon fraction within clusters does not evolve. However, a deeper understanding of the physics of baryons is required in order to calibrate them as precision tools for cosmology.

A comprehensive description of the physics of baryons in a cosmological framework needs both very high resolution and detailed codes to take into account all the complex interplay among different physical processes. Thanks to the enormous increase over the last decade in both computational power and code efficiency, direct

hydrodynamical cosmological simulations achieved a sufficient numerical resolution and a detailed description of the physical processes that allows one to predict and describe the interaction between the ICM the cluster galaxy population with a reasonable realism (e.g. Dolag et al., 2008a; Borgani & Kravtsov, 2009).

The Aim of this Thesis is to investigate, by resorting to high resolution hydrodynamic simulations, to what extend the properties that we recover from the X–ray observed IntraCluster Medium. To this purpose we carry out simulations for a large set of galaxy clusters and groups with the GADGET-2 code (Springel, 2005). The physical processes included in simulations are star formation, metal production and synthesis by different stellar populations as well as galactic winds and feedback from AGN. For the latter we included in the simulation code a prescription that accounts also for the 'radio mode' AGN feedback. To study the stability of cluster mass proxies we make use also of a set of galaxy clusters (Dolag et al., 2009), which have been simulated by changing both the source and nature of energy feedback and the numerical treatment of physical processes affecting the intracluster plasma. In fact, with this set we examine the impact of thermal conduction and artificial viscosity parametrization on the mass proxies robustness.

In summary, we cover with this Thesis three topics: (i) the metal enrichment and its evolution in the ICM, (ii) the imprint of AGN feedback on ICM X–ray properties and (iii) the robustness of cluster mass proxies and their dependence on the gas–dynamical processes in simulated galaxy clusters.

Here below we give a brief overview of the structure of this Thesis.

Chapter 1 is devoted to an introductory description of galaxy clusters. It first describes the properties of the IntraCluster Medium (ICM) in the X–ray band. Then we provide an overview of the results obtained so far in the study of the chemical enrichment of the ICM in a cosmological context. A picture of the important role that Active Galactic Nuclei (AGN) play in determining the ICM physical properties is given in the last part of this Chapter.

Chapter 2 gives a short introduction to the numerical methods and simulation techniques developed to study the process of cosmic structure formation. We first describe some numerical algorithms to perform N–body cosmological hydrodynamical simulations. Then we focus on the description of the TREE–SPH GADGET-2 code (Springel et al., 2001; Springel, 2005) that we use for cosmological simulations of galaxy clusters, with a particular emphasis on the chemo–dynamical and feedback models implemented in the code. Here we introduce the AGN feedback scheme, based on the work of Springel et al. (2005a), that was used for this Thesis (Fabjan et al., 2010). At the end of this Chapter we provide a description of the latest results from galaxy cluster simulations where the effect of different feedback schemes on the

ICM properties was studied.

In **Chapter 3** we study the evolution of the ICM metal content in simulated galaxy clusters. We analyze a set of 18 simulated clusters to investigate the relative role played by star formation, feedback processes and gas dynamics in determining the cosmic history of metal enrichment. We find that the metallicity profiles of the simulated clusters are in general too steep in outskirts with respect to observations by Vikhlinin et al. (2005). Furthermore, our simulations predict a positive evolution of the Iron abundance, comparable to what observed by Balestra et al. (2007) and Maughan et al. (2008). We study also the role of star formation and gas–dynamical processes in redistributing metals produced at high redshift, finding that their combined effect can significantly change the evolution of the ICM metallicity. The results reported in this Chapter have been published by (Fabjan et al., 2008), see also (Borgani et al., 2008b).

In **Chapter 4** we perform a detailed study of the effects that feedback from different astrophysical sources has on the ICM thermo–dynamical and chemical properties. To this purpose we use of the blackhole (BH) feedback model implemented by Springel et al. (2005a) in the GADGET-2 code. With this model the high gas accretion rates onto BHs mimic the quasar mode AGN feedback. We add to this implementation a simple scheme of radio mode AGN feedback, where BHs are allowed to accrete in a quiescent mode and a consistent fraction of the radiated energy is thermally coupled to the surrounding gas. The AGN feedback is found to be able to quench star formation in the Brightest Cluster Galaxies (BCGs) at $z < 4$, providing for galaxy groups the correct temperature profiles within cool cores. Moreover, AGN feedback causes of a widespread enrichment in cluster outskirts, since they are efficient in displacing enriched gas to the IGM at higher redshift. The main results reported in this Chapter have been published by Fabjan et al. (2010).

In **Chapter 5** we test the stability of cluster mass proxies when varying the physical processes included in the simulations. For this work we used a set of galaxy clusters simulated with different description of the physical processes affecting the evolution of the ICM: viscosity, conduction, star formation, galactic winds and AGN feedback. With this variety of simulations we test the robustness of the relations between the total cluster mass and two of the widely used proxies, gas mass and the Y_X proxy recently introduced by Kravtsov et al. (2006). Both relations show an evolution consistent with the predictions of the self–similar model, which assumes that gas follows Dark Matter under the action of gravity only. In particular, the Y_X proxy, defined as the product of gas mass and cluster temperature, is verified to be more stable than the gas mass proxy against the change in the physical process implemented in simulations. The results reported in this Chapter will be published in a future paper (Fabjan et al., in preparation).

Finally in the **Conclusions** we summarize the results obtained in this Thesis and outline future direction of investigation opened by the results presented in this

work.

The **Appendix** describes the basic concepts of cosmology, which are used through this Thesis. In particular, we briefly review the linear growth of structures and the non–linear evolution of density perturbations.

CHAPTER 1

GALAXY CLUSTERS

...that remarkable collection of many hundreds of nebulae...
W. Herschel, On the Construction of the Heavens

This Chapter provides a brief introduction about galaxy clusters focusing on the observed X–ray properties of the Medium (ICM). Main physical properties of galaxy clusters and X–ray observed thermodynamical and chemical properties are described and the most recent observational results are presented. The interaction between the thermal structure of the ICM and the central Active Galactic Nucleus (AGN) is briefly described in the light of recent observations.

1.1 Introduction

The many hundreds of nebulae W. Herschel was talking about were nothing more than galaxies, like the one we are living in. However it took hundred years more to discover the extragalactic origin of the so-called nebulae, when E. Hubble determined the distance to the nearest galaxy M31 using cepheids as *standard candles* (Hubble, 1929).

With the beginning of sky surveys and spectroscopic observations of galaxies, astronomers were able to collect data on single galaxies and on their distribution. Structures, detected in the visible part of the spectrum as overdensities of galaxies, were named galaxy clusters. The Hubble's view of a moderately uniform galaxy distribution in the sky was dismissed in favour of the observed galaxy clustering on

scales of superclusters. Galaxy clusters where then used as tracers to investigate the Large Scale Structure of the Universe.

With the publication of the Abell's catalogue of rich clusters (Abell, 1958), they started to be studied as a population of objects (see the review on "Science with galaxy clusters" by Biviano 2000). We address the reader to the reviews by Rosati et al. (2002),Voit (2005b) and Borgani & Kravtsov (2009).

■ Main physical properties

Galaxy clusters are nowadays believed to grow up from the gravitational collapse of overdense regions of size ~ 10 Mpc h^{-1} (comoving) within primordial fluctuations in the density field of the Universe. Zwicky (1937) (also Smith, 1936) argued that a hidden, invisible matter should be binding together galaxies in clusters, since the computed mass-to-light ratio for the Coma cluster was not able to explain the typical values from observations. Assuming virial equilibrium, that is valid for gravitationally bound systems where the total energy is equal to half the potential energy, both averaged over time, the resulting mass can be estimated as:

$$M \simeq \frac{R\sigma_v^2}{G} \simeq R_{[1Mpc]}\ \sigma^2_{v\,[10^3 kms^{-1}]}\ 10^{15} h^{-1} M_\odot,$$

where R is the cluster radial size and σ_v is the galaxy velocity dispersion along the line of sight. One way to avoid the assumption of dynamical equilibrium when estimating the cluster mass is to measure the deflection of light coming from background sources due to the deep cluster gravitational potential well, as proposed by Zwicky (1937). Nowadays spectacular cluster images, where the effects of *gravitational lensing* can be seen (left panel on Fig. 1.1), are indicating that under the assumption that general relativity is correct on cluster scales, the total cluster mass is dominated within a $\sim 80\%$ to 90% by a collisionless non-baryonic Dark Matter (DM hereafter), that dominates gravitationally bound objects (e.g. Narayan & Bartelmann, 1999; Bartelmann, 2003). The typical total mass range is $\sim 10^{14} - 10^{15} M_\odot$ for cluster of galaxies with hundreds to thousands galaxies inside the inner $1 - 3$ Mpc h^{-1}, while for smaller groups of galaxies masses are around $\sim 10^{13} M_\odot$.

Looking at the baryon content, galaxy clusters are more than a collection of galaxies. Most of the baryons in galaxy clusters were discovered to be present in the form of a hot tenuous plasma filling the space between galaxies and permeating the cluster potential well. The hot gas is forming a hydrostatic atmosphere, where temperature and density distribution are reflecting the gravitating mass. This atmosphere is a repository of baryons, that failed to end up in stars or galaxies, and of the heat from stellar evolution and the growth of supermassive black-holes (SMBH) during galaxy and cluster formation. In the hierarchical picture of structure formation, warm baryons were swept in the collapsing region with the dark matter

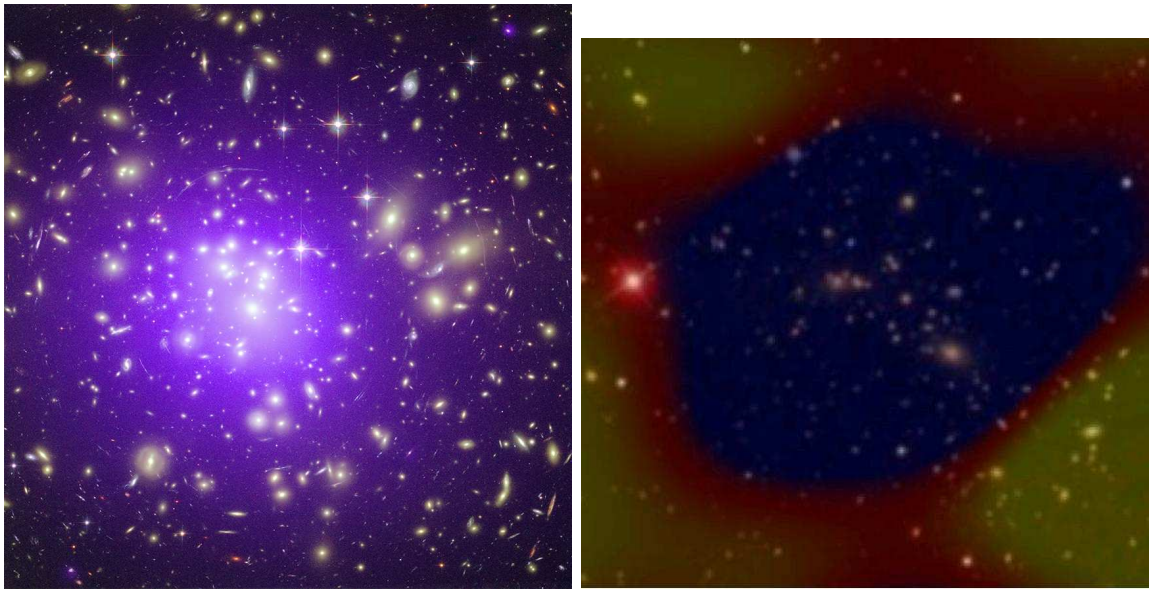

Figure 1.1: Left panel: The rich cluster of galaxies Abell 1689 located in the Virgo constellation at redshift $z = 0.18$. The image is a superposition of the X-ray observation of the intracluster hot gas (purple smoothed image) and optical observation of cluster galaxies. The long arcs seen on cluster borders are caused by gravitational lensing of distant background galaxies by the matter in this massive cluster (Credit: X-ray: NASA/CXC/MIT/E.-H Peng et al.; Optical: NASA/STScI). **Right panel:** The cluster of galaxies Abell 1914 observed in optical band by the Sloan Digital Sky Survey with a superimposed temperature map of the Cosmic Microwave Background (CMB) observed by the Sunyaev-Zeldovich array (SZA). At the cluster location the scattering of CMB photons on the IntraCluster Medium (thermal Sunyaev–Zeldovich effect) appears as a decrement in temperature of the CMB (Credit: John Carlstrom and SZA collaboration).

and subsequently heated to the virial temperature of the halo by accretion shocks and adiabatic compression. Assuming that clusters are relaxed structures, where embedded gas and galaxies follow the same dynamics, the resulting thermal energy will be of the order of

$$k_B T \simeq \mu m_p \sigma_{1v}^2 \simeq 6\sigma_{1v\,[10^3\,km\,s^{-1}]}^2 keV,$$

where m_p is the proton mass, σ_v the velocity dispersion of galaxies along the line of sight and μ is the mean molecular mass (assumed to be 0.6 in the case of primordial gas). The spectrum of these almost relaxed objects is a thermal equilibrium plasma spectrum, where ionisation is balanced by recombination. This Intra–Cluster Medium (ICM hereafter) has temperatures of about $10^6 - 10^8$ K with densities of 10^{-1} to 10^{-5} cm^{-3} from the densest central regions to the outskirts of galaxy clusters. The hot gas is primarily composed by hydrogen and helium, with traces of

heavier elements, at $\sim 1/3$ solar abundance. Most of the baryons, $\sim 90\%$, reside in the hot gas, while the 10% left are located in the total stellar component of the clusters, namely in galaxies and in the intra-cluster light, ICL (e.g. Lin et al., 2003). This can be seen in both panels in Fig. 1.1. In the left panel X–ray and optical observations are superimposed, showing that hot gas is filling up the cluster volume (purple smoothed X–ray image), while in the optical band the cluster is recognised as a concentration of galaxies. On the right panel the combined image reflects the galaxy density (optical image) and the thermal Sunyaev–Zeldovich effect (tSZ) on cluster baryons. The latter measures the distortion of the Cosmic Microwave Background (CMB) temperature due to the scattering of CMB photons by the population of thermal electrons in the hot plasma. Therefore the cluster in the right panel (Fig.1.1) appears as a temperature decrement in the CMB observations (for a review see Carlstrom et al., 2002).

1.2 X-ray properties of galaxy clusters

1.2.1. X-ray observations of galaxy clusters

Galaxy clusters are the most luminous extended X-ray sources in the sky, as found by the first X-ray satellites (Gursky et al., 1972), shining with X-ray luminosities of about $10^{43} - 10^{45}$ erg s^{-1}. Since the very high temperature of the ICM gas (seen before), the atoms are almost completely ionised (e.g. Sarazin, 1988; Rosati et al., 2002).

The main transitions occurring in the ICM plasma depend upon collisions (and close flyby's) of an electron and an ion. The processes that give rise to the observed spectrum are the bremsstrahlung (free–free), the recombination (free–bound) and the deexcitation (bound–bound). The first two are responsible for the continuum, while the line radiation occurs in bound-bound transitions. Since the ICM is a low density plasma, line radiation can occur also within the 'forbidden transitions' (e.g. Boehringer & Werner, 2009).

Collision rates of this thermal plasma are proportional to the gas temperature and ion and electron densities, therefore the observed spectrum depends at the same time on the plasma temperature and on its chemical composition. Since the ICM is a plasma characterised by a thermal equilibrium, ionisation and recombination rates are balanced for every element.

Figure 1.2 shows synthetic X–ray spectra for a plasma with solar abundance but with different temperatures. At cluster temperatures (lower panels with plasma at $T = 10^7$ and 10^8 K) the spectrum is dominated by *bremsstrahlung emission*, that occurs when a free electron is slown down (accelerated) by the Coulomb field of an ion and the energy is released in the X-ray band. Line radiation is instead

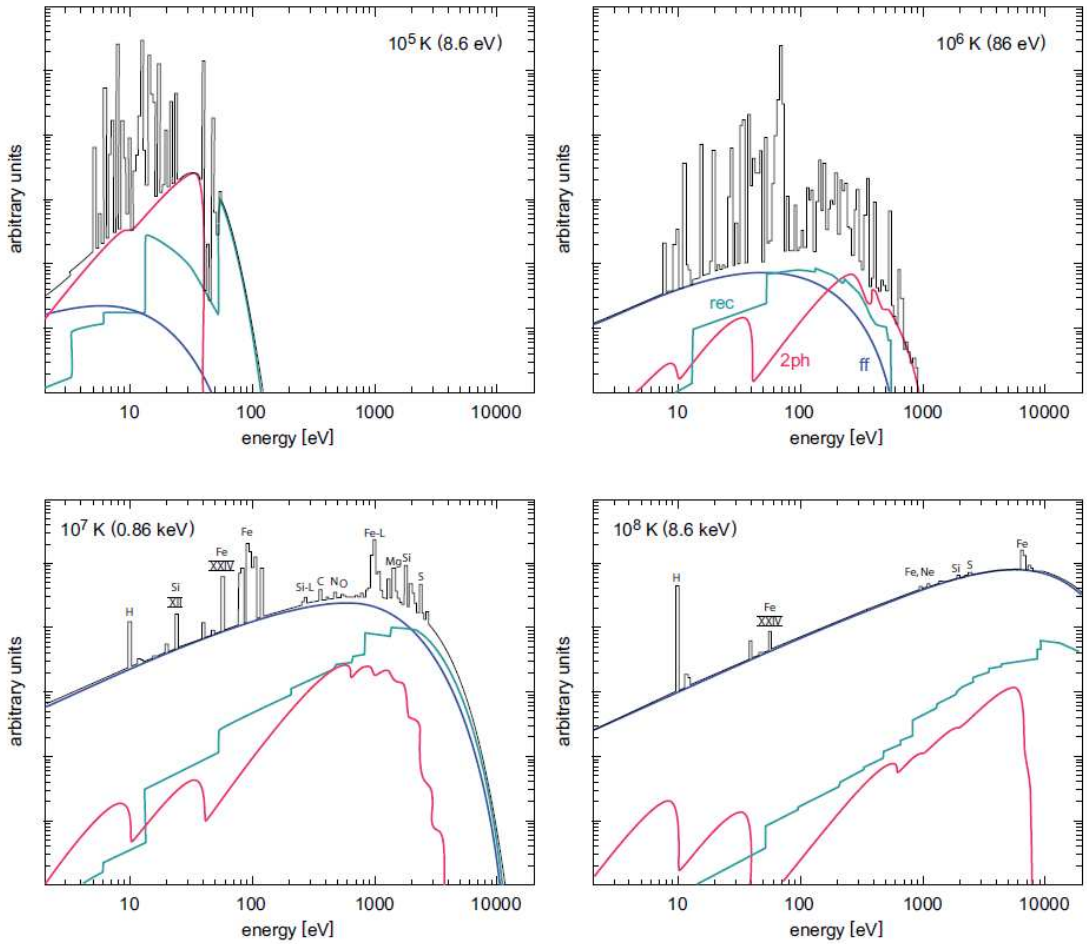

Figure 1.2: X–ray synthetic spectra for plasma with solar abundances at different temperatures. On each panel the temperature is written in the upper left corner. For each spectrum the processes that contribute to the continuum radiation are plotted: bremsstrahlung (blue), recombination (green) characterised by sharp ionisation edges and two–photon radiation (red). From Boehringer & Werner (2009), based on the work by Boehringer & Hensler (1989).

the dominant one for plasma with temperatures $\sim 10^4 - 10^6$ K (two upper panels of Fig.1.2). The spectral energy distribution for thermal bremsstrahlung for the collision between an electron and an ion i is given by Gronenschild & Mewe (1978):

$$\varepsilon(\nu) \propto n_e n_i T^{-1/2} g(T,\nu)\ \exp\left(-\frac{h\nu}{k_B T}\right),$$

with T the temperature, $g(T,\nu)$ the Gaunt factor, n_e and n_i the number densities of electrons and ions respectively. A correct temperature estimate of the ICM relies on

a good fit of the exponential cut-off $\exp(-\frac{h\nu}{k_B T})$, that is seen in the energy window of the telescopes.

Integrating on the velocity distribution of free electrons in the ICM the total radiated power is obtained as

$$\frac{dL_X}{dV} \sim 10^{-27} n_e n_i T^{1/2} erg cm^{-3} s^{-1}.$$

Due to the dependence on $\sim n_e^2$ of the X–ray emission, we must underline that X–ray luminosity measurements are most sensitive to the gas physics at cluster cores.

The cooling function relates the total amount of energy emitted per volume for a given amount of plasma with a given temperature and emissivity:

$$\frac{dL_X}{dV} \propto n_e n_i \Lambda_c(T),$$

and is calculated by integrating the emission from all processes, weighted by the photon energy. The characteristic cooling time is then defined as the thermal energy of the plasma divided by the emitted power,

$$t_c = \frac{\frac{3}{2}(1 + \frac{n_i}{n_e})kT}{\Lambda_c n_H}$$

(e.g. Kaastra et al., 2008). So, since the cooling function scales with $T^{1/2}$, the cooling time can be approximated with

$$t_c \sim 8.5 \times 10^{10} n_{H\,[10^{-3} cm^{-3}]}^{-1}\, T^{1/2}{}_{[10^8 K]} yr.$$

■ Hydrostatic equilibrium

For relaxed clusters the ICM gas is assumed to be in hydrostatic equilibrium. This assumption together with the assumption of spherical symmetry for the clusters leads to the equation

$$\frac{dp}{dr} = -\frac{GM(<r)\rho_{gas}}{r^2},$$

where the ICM gas has a pressure p, a density ρ_{gas} and mass M within the radius r. Using the equation of state of ideal gas we can derive the gravitating gas mass inside a radius r

$$M(<r) = -\frac{kTr}{G\mu m_p}\left(\frac{dlog\rho_{gas}}{dlogr} + \frac{dlogT}{dlogr}\right),$$

where T and ρ_{gas} are the temperature and density computed at the radius r, while μ is the mean molecular weight of the gas and m_p the proton mass. Masses derived

from measurements of gravitational lensing are found to be higher by $\sim 12 \pm 15\%$, which may reflect the temperature bias arising from the multi-temperature structure of the ICM (e.g. Rasia et al., 2005) or the turbulent pressure of the ICM.

The surface brightness can be used to derive gas temperature and density and is characterised by the isothermal "β profile" introduced by Cavaliere & Fusco-Femiano (1976):

$$S_X \propto \left[1 + \frac{r}{r_c}^2\right]^{-3\beta+\frac{1}{2}},$$

where r_c is the core radius of the gas distribution and β is the ratio of the energy per unit mass in galaxies with respect to the thermal energy in the gas:

$$\beta = \frac{\mu m_p \sigma_{1v}^2}{k_B T}.$$

For relaxed bright clusters the resulting β is equal to $\frac{2}{3}$. This approximation relies on the gas and dark matter being both isothermal within the potential well associated with the King dark matter density profile (King, 1966). Under this assumptions, the best fitted profile lies in the range of intermediate radii, while typically in central regions the gas density rises steeply and at high radii the observed surface brightness is decreasing below the fit.

1.2.2. The cooling flow model

The classical *cooling flow* model was introduced to explain the peak in X-ray surface brightness in the coolest and densest central regions within some of the observed clusters (see Fabian, 1994, for a review). Simple calculations reveal that the cooling time t_c of the gas in the cluster centre is shorter than the Hubble time t_H (Cowie & Binney, 1977; Fabian & Nulsen, 1977), so in absence of some heating source or mechanism, the gas with $t_{cool} < t_H$ should cool and condense, flowing inwards.

From the X-ray luminosity the rate of gas mass leaving the hot phase (mass deposition rate) can be derived assuming that the gas is cooling down from virial temperature at constant pressure (e.g. Donahue & Voit, 2004):

$$\dot{M} \sim \frac{2}{5} \frac{\mu m_p}{k T_X} \; L_X(< r_c),$$

where $L_X(< r_c)$ is the X-ray luminosity inside the cooling radius[1]. Estimates from observations lead to rates of $100 - 1000 M_\odot yr^{-1}$ (e.g. Fabian, 1994; White et al., 1994). Also X-ray emission lines can be used to estimate the cooling rate (Cowie,

[1]The cooling radius r_c is defined as the radius at which the cooling time t_{cool} equals the Hubble time $t_H = H_0^{-1}$.

1981), assuming that cooling at constant pressure produces the emission line i with luminosity

$$L_i = \dot{M} \frac{5k}{2\mu m} \int \frac{\varepsilon_i(T)}{\Lambda(T)} dT,$$

where $\varepsilon_i(T)/\Lambda(T)$ is the fraction of the cooling emissivity function due to emission line i as function of the plasma temperature T.

From early observations the mass deposition rate was found to scale with the radius, $\dot{M} \propto r$ (Peres et al., 1998), and was explained in the context of highly multiphase gas, where gas with different temperatures (and densities) is present at each radius. The luminosity expected from gas that has radiated away his thermal energy should be $\Delta L \propto \dot{M} \Delta T$. Therefore X-ray spectroscopical observations of emission lines of gas with different temperatures were used as a test for the constancy of the $\Delta L/\Delta T$ ratio (Cowie et al., 1980).

First X-ray observations (e.g. Canizares et al., 1982) were however in contrast with observations at other wavelengths (star formation rates from optical and Hα emission from gas at $\sim 10^4$ K), where such a huge amount of cool gas, $\sim 10^{11-13} M_\odot$ of mass accumulated during the cluster lifetime, was not observed (the mass sink problem, see (e.g. Donahue & Voit, 2004)).

High resolution spectroscopic observations from XMM-Newton and Chandra concretely changed this picture, revealing emission lines not as strong as predicted, with a deficit of emission from gas below $\sim T_{vir}/3$ (e.g. Peterson et al., 2001, 2003). The lack of emission from gas with $T \leq 1$ keV lead to lower mass cooling rate estimates (e.g. McNamara et al., 2000; Wise & McNamara, 2001; Edge & Frayer, 2003). Furthermore, evidence against the central multiphase gas was found in nearby clusters (Böhringer et al., 2001; David et al., 2001): this suggests the presence of a heating source (see Sec. 1.4) able to replenish the radiation losses.

Clusters are therefore often divided in two distinct categories on the basis of the presence or absence of the cool core (Molendi & Pizzolato, 2001): non cool-core clusters (NCC hereafter) are objects were the mass deposition rate is consistent with zero and often show signatures of recent mergings, while on contrary cool core clusters (CC hereafter) are relaxed systems (at least on the scale of 100 kpc, e.g. De Grandi et al., 2004), with strong emission peaks and significant drop in the ICM temperature at their centres (e.g. Peres et al., 1998; Allen et al., 2001). The local fraction of CC clusters was found to be around $50 - 70\%$ (Peres et al., 1998; Chen et al., 2007). The observed cluster bimodality could be helpful in exploring cluster physics by comparing the properties of the two subsamples (e.g. Sanderson et al., 2006, 2009a). The formation and evolution of cool cores are instead fundamental for cosmological studies, since they influence the mass calibration (and the luminosity–mass scaling relation described in Sec.1.2.3) and therefore, the derived evolution of the mass function (e.g. Santos et al., 2008).

1.2.3. The luminosity–temperature relation

If gravitation is the only force at play, the ICM thermodynamics is governed by adiabatic compression during DM collapse and shock heating from supersonic accretion. Clusters with different masses would be in this case scaled versions of each other (Kaiser, 1986; Evrard & Henry, 1991a). Usually this model is referred to as the *self–similar* model.

The relation that connects total mass M, gas temperature T and luminosity in the X-ray band L_X is

$$M \propto T^{3/2} E^{-1}(z),$$

that is valid under the assumption of hydrostatic equilibrium. that the gas distribution follows the underlying dark matter distribution, the X–ray luminosity can be written as

$$L_X \propto T^2 E(z).$$

Combining the two above relations the relation that follows between X–ray luminosity and total mass is

$$L_X \propto M^{4/3} E(z)^{7/3}.$$

$E(z)$ is defined as the scaling of the Hubble parameter $H(z)$ normalised to the present day value $H_0 = H(z = 0)$ and depends on the density parameters of the non–relativistic matter and on the dark energy contribution (see Appendix 5.5).

The deviations from self–similar scaling relations are related to non–gravitational mechanisms at work in galaxy clusters. Non–gravitational sources of energy like AGN, galactic winds and supernovae are able to heat the ICM depending on cluster mass. Also the merging history can affect the intrinsic scatter in the relation (e.g. Cavaliere et al., 1998; Voit, 2004).

The slope of the relation between X-ray luminosity and temperature $L_X \propto T^\alpha$ was observed to have $\alpha = 2.5 - 3$ at cluster scales (e.g. Pratt et al., 2009) and plausibly even steeper and with large scatter for galaxy groups (e.g. Osmond & Ponman, 2004), instead of $\alpha = 2$ derived from the self–similar model. The $L_X - T$ relation for the local cluster sample analysed by Pratt et al. (2009) is shown in the left panel of Figure 1.3. This sample contains hot clusters with temperatures in the range $2 - 9$ keV, and for this plot the two observables are extracted from the annulus $0.15 < R_{500} < 1$. Pratt et al. (2009) demonstrate that if the central cool core region ($< 0.15 R_{500}$) is excised the scatter in the observed data is reduced by a factor ~ 2 (with respect to the initial 30% scatter in data extracted from the whole region within R_{500}).

For a long time the observed $L_X - T$ slope was assumed to reflect an early episode of heating, that imposed a uniform entropy floor in the intergalactic medium (e.g. Evrard & Henry, 1991b). Galaxy groups are mostly affected in this case, since they are unable to compress the core gas due to the shallower potential well. A different

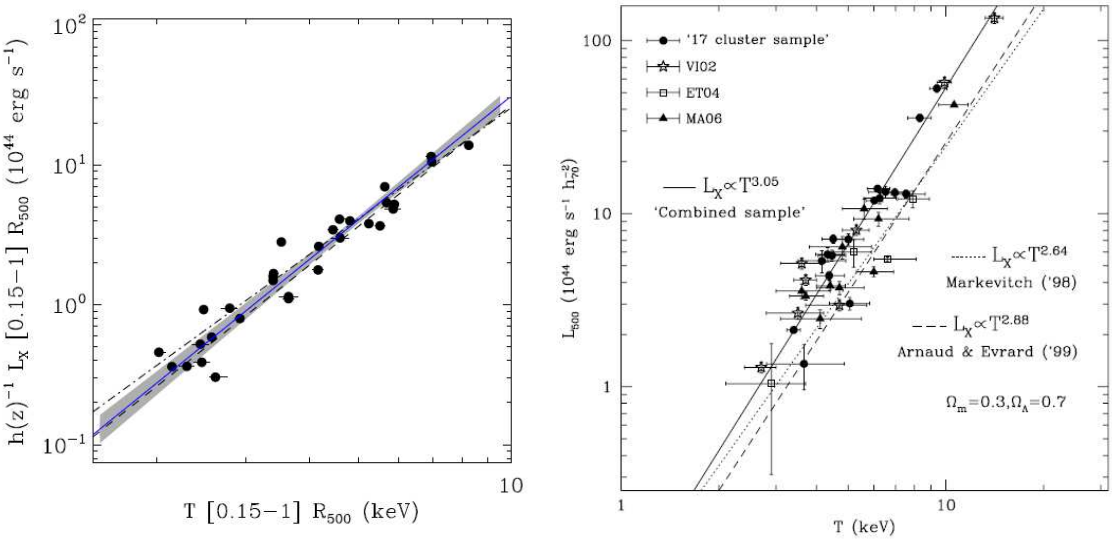

Figure 1.3: Left panel: The luminosity–temperature relation for a representative sample of local clusters (REXCESS) from Pratt et al. (2009). Both observables are extracted within the $0.15-1$ R_{500} aperture. The solid line and the shaded region are the best fitting power law and the relative 1σ deviation. The dashed and dot-dashed line are the relations derived by Arnaud & Evrard (1999) and Markevitch (1998) respectively. **Right panel:** The evolution of the X–ray bolometric luminosity–temperature relation from Branchesi et al. (2007). The "combined data sample" is composed by 36 high redshift clusters ($0.25 < z < 1.3$) from Maughan et al. (2006); Vikhlinin et al. (2002); Ettori et al. (2004) and Branchesi et al. (2007). The solid line indicates the best fit to the high redshift clusters, while dotted and dashed lines refer to the observed relations obtained by the best fit of local galaxy cluster samples by Arnaud & Evrard (1999) and Markevitch (1998).

interpretation is instead based on the role of radiative cooling: as gas cools, its entropy is diminished and the gas turns to be locked in stars. Only high entropy baryons with cooling times higher than the age of the Universe remain in the hot X–ray emitting phase (Voit, 2005b). As a consequence, X–ray luminosity is suppressed and entropy paradoxically increases due to cooling.

A number of observations were used to explore the possible evolution of the $L_X - T$ relation (e.g Maughan et al., 2006; Branchesi et al., 2007; Bignamini et al., 2008). The emerging picture (plot in the right panel of Figure 1.3) reveals that high redshift clusters are relatively brighter by a factor ~ 2 with respect to the local ones, at fixed temperature. The slope of the relation (solid line) is steeper with respect to the self–similarity model and to the local slope (dashed and dotted lines). From their analysis Branchesi et al. (2007) also conclude that there is a weak evolution of the L_X–T relation at high redshift $z > 0.3$ followed by a stronger one between $0 < z < 0.3$, possibly due to the fact that cooling and feedback processes start to

affect the relation (Voit, 2005a).

■ Y_X - a new X-ray mass indicator

Recently, Kravtsov et al. (2006) using mock Chandra images from cluster simulations presented a comparison of X–ray proxies for the total cluster mass, introducing a new quantity called Y_X.

The Y_X parameter is the X–ray analogue to the Sunyaev–Zeldovich parameter Y_{SZ}. The integrated comptonisation parameter Y_{SZ} represents the total integrated Sunyaev–Zeldovich flux within a fixed radius and is proportional to the total thermal energy of the ICM integrated within the chosen aperture:

$$Y_{SZ} = \left(\frac{k_B \sigma_T}{m_e c^2}\right) \int n_e T_e dV \propto M_{gas} T_{mw},$$

where σ_T is the Thompson scattering parameter, T_e is the electron temperature and T_{mw} is the mass–weighted temperature (see Chapter 3 and Section 3.2.4 for the definition).

The Y_X parameter is instead defined as

$$Y_X = M_{gas} T_X,$$

where M_{gas} is measured inside some defined aperture and T_X is the X–ray spectroscopic temperature (e.g. Mazzotta et al., 2004a; Vikhlinin, 2006).

This new mass proxy is presented as robust, with a very low scatter of about $\sim 5-7\%$, regardless of cluster dynamical state. The reduction in the scatter is due to the anti-correlation between the scatter in gas mass and temperature (Kravtsov et al., 2006). The Y_X proxy for the total cluster mass has been recently measured in two observed cluster set by Pratt et al. (2009) and Vikhlinin et al. (2009), based on XMM–Newton and Chandra data, respectively.

Recent analysis have measured the $L_X - Y_X$ relation and the robustness of the Y_X proxy (e.g. Maughan et al., 2006; Arnaud et al., 2007; Pratt et al., 2009). The $L_X - Y_X$ relation was found to be tight in the case when the central region within the radius $0.15R_{500}$ is excluded (with $\sim 11\%$ of scatter).

1.3 Chemical enrichment of the IntraCluster Medium

All elements beside Hydrogen and Helium are in astrophysics commonly called *metals*. Through this work we will use this definition, together with the definition of α elements for O, Mg, S, Ca, Si, that are produced by the capture of a Helium nuclei, and of Iron-peak elements for Ti, Mn, Co, Ni and Fe.

All this elements are synthetized in stars and ejected at the end of their life. In particular:

- **O, Ne, Mg** are mostly produced by SN II;
- **Fe, Ni** are mostly produced by SN Ia;
- **Si, S, Ar, Ca** (α elements) are produced by both supernova types in similar proportions.

■ Definitions

We provide here below a brief description of the used definition and the solar abundances used for this work is done.

The abundance of the element i can be expressed in several ways:

- `relative abundance` of the i-th element with respect to the primordial gas mass is
$$\frac{M_i}{M_{gas} - M^{tot}_{metal}} = \frac{M_i}{M_{gas} - \sum_{j\neq i} M_j} \, ,$$
where the primordial gas mass is computed as the difference between the total gas mass M_{gas} and the total amount of metals in gas M^{tot}_{metal}. The latter is a sum of all metals (j) except the i-th one, $M^{tot}_{metal} = \sum_{j\neq i} M_j$.

- `abundance by number` with respect to the number density of hydrogen:
$$Z_i = N_i/N_H.$$
Here we introduce the *bracket notation* for the abundance of the element i
$$[i/H] = \log_{10}(N_i/N_H) - \log_{10}(N_i/N_H)_\odot$$

- `abundance by mass` where the mass fraction of the element i and hydrogen with respect to the solar units:
$$Z_i = \frac{m_i/m_H}{(m_i/m_H)_\odot} \, .$$

In the following, when referring to a single element we will use the term *metallicity* as synonymous to abundance. Strictly speaking, however, *metallicity* should be used to indicate the abundance of all metals. For clusters with temperatures above 3 keV the extracted total ICM metallicity is dominated by Iron, and often in X-ray astronomy the two terms metallicity and Iron abundance are interchangeable.

Z	elem	GS†	AG	Lodd	Aspl†
1	H	12.00	12.0	12.0	12.0
8	O	8.830‡	8.93	8.76	8.52
14	Si	7.555	7.55	7.61	7.51
16	S	7.265	7.21	7.26	7.15
26	Fe	7.500	7.67	7.54	7.45

Table 1.1: List of logarithmic values of elements Si, S and Fe for the most used solar abundances. † denotes straight averages of photospheric and meteoritic values, that differ relevantly only in the case of Sulphur. ‡ denotes the photospheric value only. Col.1: atomic number; Col.2: element name; Col.3: GS - Grevesse & Sauval (1998) (average, see †) as reported in Baumgartner et al. (2005); Col.4: AG - Anders & Grevesse (1989) photospheric; Col.5: Lodd - Lodders (2003) protosolar; Col.6: Aspl - Asplund et al. (2005) (average, see †).

Solar abundances. Solar abundances are usually reported in logarithmic scale as

$$Z_{i,\odot} = \log(N_i/N_H) + 12 \ ,$$

where $\log_{10}(N_H) = 12$. The solar abundance by number is obtained as

$$Z^{\odot}_{i,number} = (N_i/N_H)_{\odot} = 10^{(Z_{i,\odot}-12)} \ ,$$

while to obtain the solar abundance by mass one should multiply by the atomic weight A_i of the i-th element,

$$Z^{\odot}_{i,mass} = (m_i/m_H)_{\odot} = A_i \times 10^{(Z_{i,\odot}-12)} \ .$$

The solar abundances, measured in the solar photosphere or in meteorites, can be taken from different compilations. The two mostly used ones for reporting X-ray data are Anders & Grevesse (1989) and Grevesse & Sauval (1998) (hereafter AG89 and GS98, respectively). We specify here that throughout this work abundances are scaled to the solar (averaged meteoritic and photospheric) values by Grevesse & Sauval (1998), if not stated otherwise. For Iron and Silicon, the two relevant elements in this work, these two values are rather close. More recent compilation of abundances by Asplund et al. (2005) and Lodders (2003) significantly reduced the disagreement between meteoritic and photospheric values. In Table 1.1 we report the logarithmic values for Hydrogen, Silicon, Sulphur, Oxygen and Iron for different compilations of solar abundances. In this Thesis the solar abundances by Grevesse & Sauval (1998) are adopted.

1.3.1. Global metallicity

The discovery of the Iron-K line emission in the spectra of the nearest clusters Coma, Virgo and Perseus (e.g. Mitchell et al., 1976; Serlemitsos et al., 1977; Mushotzky

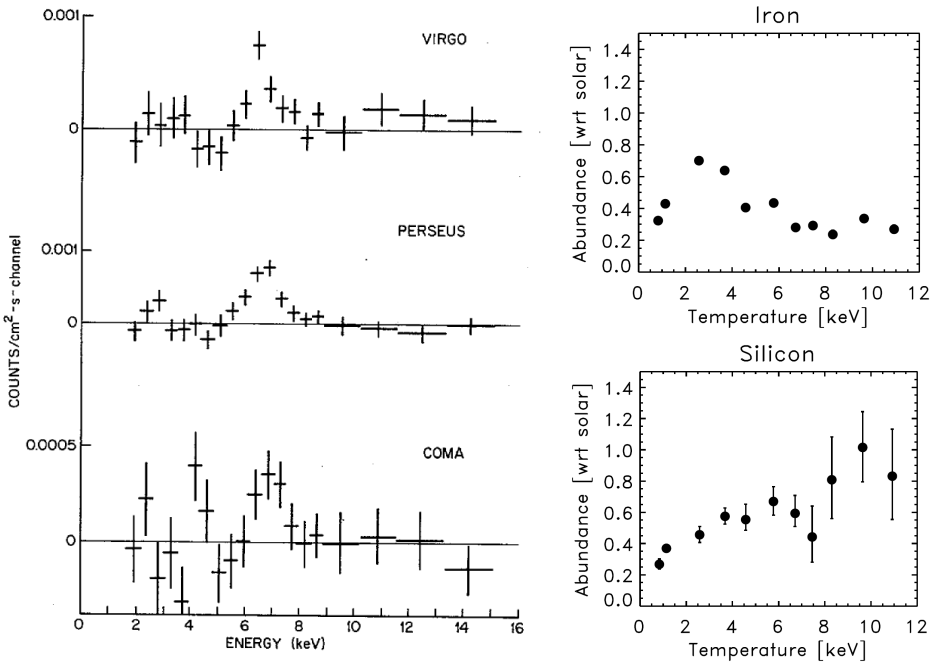

Figure 1.4: Left panel: Residual counts for Virgo, Perseus and Coma clusters, obtained once the best fit thermal continuum was subtracted. The residuals due to the Iron-K line emission are seen at $\sim$ 7 keV (from Serlemitsos et al., 1977). **Right panel:** Galaxy cluster elemental abundances for Iron (top) and Silicon (bottom) as a function of temperature. Abundances are scaled to solar abundances from GS98. The error bars are the 90% confidence interval. For Iron the error bars are smaller than the plotted points (from Baumgartner et al., 2005).

et al., 1978) confirmed the thermal origin of X-rays, discarding the hypothesis of the inverse Compton radiation from interaction between CMB and relativistic electrons in clusters. In the left panel of Figure 1.4 we show the residual counts for the three clusters, obtained by Serlemitsos et al. (1977) when fitting the spectra with a thermal continuum. The residuals are due to the Iron-K line emission at $\sim$ 7 keV. Spectroscopic analysis by Mushotzky et al. (1978) and others further reveal that the abundance of Iron in the ICM should be around one-third to one-half of the Solar value. With the Einstein observatory (Giacconi et al., 1979) emission lines at energies below 4 keV were detected, in particular K-lines from Mg, Si and S, and L-lines from Fe (e.g. Lea et al., 1982; Canizares et al., 1979). Detecting a high Oxygen abundance in M87 at the centre of the Virgo cluster, Canizares et al. (1979) deduce that the ICM is not isothermal, with cooler matter surrounding M87.

A detailed study of O, Ne, Mg, Si, S, Ar, Ca, Fe and Ni on a larger cluster set was performed by Baumgartner et al. (2005) using ASCA data. Their results on Iron and

Silicon abundances with respect to binned cluster temperatures are showed in the right panel of Fig. 1.4. In the right upper panel we can clearly see that clusters with high temperatures, $T \geq 6$ keV, have almost constant Iron abundance $\sim 0.3 Z_{Fe,\odot}$, with a 2-times higher metallicity observed for clusters around ~ 3 keV (e.g. Balestra et al., 2007). For groups < 2 keV the Iron abundance is underestimated due to the 'Iron bias' (Buote, 2000). This bias arises when a single–temperature (1T) model is used to fit the spectrum of the ICM with a mean temperature ~ 1 keV but with two temperature components. Both components are exciting different L-shell Iron emission lines, with a subsequent broadening of the spectral shape of the L-shell complex. The 1T model will then fit a lower Iron abundance, increasing the thermal continuum. Substantially larger abundances are found when fitting a multi (two) temperature models to galaxy groups < 2 keV, $\sim 0.6 - 0.7 Z_{Fe,\odot}$ (e.g. Buote, 2000; de Plaa et al., 2007).

Moreover, Baumgartner et al. (2005) found that Silicon and Si/Fe abundances increase from 0.7 to 3 in solar units from poorer to richer clusters in the temperature range $2 - 8$ keV (see also Fukazawa et al., 1998). A similar bias as found for Iron can be present for Silicon and Sulphur ('Si bias' and 'S bias', see Buote, 2000). In particular, since the low temperature component of the gas produces strong Si and S emission, their abundance tend to be overestimated. Despite the same production source, α elements observed by Baumgartner et al. (2005) were found not to behave homogeneously, in particular Sulphur was found to be almost constant with respect to cluster temperature, not following the Silicon behaviour (bottom right panel on Fig. 1.4). Recently, however, XMM-Newton observations by de Plaa et al. (2007) found the abundance ratios Si/Fe and S/Fe within $0.2 R_{500}$ to be constant as function of cluster temperature (Figure 1.5).

■ The Iron Mass-to-Light ratio (IMLR)

The Iron Mass-to-Light Ratio (IMLR) is defined as the ratio between the total iron mass in the ICM, M_{ICM}^{Fe}, and the total B-band luminosity of the galaxies in the cluster. Similarly, also the *metal* mass-to-light ratio can be defined. The rationale behind this lies in the fact that most of the metal mass in the ICM is produced by stars with $M > 8\, h^{-1}\mathrm{M}_{\odot}$ exploding as SN II. The light from early type galaxies is instead dominated by the oldest stars from the same stellar population (stars with $M \sim 1\, h^{-1}\mathrm{M}_{\odot}$). This ratio gives informations on the relevant mechanisms acting on different cluster scales (e.g. Renzini, 2004) and on the slope of the IMF when Silicon or Oxygen are investigated (e.g. Renzini, 2004; Finoguenov et al., 2003).

The $\mathrm{M}_{ICM}^{Fe}/\mathrm{L}_B$ was found to be typically $\simeq 0.01 - 0.02\, h^{-1}\mathrm{M}_{\odot}/L_{\odot}$ (Pratt & Arnaud, 2003). The IMLR is constant for hot clusters, implying that most of metal mass was produced by elliptical and bulges when they were young. Differently,

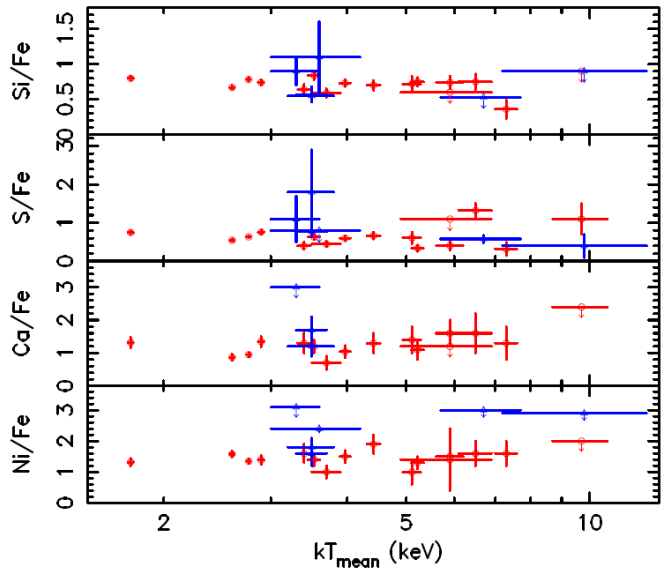

Figure 1.5: Abundance ratios of Si, S, Ca and Ni with respect to Fe (solar abundance values from Lodders (2003) as a function of cluster temperature, compiled by de Plaa et al. (2007). Cool core clusters are shown with red circles and non-cool core clusters with blue triangles. All the ratios are consistent with being constant with cluster temperatures (from Werner et al., 2008).

groups seem to contain less gas mass, with a number of possible explanation (e.g. mass loss by galactic winds, gas heated by winds, see Renzini, 2004).

1.3.2. Metallicity profiles

The chemical enrichment process inside galaxy clusters can be investigated using radial abundance profiles. In fact, the spatial distribution of metals is linked to the underlying galaxy distribution and to mechanisms related to the galactic evolution (e.g. SN driven galactic winds, AGN), galaxy-ICM interaction (e.g. ram pressure stripping, viscous stripping) and gas-dynamics (e.g. turbulence) that are all able to transport and diffuse metals inside the cluster potential well.

■ The distribution of Iron

The observed dichotomy of central temperature profiles that leads to the definition of cool-core (CC) and non cool-core (NCC) galaxy clusters (see Sec. 1.2.2) reflects in Iron abundance radial profiles. CC clusters show a relevant central peak, while NCC

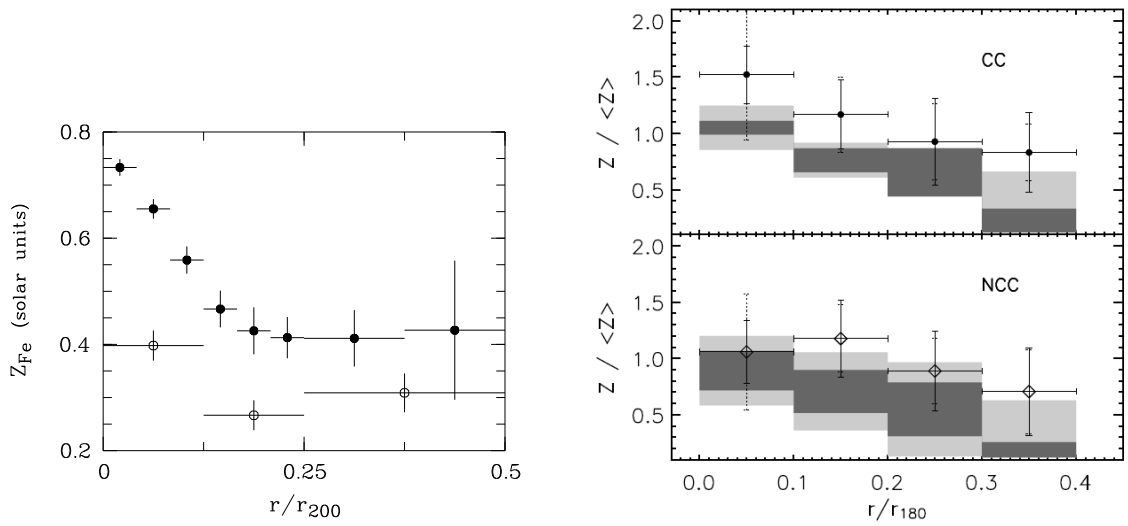

Figure 1.6: Left panel: The Iron abundance radial profiles for cool core (filled circles) and non-cool core (empty circles) nearby clusters from De Grandi et al. (2004). Iron abundance is scaled to the Iron solar values of Grevesse & Sauval (1998) while radial distance is scaled to the R_{200} radius. **Right panel:** The Iron abundance profiles for cool core (upper plot, filled circles) and non-cool core (lower plot, empty diamonds) clusters at intermediate redshifts from Baldi et al. (2007). Radial distance is scaled to R_{180}. Iron abundance is scaled to the mean cluster abundance. The shaded regions represent the metallicity profiles of the local cluster sample analysed by De Grandi & Molendi (2002).

clusters provide a flatter central profile. First evidences of an enhanced Iron abundance at the cluster centres with ASCA (White et al., 1994; Fukazawa et al., 1994) were confirmed by BeppoSAX observations of De Grandi et al. (2004), where the different behaviour of CC and NCC clusters was unveiled. The results of De Grandi et al. (2004) (left panel of Fig. 1.6) concern a sample of 22 nearby clusters splitted in CC and NCC clusters; the CC subsample is characterised by an enhanced Iron profile toward the cluster centre, while the NCC clusters show almost constant Iron abundances at all radii. The same dichotomy was discovered by Baldi et al. (2007) in their archival study of Chandra intermediate redshift clusters ($0.1 < z < 0.3$), but only in the most central bin. Their results are reported in the right panel of Fig. 1.6 (CC - filled circles, NCC - empty diamonds), where we can appreciate also the difference with respect to the metallicity profiles measured in nearby clusters by De Grandi & Molendi (2002) (shaded regions). However, Sanderson et al. (2009a) recently studied 20 galaxy clusters, observing the CC-NCC bimodality in temperature, gas density and entropy profiles, but metallicity profiles seem not to be affected, as can be seen in Fig. 1.7.

The spatial distribution of Iron has been studied by a number of groups (e.g.

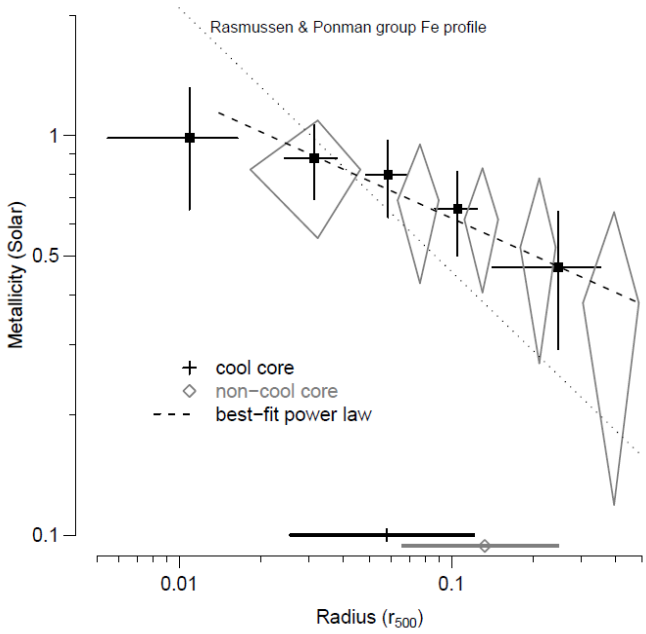

Figure 1.7: Iron abundance radial profiles from Sanderson et al. (2009a) for cool core clusters (crosses) and non-cool core clusters (diamonds). The best fit power law is shown with dashed line. (crosses - CC clusters, diamonds - NCC clusters). On the same plot the best fit relation for Rasmussen & Ponman (2007) observed groups is shown with the dotted line.

Vikhlinin et al., 2005; Pratt et al., 2007). With a careful background subtraction Leccardi & Molendi (2008a) were the first to explore the behaviour of Iron profiles of ~ 50 hot XMM–observed clusters to the largest radii, $0.4R_{180}$, finding a mean central metallicity of $0.45Z_{\odot,Fe}$ (scaled to Anders & Grevesse, 1989, solar abundances) decreasing to $0.2R_{180}$. Above that radius the metallicity is flat with a value around $\sim 0.2Z_{\odot,Fe}$.

Differently, galaxy groups have metallicity profiles with oversolar abundance at the centre and a steeper decrease to the external parts, about -0.66 in logarithmic scale as found by Rasmussen & Ponman (2007). This difference can be appreciated in Fig. 1.7, where the Iron profiles of galaxy clusters data by Sanderson et al. (2009a) (CC clusters with crosses and NCC clusters with diamonds) are compared with the mean metallicity of 15 galaxy groups (dotted line) observed by Rasmussen & Ponman (2007) with Chandra.

■ The correlation between Iron peak and galaxy population

X-ray observed gas metallicity is obviously linked to the underlying galaxy population in clusters. A connection between the presence of the Iron peak in CC clusters

and the Brightest Central Galaxy (BCG) was suggested by De Grandi et al. (2004). Iron mass excess in CC clusters was found to correlate with the optical magnitudes of BCGs (De Grandi et al., 2004). In this way, the Iron profile can be explained by the optical light distribution of late-type galaxies, with the central Iron peak ascribed to the presence of a massive cD at cluster centre (De Grandi et al., 2004). Under the assumption that metal ejection from the BCG is the mechanism that produces the central abundance peak, Rebusco et al. (2005) demonstrate that stochastic gas motion can account for it. A transport mechanism for metals originating in the BCG is needed, since the abundance peak is significantly broader than the underlying BCG light distribution. Rebusco et al. (2005) further speculate that the stochastic gas motions are driven by the activity of the supermassive black hole hosted by the BCG. The observed abundance peak, produced in > 5 Gyrs, is also indicating that cool cores are preserved from cluster mergers over very long time (e.g. Böhringer et al., 2004). A major role played by the BCG in the enrichment of the ICM with Iron was recently confirmed also by the analysis of Laganá et al. (2008), who interpreted the correlation between cluster Iron mass and optical luminosity of the BCG as partially due to ram pressure stripping mechanism with tidal disruption near the cluster centre. The importance of the BCG in the cluster enrichment was further underlined also by the recent work of Simionescu et al. (2008), who found that the central AGN in M87 is able to uplift highly enriched cool gas, polluting the ICM soon after his outbursts (see also Kirkpatrick et al., 2009). In Figure 1.8 the Iron metallicity map around M87 is observed by Simionescu et al. (2008). The region with higher metallicity is bounded by the 90 cm radio emission contours of the radio arms. The highest metallicity is found in the Eastern arm.

■ The distribution of relative abundances

The relative abundances of elements produced by different SN types can give information on both the shape and evolution of the initial mass function (IMF) as well as on the relative role of two type of supernovae at different clustercentric distances.

The early investigation of Si/Fe profiles, initially found to be centrally flat but increasing toward cluster outskirts, lead to the conclusion that cores are dominated by SN Ia products while SN II are enriching uniformly the ICM (e.g. Finoguenov et al., 2000; Rasmussen & Ponman, 2007). On the other hand, Suzaku observations by Sato et al. (2008) do not reveal any increase in the profile, but rather a flat Si/Fe distribution within at least $\sim 0.3 R_{vir}$.

Silicon is produced in large amounts by SNII and, within the described picture, should be distributed uniformly in galaxy clusters. Despite this, Böhringer et al. (2001) and Finoguenov et al. (2002) found that Silicon profiles are similar to Iron profiles, which is instead mostly produced by SNIa. Therefore Finoguenov et al. (2002) proposed two types of SNIa with different Si/Fe yields. Based on observations

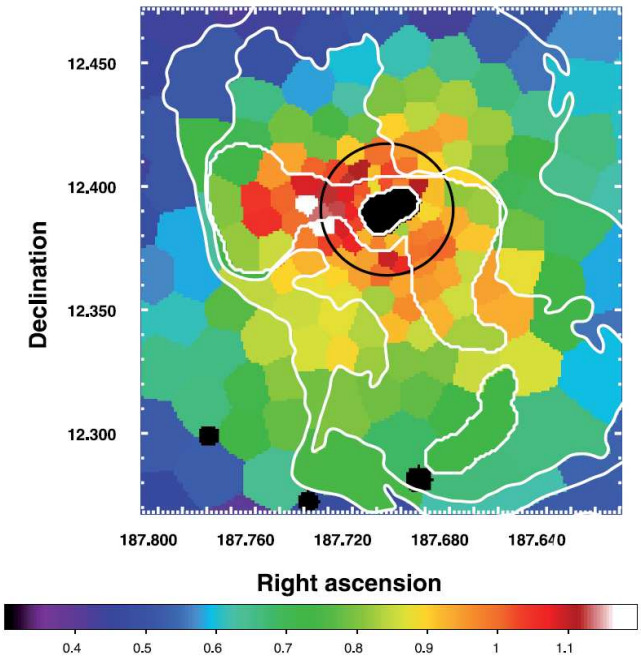

Figure 1.8: Iron metallicity map of M87 from Simionescu et al. (2008). The colour bar indicates the Iron abundance with respect to Lodders (2003) solar values. Radio contours from 90 cm emission (Owen et al., 2000) are superimposed on the map, showing an enhanced metallicity overlapping with the radio arms, especially within the Eastern arm. The black circle indicates the half light radius of M87.

of star formation rates in galaxies and of the radio–loud or quiet state of galaxies, Mannucci et al. (2006) recently proposed a bimodality in the delay time distribution of SNIa, that could also help in solving the problem.

A different picture emerged also for Oxygen (produced exclusively by SNII), since the radial profiles in the Hydra A cluster show a central peak (Simionescu et al., 2009). Combining profiles of Iron and Oxygen for a set of 5 clusters, Simionescu et al. (2009) found also a faster decrease in the Iron profile with respect to the Oxygen one. The most straightforward interpretation is that the SNII products are also centrally peaked (see Werner et al., 2008; Boehringer & Werner, 2009, for recent reviews).

In several observational analyses (e.g. de Plaa et al., 2007) the abundance ratios measured in the ICM were interpreted in terms of stellar yields, in order to provide constraints on the nucleosynthesis models for SN Ia and on the relative proportion of SN II and Ia produced elements (e.g. Gastaldello & Molendi, 2002). In this case however the instantaneous recycling approximation (I.R.A., see Tinsley, 1980) is used, so that stellar lifetimes and the delayed release of elements in the ICM are

ignored (Matteucci & Chiappini, 2005), therefore introducing an approximation for the study of the Fe evolution. Recently de Grandi & Molendi (2009) performed a detailed study of Silicon, Nickel and Iron abundances in the cores of 26 nearby CC clusters. They demonstrate that the large uncertainties in the stellar yields prevent any estimate of the constraints about the relative contribution of the two SN types to the enrichment of the galaxy cluster cores. Nevertheless, de Grandi & Molendi (2009) show that both SNIa and II contribute to the enrichment of the ICM in the CC region.

1.3.3. Evolution of the ICM metal content

Moving to high redshift the X-ray cluster spectrum is shifted toward lower energies and the photon flux is reduced, therefore only the Iron-K line emission can be revealed, while the observed population of clusters is (observationally) limited to the most luminous and hottest ones. In this case global metallicity and Iron abundance have the same meaning, since it is assumed that the ICM derived metallicity is well traced by Iron for the detected high temperature systems (e.g. Baldi et al., 2007).

The Iron abundance evolution can be used to derive the epoch when most of Iron was produced by stars and can give useful information about the mechanisms of metal release. Some authors (e.g. Madau et al., 1996; Renzini, 2000; Pipino et al., 2002) suggest the epoch of major Iron production to be around $z \sim 2$, when most of the star formation of giant ellipticals in dense cluster environment was over.

Initially the data from ASCA satellite show that the Iron abundance was not evolving out to $z \sim 0.4$ (Mushotzky & Loewenstein, 1997; Matsumoto et al., 2000, 2001) and even at higher redshift ($z \sim 0.8$) the metallicity was found to be consistent with $Z_{Fe} \sim 0.3\, Z_{\odot}$ (Donahue et al., 1999; Tozzi et al., 2003).

This issue was taken up by Balestra et al. (2007), extending the initial Chandra cluster sample of Tozzi et al. (2003) to 56 objects observed both with Chandra and XMM-Newton. At variance with previous results, below $z < 0.5$ a relevant evolution of the Iron abundance was found, with a constant metallicity of $\sim 0.25 Z_{\odot}$ in the redshift range $z = 0.5 - 1$, as shown on left panel of Fig. 1.9. Extraction radius of each cluster was chosen to minimize the signal-to-noise ratio, with values in the range $0.15 - 0.3$ R_{vir}. These observations suggest that the mean Iron abundance increases at recent epochs and can be described by a simple power law with $< Z_{Fe} >= Z_{Fe}(0)\ (1+z)^{-\alpha_z}$ and $\alpha_z \simeq 1.25$.

A similar result was found also by Maughan et al. (2008), who adopted two different spectral apertures of $(0.15-1)$ R_{500} and $(0-1)$ R_{500} for all clusters. The right panel of Fig. 1.9 shows how cool cores affect the abundance, since excising the most central part of the clusters lowers the mean ICM abundance. However, both extraction areas confirm the enhancement of metallicity at low redshift. This plot also reports the prediction of the model by Ettori (2005). Starting from phenomenologi-

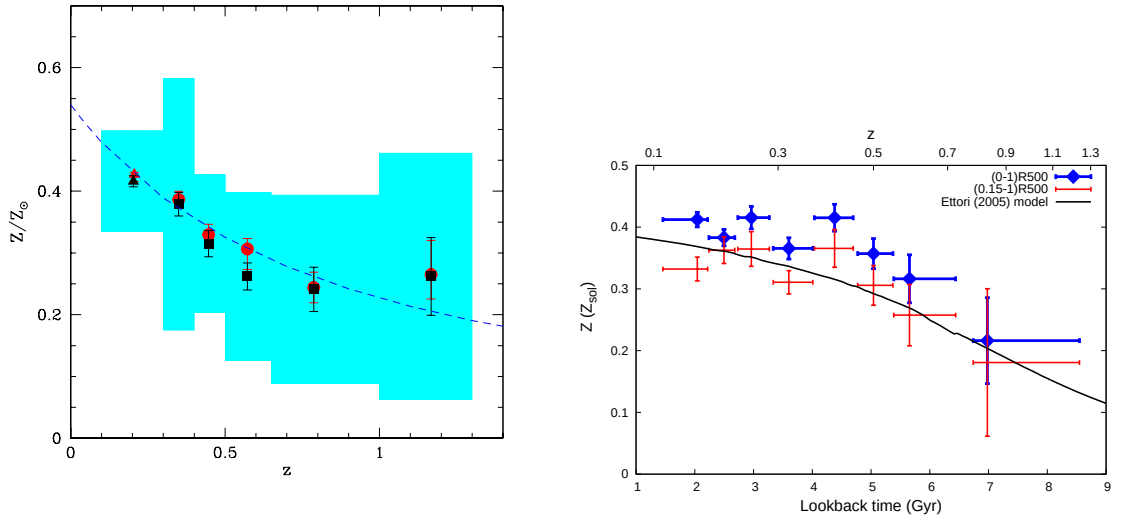

Figure 1.9: Left panel: the mean Iron abundance for 56 clusters binned in redshift, taken from Balestra et al. (2007). Weighted averages of the single-source measurements are plotted with black squares, combined fits on each redshift bin are marked with red circles and for both the errorbars are at 1σ level. The shaded area shows the rms dispersion of the data, while the dashed line is a power law fit to the data. **Right panel:** Mean Iron abundance from a joint spectral fit of 115 clusters binned in lookback time by Maughan et al. (2008). The red and blue data refer to abundances measured in the annulus $(0.15 - 1)$ R_{500} and inside R_{500}, respectively. The solid black line represents the model by Ettori (2005).

cal models of cosmic star formation history and adopting SN rates able to reproduce observations at $z \lesssim 0.3$, Ettori (2005) derived the corresponding cluster metal accumulation history. His main results, besides reproducing the enrichment evolution by Maughan et al. (2008) and Balestra et al. (2007), are that half of the Iron mass present locally is produced by SNIa ejecta and that SNII (or core–collapse supernovae, SN_{CC}) become dominant between redshifts 0.5 and 1.4 with an enhancement of α/Fe elements.

Also Calura et al. (2007) performed a study of the Iron evolution using chemical evolution models for different galaxy types. In order to reproduce both the observed ICM Iron abundance evolution and the SNIa rates in galaxy clusters they assume that after $z < 0.5$, progenitors of S0 galaxies lost the Iron–rich InterStellar Medium (ISM). This stripping of the ISM is consistent with the ram pressure stripping found in numerical simulations (e.g. Schindler et al., 2005). However, as noted by Renzini (1997), if ram pressure stripping is the dominant mechanism in the ICM enrichment, then massive clusters, where the ICM has a higher pressure, should be richer with metals than low–mass systems, a prediction which is in fact contradicted by

observational results by Baumgartner et al. (2005) (right panel of Figure 1.4).

The results by Maughan et al. (2008) were recently combined by Anderson et al. (2009) with 29 XMM-Newton cluster observations and a lower redshift sample of Snowden et al. (2008). In agreement with previous results, they found a decrease of Z_{Fe} by about a factor 2 from $z = 0$ to $z \sim 1$, while the uncertainty in the iron abundance evolution is mainly driven by the paucity of high-redshift ($z > 0.7$) clusters.

The physical processes that drive the increase of Iron abundance in the ICM at low redshift can be related to ram pressure or tidal stripping (e.g. Domainko et al., 2006; Murante et al., 2004), by a different branch of SNIa progenitors enriching the ICM at lower redshifts (Mannucci et al., 2006) or a top-heavier IMF in spheroids (Loewenstein, 2006). This issue will be discussed with more details in Chapter 3.

1.4 AGN feedback in clusters and groups

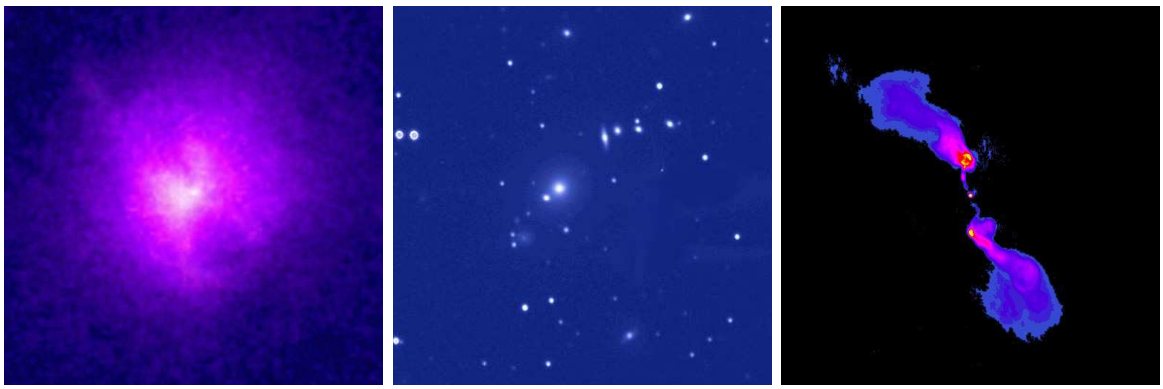

Figure 1.10: Recently published multiwavelength observations of the active galactic nucleus interacting with the ICM in the nearby cluster Hydra A (Kirkpatrick et al., 2009). Each image is 2.7 arcmin large. **Left panel**: X-ray image of the ICM (NASA/CXC/SAO). **Middle panel**: optical image taken at La Palma Observatory (B. McNamara). **Right panel**: radio image taken at the National Radio Astronomy Observatory (Greg Taylor).

As pointed out in Sec. 1.2.2, high resolution spectroscopy in X-rays ruled definitely out the classical cooling flow model, with a consequent search for a suitable heat source, able to offset the radiative losses of the system.

Many of the CC clusters were observed to contain a strong radio source with recent nuclear activity (e.g. Burns, 1990; Sun, 2009). Disturbances in the hot gas were noted early on in bright clusters, but only deep exposures of nearby clusters, like Perseus or Hydra A (Fabian et al. 2000, 2003; Kirkpatrick et al. 2009, see left panel on Fig. 1.10), reveal X-ray surface brightness depressions of about 20% to

40% below the level of the surrounding gas. This elliptical cavities are usually found in pairs and are related to the radio activity of the central active galaxy, with an observed 1.4 GHz radio emission (e.g. recent review by McNamara & Nulsen, 2007). Within the nucleus of this active galaxy (Active Galactic Nucleus, AGN) a huge amount of energy is generated and emitted in form of jets of highly energetic charged particles up to relativistic speed. Ghost cavities, filled with low frequency emission, were found and interpreted as radio relics that had risen $20 - 30$ kpc in the ICM atmosphere (McNamara et al., 2000).

Since not all CC clusters host central galaxies with ongoing nuclear activity, the AGN heating is thought to be periodic. The mean jet power released in the ICM over $\sim 10^8$ years is estimated to be $10^{41} - 10^{46}$ erg s^{-1}, the latter one comparable to the energy released by a powerful quasar. This values are comparable to the power required to quench cooling flows (e.g. Bîrzan et al., 2004; Rafferty et al., 2006; Nulsen et al., 2007) and most of the energy is expected to heat the surrounding gas (Churazov et al., 2001; Voit & Donahue, 2005). The spatial distribution and form of the energy deposition is studied by means of simulations (e.g. Omma & Binney, 2004; Heinz et al., 2006). However, coupling the energy from the source to the cooling plasma remains a complex issue.

The AGN activity is powered by the gas accretion on supermassive black holes (BHs), located in the central BCG (Allen et al., 2006; Rafferty et al., 2006), with typical rates of $\sim 10^{-2} M_\odot$ yr^{-1}. In fact most of spirals and elliptical galaxies contain at their centre a blackhole (e.g. Kormendy & Richstone, 1995). The mass of the blackholes is tightly coupled with the mass of the hosting galaxy (Magorrian et al., 1998) as well as the velocity dispersion of spheroids (Ferrarese & Merritt, 2000; Gebhardt et al., 2000). Upper limits on BH masses were recently explored by Dalla Bontà et al. (2009), looking at the cluster BCGs with the Hubble Space Telescope spectrographs (Fig. 1.11) using kinematics of the ionised gas in the nuclear region (direct dynamical measurements are unfortunately too difficult within BCGs). Recently also two black hole fundamental planes were found, correlating AGN X-ray luminosity, radio luminosity and BH mass (Merloni et al., 2005) but also the accretion rate $\dot{M}_\bullet$, stellar velocity dispersion σ and mass of the hosting galaxy (Hopkins et al., 2007).

Due to the existing correlation with the galaxy growth, the widely accepted picture for BHs is that of an accretion at high rate directly linked to mergers of gas-rich galaxies. Once grown considerably, BHs are observed as bright quasars (e.g. Fan et al., 2001, for high redshift observations). In contrast, outflows in form of radio emitting plasma found in bubbles are connected with low accretion rates within the local supermassive BHs. Churazov et al. (2005) explored the analogy between X-ray binaries, where radio emitting outflows are commonly found, and supermassive BHs. Within this scheme, the feedback power depends on the mass accretion rate by the BH, leading to the scenario where elliptical galaxies grow with a quasar-like nucleus

at early epochs, while passive nucleus evolution is going on at late times. The gas heating rate is maximum well below Eddington rates ($\dot{M}/\dot{M}_{edd} \sim 0.04$), while it decreases near the Eddington rate (Churazov et al., 2005).

To prevent gas from cooling many heating mechanisms were proposed, like conduction (see e.g. Donahue & Voit, 2004). Electron thermal conduction carries heat from warmer regions to cooler ones. However it is not stable enough to preserve the observed gradients in temperature and density for longer periods, ≥ 1 Gyr (e.g. Cowie & Binney, 1977). Conduction is also difficult to test because it depends on the unknown geometry of the magnetic fields inside clusters. It can be however coupled with AGN feedback in hybrid models, where it acts on outern parts of the core while AGN is acting in the inner parts (e.g. Brighenti & Mathews, 2003). However, the conduction acting alone is not able to suppress star formation in cluster cores, as found in simulations (Dolag et al., 2004).

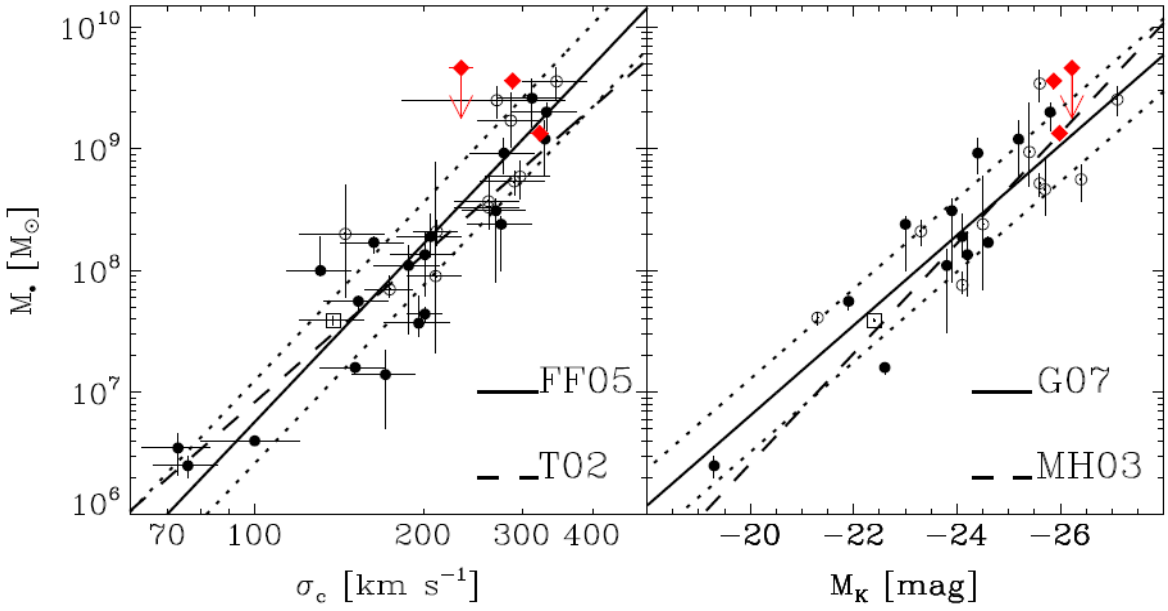

Figure 1.11: Left panel: The relation between the mass $M_\bullet$ of BHs and the circular stellar velocity dispersion σ_c by Ferrarese & Ford (2005) (Figure from Dalla Bontà et al. (2009)). The red diamonds are the observational points for three supermassive BHs observed in cluster BCGs by Dalla Bontà et al. (2009). The dashed line is the Tremaine et al. (2002) $M_\bullet - \sigma$ relation. **Right panel:** The relation between the mass $M_\bullet$ of the BHs and the bulge K-band luminosity M_K by Graham (2007). The dashed line is the Marconi & Hunt (2003) relation. As on left panel, the three supermassive BHs observed by Dalla Bontà et al. (2009) are shown with red diamonds.

Finally, AGN feedback is also believed to be a very powerful solution to many of the outstanding problems in the modelling of galaxies and the interaction with the

ICM (see Chapter 2). The energy released by the BH in the central cluster galaxy should help in (i) quenching the excess star formation that is seen at low redshift, (ii) solve the problem of the exponential decay of bright galaxies, (iii) be able to onset the relation between the mass of the galaxy bulge and BH mass and (iv) contribute to the excess entropy in cluster cores. All those points will be addressed in Chapter 4, where we will describe the AGN feedback effect on simulated galaxy clusters. We will focus in particular on its effect on star formation inside the BCG and in the whole cluster as well as on the impact of feedback on ICM thermodynamics. Furthermore we will explore which is the net effect on the metallicity production and distribution in the ICM.

CHAPTER 2

NUMERICAL COSMOLOGY

In this Chapter the simulation techniques are briefly reviewed. Here we give also an updated overview on the latest results in numerical simulations of galaxy clusters, focusing on two main topics: the chemical enrichment of the Intra–Cluster Medium and the feedback processes acting in galaxy clusters, in particular galactic winds from supernovae explosions and energy emission by Active Galactic Nuclei in the central galaxy. Furthermore, the code GADGET-2 , that was used for the simulations presented in this Thesis, is introduced with a detailed description of the chemical enrichment scheme and of the implemented feedback by Active Galactic Nuclei.

2.1 Introduction

The formation of structure in the early Universe, when tiny inhomogeneities in the primeval density field left by the cosmic inflation are amplified under the action of gravity, is described by the linear theory (see Appendix 5.5). In the standard hierarchical Cold Dark Matter (CDM) paradigm the galaxy formation begins with the gravitational collapse of dark matter overdense regions that can be instead followed with the non–linear theory (see Appendix 5.5). Furthermore, the formation of galaxies includes astrophysical processes such as gas cooling and star formation, that are adding complexity to the initial picture. The highly non–linear dynamics of the formation of cosmic structures can be followed by means of numerical simulations, that are able to model the observed processes realistically (for reviews see

Coles & Lucchin, 2002a; Dolag et al., 2008a; Borgani & Kravtsov, 2009).

Simulations start with early epoch initial conditions, that define a density field with statistical properties of the assumed cosmological model. The evolution of the dark matter component is followed by means of numerical N–body simulations. A number of numerical algorithms, that are described in Section 2.2.1, can be used to evaluate the gravitational potential of the dark matter distribution.

Hydrodynamical simulations are used when more complex baryon physics wants to be included in the simulations and can be treated by resorting to the fluid dynamics equations. The collisional gas elements can be followed by integrating equations governing the gas dynamics using the grid–based Eulerian method or of the particle–based Lagrangian method. In these simulations the collisionless dark matter and normal baryonic matter co–evolve and interact only with gravity (Section 2.2.3).

Any simulation is always a compromise between the size of the region where resides the object of interest and the needed resolution limit. Depending on the simulated object, the sizes of the simulation box can vary between few megaparsecs (for an individual galaxy) up to hundreds of megaparsecs and more (for galaxy clusters).

In Section 2.2 a review of numerical methods for N–body and hydrodynamical simulations is provided. Section 2.4 is focused on the main achievements and issues regarding the characterisation of the physics of baryons inside galaxy clusters. In Section 2.3 the description of the GADGET-2 code is given, highlighting the implementation of chemical enrichment and the modelling of feedback by gas accretion onto black holes (BH hereafter).

2.2 Simulation techniques

2.2.1. N-body simulations

The problem of computing the motion of N particles under the influence of the gravitational force is commonly called the "N-body problem" and can be solved for a large number of particles only by means of numerical solutions. These solutions are obviously used in cosmological N–body simulations, where a limited portion of the Universe is reproduced by a finite number N of tracer particles with the dynamics driven only by the gravitational force between them. In the most favourable cosmological model the cold dark matter represents the tracer that is driving the formation and growth of cosmic structures (e.g. Peebles, 1980). The dark matter is thought to be collisionless and can be described as a non-relativistic fluid interacting only gravitationally with the visible matter. In terms of the phase-space density $f(\mathbf{x}, \mathbf{v}, t)$ the motion of the dark matter fluid is described with the collisionless Boltzmann

equation

$$\frac{\mathrm{d}\, f}{\mathrm{d}t} = \frac{\partial\, f}{\partial t} + \mathbf{v} \cdot \frac{\partial\, f}{\partial \mathbf{x}} - \nabla\Phi \cdot \frac{\partial\, f}{\partial \mathbf{v}} = 0$$

where $\Phi(\mathbf{x}, t)$ is the gravitational potential recovered using the Poisson equation

$$\nabla^2\Phi(\mathbf{x}, t) = 4\pi G \int f(\mathbf{x}, \mathbf{v}, t) d\mathbf{v}.$$

The function $f(\mathbf{x}, \mathbf{v}, t)$ represents the distribution of positions $\mathbf{x}$ and velocities $\mathbf{v}$ at a fixed time t. [1]. The particles in N-body simulations do not represent a single dark matter particle but rather a dark matter mass distribution and therefore only the statistical properties should be considered.

The total number of particles in a simulation depends on the studied astrophysical problem: the simulation box size should represent a portion of the Universe with the object of interest in it and with enough particles to achieve a good (spatial and mass) resolution to address the specific problem. A main limit to the number of employed particles is represented by the algorithm used to compute the gravitational force among them, since the computational cost of a simulation is determined by the number of performed operations (that depends on the number of particles). The number of tracer particles is therefore always a compromise between the size and the resolution of the simulation box and of course depends on the available computing resources.

To compute the evolution of the dynamics of a number of particles under the action of the gravitational force, one needs to solve directly the motion of particles. Some of the methods applied in N-body simulations to calculate mutual gravitational forces among particles are described below.

■ Particle-particle (PP) method

The most immediate way of solving the motion of N particles is to directly sum the contributions of individual particles to the gravitational potential on the position $\mathbf{x}_i$ where the i-th particle is located:

$$\Phi(\mathbf{x}_i) = -G \sum_{\substack{j=1 \\ j\neq i}}^{N} \frac{m_j}{(|\mathbf{x}_i - \mathbf{x}_j|^2 + \varepsilon^2)^{1/2}}.$$

Here G is the gravitational constant, m_j is the j-th particle mass, $\mathbf{x}_i$ and $\mathbf{x}_j$ the vectors of the particle positions and ε the *smoothing length* or *gravitational softening*. The gravitational force $\mathbf{F}_i = -m_i\, \nabla\Phi(\mathbf{x}_i)$ acting on the i-th particle would diverge when two particles are too close to each other. To avoid this possibility a constant

[1] NOTE: Here and in the following, vectors will be represented with boldface characters.

smoothing length ε is added in the denominator. This smoothing length defines the spatial resolution limit of the simulation and is helpful in reducing spurious numerical effects coming from the discreteness in the tracer particles (e.g. the two body relaxation, see El-Zant, 2006). The usually adopted value for ε is between 1/20 to 1/50 of the mean interparticle separation length.

Despite the accuracy in the final results, the main disadvantage of this method is the high computational cost, since $N(N-1)/2$ operations are required at each timestep to evaluate the gravitational force.

■ Particle-Mesh (PM) method

To gain a substantially faster algorithm for computing N-body interactions one needs to reduce the number of operations. This can be achieved by computing smartly the gravitational force. The Particle-Mesh (PM) technique makes use of a mesh to compute the force field. The algorithm is computed through three steps: (i) starting from the particle positions the density is computed on the mesh points, (ii) the Poisson equation is solved in the Fourier space, where also the potential is obtained using the Green's theorem and (iii) gravitational forces on the individual particles are obtained by interpolating the derivatives of the potentials to the particle positions. The computational cost is reduced to about $N + N_g \log N_g$ number of operation for a fixed number N_g of mesh cells with a total number of N particles. In this case the spatial resolution is limited by the grid spacing.

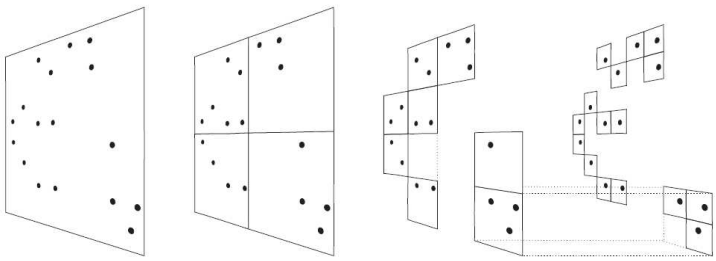

Figure 2.1: The schematic illustration of the bi-dimensional TREE algorithm by Barnes & Hut (1986) used to compute the partial forces. All the particles of the simulation belong to the main square called *root* (on left side). The square is divided into four sub-squares with half of the side-length each. The division is reiterated until a single particle is contained in a sub-square, called *leave* (on right side). All the scheme is stored in the global *tree*. At each subdivision the resulting mass distribution in sub-squares is stored, while empty squares are not saved.

■ Tree algorithm

Another way of keeping the highest possible spatial resolution with a lowest computational cost is using the Tree algorithm developed by Barnes & Hut (1986). The idea is to use a hierarchical multipole expansion algorithm that treats the distant particles as one single massive particle. The particles distributed in the simulation box are divided into subcells from the main *root* containing the full mass distribution to the *nodes* and *leaves* (with only one particle). As shown in Figure 2.1, each square starting from the *root* is subdivided into nodes of half the side-length until the smallest node is reached with only a single particle inside. Each cell, small or large, is characterized by the enclosed total mass and the center-of-mass of the particles. The force computation is done iteratively. The contribution of each node is added to the force and when highest accuracy is needed the node is "opened", meaning that multipole expansion is added at the force contribution by *walking up* the tree. The accuracy is determined by the opening criterion defined with the angle θ, usually fixed at 0.5 rad. This condition depends upon the cell length, l, and the distance D from the cell's centre-of-mass to the particle. If $l/D < \theta$ the contribution of the cell content to the total force acting on the considered particle is computed as a single particle. Otherwise the tree is "walked" until the above condition is fulfilled (the resolution criterion is satisfied) or until the single-particle cell is reached. It should be noted that the final force is only an approximation of the true value. With this method the force is evaluated faster, approximately with $N \log N$ iterations, but on the other hand at each timestep all the tree should be stored. This method is therefore the most memory consuming.

■ Hybrid methods

The GADGET-2 code that we will present in Section 2.3 is based on a hybrid method where the Tree and PM algorithms are used on different spatial scales. Within the hybrid *TreePM* scheme a spatial scale is introduced for splitting the force in two components. In Fourier space the potential is splitted in two components: (i) the long-range component computed on a mesh with the more accurate PM algorithm and (ii) the short-range component computed instead in the real space using the Tree algorithm. This mixed scheme gains the accuracy of the PM algorithm on large-scales and the sensitivity to the clustering on small-scales from the Tree algorithm. The dynamical range in this case is essentially unlimited. We report in Figure 2.2 the exponential growth of the number of particles used in the largest high resolution N–body simulations of cosmic structure formation in the years from 1970 to 2005 (Springel et al., 2005b). In the same Figure different symbols are used for different classes of computational algorithms. In particular, Tree algorithms have recently become competitive with the traditional P^3M codes, especially when combined with

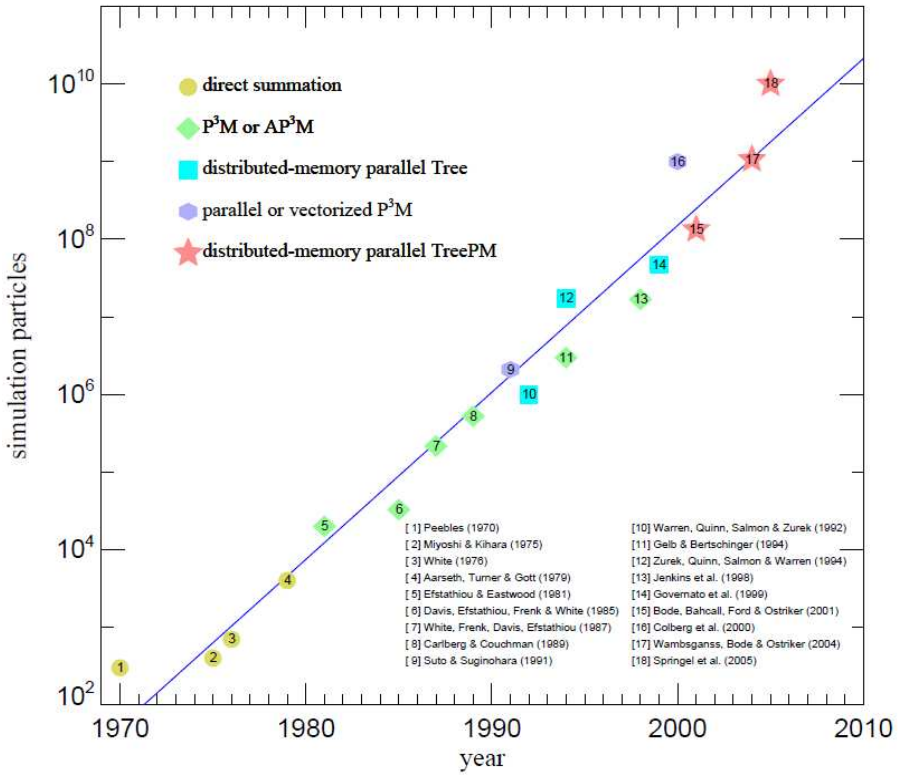

Figure 2.2: The number of particles in high resolution N-body simulations of cosmic structure formation as a function of the pubblication year (Moore's empirical law). The compilation is taken from Springel et al. (2005b). Only the largest simulations at a given time are shown with different symbols for the adopted computational algorithm. In this plot the exponential growth of the computational power can be appreciated (blue continuous line) together with the evolution in the used algorithms.

the PM algorithm.

Another hybrid method used in earlier simulations is the P^3M algorithm, where differently from TreePM the short-range force is computed by means of direct summation. Since the spatial resolution is limited by the grid spacing, within the P^3M algorithm a direct summation of the force among single particles is adopted on scales below the mesh size. An improvement of this technique is in the use of the adaptive mesh (Adaptive P^3M, see e.g. Couchman, 1991). In this case the dynamical range is increased by adapting the mesh in very clustered (dense) regions, refining it by varying the mesh size (AMR - Adaptive Mesh Refinement technique, see e.g. Kravtsov et al., 1997).

2.2.2. Initial conditions

The large scale galaxy distribution and the first light of the Cosmic Microwave Background observed by various experiments (e.g. Komatsu et al., 2009) support the picture where the growth of large scale structure in the Universe starts from the gravitational collapse of tiny perturbations in an initial Gaussian random density field. The spatial perturbations are described by the power spectrum of the density field (see Appendix 5.5) that depends on the cosmological model and on the nature of the Dark Matter.

To generate the initial conditions two steps are needed: (i) to create a uniform distribution of particles that samples an unperturbed portion of Universe and (ii) to generate initial fluctuations in the density field.

The random Gaussian field is obtained by generating a set of random phases and assuming a normally distributed amplitudes with variance defined by the desired spectrum. The particles can be arranged on a cubic regular grid that introduces a characteristic scale, the intergrid distance. To overcome the discretness effect introduced by this regular distribution, the particles can be positioned in a random way and the simulation can be run by reversing the gravitational force (changing the gravitational force to be repulsive instead of attractive) until a glass-like distribution is reached. In this configuration the gravitational force on each particle is close to zero (e.g White, 1994).

To generate density perturbations on the initial field the potential $\Phi(\mathbf{q})$ is computed on a grid $\mathbf{q}$ using the Fourier transform. The displacement field is then computed by means of the Zel'dovich approximation (Zel'Dovich, 1970) using the linear growth factor The details about the computation can be found in the Appendix 5.5.

In the region of interest a higher mass resolution can be achieved when the Zoomed Initial Condition (ZIC) technique is used (Tormen et al., 1997). Starting from the evolved low–resolution simulation the region of interest (e.g. a galaxy cluster) is selected. Particles within a defined sphere (usually few times the virial radius) are traced back to the unperturbed initial (Lagrangian) coordinates and replaced by a high number of low mass particles. The large-scale tidal field of the original simulation is preserved by interpolating masses and velocities of particles outside the high resolution region on a spherical grid. With this method the number of particles in the simulation is partially reduced, obtaining a higher mass resolution in the region of interest at a lower computational cost.

Boundary conditions. In simulations we often deal with periodic boundary conditions on opposite faces of the cubic simulation box in order to avoid artificial boundaries (e.g. Hernquist et al., 1991). The use of periodic boundaries implies that the average density of the simulation box is the same as the average density in the Universe, meaning that the we assume there are no perturbations at the scale

of the simulation volume or larger. The amplitude of fluctuations at the scale of the simulation volume (and larger) should be ignorable (e.g. Bagla & Ray, 2005). With respect to the vacuum boundary conditions (where the rest of the Universe is ignored) the periodic conditions can be more time consuming, since the tidal effects depend on the particles outside of the studied object.

2.2.3. Hydrodynamical methods

In computational astrophysics a variety of numerical codes couple N–body methods with hydrodynamical methods to follow at the same time the collisional baryonic matter and the collisionless dark matter. Hydrodynamical methods provide a suitable way to describe the behaviour of the gas component using fluid dynamics.

For this purpose the Navier-Stokes hydrodynamic equations have to be solved, namely the equation of

$$\begin{aligned}
\text{mass conservation (continuity eq.)} \quad & \frac{D\rho}{Dt} = \rho \nabla \cdot \mathbf{v} \\
\text{momentum conservation (Euler eq.)} \quad & \frac{D\mathbf{v}}{Dt} = -\frac{\nabla p}{\rho} + \text{viscosity terms} - \nabla\Phi \\
\text{and energy conservation} \quad & \frac{D\epsilon}{Dt} = -\frac{p}{\rho}\nabla \cdot \mathbf{v} + \text{viscosity terms} - \frac{\mathcal{L}(\epsilon,\rho)}{\rho}.
\end{aligned}$$

In this equations $D/Dt = \partial/\partial t + \mathbf{v} \cdot \nabla$ is the Lagrangian derivative, ρ is the gas density, ϵ is the energy density (per unit mass), p is the gas pressure, Φ the gravitational potential and the function $\mathcal{L}(\epsilon, \rho)$ represents the heating and dissipative processes of the gas. These equations are a close set of equations with the equation of state

$$p = (\gamma - 1)\rho\epsilon,$$

that relates pressure p to the internal energy per unit mass ϵ and where $\gamma = 5/3$ for the ideal monoatomic gas. The gravitational potential Φ is solved using one of the N–body methods described in the previous section.

To solve the equations of fluid dynamics the two possible approaches are the Lagrangian or the Eulerian method. In the Lagrangian method the single particle carries information on physical properties of a fluid element, while in the Eulerian method the equations are solved on a grid, that contains all the informations about the system.

■ Eulerian methods

The Eulerian method is a grid-based method that solves the fluid equations on a fixed spatial grid. The thermodynamical quantities as density, temperature, entropy,

pressure are defined in every point of the space. If a high density region needs to be sampled accurately, the Mesh Refinement technique can be applied, where the mesh length is suitably diminished. The grid can be adapted automatically with the Adaptive Mesh Refinement (AMR) technique. Some of the widely adopted AMR codes for numerical astrophysics and cosmology are ART (Kravtsov et al., 1997) and Enzo (O'Shea et al., 2004).

■ Lagrangian methods

The Lagrangian methods are particle-based methods, as pointed out before, where information on physical quantities of the system are carried by each particle. At difference with the Eulerian methods, fluid equations are solved for every single particle.

SPH - Smoothed Particle Hydrodynamics. The Smoothed Particle Hydrodynamics (SPH) technique (Lucy, 1977; Gingold & Monaghan, 1977) solves the Lagrangian form of Euler equations (see Monaghan, 1992; Monaghan & Price, 2004; Dolag et al., 2008a, for recent reviews). Variants of the Smoothed Particle Hydrodynamics are commonly used in numerical hydrodynamical cosmology. The code GADGET-2 , that is described in this Chapter (Sec. 2.3, uses the SPH technique to follow the dynamics of gas particles in simulations.

The basic idea of SPH is to sample the fluid with a finite number of particles (mass elements). The main advantage of this method is the good spatial resolution achieved in densest regions (with more particles and shorter mean interparticle distance), while low–density regions are poorly resolved.

The main drawback of this technique is the artificial viscosity that is used to capture shocks and that in the original implementation by Monaghan & Gingold (1983) smoothes out small-scale velocity fluctuations and damps random gas motions above the resolution limit. Dolag et al. (2005) study a new time–variable viscosity in the context of galaxy cluster formation, with which the difference between SPH and AMR simulations was reduced.

The smoothing kernel and basic equations. The field properties (e.g. density) are evaluated statistically using the *smoothing kernel*. Starting from the particle position, that is used as the interpolation centre, local field properties and their derivatives are computed with a weighted mean of the values of neighbour particles. This computation is done with a kernel that depends on the interparticle distance and on the *smoothing length* h that defines the maximum length of interaction. For scales $l << h$ the physical properties are smoothed out.

The general definition of a continuous fluid quantity $\langle A(\mathbf{x})\rangle$ computed with a smoothing kernel method is

$$\langle A(\mathbf{x})\rangle = \int W(\mathbf{x}-\mathbf{x}', h)A(\mathbf{x}')d\mathbf{x}',$$

where $W(\mathbf{x}-\mathbf{x}', h)$ is the smoothing kernel function, that collapses to a delta function when $h \to 0$,

$$\lim_{h\to 0} W(\mathbf{x}-\mathbf{x}', h) = \delta_D(\mathbf{x}-\mathbf{x}', h)$$

(h approaches zero when the number of particles approaches infinity) and is normalised so that $\int W(\mathbf{x}, h)d\mathbf{x} = 1$.

The continuous fluid quantities at the position of the i-th particle, $\langle A_i\rangle$, are written by means of the discretized values A_j at the position $\mathbf{x}_j$ of the particle with mass m_j and density ρ_j:

$$\langle A_i\rangle = \sum_{j=1}^{N} \frac{m_j}{\rho_j}\, A_j\, W(\mathbf{x}_i - \mathbf{x}_j, h).$$

In this equation the volume element $d\mathbf{x}$ was substituted by the particle volume m_j/ρ_j. Moreover, the kernel depends only on the distance modulus $|\mathbf{x}-\mathbf{x}'|$ between the particles.

The derivative of the interpolant $\langle A_i\rangle$ is obtained by applying the ∇ operator to the kernel function itself,

$$\nabla_i \langle A_i\rangle = \sum_{j=1}^{N} \frac{m_j}{\rho_j}\, A_j\, \nabla_i W(\mathbf{x}_i - \mathbf{x}_j, h).$$

In SPH simulations the most frequently used kernel is the B_2-spline kernel defined as

$$W(\vec{x}, h) = \frac{\sigma}{h^\nu}\begin{cases} 1 - 6\left(\frac{x}{h}\right)^2 + 6\left(\frac{x}{h}\right)^3, & 0 \le \frac{x}{h} < 0.5, \\ 2\left(1-\frac{x}{h}\right)^3, & 0.5 \le \frac{x}{h} < 1, \\ 0, & 1 \le \frac{x}{h}, \end{cases}$$

where ν is the dimensionality and σ is the normalisation,

$$\sigma = \begin{cases} \frac{16}{3}, & \nu = 1 \\ \frac{80}{7\pi}, & \nu = 2 \\ \frac{8}{\pi}, & \nu = 3. \end{cases}$$

The B_2-spline kernel is a kernel with compact support, because for distances above the smoothing length equals zero. Adopting this kernel saves computational time, since the particles over which the kernel is evaluated are only the neighbour ones.

The smoothing length depends on the precision we want to achieve. For a good resolution the minimum number of neighbours should be around $\sim 30-50$ particles. As we will see in Section 2.3, newer SPH codes adopt a smoothing length that varies from particle to particle and depends on local conditions. With this adaptive length the underdense regions are much better resolved.

More detailed explanation about the SPH technique can be found in Monaghan & Lattanzio (1985); Monaghan & Price (2004); Rosswog (2009); Dolag et al. (2008a).

2.3 The GADGET-2 code

The GADGET-2 code[2] is a MPI[3] parallelized code written by Volker Springel (Springel et al., 2001; Springel, 2005) and is widely used for cosmological simulations. The computational scheme used in our simulations is a hybrid between PM and Tree–SPH (Hernquist & Katz, 1989), where a fast PM scheme is used to compute gravitational forces on large scales, while the Tree algorithm is used to compute forces on smaller scales (e.g. Bagla, 2002). The evolution of the baryonic component depends on the gravitational interactions, which are followed by means of the Tree algorithm, and on the hydrodynamical interactions computed within the SPH scheme.

The GADGET-2 code is used to address a wide range of astrophysically interesting problems, from colliding and merging galaxies to the formation of large–scale structure. If physical processes such as radiative cooling and heating are included, one can study also the gas dynamics of the intergalactic medium as well as star formation and feedback processes.

2.3.1. The gravitational interaction

In GADGET-2 both memory and computational time are saved using the gravitational monopole and smartly keeping low the errors on the gravitational force. Working with monopoles allows also a simple dynamical tree update consistent with the time integration scheme.

The opening criterion in GADGET-2 is changed and a node with mass M, extension l and at distance r is opened when

$$\frac{GM}{r^2}\left(\frac{l}{r}\right)^2 \leq \alpha|\mathbf{a}|$$

[2]Galaxies with Dark matter and Gas intEracT, http://www.mpa-garching.mpg.de/gadget/

[3]The Message Passing Interface (MPI, www.mpi-forum.org) is a language-independent protocol used in high performance computing for passing informations between processors. MPI adapted codes are written for parallel computing, when the same code run on more processors simultaneously. MPI parallelized codes can reach high performances and are portable (Aoyama, Nakano 1999).

where $|\mathbf{a}|$ is the total acceleration of the particle in the previous time interval and α is a tolerance parameter. This criterion tries to limit the error on the absolute force by comparing the truncation error with the size of the total expected force. Moreover, the opening angle is small when the distribution is nearly homogeneous and becomes larger when denser structures are formed.

Beside the opening criterion one more condition is employed to avoid spurious errors on the particle–node force evaluation, when the particle is close to the node boundary:

$$|r_k - c_k| \leq 0.6l\,.$$

This condition is computed separately on each component of the position vector $\mathbf{r}$ of the particle and the position of the centre of mass of the node $\mathbf{c}$. Thus the requirement is that the particle lies outside a box 20% larger that the tree node (or 0.6 times the extension l).

In our simulations we employ the Tree–SPH algorithm (Xu, 1995; Bode et al., 2000; Bagla, 2002) similar to the implementation by Bagla & Ray (2003). More details can be found in the paper by Springel (2005).

2.3.2. Hydrodynamics

The GADGET-2 code uses the gridless SPH scheme, where the finite number of gas particles describe the fluid. Dynamical equations that are obtained from the Lagrangian form of the conservation laws are reported in Section 2.2.3 (e.g. Monaghan, 2006).

Smoothing length. The *smoothing length* h is defined for each particle in order to contain inside the kernel W volume constant mass. The length is thus adaptive for each particle and can be labelled as h_i. The relation that defined h_i of the i-th particle is

$$\frac{4\pi}{3}h_i^3\rho_i = N_{sph}\bar{m}$$

where N_{sph} is the number of neighbour particles over which the smoothing kernel is evaluated, ρ_i is the particle density and $\bar{m}$ is the mean particle mass. Once the number of neighbours N_{sph} is fixed (usually the adopted values are 32 or 64) the *smoothing length* is defined.

Equation of motion. Once the adaptive smoothing length is introduced, the equation of motion can be written as

$$\frac{d\mathbf{v}_i}{dt} = -\sum_{j=1}^{N} m_j \left[f_i \frac{P_i}{\rho_i^2}\nabla_i W_{ij}(h_i) + f_j \frac{P_j}{\rho_j^2}\nabla_i W_{ij}(h_j) \right],$$

where the smoothing kernel is shortened to $W_{ij}(h) = W(|\mathbf{r}_i - \mathbf{r}_j|, h)$ and the coefficients f_i and f_j have the form

$$f_i = \left[1 + \frac{h_i}{3\rho_i}\frac{\partial \rho_i}{\partial h_i}\right]^{-1} .$$

In the above equations P_i and P_j describe the particle pressure, where $P_i = A_i\rho_i^\gamma$ and for an ideal fluid A_i depends only on the entropy (it is conserved in adiabatic flows).

Artificial viscosity. We already mentioned that the main disadvantage of the SPH technique is the necessity to introduce an artificial viscosity to capture shocks of ideal gas flows.

The viscous force in GADGET-2 code is

$$\left.\frac{d\mathbf{v}_i}{dt}\right|_{visc} = -\sum_{j=1}^{N} m_j \Pi_{ij} \nabla_i \overline{W}_{ij} ,$$

where Π_{ij} (≥ 0) is a parametization of the viscosity (Monaghan 1997) and is non–zero when the i-th and j-th particle approach each other in the physical space. $\overline{W}_{ij}$ is instead the mean value of the two kernels $W_{ij}(h_i)$ and $W_{ij}(h_j)$. The entropy generation by shocks is captured by the viscosity term and included in the equation of motion, that can be written as

$$\frac{d\mathbf{v}_i}{dt} = -\sum_{j=1}^{N} m_j \left[f_i \frac{P_i}{\rho_i^2}\nabla_i W_{ij}(h_i) + f_j \frac{P_j}{\rho_j^2}\nabla_i W_{ij}(h_j) + \Pi_{ij}\nabla_i \overline{W}_{ij}\right] .$$

This formalism implemented in the GADGET-2 code explicitly conserves internal energy and entropy at the same time. A detailed derivation can be found in Springel & Hernquist (2003b) and Dolag et al. (2008a).

2.3.3. Cooling and star formation physics

■ Cooling processes

In the standard implementation the radiative cooling rates are included in the function $\mathcal{L}(\epsilon, \rho)$, introduced on page 40 in the energy conservation equation. To compute the radiative cooling the primordial gas is assumed to be optically thin and in ionisation equilibrium. The relevant cooling processes included in the computation are the two–body processes described in table 2.1, while three–body cooling processes are neglected (they are unimportant at the resolved densities). In addition

the GADGET-2 code assumes a cosmological ultraviolet (UV) radiation background (Haardt & Madau, 1996), that treats the reionization of atoms by quasars and first stars at $z \sim 6$ (e.g. Loeb & Barkana, 2001). This ionizing background is uniform and time dependent and can significantly alter the cooling function, especially at low densities. In Fig. 2.3 the cooling function is plotted as a function of gas temperature for different gas mmetallicity. This emphasises the importance of metals in simulations, especially in the context of the present Thesis, where we are looking for a suitable energetic process able to solve the 'overcooling' problem in central regions of simulated clusters.

The cooling rates are solved iteratively using the pre-computed cooling function by Sutherland & Dopita (1993) for different metallicities of the gas. As stressed by Dolag et al. (2008a), the computation of rate equations is decoupled from the hydrodynamics in the sense that the density is fixed across the computation time step, that is not related to the cooling time-scale. The effects of this approximation are not yet explored.

The radiative processes accounted in GADGET-2 are listed in Table 2.1 (for the detailed description see Katz et al. 1996).

PROCESSES	SPECIES
collisional excitation	H^0, He^+
collisional ionization	H^0, He^0, He^+
recombination	H^+, He^+, He^{++}
dielectric recombination	He^+
bremsstrahlung	all ions

Table 2.1: Table of cooling processes computed in the GADGET-2 code, described in Katz et al. (1996).

■ Star formation

Cooling is a runaway process that is partially mitigated by the formation of stars and by the feedback of supernovae explosions. The building block in GADGET-2 code is the treatment of the InterStellar Medium (ISM) within a sub-grid model implemented by Springel & Hernquist (2003a). Starting from the key theoretical work by McKee & Ostriker (2007) the ICM is described as a three–component medium: large fraction of the volume is filled with a low density tenuous gas, where reside cold and dense gas clouds, that eventually collapse and form stars. This ISM picture is maintained and regulated by the supernovae explosions.

The Springel & Hernquist (2003a) model is an effective subresolution model that uses spatially averaged properties to describe the ISM. The model describes the

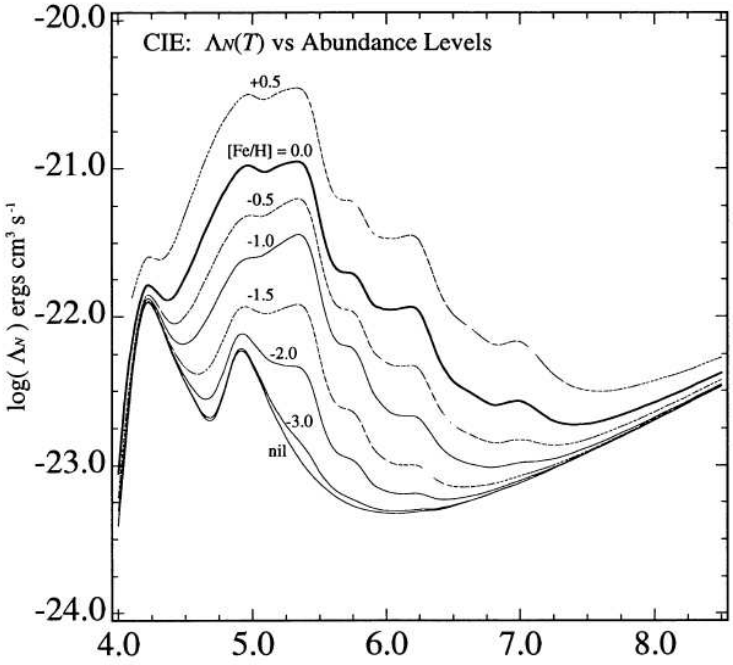

Figure 2.3: The cooling function for a plasma in Collisional Ionization Equilibrium (CIE) as a function of metallicity (Sutherland & Dopita, 1993). The curves represent the models for metallicities fixed at $[Fe/H] = 0.5, 0.0, -0.5, -1.0, -1.5, -2.0, -3.0$ and 0. The heavy solid line represents the cooling function for a plasma with solar metallicity.

global dynamical behaviour of the ISM and does not attempt to explicitly resolve the spatial multiphase structure of the ISM. In the model the cold clouds are assumed to be in pressure equilibrium with hot gas and represent the reservoir supplying matter that forms stars. The model is effective, since the conditions for self regulated star formation hold always.

The baryons in the ISM reside in one of the three allowed phases, with densities of ρ_h for the hot component, ρ_c for the cold clouds and $\rho_\star$ for stars. The three phases interact with each other by exchanging mass: hot gas cools down into clouds, stars are formed in the cooled gas clouds and end their life as supernovae explosions, that in turn restore mass and energy in the ambient gas.

Stars form from the collapse of cold gas clouds and the star formation rate is thought to follow the Schmidt law (Schmidt, 1959):

$$\psi(t) \propto \rho_{gas}^{n},$$

where $\psi(t)$ is the star formation rate and the exponent n is calibrated by observa-

tions. In our case, the star formation is regulated by the equation

$$\frac{d\rho_\star}{dt} = -\frac{d\rho_c}{dt} = \frac{\rho_c}{t_\star}\,,$$

where $t_\star$ is the characteristic time of star formation. The assumption used by Springel & Hernquist (2003a) is that $t_\star$ is proportional to the local dynamical time of the gas. This results in a Schmidt–type law for the dependence of star formation on density,

$$t_\star = t_0^\star \left(\frac{\rho}{\rho_{th}}\right)^{-1/2}\,,$$

where the timescale $t_0^\star$ and the threshold density ρ_{th} are two additional parameters of the model.

The total gas density ρ_{gas} is a sum of the hot and cold ISM component averaged on a constant volume, $\rho_{gas} = \rho_h + \rho_c$. The energy per unit mass of the gas is described as $\epsilon = \rho_h u_h + \rho_c u_c$, where u_h and u_c are the energy densities of the hot and cold phases.

Some of the stars can explode as supernovae and load a fraction β of their mass to the ambient medium and heat it up with the energy released by the explosion. The equation of star formation is therefore properly changed to

$$\frac{d\rho_\star}{dt} = (1-\beta)\frac{\rho_c}{t_\star}\,.$$

Due to the released energy the gas clouds evaporate with a rate proportional to the mass of the supernovae,

$$\left.\frac{d\rho_c}{dt}\right|_{EV} = A\beta\frac{\rho_c}{t_\star}\,,$$

where the efficiency of evaporation A depends on the density of the cold gas.

Moreover, also the thermal instability (TI) that produces cold clouds is accounted for by the equation

$$\left.\frac{d\rho_c}{dt}\right|_{TI} = \left.\frac{d\rho_h}{dt}\right|_{IT} = \frac{\Lambda(\rho_h, u_h)}{u_h - u_c}\,,$$

where $\Lambda(\rho_h, u_h)$ is the cooling function.

The variation of the specific energy of both phases of the gas is described by the equations

$$\frac{\mathrm{d}}{\mathrm{d}t}(\rho_c u_c) = -\frac{\rho_c}{t_\star}u_c - A\beta\frac{\rho_c}{t_\star}u_c + \frac{(1-f)u_c}{u_h - u_c}\Lambda_{net}(\rho_h, u_h) \qquad (2.1)$$

$$\frac{\mathrm{d}}{\mathrm{d}t}(\rho_h u_h) = \beta\frac{\rho_c}{t_\star}(u_{SN} + u_c) + A\beta\frac{\rho_c}{t_\star}u_c - \frac{u_h - f u_c}{u_h - u_c}\Lambda_{net}(\rho_h, u_h)\,, \qquad (2.2)$$

where $u_{SN} = \epsilon_{SN}(1-\beta)/\beta$ is the energy density released by the already formed stars exploding as supernovae with the mean energy of $\epsilon_{SN} = 10^{51}$ erg and f is the parameter that distinguishes between the thermal instability regime ($f = 0$) and the normal cooling ($f = 1$).

The stellar feedback by supernovae leads to a self–regulation of the star formation.

■ Star formation threshold

In a self–regulated regime the effective pressure P_{eff} of the medium is expected to be constant in time. It can be described by the equation

$$P_{eff} = (\gamma - 1)(\rho_h u_h + \rho_c u_c) = (\gamma - 1)\rho[(1-x)u_h + x\, u_c]\,,$$

where $x = \rho_c/\rho$ is the mass fraction of cold clouds and the term in square brackets is the effective mass–weighted 'temperature' u_{eff} of the medium.

In their model Springel & Hernquist (2003a) assume that the effective pressure should be a continuous function of density when star–formation is in the self–regulated regime. The gas below the treshold cools down to temperatures of 10^4 K, when becomes neutral. Therefore, the density treshold for the star formation ρ_{th} is computed imposing the condition that u_{eff} is fixed at the specific energy corresponding to the temperature of 10^4 K. In this case the the value for the density treshold, expressed in hydrogen number density, is $n_H = 0.1$ cm^{-3}.

■ Stochastic star formation

In the star formation recipe implemented by Katz (1992) the gas particle looses some of its mass to form a new star particle. However for cosmological simulations of wide regions of the Universe this kind of implementation can produce a huge amount of particles and increase the computational cost of the simulation.

The GADGET-2 code uses instead a stochastical star formation introduced by Katz et al. (1996). Under the conditions described above a gas particle can turn into a *star forming* particle, that is formed by two parts: the collisional gas component and the non-collisional star component. The particle can have a schizophrenic behaviour, since only the gas component is hydrodynamically coupled to the surrounding particles (e.g. in the presence of shocks gas will slow down, while stars will not experience the same effect). To avoid this spurious interactions, the number of star particles (or star *generations*, N_g) that are spawned from the star forming particle are usually 2 or 3.

At every timestep Δt a new star generation with mass $m_\star = m_{gas}/N_g$ can be created if a randomly generated number q is lower than

$$p = \frac{m_{gas}}{m_\star}\left[1 - exp\left(-\frac{(1-\beta)x\Delta t}{t_\star}\right)\right],$$

where m_{gas} is the mass of the gas particle and x is the mass fraction locked in cold clouds. In this way the uncontrolled proliferation of star particles is avoided as well as the artificial dynamical coupling of the gas with stars.

Each star generation is considered as a Simple Stellar Population (SSP), a population of coeval stars formed out from the same gas and having the same initial chemical composition. For each population the fraction of stars that end up in SN Ia or SN II is easily computed once a stellar Initial Mass Function is assumed. Each star particle has at the end a mass of about $10^6 - 10^8 M_\odot$, depending on the resolution reached in a typical simulation.

2.3.4. The equations of chemical evolution

The key ingredients that define a model of chemical evolution are

- the SNe explosion rates
- the adopted stellar lifetime function
- the adopted stellar yields
- the stellar Initial Mass Function (IMF)

The chemo–dynamical model described below is implemented by Tornatore et al. (2007a) and is based on the equations of chemical evolution from the textbook by Matteucci (2003).

■ Supernovae explosion rates

Type Ia supernovae. We provide here below a short description of how Type Ia SN are included in a model of chemical evolution. For a comprehensive review of analytical formulations we refer to the paper by Greggio (2005). Following Greggio & Renzini (1983), we assume here that SNIa arise from stars belonging to binary systems, having mass in the range 0.8–8 $M_\odot$. Accordingly, in the single–degenerate white dwarf scenario (Nomoto & et al., 2000), the rate of explosions of SNIa can be written as

$$R_{\rm SN\,Ia}(t) \;=\; A \int_{M_{\rm B,inf}}^{M_{\rm B,sup}} \phi(m_{\rm B}) \int_{\mu_{\rm m}}^{\mu_{\rm M}} f(\mu)\,\psi(t-\tau_{m_2})\,{\rm d}\mu\,{\rm d}m_{\rm B}\,. \qquad (2.3)$$

In the above equation, $\phi(m)$ is the IMF, $m_{\rm B}$ is the total mass of the binary system, m_2 is the mass of the secondary companion, τ_m is the mass–dependent life–time and $\psi(t)$ is the star formation rate. The variable $\mu = m_2/m_{\rm B}$ is distributed according to the function $f(\mu)$, while A is the fraction of stars in binary systems of that particular type to be progenitors of SN Ia (see Matteucci & Recchi 2001 for more details). For instance, in the model by Greggio & Renzini (1983) μ varies in the range between $\mu_{\rm m}$ and $\mu_{\rm M} = 0.5$, with $\mu_{\rm m} = \max\left[m_2(t)/m_{\rm B}, (m_{\rm B} - 0.5 M_{\rm BM})/m_{\rm B}\right]$, where $m_2(t)$ is the mass of the companion which dies at the time t, according to the chosen life-time function. Furthermore, let $M_{\rm Bm}$ and $M_{\rm BM}$ be the smallest and largest value allowed for the progenitor binary mass $m_{\rm B}$. Then, the integral over $m_{\rm B}$ runs in the range between $M_{\rm B,inf}$ and $M_{\rm B,sup}$, which represent the minimum and the maximum value of the total mass of the binary system that is allowed to explode at the time t. These values in general are functions of $M_{\rm Bm}$, $M_{\rm BM}$, and $m_2(t)$, which in turn depends on the star formation history. The exact functional dependence is defined by the SN Ia progenitor model. For instance, in the model by Greggio & Renzini (1983) it is $M_{\rm B,inf} = \max[2m_2(t), M_{\rm Bm}]$ and $M_{\rm B,sup} = 0.5 M_{\rm BM} + m_2(t)$. Under the assumption of a short duration burst of star formation, the function $\psi(t)$ can be approximated with a Dirac δ–function. This case applies to hydrodynamical simulations, which include star formation, where the creation of a SSP is described by an impulsive star formation event, while more complex descriptions should take into account the continuous star formation history $\psi(t)$. Under the above assumption for $\psi(t)$ and using the functional form of $f(\mu)$ derived from statistical studies of the stellar population in the solar neighbourhood (Tutukov & Iungelson, 1980; Matteucci & Recchi, 2001), we find

$$R_{\rm SN\,Ia}(t) \;=\; -\frac{{\rm d}m_2(t)}{{\rm d}t}\bigg|_{m_2 \equiv \tau^{-1}(t)} 24\, m_2^2\, A \int_{M_{\rm Bm}}^{M_{\rm BM}} \phi(m_{\rm B}) \frac{1}{m_{\rm B}^3} {\rm d}m_{\rm B}\,.$$

Since the current understanding of the process of star formation does not allow to precisely determine the value of A, its choice can be fixed from the requirement of reproducing a specific observation, once the form of the IMF is fixed. For instance, Matteucci & Gibson (1995) found that $A = 0.1$ was required to reproduce the observed iron enrichment.

Supernova Type II and intermediate and mass stars. Computing the rates of SN II and intermediate and low mass stars (ILMS) is conceptually simpler, since they are driven by the lifetime function $\tau(m)$ convolved with the star formation history $\psi(t)$ and multiplied by the IMF $\phi(m = \tau^{-1}(t))$. Again, since $\psi(t)$ is a delta–function for the SSP used in simulations, the SN II and ILMS rates read

$$R_{SN\,II|ILMS}(t) = \phi(m(t)) \times \left(-\frac{{\rm d}\,m(t)}{{\rm d}\,t}\right)$$

where $m(t)$ is the mass of the star that dies at time t. We note that the above expression must be multiplied by a factor of $(1-A)$ for rates concerning the Asimptotic Giant Branch (AGB) stars, if the interested mass $m(t)$ falls in the same range of masses which is relevant for the secondary stars of SN Ia binary systems.

In order to compute the metal release by stars (binary systems in case of SN Ia) of a given mass we need to take into account the yields $p_{Z_i}(m, Z)$, which provide the mass of the element i produced by a star of mass m and initial metallicity Z. Then, the equation which describes the evolution of the mass $\rho_i(t)$ for the element i, holding for a generic form of the star formation history $\psi(t)$, reads:

$$\begin{aligned}
\dot{\rho}_i(t) &= -\psi(t) Z_i(t) \\
&+ A \int_{M_{\rm Bm}}^{M_{\rm BM}} \phi(m) \left[\int_{\mu_{\rm min}}^{0.5} f(\mu) \psi(t - \tau_{m_2}) p_{Z_i}(m, Z)\, {\rm d}\mu \right] {\rm d}m \\
&+ (1-A) \int_{M_{\rm Bm}}^{M_{\rm BM}} \psi(t - \tau(m)) p_{Z_i}(m, Z) \varphi(m)\, {\rm d}m \\
&+ \int_{M_{\rm L}}^{M_{\rm Bm}} \psi(t - \tau(m)) p_{Z_i}(m, Z) \varphi(m)\, {\rm d}m \\
&+ \int_{M_{\rm BM}}^{M_{\rm U}} \psi(t - \tau(m)) p_{Z_i}(m, Z) \varphi(m)\, {\rm d}m.
\end{aligned} \tag{2.4}$$

In the above equation, $M_{\rm L}$ and $M_{\rm U}$ are the minimum and maximum mass of a star, respectively. Commonly adopted choices for these limiting masses are $M_{\rm L} \simeq 0.1$ M$_\odot$ and $M_{\rm U} \simeq 100$ M$_\odot$. The term in the first line of Eq. 2.4 accounts for the metallicity sink due to the locking of metals in the newborn stars. The term in the second line accounts for metal ejection contributed by SN Ia. The terms in the third and fourth lines describe the enrichment by mass–loss from intermediate and low mass stars, while the last line accounts for ejecta by SN II.

■ The lifetime function

Different choices for the mass–dependence of the life–time function have been proposed in the literature. For instance, Padovani & Matteucci (1993) (PM93 hereafter) proposed the expression

$$\tau(m) = \begin{cases} 10^{[(1.34 - \sqrt{1.79 - 0.22(7.76 - \log(m))})/0.11] - 9} & \text{for } m \leq 6.6 \text{ M}_\odot \\ 1.2\, m^{-1.85} + 0.003 & \text{otherwise.} \end{cases} \tag{2.5}$$

An alternative expression has been proposed by Maeder & Meynet (1989) (MM89 hereafter), and extrapolated by Chiappini et al. (1997) to very high (> 60 M$_\odot$) and very low (< 1.3 M$_\odot$) masses:

$$\tau(m) = \begin{cases} 10^{-0.6545 \log m + 1} & m \leq 1.3 \text{ M}_\odot \\ 10^{-3.7 \log m + 1.351} & 1.3 < m \leq 3 \text{ M}_\odot \\ 10^{-2.51 \log m + 0.77} & 3 < m \leq 7 \text{ M}_\odot \\ 10^{-1.78 \log m + 0.17} & 7 < m \leq 15 \text{ M}_\odot \\ 10^{-0.86 \log m - 0.94} & 15 < m \leq 53 \text{ M}_\odot \\ 1.2 \times m^{-1.85} + 0.003 & \text{otherwise.} \end{cases} \tag{2.6}$$

The main difference between these two functions concerns the life–time of low mass stars ($< 8\,$M$_\odot$). The MM89 life–time function delays the explosion of stars with mass $\gtrsim 1$ M$_\odot$, while it anticipates the explosion of stars below 1 M$_\odot$ with respect to the PM93 life–time function. Only for masses below 1 M$_\odot$ does the PM93 function predict much more long–living stars. This implies that different life–times will produce different evolution of both absolute and relative abundances (we refer to Romano et al. (2005) for a detailed description of the effect of the lifetime function in models of chemical evolution).

We point out that the above lifetime functions are independent of metallicity, whereas in principle this dependence can be included in a model of chemical evolution (e.g., Portinari et al. 1998). For instance, Raiteri et al. (1996) used the metallicity–dependent lifetimes as obtained from the Padova evolutionary tracks (Bertelli et al., 1994).

■ Stellar yields

The stellar yields specify the quantity $p_{Z_i}(m, Z)$, which appears in Eq. 2.4 and, therefore, the amount of different metal species which are released during the evolution of a SSP. A number of different sets of yields have been proposed in the literature, such as those by Renzini & Voli (1981), van den Hoek & Groenewegen (1997), Marigo (2001) for the ILMS and those by Nomoto et al. (1997), Iwamoto et al. (1999), Thielemann et al. (2003) for SN Ia. As for SN II, there are many proposed sets of metallicity–dependent yields; among others, those by Woosley & Weaver (1995), by Portinari et al. (1998), by Chieffi & Limongi (2004), which are based on different assumptions of the underlying model of stellar structure and evolution.

As an example of the differences among different sets of yields, we show in the left panel of Fig. 2.4 the ratios between the abundances of different elements produced by the SN II of a SSP, as expected from Woosley & Weaver (1995) and from Chieffi

& Limongi (2004). Different curves and symbols here correspond to different values of the initial metallicity of the SSP. Quite apparently, the two sets of yields provide significantly different metal masses, by an amount which can sensitively change with initial metallicity. This illustrates how a substantial uncertainty exists nowadays about the amount of metals produced by different stellar populations. There is no doubt that these differences between different sets of yields represent one of the main uncertainties in any modelling of the chemical evolution of the ICM.

■ The initial mass function

The initial mass function (IMF) is one of the most important quantities in a model of chemical evolution. It directly determines the relative ratio between SN II and SN Ia and, therefore, the relative abundance of α–elements and Fe–peak elements. The shape of the IMF also determines how many long–living stars will form with respect to massive short–living stars. In turn, this ratio affects the amount of energy released by SNe and the present luminosity of galaxies, which is dominated by low mass stars, and the (metal) mass–locking in the stellar phase.

As of today, no general consensus has been reached on whether the IMF at a given time is universal or strongly dependent on the environment, or whether it is time–dependent, i.e. whether local variations of the values of temperature, pressure and metallicity in star–forming regions affect the mass distribution of stars.

The IMF $\phi(m)$ is defined as the number of stars of a given mass per unit logarithmic mass interval. A widely used form is

$$\phi(m) \, = \, dN/d\log m \propto m^{-x(m)} \, . \tag{2.7}$$

If the exponent x in the above expression does not depend on the mass m, the IMF is then described by a single power–law. The most famous and widely used single power–law IMF is the Salpeter (1955) one that has $x = 1.35$. Arimoto & Yoshii (1987, AY hereafter) proposed an IMF with $x = 0.95$, which predicts a relatively larger number of massive stars. In general, IMFs providing a large number of massive stars are usually called top–heavy. More recently, different expressions of the IMF have been proposed in order to model a flattening in the low–mass regime that is currently favoured by a number of observations. Kroupa (2001) introduced a multi–slope IMF, which is defined as

$$\phi(m) \, \propto \, \begin{cases} m^{-1.3} & m \geq 0.5\,\mathrm{M}_\odot \\ m^{-0.3} & 0.08 \leq m < 0.5\,\mathrm{M}_\odot \\ m^{\,0.7} & m \leq 0.08\,\mathrm{M}_\odot \end{cases} \tag{2.8}$$

Chabrier (2003) proposed another expression for the IMF, which is quite similar to that one proposed by Kroupa

$$\phi(m) \propto \begin{cases} m^{-1.3} & m > 1\,\mathrm{M}_\odot \\ e^{\frac{-(\log(m)-\log(m_c))^2}{2\,\sigma^2}} & m \leq 1\,\mathrm{M}_\odot \end{cases} \tag{2.9}$$

Theoretical arguments (e.g. Larson 1998) suggest that the present–day characteristic mass scale, where the IMF changes its slope, $\sim 1\ \mathrm{M}_\odot$ should have been larger in the past, so that the IMF at higher redshift was top–heavier than at present.

While the shape of the IMF is determined by the local conditions of the inter–stellar medium, direct hydrodynamical simulations of star formation in molecular clouds are only now approaching the required resolution and sophistication level to make credible predictions on the IMF (e.g., Bonnell et al. 2006, Padoan et al. 2007; see McKee & Ostriker 2007 for a detailed discussion).

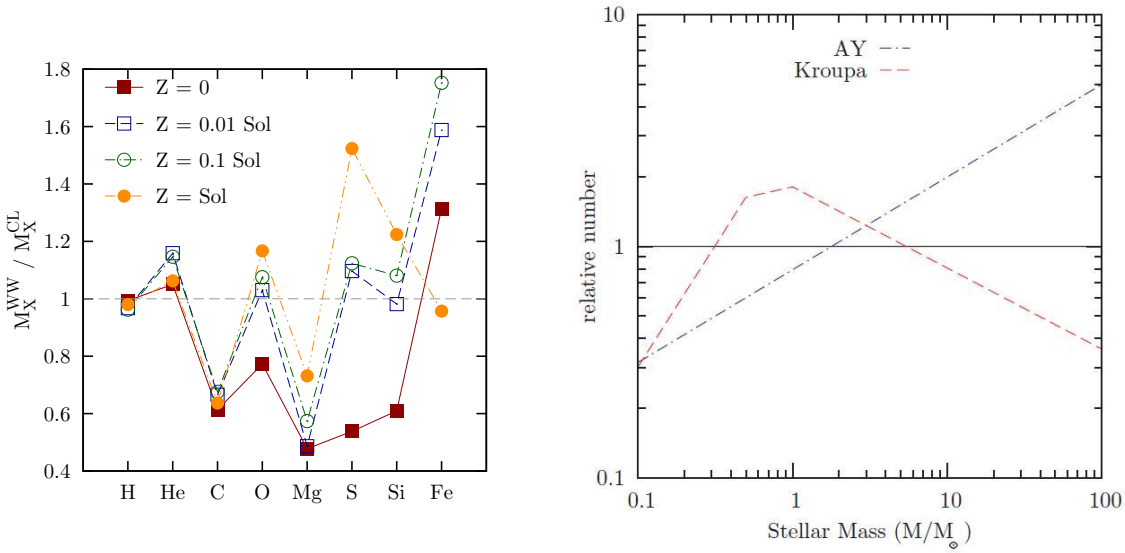

Figure 2.4: Left panel: the ratio $M_j^{\mathrm{WW}}/M_j^{\mathrm{CL}}$ between the mass of species j, produced by the SN II of a SSP, when using the two sets of yields by Woosley & Weaver (1995) and by Chieffi & Limongi (2004) for different values of the initial SSP metallicity (Tornatore et al., 2007a). Different symbols are for different values of the initial metallicity of the SSP, as reported by the labels. **Right panel:** The relative role of different stellar Initial Mass Functions (IMFs) (from Tornatore et al., 2007a). The IMFs are normalised to the value of the Salpeter IMF (constant black line). The other two IMFs are the Arimoto–Yoshii Arimoto & Yoshii (1987) IMF labelled AY (blue dot–dashed line) and the Kroupa (2001) IMF (red dashed line).

We show in the right panel of Fig. 2.4 the number of stars, as a function of their mass, predicted by different IMFs, relative to those of the Salpeter IMF. As

expected, the AY IMF predicts a larger number of high–mass stars and, correspondingly, a smaller number of low–mass stars, the crossover taking place at $\simeq 2\ M_{\odot}$. As a result, we expect that the enrichment pattern of the AY IMF will be characterised by a higher abundance of those elements, like oxygen, which are mostly produced by SN II. Both the Kroupa and the Chabrier IMFs are characterised by a relative deficit of very low–mass stars and a mild overabundance of massive stars and ILMS. Correspondingly, an enhanced enrichment in both Fe–peak and α elements like oxygen is expected, mostly due to the lower fraction of mass locked in ever–living stars. For reference we also show a different IMF, also proposed by Kroupa et al. (1993), that exhibits a deficit in both very low– and high–mass stars; for this kind of IMF a lower α / Fe ratio with respect to the Salpeter IMF is expected.

Different variants of the chemical evolution model have been implemented by different authors in their simulation codes. For instance, the above described model of chemical evolution has been implemented with minimal variants by Kawata & Gibson (2003a), Kobayashi (2004), who also included the effect of hypernova explosions, and Tornatore et al. (2007a), while Tornatore et al. (2007b) also included the effect of metal enrichment from low–metallicity (Pop III) stars. Raiteri et al. (1996) and Valdarnini (2003) also used a similar model, but neglected the contribution from low- and intermediate-mass stars. Mosconi et al. (2001) and Scannapieco et al. (2005) neglected delay times for SN II, assumed a fixed delay time for SN Ia and neglected the contribution to enrichment from low- and intermediate-mass stars.

Clearly, a delicate point in hydrodynamical simulations is deciding how metals are distributed to the gas surrounding the star particles. The physical mechanisms actually responsible for enriching the inter–stellar medium (ISM; e.g., stellar winds, blast waves from SN explosions, etc.) take place on scales which are generally well below the resolution of current cosmological simulations of galaxy clusters (see Schindler & Diaferio, 2008). For this reason, the usually adopted procedure is that of distributing metals according to the same kernel which is used for the computation of the hydrodynamical forces, a choice which is anyway quite arbitrary. Mosconi et al. (2001) and Tornatore et al. (2007a) have tested the effect of changing in different ways the weighting scheme to distribute metals and found that final results on the metal distribution are generally rather stable. Although this result is somewhat reassuring, it is clear that this warning on the details of metal distribution should always be kept in mind, at least until our simulations will have enough resolution and accurate description of the physical processes determining the ISM enrichment (Schindler & Diaferio, 2008).

2.3.5. Feedback models

■ **Winds**

The superwinds that are observed in galaxies (e.g. Martin, 1999) are originally modelled in GADGET-2 by Springel & Hernquist (2003a) with the energy-driven scheme. This scheme is also adopted in our simulations. However, a new momentum-driven scheme was recently implemented by Davé et al. (2008) and Tescari et al. (2009), and will be shortly described in the following.

Energy-driven winds. The model for energy-driven winds was developed within the multiphase model by Springel & Hernquist (2003a). Superwinds were initially proposed as an efficient mechanism to thermalize the energy ejected by SNe and to regulate star formation, thus acting against the overcooling problem. The phenomenological description of the winds is based on the work by Martin (1999), where the warm gas uplifted by supershells (driven by SNe explosions) was found to be proportional to the star formation rate in galaxies.

The wind momentum and kinetic energy are regulated by two parameters. The first defines the mass upload, that according to Martin (1999) is proportional to the star formation rate $\dot{M}_\star$,

$$\dot{M}_W = \eta \dot{M}_\star,$$

where we assume $\eta = 3$. A fraction of energy coming from SNII is used to power the wind, with an energy rate of

$$\frac{1}{2}\dot{M}_W v_W^2 = \chi \epsilon_{SNe} \dot{M}_\star,$$

where v_W is the wind velocity, χ is the fraction of SNe energy coupled to winds and ϵ_{SNe} is the energy feedback provided by SNe under the istantaneous recycling approximation (IRA) for each $M_\odot$ of stars formed.

Gas particles to be uploaded in winds are selected stochastically in the time interval Δt among the multiphase particles, with a probability p_W proportional to their SFR,

$$p_W = 1 - \exp\left[-\frac{\eta(1-\beta)x\Delta t}{t_\star}\right] = 1 - \exp\left[-\frac{\eta \dot{M}_\star \Delta t}{M_{gas}}\right].$$

The velocity vector of the gas particle is then $\mathbf{v}' = \mathbf{v} + v_W \mathbf{n}$ where $\mathbf{v}$ is the initial velocity vector of the particle and $\mathbf{n}$ determines the wind direction and is prependicular to the galaxy rotating disc (determined by the gradient of the gravitational potential, $\nabla\phi \times \mathbf{v}$). Multiphase particles eligible to become wind particles originate from star forming regions and are highly enriched. They are temporarily decoupled

from the dense interstellar medium. Two parameters define the decoupling: ρ_{dec} that defines the minimum density that should be reached by the particle to couple hydrodynamically with the surrounding particles and l_{dec} that defines the maximum travelling length of a particle before being hydrodynamically coupled. ρ_{dec} is assumed to be 0.5 times the threshold for star formation, while l_{dec} is assumed to be $10h^{-1}$ kpc. This decoupling scheme was recently discussed by Dalla Vecchia & Schaye (2008) using high–resolution simulations of galactic disks. Comparing coupled and decoupled winds they found that the coupled winds drive a large–scale bipolar outflow from the dwarf galaxy and a clumpy galactic fountain from the massive galaxy, while the decoupled winds produce isotropic outflows in both cases.

The energy driven winds originally introduced by Springel & Hernquist (2003a) are defined by two parameters, η and χ. In our case we fixed instead the wind velocity v_W. Once fixed to 500 km s^{-1} and assuming that each SN provides 10^{51} ergs in energy, the adopted wind velocity value corresponds to $\epsilon_{SNe} \sim 1$ in the case of a Salpeter stellar IMF.

Momentum–driven winds. The momentum–driven winds have been implemented in GADGET-2 by Davé et al. (2008); Davé & Oppenheimer (2007) to study the properties of the high–redshift InterGalactic Medium. A similar implementation was recently performed also by Tescari et al. (2009).

The reason to switch from energy to momentum driven winds is based on more recent observations by Martin (2005) that found the wind velocity in galaxies to be related to the their circular velocity. The theoretical explanation for this is that the radiation pressure from the outburst in galaxies drives an outflow that transfers momentum to a component (e.g. dust) that is coupled to the gas. The pressure is thus acting to drag the gas out from the galaxy.

In this case the relevant parameters v_W and η are defined in the following way:

$$v_w = 3\sigma\sqrt{f_L - 1}$$

and

$$\eta = \frac{\sigma_0}{\sigma},$$

where f_L is the luminosity factor in units of galactic Eddington luminosity and σ_0 the normalisation of the mass loading factor. We refer to the work by Davé et al. (2008) and Tescari et al. (2009) for a more detailed description.

■ AGN feedback

We already discussed what is the observed effect of AGN feedback on the ICM properties in Sec. 2.4.4. In this section we will present the current implementation of black hole growth and energy feedback by Springel et al. (2005a); Di Matteo et al.

(2005, 2008) and by Sijacki et al. (2007). The implementation by Di Matteo et al. (2008) was further modified for the purposes of the present Thesis.

The theoretical link between galaxy mergers and starburst events as well as active AGN phases have been established by a number of observations (e.g. McNamara & Nulsen, 2007). Hydrodynamical simulations of galaxy mergers (e.g. Di Matteo et al., 2005) predict that these events are responsible for the rapid growth of the central black hole (e.g. Kapferer et al., 2007b; Springel et al., 2005a). However, the lack of spatial resolution in hydrodynamical simulations prevents one from resolving the properties of the accretion around the black hole in the galactic nucleus or to consider other channels of energy release, as for example jets.

If we consider a black hole (BH hereafter) with initial mass M_{BH} that accretes spherically from a stationary and uniform gas distribution, the gravitational radius r_{BH} is computed with the Bondi formula (Bondi, 1952)

$$r_{BH} = \frac{GM_{BH}}{c_s^2},$$

where c_s is the sound speed and G the gravitational constant. For a BH with mass M_{BH} the gravitational radius is

$$r_{BH} = 50pc \left(\frac{M_{BH}}{10^7 M_\odot}\right) \left(\frac{c}{30kms^{-1}}\right)^{-2},$$

while the Schwarzschild radius is

$$r_S = \frac{2GM_{BH}}{c^2} = 10^{-6}pc \left(\frac{M_{BH}}{10^7 M_\odot}\right).$$

The simulations we will use do not achieve enough spatial resolution to properly treat the BH growth at the Bondi radius.

The procedure adopted by Springel et al. (2005a) is to use a coarse–grained description with a subresolution model. The basic assumption in this model are:

- BHs are defined as collisionless particles that can grow either by accreting gas or by merging with other black holes;
- a fraction of their radiative energy released by the accreted material is assumed to be coupled thermally to the surrounding gas.
- BH particles with a certain mass are seeded using a friend–of–friends algorithm that identifies halos with a given mass (the procedure is described below).

The unresolved accretion on the BH is related to the resolved gas distribution by means of the Bondi–Hoyle–Lyttleton formula (Hoyle & Lyttleton, 1939; Bondi & Hoyle, 1944; Bondi, 1952), where the accretion on the BH is described by:

$$\dot{M}_B = \frac{4\pi\alpha G^2 M_{BH}^2 \rho}{(c_s^2 + v^2)^{3/2}},$$

where α is a dimensionless parameter and v is the velocity of the BH relative to the gas. The accretion on the BH is Eddington–limited, where the Eddington accretion rate is

$$\dot{M}_{Edd} = \frac{4\pi G M_{BH} m_p}{\epsilon_r \sigma_T c},$$

with m_p as the proton mass, σ_T the Thomson cross section and ϵ_r the radiative efficiency.

The radiative efficiency assumes a fixed value and represents the fraction of energy released by accretion of gas onto BH that goes into radiation,

$$L_r = \epsilon_r \dot{M}_{BH} c^2.$$

Following Springel et al. (2005a) we assume $\epsilon_r = 0.1$, that is the mean value for a radiatively efficient accretion onto a Schwarzschild BH (Shakura & Syunyaev, 1973). The radiative efficiency depends on the accretion disk physics and can have values of $\epsilon_r \sim 0.2 - 0.3$ for magnetised disk accretion models (Krolik et al., 2005; Hawley et al., 2007) or $\epsilon_r \sim 0.3$ for non–magnetised disk accretion (Thorne, 1974). In any case, radiatively inefficient accretion phases are ignored.

In the original AGN feedback version included in GADGET-2 the accretion is limited by the Eddington rate,

$$\dot{M}_{BH} = \min(\dot{M}_{Edd}, \dot{M}_B)\,.$$

However in Di Matteo et al. (2008), where the growth of black holes in the 'quasar' mode was explored with direct cosmological simulations, also the accretion at super Eddington rates ($2 \times \dot{M}_{Edd}$) was considered.

A fraction ϵ_f of the radiated luminosity L_r is coupled thermally and isotropically with the surrounding gas as

$$\dot{E}_{feed} = \epsilon_f L_r = \epsilon_f \epsilon_r \dot{M}_{BH} c^2.$$

As we will discuss in the following, the most important parameter for this AGN feedback prescription is the coupling fraction ϵ_f. Based on the theoretical work by Churazov et al. (2005), AGN should be characterized by two 'main' modes (although observations reveal also intermediate states):

- *quasar mode:* at high redshift and high accretion rate the bulk of AGN feedback is powering luminous quasars, where only a small fraction of the power is coupled thermally to the gas;

- *radio mode:* at low redshift the accretion rate is low and the feedback is radiatively inefficient, but powers outflows (mechanical feedback).

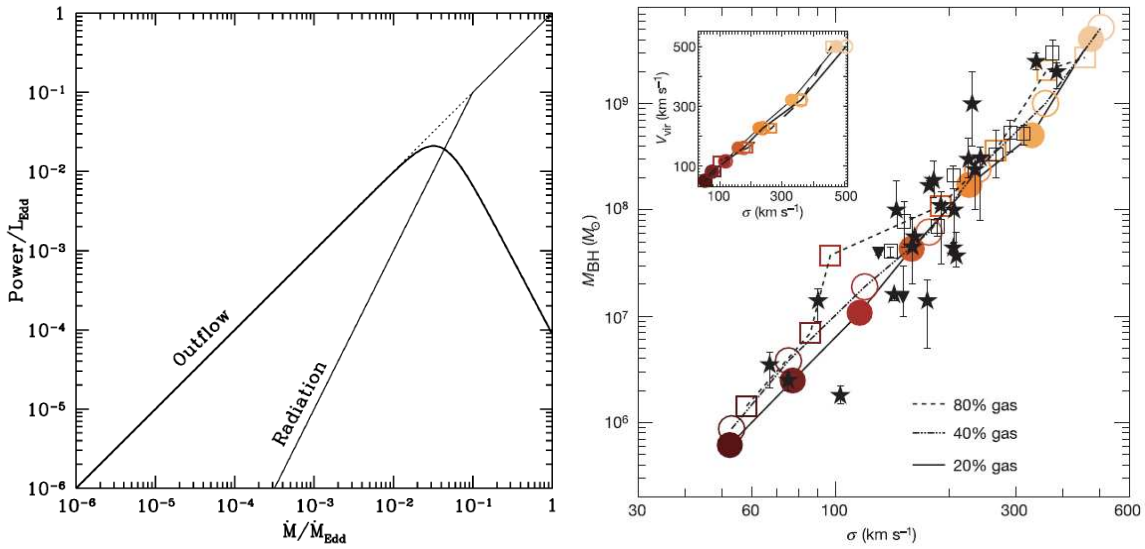

Figure 2.5: Left panel: Black hole energy release as a function of the mass accretion rate, normalised to the Eddington value (from Churazov et al., 2005). The outflow power decreases above a certain threshold in mass accretion, where radiation power becomes important. **Right panel:** The relation between the final black hole mass M_{BH} and the velocity dispersion of stars from galaxy mergers simulations by Di Matteo et al. (2005). Results from six galaxy merger simulations with gas fractions of 20%, 40% and 80% are plotted with filled circles, empty circles and empty squares respectively. Observations from Ferrarese & Ford (2005) and Barger et al. (2005) are plotted with black symbols.

The dependence of the released energy on the mass accretion rate is schematically described in Figure 2.5 (left panel) from Churazov et al. (2005), with the outflow being important at low accretion rates and conversely radiative feedback dominating at high accretion rates.

The main uncertainties in the Springel et al. (2005a) model are related to the origin of BHs. The assumption in this case is that all halos above a certain mass contain at least one of the seed BHs (Di Matteo et al., 2008). In cosmological simulations this is done by identifying the halos above a certain mass (in simulations we perform the halo mass is fixed at $M_{halo} = 10^{10}h^{-1}M_{\odot}$) using a on–the–fly friends–of–friends algorithm that links together particles. This algorithm is called at equally spaced intervals $\Delta \log a = \log 1.25$, where a is the scale factor. If the identified halos do not already contain a BH, a seed BH is deposited with some initial mass, in our case $M_{\bullet} = 10^5 h^{-1} M_{\odot}$. This choice for the seed value is an approximation, since the formation of a supermassive BH is not well known. Some hypothesis are (i) the collapse of gas clouds in protogalaxies (e.g. Begelman et al., 2006) leading to an initial $M_{\bullet} \sim 10^4 - 10^6 M_{\odot}$ or (ii) formation from PopIII stars at very high redshifts $z \sim 30$ with $M_{\bullet} \sim 10^2 M_{\odot}$. For the latter, assuming Eddington accretion rate, the value around $10^5 M_{\odot}$ is obtained at $z \sim 10$, when haloes with masses around $10^{10}h^{-1}M_{\odot}$ start to collapse. The growth of seeded BHs is regulated by the above formula on mass accretion.

Quasar mode feedback. In the quasar mode feedback a tiny fraction of the radiated luminosity is coupled thermally and isotropically to the surrounding gas particles. In simulations of quasars the adopted value $\epsilon_f \sim 0.05$ has been shown to reproduce the $M_{BH} - \sigma$ relation (Di Matteo et al., 2005). The results from six galaxy mergers simulation are reported in the right panel of Figure 2.5. Di Matteo et al. (2005) also note that the final BH mass obtained in simulations is proportional to the inverse value assumed for the feedback efficiency ϵ_f. The choice of this parameter is also consistent with values assumed in SAMs to explain the evolution of the number density of quasars (e.g. Wyithe & Loeb, 2003).

Radio mode feedback with buoyant bubbles. Sijacki et al. (2007) introduced the 'radio' mode feedback within the previously defined scheme simply by adding a threshold parameter

$$\chi_{radio} = \frac{\dot{M}_{BH}}{\dot{M}_{Edd}}.$$

The adopted value is 10^{-2} that can be also inferred by looking at the transition between outflow/radiation in the left panel of Fig.2.5. Quasar heating is operated when $\chi_{radio} > 10^{-2}$, while radio mode is active in the case $\chi_{radio} < 10^{-2}$. In the case when radio mode is on, Sijacki et al. (2007) assume a periodic injection of AGN

jets that produces hot bubbles in the ICM gas. The lack of resolution, as discussed above, does not allow to use any description of jets, but the jet–inflated bubbles can be implemented. Basically, the model for radio feedback assumes that when a BH increases its mass by a certain fraction $\delta_{BH} = \delta M_{BH}/M_{BH}$ the AGN–driven bubble is created.

The energy inflated in a bubble, E_{bub}, is related to the variation of the BH mass according to:

$$E_{bub} = \epsilon_m \epsilon_r c^2 \delta M_{BH},$$

where ϵ_m is the mechanical feedback provided by the bubble. The bubble is able to expand within the hot plasma, since its radius depends both on the inflated energy and the mean density of the surrounding gas:

$$R_{bub} = R_{bub,0} \left(\frac{E_{bub}/E_{bub,0}}{\rho_{ICM}/\rho_{ICM,0}} \right)^{1/5},$$

where $R_{bub,0}$, $E_{bub,0}$ and $\rho_{ICM,0}$ are normalisation constants for the bubble radius, energy and density of the ICM. The typical values for cosmological simulations of galaxy clusters reported by Sijacki et al. (2007) are $R_{bub,0} = 30$ kpc h^{-1}, $E_{bub,0} = 10^{55}$ erg and $\rho_{ICM,0} = 10^4$ h^2 M$_\odot$ kpc^{-3}.

Radio mode feedback without buoyant bubbles. In Chapter 4 we performed simulations with a 'radio' mode AGN feedback that was changed with respect to the original implementation. Instead of inflating energy in the IntraCluster Medium with buoyant bubbles, we change the following features of the GADGET-2 code:

- using the same threshold χ_{radio} as Sijacki et al. (2007) we simply add more energy to the surrounding gas by increasing the coupling efficiency from $\epsilon_f = 0.05$ ('quasar' mode case) to $\epsilon_f = 0.2$ ('radio' mode case);
- the energy was supplied to the BH surrounding gas particles not by using the B–spline kernel weighting, but instead with a Top–Hat kernel (all the particles receive the same amount of energy);
- the fraction of mass radiated as energy by the BH was subtracted in the evaluation of the total BH mass (not included in the original implementation);
- gas is swallowed in a stochastic way and each selected particle contributes to the accretion with 1/3 of its mass instead of being completely swallowed; therefore the accretion is followed in a more continuous way.

The reason behind the different weighting scheme for adding energy from BH to gas particles lies in the fact that with a Gaussian weighting scheme the gas

particles close to the BHs were receiving more energy and radiated it away in a very short time. Instead with a Top–Hat weighting kernel more particles are heated thus preventing the overcooling effect in cluster cores.

The accretion of gas in 'slices' is instead needed due to the coarse–grained representation of the gas distribution, thus preventing also a too high and unrealistic mass accretion on the BH.

2.4 Overview of results from simulations

2.4.1. Chemical enrichment of the ICM

The chemical enrichment in simulations can be studied with very different approaches. One of them is the Semi–analytical modelling (SAM) of galaxy formation, that provides a suitable tool to explore the parameter space for galaxies and their evolution. These models are coupled to a pre–existing dark matter cosmological simulation in order to trace the history of mergers between different haloes, where galaxies are born. Within this scheme the chemical enrichment from SN Ia and II was implemented by De Lucia et al. (2004) and Nagashima et al. (2005). The main overcome of this modelling is the absence of gas dynamical processes and thus the inability to trace the metal spatial distribution. However this scheme allows to explore the global metal content and its evolution (see Baugh, 2006, for a recent review on SAMs).

A new approach by Cora (2006) is instead based on a non–radiative hydrodynamical simulation of galaxy clusters, that is used to trace both the dark matter haloes and the gas dynamics, coupled with a semi–analytical model. The special feature in this hybrid model is that the metal production of galaxies in the SAM is linked to the enrichment of particles in the SPH simulation. With a slightly different approach also Domainko et al. (2006) and Kapferer et al. (2007b) study the role of gas dynamics in enriching the ICM, focusing on the ram–pressure stripping and the effect of galactic winds.

For a fully self–consistent approach one needs to make use of SPH simulations, that can follow the enrichment of a wide range of objects, from galaxies (e.g. Raiteri et al., 1996; Kawata & Gibson, 2003b) up to galaxy clusters (e.g. Valdarnini, 2003; Romeo et al., 2006a). In these simulations the metal production is included in models with a different level of complexity. For example, Lia et al. (2002) followed a statistical approach for star formation. Instead Scannapieco et al. (2005) include in GADGET-2 a numerical implementation where metals were produced by both SN Ia and II. In this case massive stars were allowed to restore all their metals immediately after their explosion as SN II. The model by Tornatore et al. (2004, 2007a) enhances the details of the stellar restoration of metals, since also the mass loss from

intermediate and low–mass stars in the Asymptotic Giant Branch phase (AGB) is included as well as an accurate time–delay for SN II. This is the model adopted in simulations we present in this Thesis. With a similar scheme Wiersma et al. (2009)used the smoothed description of the metallicty to overcome the numerical effect of the lack of metal mixing. Covering with cosmological simulations a wide range of spatial scales and physical processes, from large–scale structure assembly to formation of stars, can be quite expensive in terms of CPU time. Therefore the star formation and metal production during the evolution of stars are followed by means of a sub–resolution model.

■ Global abundances

Every chemo–dynamical model should in principle account for the time–delayed release of metals by different types of stars. As we will see in Sec. 2.3.4 this is a crucial ingredient if we want to study the distribution of metals in the IntraCluster Medium.

Tornatore et al. (2007a) show that products of supernovae type Ia and II are spatially segregated, as a result of different lifetimes of their progenitor stars. SNII ejecta released on short time scales preferentially pollute star forming regions, while SNIa products are found in more distant regions. The latter are produced after larger time scales, therefore the star particle is allowed to move from the region where it was formed, polluting the ICM in more distant regions.

Hybrid simulations by Cora (2006) show that Iron mass ejection from SNII trace the star formation rate in clusters, peaking at higher redshift, while SNIa enrich with a rate that depends not only on the star formation but also on the lifetime function of the progenitors. In particular Cora (2006) demonstrates that the rate of enrichment depends on the environment, since for the BCG everything happens at slightly earlier epochs.

As we already pointed out SAMs are able to follow the delayed enrichment of the interstellar medium and intergalactic medium due to SNe explosions (e.g. De Lucia et al., 2004). In particular they can predict the amount of produced Oxygen, Magnesium and Iron–peak elements, as can be seen in Fig. 2.6 from Nagashima et al. (2005). If a standard (Kennicutt) IMF is adopted (black crosses), SAMs do not reproduce the observed oversolar α/Iron ratio. An improvement is achieved when a top–heavy IMF is included in the SAM during star bursts phenomena (red dots), bringing the simulation outcome in better agreement with observations.

The conclusions from Nagashima et al. (2005), as we will see in Chapter 3, are not in agreement with what we obtained in our simulations. It is worth noticing that the results concerning chemical enrichment in simulations can differ not only by the different modelling of the chemical evolution, but also depend on the adopted IMF and on the stellar yields. It is important to highlight the results by Wiersma et al.

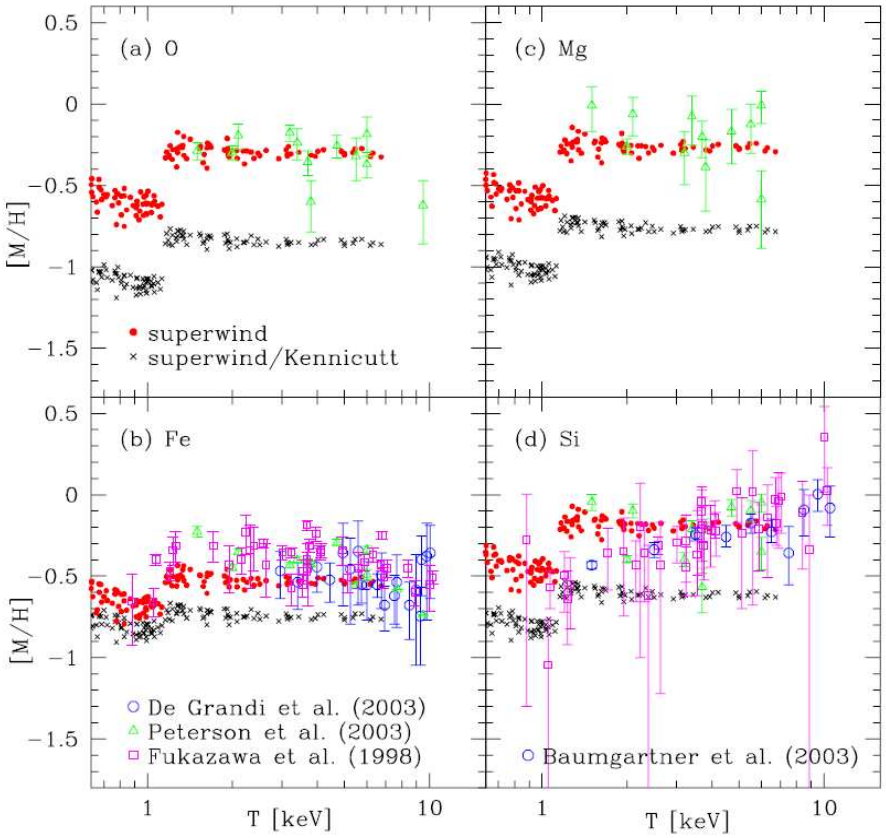

Figure 2.6: Abundances of Oxygen, Magnesium, Iron and Silicon with respect to Hydrogen for galaxy clusters with different temperatures (Nagashima et al., 2005). The clusters extracted from the semi–analytical simulation were simulated with superwinds. The black crosses refer to simulations with the Kennicutt law for the stellar IMF, while the red dots are assigned to simulations where the IMF is changed to the Top–Heavy one when galaxies are merging. Observational data are taken from De Grandi et al. (2004) (only for Iron, blue empty dots), Peterson et al. (2003) (green empty triangles), Baumgartner et al. (2005) (only for Silicon, blue empty dots) and Fukazawa et al. (1998) (pink empty squares).

(2009), who found that when comparing nucleosynthetic yields within simulations the relative abundance ratios can be reliable only at the factor of 2 level, even when the same IMF is adopted.

■ Metallicity profiles

Looking at metallicity profiles gives us the information about the spatial distribution of metals and the relative role played by different mechanisms, such as the galactic winds, ram–pressure stripping and buoyant bubbles in displacing it.

By means of an Eulerian grid–based code Kapferer et al. (2007b) studied the relative role of galactic winds and ram–pressure stripping in distributing the metals in galaxy clusters. The results are shown in Fig. 2.7, where in the centres of massive clusters winds are suppressed (flat profiles), while ram–pressure stripping is more efficient (steep central profiles). The final metallicity profile depends on both mechanisms, with the relative role of winds and ram–pressure stripping that change with clustercentric distance. Mass loss by winds was also found to be stronger at early times.

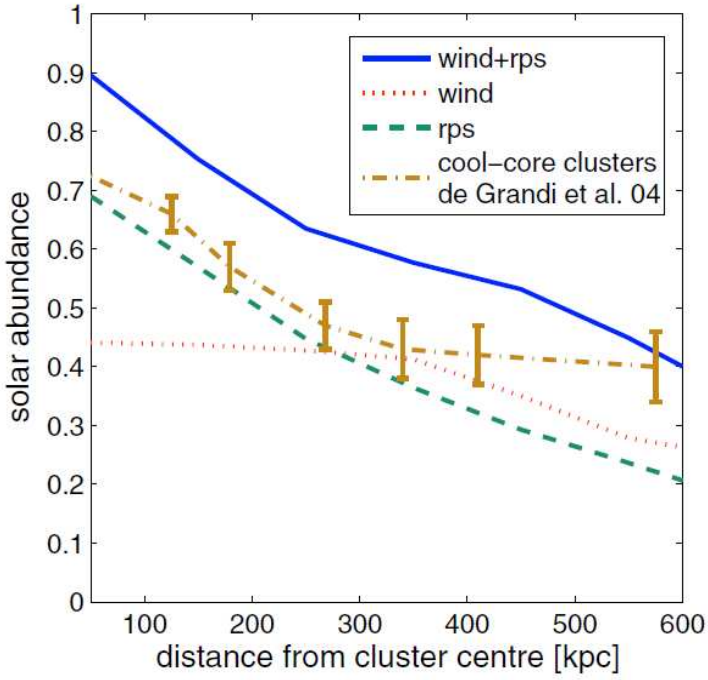

Figure 2.7: The metallicity profiles for simulated clusters by Kapferer et al. (2007b) with the relative contribution of galactic winds (dotted line) and ram pressure stripping (dashed line). The summed profile for the two contributions is plotted with the continuous line. The profiles are compared with the metallicity profiles extracted from cool core clusters by De Grandi et al. (2004) (dashed–dotted line).

Romeo et al. (2006a) performed a set of galaxy cluster simulations with different feedback prescriptions. They found that metallicity profiles are always steeper than observations, with an overall low level of Iron abundance at least for radii $< 0.1 R_{vir}$. However they were able to reproduce results regarding the $L_X - T$ relation, entropy profiles and the cold gas fraction using a top–heavy IMF within a superwind scheme.

Cora (2006) found that radial abundances of Oxygen and Iron are enhanced inside $100\,h^{-1}$kpc because of the highly enriched low–entropy gas that sinks toward

the cluster centre. The centrally peaked metallicity could not be explained by means of galaxy population enrichment since their metal ejection rate is very low at low redshift.

The effect that AGN feedback has on the metallicity profiles was instead explored by Sijacki et al. (2007), that include a model of energy release by accretion of gas on black holes. They do not use a detailed model for chemical enrichment, however they found that the share of metals between stars and gas changes when the AGN feedback is acting. In particular, AGN are able to suppress star formation and therefore less metals are locked to stars, ending up in the hot gas phase. This effect in our simulations will be discussed in detail in Chapters 3 and 4.

Finally, for a much realistic comparison with data one should extract mock X-ray spectra simulations and use the same data reduction procedure as for observations. This was done by Rasia et al. (2008) that investigate the sources fo bias or systematic effects connected to the plasma physics when recovering metal abundances from X–ray spectra. They found a systematic overestimate in the Iron abundance measured for clusters with temperatures of $2-3$ keV, while for both cold and hot systems the Iron abundance is recovered with good accuracy. They explained it as due to the fact that for spectra of clusters with intermediate temperatures there is a transition between the relative importance of the lines (Fe-L and Fe-K) used in determining the Iron content.

■ Evolution of the ICM metallicity

Recent observations of galaxy clusters at high redshift reveal that below $z = 1$ there is some evolution of the Iron global content inside the IntraCluster Medium (e.g Balestra et al., 2007; Maughan et al., 2008, see also Chapter 1).

Up to now only few authors attempted to reproduce the evolution of the Iron abundance in clusters. Cora (2006) found that low–entropy gas that was enriched at high redshift is sinking in the cluster core at low redshift, enhancing the metallicity profiles. When looking at the time evolution of the cluster core metallicity the same effect of sinking can be seen as an enhancement of the central metallicity in galaxy clusters.

Using SAM modelling of the ICM Nagashima et al. (2005) found a very mild enhancement of metallicity with redshift, that is essentially driven by the low–redshift star formation. Instead, Romeo et al. (2006a) achieved by means of hydrodynamical simulations an unchanged abundances from $z = 1$ to $z = 0$, with a lack of evolution also in metallicity profiles. With our simulations we obtain an increase of the central abundance with redshift. This results will be discussed in detail in Chapter 3 of this Thesis.

2.4.2. Heating and cooling of the ICM

The simplest, purely gravitational, models of structure formation predict that galaxy clusters are self-similar in shape and that scaling laws relate each physical property to the cluster total mass and redshift (see 1.2.3). However, to recover the observed cluster properties, a non–gravitational mechanism is required.

The first mechanism introduced to break the self–similarity of the ICM properties was the non–gravitational heating (e.g. Evrard & Henry, 1991b; Kaiser, 1991; Tozzi & Norman, 2001). Early studies explored the effect of the high–redshift heating (pre–heating) on ICM properties.

Increasing the energy of each gas particle by a fixed amount of energy E_h will in principle prevent the gas to sink in the cluster centre, thus reducing the gas density and the X–ray emissivity. This will be true for small–mass systems, where $k_BT \leq E_h$, but not for massive systems with $k_BT >> E_h$, leading to the steepening of the $L_X - T$ relation, as required by observations.

In fact tuning the amount of extra energy and the redshift at which the pre–heating acts reproduces quite well the observed $L_X - T$ relation. It fails however to reproduce the entropy profiles in the galaxy cluster core. Relaxed clusters are observed to have low entropy at their centre (e.g. Donahue et al., 2006), while pre–heating models generally predict large isentropic cores. Constraints on the Lyman α forest affect the entropy–temperature relation for galaxy groups, as shown in Fig. 2.8 (Borgani & Viel, 2009). In this Figure all particles with mean overdensities above a certain threshold (see the different panels on Fig. 2.8) were heated up to a mean entropy floor K_{fl} at $z > 4$. The conclusions are that since injecting energy at high redshift should not destroy the void statistics of the Lyman α forest, pre–heating should to take place only in high density regions, with an overdensity threshold of $\delta > 30$, or to act at lower redshift, ≤ 1 (e.g. Shang et al., 2007; Borgani & Viel, 2009).

An alternative way to reduce the luminosity and density in low–mass systems is radiative cooling, that selectively removes low–entropy gas from the hot phase (e.g. Bryan, 2000; Voit & Bryan, 2001). In this case the hot emitting ICM is composed only by high entropy gas with cooling time longer than the Hubble time. The main problem is the *overcooling* problem, since too much gas, around $\sim 35 - 55\%$, is converted into stars or is in the cold phase, thus in disagreement with the observed stellar fraction of about $\sim 10 - 20\%$ (e.g. Balogh et al., 2001; Lin et al., 2003; Giodini et al., 2009). Furthermore, removing low–entropy gas causes a lack of pressure support, therefore gas from outern parts flows to the cluster centre. This gas is heated by adiabatic compression and leads to an increase in the temperature at the centre, steepening the profiles inside $0.3R_{vir}$.

2.4.3. Galactic ejecta in simulations

As discussed above, a single effect could not explain the observed break of self–similarity of the IntraCluster Medium. The problem of overcooling should in principle be avoided by introducing a suitable heating mechanism that (i) counterbalances the radiative losses, (ii) brings enough pressure support and (iii) regulates the star formation. Feedback by supernovae was initially proposed to regulate star formation and energy release.

SNe explosions can provide a large amount of thermal energy and can drive an outflow from the galaxy (e.g. Heckman, 2003). In particular strong winds are associated to starburst galaxies (e.g. Dahlem et al., 1998), with galactic–scale gas outflows, called superwinds, with velocities of about $400-800$ km s^{-1} (e.g. Heckman et al., 2000). This kind of mechanism was introduced in simulations by Springel & Hernquist (2003a) to produce a realistic cosmic star formation rates. The adopted recipe (see Sec. 3.2.3) is based on a relation recovered in observations by Martin (1999), where the wind outflow rate is proportional to the star formation rate of the galaxy.

Results from simulations show that SNe powered winds are able to reduce the baryon fraction (Springel & Hernquist, 2003a), but some problems still remain unsolved. One of the questions is related to the BCG, that in simulations ends up with values of star formation of about $500 M_{\odot} yr^{-1}$ (Saro et al., 2006), about ten times or more higher than observed ($\sim 10 M_{\odot} yr^{-1}$, e.g. Rafferty et al. 2006). Moreover the cooling efficiency increases with numerical resolution in galaxy clusters simulations (e.g. Borgani et al., 2006), while ideally the feedback mechanism should be resolution independent.

Observations reveal that BCGs are composed primarily by an old stellar population, therefore we cannot expect a number of supernovae enough to drive powerful feedback. The best candidate to power the feedback mechanism are Active Galactic Nuclei (see 2.4.4).

2.4.4. AGN feedback in simulations

We already emphasized in Section 1.4 how important is the effect that AGN feedback has on the evolution of cosmic structures and in particular on central regions of relaxed clusters. The excess of cooling in the cool–cores of simulated clusters causes an overestimated stellar mass fraction and incorrect temperature and entropy of the ICM. AGN heating from the central cluster galaxy is believed to be the solution to these problems. The main difficulty we are faced with in simulations is that we still poorly know the details about the coupling between the energy released by the AGN and the cooling of the ICM plasma in the cluster core.

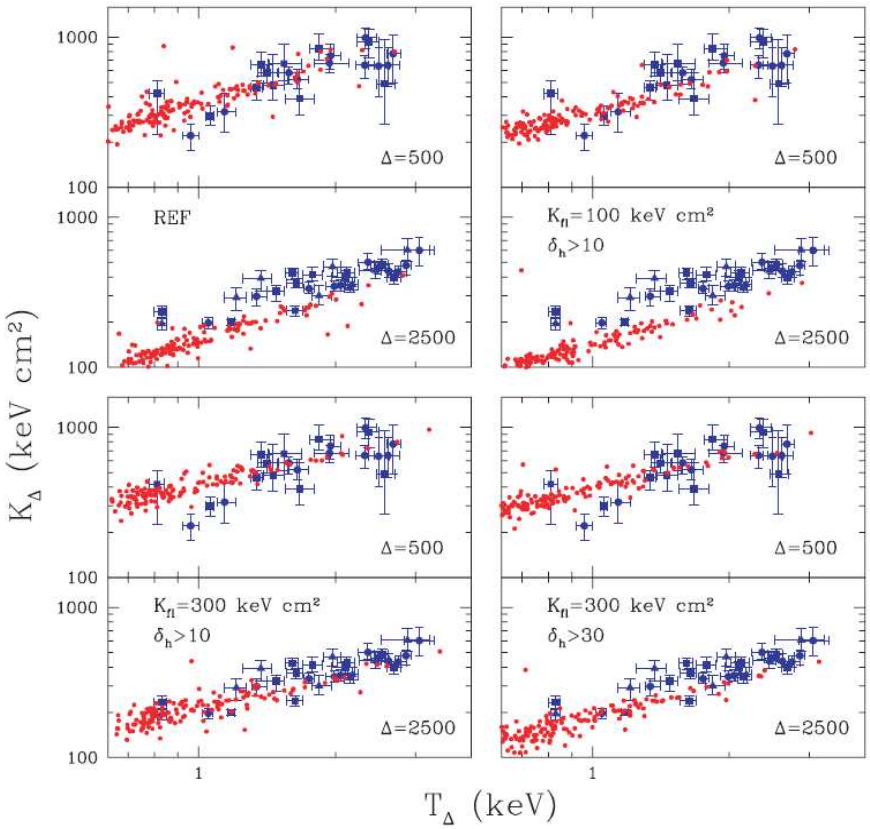

Figure 2.8: The entropy–temperature relation for galaxy groups extracted from simulations by Borgani & Viel (2009) (red dots) and Chandra groups observed by Sun et al. (2009). Four panels represent the results from simulations where the entropy of gas particles at mean overdensities above the value δ_h were increased to K_{th} (the values are reported on each figure). In the top left–hand panel the reference simulation without preheating is reported. For each figure data are extracted at two radii at the cluster overdensities of $500\rho_c$ and $2500\rho_c$ (from Borgani & Viel, 2009).

The main requirement for the AGN feedback mechanism is the ability of balancing radiative cooling in cluster cores. Finding a longterm balance in a self–regulated way seem to be hard in simulations with episodic AGN heating powers jets into the ICM (e.g. Vernaleo & Reynolds, 2006). This is because (i) episodic jets deposit energy away from the cluster centre (and maybe also from the region where radiative cooling acts) and (ii) because cooling depends on the squared gas density, while heating depends on the volume.

Several models of AGN heating of the ICM have been developed in last years (e.g. Binney & Tabor, 1995; Churazov et al., 2001; Ruszkowski & Begelman, 2002; Dalla Vecchia et al., 2004; Sijacki & Springel, 2006a; Vernaleo & Reynolds, 2006),

but without considering the structure formation in a fully cosmological context.

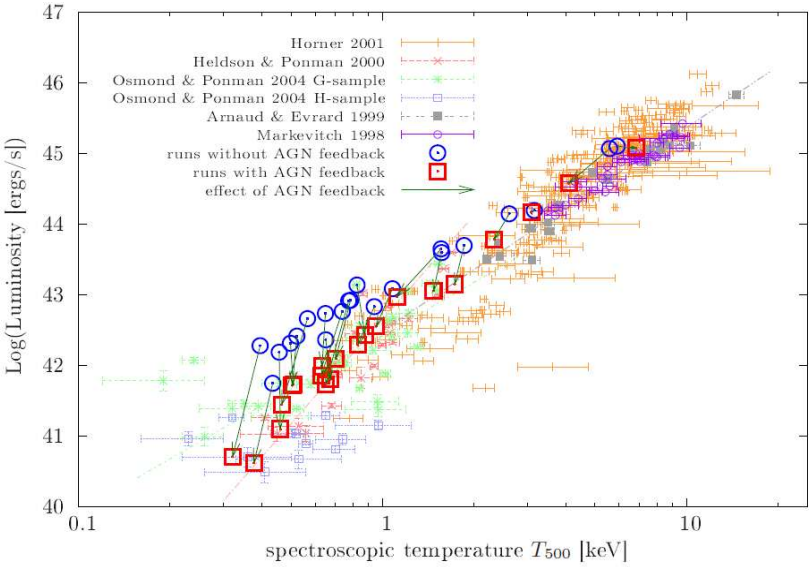

Figure 2.9: Comparison between observations and hydrodynamical simulation of the X–ray luminosity–temperature relation. High–resolution resimulation of clusters extracted from the Millennium run were performed with (red empty squares) and without (blue empty circles) AGN feedback. Arrows show the effect of AGN feedback on each simulated halo (from Puchwein et al., 2008).

First cosmological hydrodynamical simulations of the growth of blackholes (BHs) and galaxies were performed by Di Matteo et al. (2008). They are based on the model developed by Springel et al. (2005a) that will be introduced in Section 2.3.5. Di Matteo et al. (2008) study the 'quasar' mode of the AGN feedback, where high accretion rates are powering luminous quasars. They focus on the BH properties (e.g. black hole population, evolution of the cosmic BH mass density) and their co–evolution with host galaxies at high redshift ($z > 1$). The extension of this work was provided by Sijacki et al. (2007), where the 'radio' mode AGN feedback was implemented, accounting for hot thermal bubbles. This 'unified' model of AGN feedback is able to provide temperature profiles in better agreement with observations and to form less massive BCGs with redder and older stellar population. However entropy profiles obtained by Sijacki et al. (2007) are still inconsistent with observational data in the cluster centre, where very low entropy was observed (e.g. Donahue et al., 2006). Instead, Puchwein et al. (2008), demonstrate that this AGN feedback scheme is able to produce a X–ray luminosity–temperature relation and cluster gas fraction in agreement with observations. In Figure 2.9 (Puchwein et al., 2008) we see the effect of feedback on the $L_X - T$ relation, where arrows connect halos simulated without and with AGN feedback (blue empty circles and red empty

squares, respectively). AGN heating removes a larger fraction of gas from galaxy groups, solving the discrepancy with observations.

The 'unified' model (Sijacki et al., 2007) was further extended by Sijacki et al. (2008) to include also the non–thermal relativistic particles (cosmic rays, CR) in the AGN–inflated bubbles (Sijacki et al., 2008). The clusters simulated with CR feedback show a declining temperature profile toward the cluster centre, with a steepening of the entropy profile, that brings it in closer agreement with X–ray observations at intermediate radii ($\sim 20 - 300$ h^{-1} kpc).

AGN feedback effect is also implemented in semi-analytical models. Starting from the Millennium run hierarchical tree Croton et al. (2006) demonstrate that their AGN feedback prescription solves the 'cooling flow' problem and strongly affects the galaxy population. The luminosity function at the bright end and the colour–magnitude distribution of galaxies were found to be in good agreement with observations. Recently the interaction between BHs and the ICM was investigated by Bower et al. (2008). In Figure 2.10 we report their $L_X - T$ relation, that was obtained changing the AGN feedback model in Bower et al. (2006) (left panel) by allowing gas mass escape from AGN–heated halos (results on right panel). With this prescription Bower et al. (2008) obtained a better agreement with the observed L_X-T relation by Horner (2001) and Osmond & Ponman (2004).

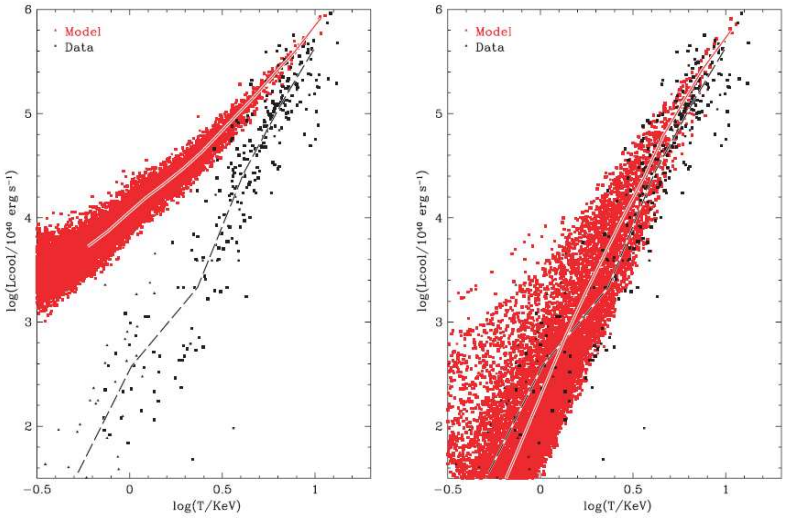

Figure 2.10: The luminosity-temperature relation from the semianalytical modelling with feedback from Active Galactic Nuclei. The two figures refer to the original model by Bower et al. (2006) (left panel) where a fraction of gas was allowed to escape from the AGN heated halos (right panel). Observations from Horner (2001) and Osmond & Ponman (2004) are plotted with black dots, results from SAM are reported with red dots (Bower et al., 2008).

CHAPTER 3

METAL ENRICHMENT of the ICM and its EVOLUTION

In this Chapter we study the evolution of the metal content inside galaxy clusters. The aim is to study the relative role played by star formation, feedback processes and gas dynamics in determining the cosmic history of metal pollution. The main observational results on the abundance ratios, Iron abundance profiles, the evolution of the global metallicity in cluster cores and the rates of SNIa in galaxy clusters were compared with a large set of simulated galaxy clusters.

3.1 Introduction

The high quality X–ray observations of galaxy clusters from the current generation of X–ray satellites are allowing us to trace in detail the pattern of the metal enrichment of the intra–cluster medium (e.g., Mushotzky, 2004; Werner et al., 2008, for reviews). In turn, this information is inextricably linked to the history of formation and evolution of the galaxy population as observed in the optical/near–IR band (e.g., Renzini, 2004, and references therein). A number of independent observations have established that significant radial gradients of the Iron abundance are present in the central regions, $R \lesssim 0.1 R_{500}$, of relaxed clusters and groups (e.g., De Grandi et al., 2004; Vikhlinin et al., 2005; Rasmussen & Ponman, 2007), with enhancement of the metallicity associated to the BCGs, while no evidence has been found that these gradients extend at larger cluster–centric distances (e.g., Snowden et al. 2008,

but in disagreement with Leccardi & Molendi 2008a). Furthermore, deep exposures with the Chandra and XMM–Newton satellites have opened the possibility of tracing the evolution of the ICM metal content within the central regions out to the highest redshifts, $z \simeq 1.3$, where clusters have been identified so far. Balestra et al. (2007) and Maughan et al. (2008) have analysed fairly large samples of distant clusters, extracted from the Chandra archive and found that the metallicity of the ICM within the central cluster regions has increased by about 50 per cent since $z \simeq 1$.

This positive evolution of the ICM metallicity in the central cluster regions is apparently in contradiction with the lack of significant star formation at low redshift (e.g., Rafferty et al., 2006). Based on a phenomenological approach, Ettori (2005) showed that the evolution of the ICM metallicity is in line with the expectations from the observed cosmic rates of supernova (SN) explosions and of star formation. Loewenstein (2006) combined observations of the evolution of the ICM metallicity with data on the SN rates and star formation rates to infer the relative role played by type Ia and II SN (SNIa and SNII hereafter).

A different approach was pursued by other authors, which considered gas–dynamical mechanisms acting at relatively low redshift, that are responsible for redistributing previously produced metals. For instance, Cora et al. (2008) suggested that clumps of low–entropy highly enriched gas may sink in the central cluster regions, thereby leading to an increase of the observed emission–weighted metallicity. Also ram–pressure stripping of the ISM of merging galaxies has been suggested as a mechanism to pollute at relatively low redshift a metal–poor ICM with highly enriched gas (e.g., Domainko et al., 2006, and references therein), while causing a morphological transformation of cluster galaxies (e.g., Calura et al., 2007; Roediger & Brüggen, 2007). Although possible evidences of ram–pressure stripping of cluster galaxies have been detected (e.g., Chung et al., 2007) the question remains as to whether this mechanism dominates the evolution of the ICM enrichment. Indeed, since ram pressure is expected to be more efficient in high–temperature clusters, one expects an increasing trend of metallicity with ICM temperature (e.g., Renzini, 1997). If any, observations suggest that hotter systems have a relatively lower metallicity (e.g., Baumgartner et al., 2005), thus suggesting that ram–pressure stripping is not the dominant process in enriching the ICM.

Understanding the history of the ICM enrichment in cosmological context, during the cluster hierarchical build up, requires a detailed description of the gas dynamics related to the merging processes, while including a self–consistent treatment of star formation and chemical evolution. In this context, cosmological hydrodynamical simulations offer a unique means to capture in full detail the complexity of these processes (e.g., Valdarnini 2003; Tornatore et al. 2004; Romeo et al. 2006b; Tornatore et al. 2007a, hereafter T07, see Borgani et al. 2008b, for a recent review). In their most advanced versions, chemo–dynamical simulation codes treat the production of different metal species, released by different stellar populations by resorting to

detailed stellar yields, also accounting for the mass–dependent stellar lifetimes.

In this Chapter we present results concerning the evolution of ICM metal abundance within cosmological simulations of galaxy clusters, using the chemo–dynamical version of the GADGET-2 code described in Chapter 2. We compare the simulations with observational results on the metallicity-temperature relation for Fe, Si and S and their abundance ratios, on the Iron abundance profiles, $Z_{\rm Fe}$, of nearby clusters, on the evolution of the ICM metallicity and on the SNIa rates. This comparison was performed with the aim of shading light on the relative role played by star formation, feedback processes and gas dynamics in determining the cosmic history of metal enrichment.

The plan of this Chapter is as follows. In Section 3.2 we present our set of simulations, in particular the relevant parameter settings of the GADGET-2 code and of the adopted chemo–dynamical and physical model for the cluster simulations. Section 3.3 is devoted to the comparison between simulation results and observations about:

- metallicity-temperature relation
- profiles of the Iron abundance
- evolution of the ICM metallicity
- rate of SNIa

We summarize the main conclusions in Section 3.4.

All abundance values quoted in the following are scaled to the solar abundance value by Grevesse & Sauval (1998). The main results described in this Chapter are included in two published papers by Fabjan et al. (2008) and Borgani et al. (2008b).

3.2 The simulations

3.2.1. Set of simulated clusters

In this Section we present the set of simulations for this particular study. The adopted set of simulated galaxy clusters and groups used throughout this work is described by Dolag et al. (2009). We devote this section to specify the physical processes and the numerical choices we made for the studied runs.

The main set of simulations is composed by 18 galaxy clusters and groups, which have been identified in a Dark–Matter only simulation with a box size of $479\,h^{-1}$Mpc (Yoshida et al., 2001). This parent simulation was performed for a flat ΛCDM cosmological model with $\Omega_m = 0.3$ for the matter density parameter, $h_{100} = 0.7$ for the Hubble parameter, $\Omega_b = 0.04$ for the baryon density parameter and $\sigma_8 = 0.9$ for

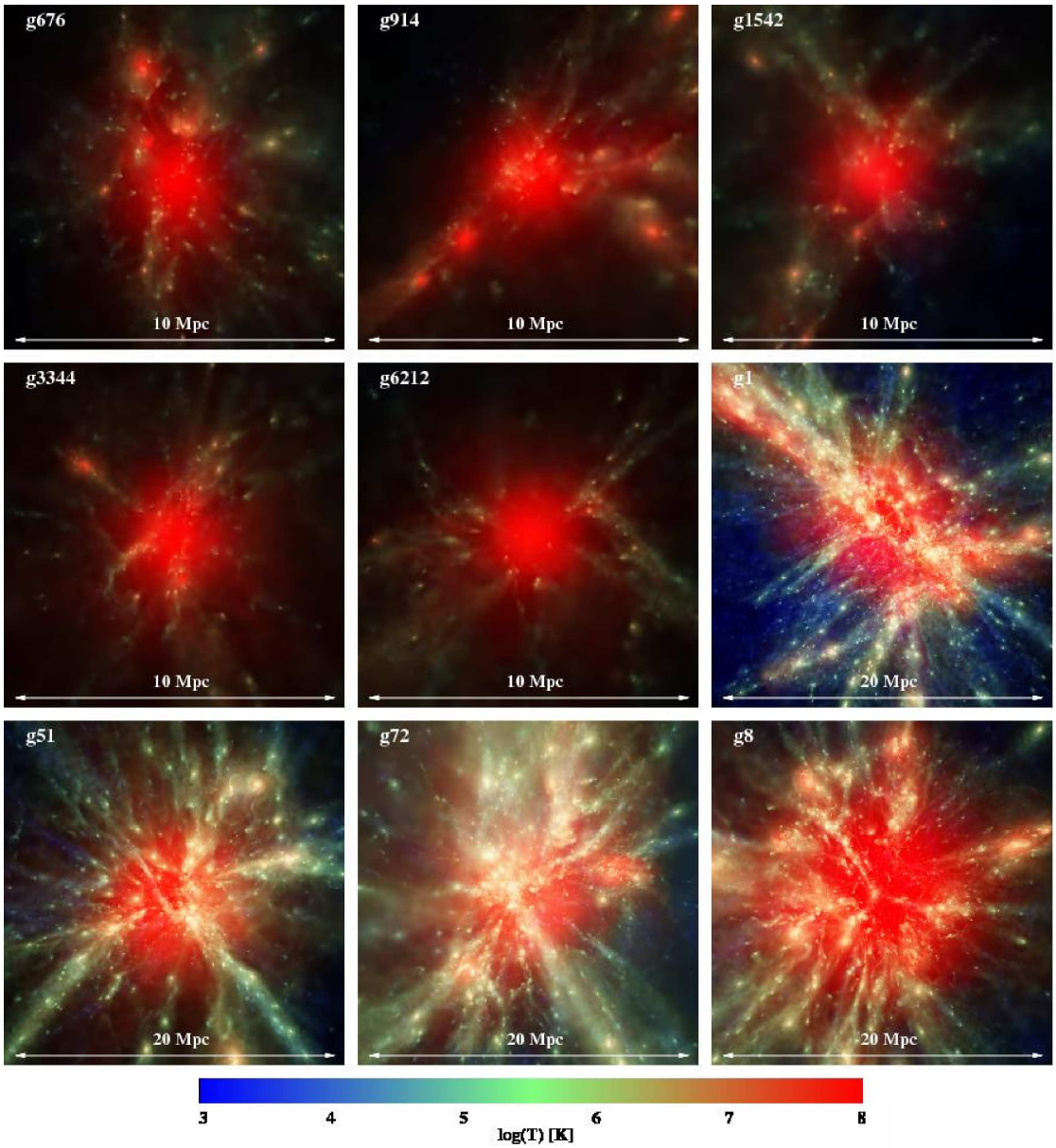

Figure 3.1: Temperature maps of the most massive galaxy clusters and groups inside the nine Lagrangian regions described in the Chapter. The figure is taken from Dolag et al. (2009) and refers to a particular set of simulations (*ovisc*, presented in Chapter 5). Ray-tracing images are obtained with the SPLOTCH package (Dolag et al., 2008b).

the normalization of the power spectrum. The values of Ω_m and σ_8 are higher than the best-fitting values obtained from the analysis of 5-year WMAP data (Komatsu et al., 2009), but still consistent with the current cosmological constraints. As stated by Li et al. (2007) changing the σ_8 and Ω_m to the lower values reported by WMAP-5 will lower the amplitude of the power spectrum, having the main effect of delaying the structure formation.

The nine Lagrangian regions extracted from the DM only simulations are centered on the more massive structure and have been resimulated using the Zoomed Initial Condition (ZIC) technique by Tormen et al. (1997). This technique allows one to increase force and mass resolution once the region of interest is selected. The high–resolution DM particles have masses of $m_{DM} = 1.13 \times 10^9\, h^{-1}\mathrm{M}_\odot$, while in order to reproduce the assumed baryonic fraction gas particles with a mass of $m_{gas} = 1.7 \times 10^8\, h^{-1}\mathrm{M}_\odot$ have been added. The initial conditions for the simulations were determined for a redshift of $z_{ini} = 60$ and tested not to have contaminant low-resolution DM particles inside 5 virial radii at $z = 0$.

Among the nine regions four contain one central main cluster with $M_{vir} > 10^{15}\, h^{-1}\mathrm{M}_\odot$ and more satellite clusters. The other five regions contain only isolated galaxy groups with $M_{vir} \sim 10^{14}\, h^{-1}\mathrm{M}_\odot$. Temperature maps for each most massive group of cluster are represented on Fig.3.1.

The complete set of selected objects is composed by 18 galaxy clusters and groups, with virial masses in the range $M_{\rm vir}$ =0.7–23 $\times 10^{14}\, h^{-1}\mathrm{M}_\odot$. Other basic characteristics of the simulated clusters are summarized in Table 3.1. The shaded rows indicate a subset of four massive objects that were used for the comparison with data on massive clusters alone (e.g. $Z_{\rm Fe}$ profiles).

The simulations were performed using the hydrodynamical TREE PM-smoothed particle hydrodynamics (SPH) code GADGET-2 (Springel, 2005) with the implementation of chemical enrichment by T07 (see Sec.2.3.4). The Plummer–equivalent softening length for gravitational force is set to $\epsilon = 5\, h^{-1}$kpc in physical units from $z = 2$ to $z = 0$, while at higher redshifts is $\epsilon = 15\, h^{-1}$kpc in comoving units. Our simulations include heating from a uniform time-dependent UV background (Haardt & Madau, 1996) and metallicity-dependent radiative cooling based on the tables by Sutherland & Dopita (1993) for an optically thin plasma. The star formation process (SF hereafter) is encompassed within the sub-resolution model by Springel & Hernquist (2003b), where the ISM (Inter-Stellar Medium) is treated as composed by phases (cold gas, hot gas and stars) in pressure equilibrium (see Sec.2.3.3). The density threshold for the onset of SF was set to $n_H = 0.1$ cm^{-1}. More details about the code can be found in Chapter 2.

Characteristics of clusters at $z = 0$ (simulated with Salpeter IMF)

Cluster	$M_{\rm vir}$	M_{500}	$R_{\rm vir}$	R_{500}	T_{vir}^{sl}	T_{500}^{sl}
g1.a	14.85	10.11	2.33	1.20	7.90	8.33
.b	4.35	2.37	1.55	7.42	2.75	2.90
.c	1.71	0.96	1.14	5.49	1.70	1.90
.d	1.25	0.48	1.02	4.35	1.42	1.57
.e	0.76	0.47	8.66	4.34	1.22	1.35
g8.a	22.42	13.73	2.68	1.33	9.47	9.90
.b	1.25	0.68	1.02	4.90	1.58	1.72
.c	0.91	0.47	9.19	4.31	1.31	1.43
.d	0.91	0.37	9.20	3.97	1.19	1.35
.e	0.71	0.45	8.48	4.25	1.17	1.27
g51.a	12.99	8.12	2.23	1.12	7.19	7.40
g72.a	13.41	7.85	2.25	1.10	6.23	6.61
.b	1.89	0.87	1.17	5.31	1.76	1.90
g676.a	1.03	0.68	9.59	4.90	1.84	1.97
g914.a	1.09	0.67	9.78	4.86	1.81	1.97
g1542.a	1.03	0.64	9.59	4.80	1.68	1.87
g3344.a	1.10	0.76	9.81	5.08	1.94	2.10
g6212.a	1.13	0.69	9.89	4.92	1.75	1.96

Table 3.1: Characteristics of the simulated clusters (at $z = 0$). Column 1: cluster name (<Lagrangian region>.<sequential letter>); Column 2,3: virial mass and mass within R_{500} (units of $10^{14}\,h^{-1}{\rm M}_{\odot}$); Column 4,5: virial radius and radius within R_{500} (units of $h^{-1}{\rm Mpc}$); Column 6,7: spectroscopic–like temperature within $R_{\rm vir}$ and R_{500} (keV, see Mazzotta et al. 2004b for its definition); the table refers to the entire cluster set simulated with a Salpeter (1955) IMF with the wind feedback scheme. The shaded subset of clusters was used when comparing with data on massive structures only.

3.2.2. Chemo-dynamical model parameters

While relevant features of the chemical evolution model are described here below, we address the reader to Sec. 2.3.4 for a more detailed description of the implemented model.

The chemo-dynamical code by T07 accounts for metal production by both SNII and SNIa and by intermediate and low–mass stars (ILMS hereafter). However only SNIa and SNII provide energy feedback to the gas particles. SNII are assumed to arise from stars having mass above $8M_{\odot}$. As for the SNIa, we assume their progenitors to be binary systems, whose total mass lies in the range (3–16)$M_{\odot}$ (see also Matteucci, 2003). The fraction of stars belonging to binary systems that produce a SNIa explosions are set to 0.1 unless differently stated. Metals and energy are released by stars of different mass by properly accounting for mass–dependent lifetimes. For these simulations we assume the lifetime function proposed by Padovani & Matteucci (1993).

We adopt the metallicity–dependent stellar yields by Woosley & Weaver (1995) for SNII, the yields by van den Hoek & Groenewegen (1997) for the ILMS and by Thielemann et al. (2003) for SNIa. The version of the code used for the simulations presented here allowed us to follow H, He, C, O, Mg, S, Si and Fe. Once produced by a star particle, metals are then spread to the surrounding gas particles by using the B-spline kernel with weights computed over 64 neighbours and taken to be proportional to the volume of each particle. The final results on the pattern of chemical enrichment are rather insensitive to the weighting scheme (kernel shape and number of neighbours) used to spread metals (see T07 for more details).

In our comparison with observational data, we first explore the effect of changing the IMF. We use the IMF by Salpeter (1955) and that by Arimoto & Yoshii (1987), for which the number N of stars per unit mass interval is defined as $\varphi(m) \propto \mathrm{d}N/\mathrm{d}m \propto m^{-(1+x)}$, with $x = 1.35$ and $x = 0.95$ respectively. Simulations based on the Salpeter IMF have been run for the entire cluster set, while only a sample of a cluster and galaxy group (g51 and g676 respectively) were simulated with the Arimoto–Yoshii IMF. Furthermore, when studying Iron profiles and the evolution of its content in high mass clusters we also use the multi–slope IMF proposed by Kroupa (2001) with $x = -0.7, 0.3$ and 1.3 respectively for $m \leq 0.08M_{\odot}$, $0.08 \leq m < 0.5M_{\odot}$ and $m \geq 0.5M_{\odot}$. The Kroupa IMF was used to carry out the simulation of a massive halo (g51). In the following, we label the runs that use the Salpeter, Arimoto–Yoshii and Kroupa IMFs with *Sal*, *AY* and *Kr* respectively.

An important parameter entering in the model of chemical evolution is the fraction A of stars, in the mass range 0.8–8 $M_{\odot}$, belonging to binary systems which explodes as SNIa in the single–degenerate scenario (Greggio & Renzini, 1983; Matteucci & Greggio, 1986). For our reference runs we will use $A = 0.1$, as suggested by Matteucci & Gibson (1995) to reproduce the observed ICM metallicity (see also

Portinari et al. 2004). As we shall discuss in the following, the simulation with the Arimoto–Yoshii IMF tends to overproduce Iron. In the attempt to overcome this problem, we also carried out a run with the Arimoto–Yoshii IMF using also $A = 0.05$, labelled $AY\,(0.05)$.

The simulations are listed on the upper panel of Table 3.2.

3.2.3. Galactic winds

This simulations include only the kinetic feedback model implemented by Springel & Hernquist (2003a), since in this phase of the project we did not started yet the implementation of the AGN feedback in simulations. A detailed description of the model of AGN feedback implemented in the GADGET-2 code is provided in Sec.2.3.5. SNII explosions trigger energy driven galactic winds. Wind particles are selected stochastically among all star-forming particles and are decoupled from the hydrodynamics until their density has fallen below a density 10 times lower than the density threshold for SF, set to 0.1 cm^{-1} in number density of hydrogen atoms.

The wind mass upload rate is assumed to be proportional to the star formation rate, $\dot{M}_W = \eta \dot{M}_\star$. Therefore, fixing the parameter η and the wind velocity v_W amounts to fix the total energy carried by the winds. Our choice of $\eta = 2$ and $v_W = 500\,\mathrm{km\,s}^{-1}$ corresponds to assume, for the initial mass function (IMF) by Salpeter (1955), with SNII releasing 10^{51} ergs each, nearly unity efficiency in powering galactic outflows (for a detailed description see Sec.3.2.3). Observations of the energetics of galactic winds (e.g. Martin, 1999) justify the above values for η and v_W.

Simulations of galaxy clusters, which include the scheme of feedback adopted here, are already known to produce an excess of low–redshift star formation, mostly associated with the BCG (e.g., Romeo et al., 2005; Saro et al., 2006). This recent star formation is expected to significantly affect the history of the ICM enrichment. From one hand, it should provide an excess of recent metal production, thus possibly enhancing the enrichment at small cluster-centric radii. On the other hand, a recent star formation is also expected to lock back in the stellar phase a significant amount of highly enriched gas, which has shorter cooling time, thus leaving in the hot ICM only relatively metal–poorer gas.

In order to quantify the effect of recent star formation on the ICM enrichment history, we have also simulated the *Sal* version of the g51 cluster by switching off radiative cooling and star formation below $z = 1$, considering both the case in which already formed stars keep producing metals with the appropriate lifetimes (CS run) and the case in which also the metal production is stopped at the same redshift (CMS run) (these runs are listed on the lower panel of Table 3.2). While this prescription of suppressing low–redshift star formation and metal production is admittedly oversimplified, it allows us to address the following questions:

List of simulations with brief description

label	*IMF*	*A*	*simulations*
Sal	Salpeter	0.1	all
AY	Arimoto–Yoshii	0.1	g676, g51
AY (0.05)	Arimoto–Yoshii	0.05	g51
Kr	Kroupa	0.1	g51

label	*description*	*simulations*
Sal	reference	all
CS	stop SF at $z = 1$	g51
CMS	stop SF and metal production at $z = 1$	g51

Table 3.2: List of simulations with labels and short description. Upper table columns: (1) label; (2) adopted IMF; (3) adopted fraction of stars in binary systems (A); (4) simulated clusters;
Lower table columns: (1) label; (2) description; (3) simulations.

(i) to what extent the low–redshift SF excess in simulations affects the enrichment evolution of the ICM?

(ii) which is the role of gas-dynamical processes in redistributing at relatively low redshift the metals that have been produced at earlier epochs?

3.2.4. Simulation analysis

To identify groups and clusters inside each simulation we initially perform the identification of dark matter particles linked together using a *friend-of-friends* algorithm (FoF). Particles are considered as belonging to the same FoF group when their separation is 0.15 times the mean separation of particles. In our case, the value of the FoF linking parameter is $37.5\,h^{-1}$kpc, since the mean separation of high-resolution DM particles is fixed at $250\,h^{-1}$kpc. Also in the case when two particles are more distant but with a common linked particle, they are linked to the same FoF group. Within this scheme galaxy clusters and groups are recognized and by definition their centre is identified with the position of the dark matter particle with the minimum value of gravitational potential.

We define the virial mass $M_{\rm vir}$ as the mass contained within the virial radius $R_{\rm vir}$. This is defined as the radius within which the average density $\rho_{\rm vir}$ is that predicted

by the spherical collapse model. For the cosmology assumed in our simulations, $\rho_{\rm vir} \simeq 100\rho_c$, with the critical cosmic matter density $\rho_{cr} = 3H^2/8\pi G$ (Eke et al., 1996). More in general, we define R_Δ to be the radius at which the density is Δ times the critical density ρ_c. Here and in the following, physical quantities with subscript Δ are computed within R_Δ.

For each FoF group with $M_{tot} > 5 \times 10^{13}\, h^{-1}\mathrm{M}_\odot$ we compute global values of mass, temperature, X-ray luminosity (in different bands) and entropy inside radii $R_{\rm vir}$ and R_Δ, with $\Delta = 2500, 500, 200$. Radial profiles for different ICM properties are computed inside $2R_{vir}$, with the innermost region containing at least 100 gas particles.

The choice of the number of gas particles contained in the innermost region depends on the mass resolution of the simulation. As demonstrated by Borgani et al. (2002) at the radius containing 100 particles a good numerical convergence is achieved for X–ray observables extracted from hydrodynamical simulations. More in general, the minimum radius corresponds to the radius encompassing about three times the number of neighbours over which the SPH smoothing length is estimated.

The purpose of our work is to faithfully reproduce the X-ray observations, therefore reliable estimators of observed quantities are needed.

The X–ray luminosity in a given energy band is evaluated in galaxy cluster simulations as

$$L_X = (\mu m_p)^{-2} \sum_{i=1}^{N_{gas}} m_{h,i}\rho_{h,i}\Lambda_c(T_i, Z_i),$$

where the sum is computed over the number N_{gas} of gas particles inside the chosen radius, considering the gas mass and density of the hot phase in the i-th particle, $m_{h,i}$ and $\rho_{h,i}$. The cooling function Λ_c is calculated in the selected energy band and depends on the temperature T_i and the metallicity Z_i of the i-th particle. The contribution of metals to the cooling function is computed using the cooling tables by Sutherland & Dopita (1993). Finally, μ is the mean molecular weight of 0.6 for a gas with primordial composition and m_p is the proton mass. The distinction between hot and cold gas phases is relevant only in the case of star-forming particles that reside in dense regions. The multiphase model adopted in the GADGET-2 code allows one to compute the relative contribution of each phase, that depends on the local density and temperature (Springel & Hernquist, 2003a). The neutral cold component of the plasma is not considered in the computation. Moreover, X–ray emissivity is not computed for particles with the ionized component with $T < 3 \times 10^4$ K and density $\rho > 500\bar{\rho}(z)$, where $\bar{\rho}(z)$ is the mean local density at redshift z (Borgani et al., 2004). These particles lie in the region of the $\rho - T$ plane where only already cooled gas resides (Kay et al., 2002).

In numerical simulations the temperature is usually estimated using the formula

$$T = \frac{\sum_i w_i T_i dV}{\sum_i w_i dV},$$

where T_i is the temperature of the gas element, dV is the volume along the line of sight and w_i depends on the adopted weighting scheme. Two widely used estimators are the mass-weighted and emission-weighted temperature, T_{mw} and T_{ew} respectively. The former is weighted in terms of mass of the gas element and is directly linked to the total thermal energy content of the cluster, $E_{th,tot} \sim mT_{mw}$. However the X-ray emissivity is proportional to the square of the gas density. A better representation of what is derived through spectral analysis is therefore the emission–weighted temperature T_{ew}, where the weighting function is proportional to the emissivity of each gas element, $w = \Lambda(T_i, Z_i)n_i^2$. Here $\Lambda(T_i, Z_i)$ is the metallicity dependent cooling function and n_i the gas density of the i-th gas particle.

As pointed out by Mazzotta et al. (2004b), the emission-weighted temperature overestimates the observed (spectroscopic) temperature.

They found that the inhomogeneous thermal structure of the ICM can not be fitted by a single–temperature model, in particular when one of the components has temperature $< 2 - 3$ keV. The observed temperature is not only biased toward the densest regions of the cluster, but also to the coolest regions. Therefore these authors proposed a new formula where the weight depends both on the squared density (the emission measure), and on the inverse of the temperature, as $w = \frac{n^2}{T^{3/4}}$.

We adopt this new, spectroscopic–like temperature T_{sl}, in all our comparison with data. This formula is limited to clusters with $T > 3$ keV and has been extended by Vikhlinin (2006) to lower temperatures, $T \gtrsim 0.5$ keV, and a generic value of the ICM metallicity.

Similarly two estimators can also be introduced for the metallicity, namely the mass–weighted and the emission–weighted metallicity, Z_{mw} and Z_{ew} respectively. The first is defined as

$$Z_{mw} = \frac{\sum_i Z_i m_i}{\sum_i m_i}$$

where m_i is the mass of the i-th gas element and Z_i its the metallicity. From observational data, the metallicity is computed trough a spectral fitting procedure, by measuring the equivalent width of an emission line associated to a transition between two heavily ionized states of a given element. Since the central cluster regions are characterized by a stronger emissivity, one expects that this region provides a dominant contribution to the global spectrum and to the observed emission lines. A better proxy is therefore the emission-weighted metallicity:

$$Z_{ew} = \frac{\sum_i Z_i m_i \rho_{gas,i} \Lambda(T_i, Z_i)}{\sum_i m_i \rho_{gas,i} \Lambda(T_i, Z_i)}.$$

In this equation the weighting function depends on the mass m_i and density $\rho_{gas,i}$ of the i-gas element and on the metallicity dependent cooling function $\Lambda(T_i, Z_i)$. Mock spectral observations have shown that the Z_{ew} definition is quite close to the spectroscopic value (Kapferer et al., 2007a; Rasia et al., 2008), at least for Iron. On the other hand, as pointed out by Rasia et al. (2008), the derived abundances for some elements, as Oxygen, can be significantly biased. This bias is related to the limited spectral resolution of the CCDs on Chandra and XMM-Newton. In particular, Oxygen emission line in hot systems is very weak and an underestimate of the continuum level lead to an overestimate of the Oxygen abundance.

3.3 Results and discussion

3.3.1. Abundances as a function of cluster temperature

The global ICM abundances were found to be almost constant (~ 0.3 $Z_\odot$, depending on data and solar abundances) and with a very small dispersion for clusters hotter than ~ 2.5 keV (e.g. Renzini, 1997; Baumgartner et al., 2005; de Plaa et al., 2007). On the galaxy group scales data on global metallicities turn out to have a larger spread (see Sec.1.3). The observed trend of nearly 2 times higher $Z_{\rm Fe}$ abundance in galaxy groups with respect to the almost constant ~ 0.3 $Z_{Fe,\odot}$ for clusters above 5 keV was also observed by Balestra et al. (2007). From Chandra data of about 56 clusters they derived a best fit metallicity-temperature relation of $Z/Z_\odot \simeq 0.88T^{-0.47}$ (for solar metallicity values from Anders & Grevesse 1989).

This observed trend could be related to the change in the stellar over gas mass ratio in clusters. A recent work by Giodini et al. (2009) on a large sample of 118 groups and clusters with $z \leq 1$ confirmed the previously reported increase of gas mass fraction with cluster temperature and the anti-correlation of the stellar mass fraction with temperature for nearby clusters (see also Lin et al., 2003). This information coupled with Iron mass to optical light ratio and ICM mass to light ratio in galaxy clusters lead to an early interpretation by Renzini (1997), that the observed trend in metallicity-temperature relation reflects a decreasing star formation efficiency with increasing cluster mass (see also Pipino et al., 2002).

However the spread in global metallicity for galaxy groups can be partially due to a different line complex used for low and high temperature systems (iron-L complex at ~ 1 keV; iron-K complex at ~ 7 keV respectively), while also using a single-temperature model on a two temperature plasma with average temperature of 1 keV can lead to a significant underestimate the metallicity (Buote, 2000).

Initially we focus on the abundances of Fe, Si and S trying to explore the contribution of different stellar population to the element production starting from

the results on two different stellar Initial Mass Functions (Salpeter and Arimoto–Yoshii) for our cluster set.

To this purpose we compare the abundances of simulated clusters and groups with two different data sets:

- **The ASCA Cluster Catalog (ACC)**

  Cluster observations were extracted from the ASCA archive by Horner (2001). As stated by these authors, the catalog was designed to maximize the number of clusters found, therefore it is not necessarily complete to any flux or redshift. Trying to represent at best the cluster total flux, the extraction regions were chosen to contain as much photons as possible, thus avoiding the choice of a common extraction radius.

  The signal-to-noise for single cluster observations (353 observations; 273 clusters) was too low for a good spectral fitting, therefore clusters were binned in temperatures. In each bin data on clusters were stacked on the base of their global abundance values. Abundances of different elements were then obtained by fitting the stacked spectrum.

- **The sample by de Plaa et al. (2007)**

  This more recent data set is based on a sample of 22 clusters observed with XMM-Newton. Since the XMM EPIC instrument has a better spatial resolution, although with a high background level, the more central regions within 0.2 R_{500} were inspected, thus allowing to study Si, S, Ar, Ca and Ni abundances and the relative contribution from SNIa and II. Clusters belonging to this sample were also classified in cool core (CC) and non-cool core (NCC).

In Fig.3.2 we present the comparison of $Z_{\rm Fe}$ from simulations with the two data sets (XMM data by de Plaa et al., 2007) in the left panel, ASCA observations by Baumgartner et al. (2005) in the right panel). In both observed samples we notice the spread in $Z_{\rm Fe}$ for galaxy groups, while clusters with temperatures above 4 keV show abundances which are nearby independent of the ICM temperature. From Fig.3.2 we can see that the mean enrichment is higher in central part of clusters, with $Z_{\rm Fe} \sim 0.4 - 0.9$ for the sample of de Plaa et al. (2007), while for ASCA data on left panel of Fig.3.2 $Z_{\rm Fe}$ is somewhat lower ($\sim 0.3 - 0.7$), especially for galaxy groups. This is not surprising, since we know that gradients with a declining ICM metallicity are observed as a function of clustercentric distance (see also Sect.3.3.2). Moreover, steeper profiles and central supersolar abundance values are observed in galaxy groups (e.g. Rasmussen & Ponman, 2007), while central abundances in rich clusters are generally subsolar (e.g Leccardi & Molendi, 2008a).

In Fig.3.2 we compare both observational samples with predictions of simulations based on the Salpeter IMF for all the cluster sample (green and empty squares for

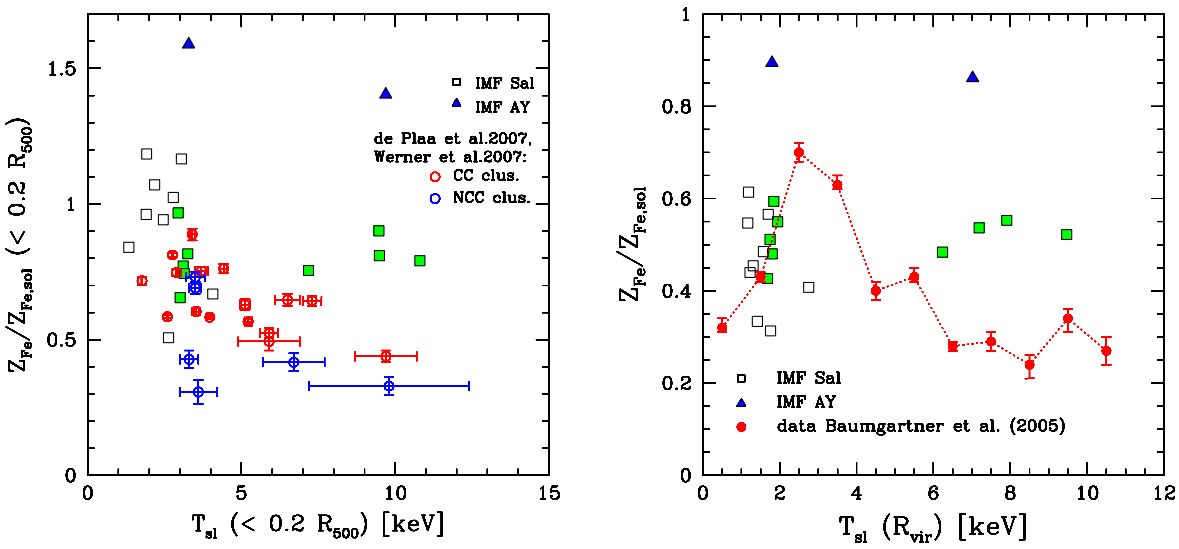

Figure 3.2: The relation between $Z_{\rm Fe}$ and clusters temperature. **Left panel:** comparison with data for 22 XMM-Newton observed clusters from de Plaa et al. (2007). For a better comparison we compute from simulations the emission weighted metallicity (Rasia et al., 2008) and the spectroscopic–like temperature (Mazzotta et al., 2004b). $Z_{\rm Fe}$ and temperatures are evaluated inside $0.2R_{500}$. **Right panel:** comparison with ASCA data from Baumgartner et al. (2005). Since no common extraction radius was used in their work, we plot $Z_{\rm Fe}$ and $\rm T_{\it sl}$ for simulations as evaluated inside $\rm R_{\it vir}$. On both panels simulations with Salpeter IMF are represented by squares (green: main cluster; empty: satellite cluster), while simulations with Arimoto–Yoshii IMF are represented by blue triangles.

main and satellite clusters respectively) and simulations based on Arimoto–Yoshii IMF for two clusters (triangles).

In the case of Salpeter IMF the simulated galaxy groups below 2 keV are consistent with data both in normalization and scatter. However some of the satellite galaxy groups have $Z_{\rm Fe} > 1\ _{Fe,\odot}$ inside 0.2 $\rm R_{500}$. High temperature clusters instead show a discrepancy with respect to observations, with abundances that are higher by about $\Delta_{Z_{Fe}} \sim 0.5\ \rm Z_{Fe,\odot}$ and $\Delta_{Z_{Fe}} \sim 0.2\ \rm Z_{Fe,\odot}$ for the estimate inside $0.2R_{500}$ and R_{vir} respectively.

The two clusters simulated with Arimoto–Yoshii IMF (blue triangles) have $Z_{\rm Fe}$ above the observed data in both panels of Fig.3.2, indicating that the larger number of SNII arising from the high-mass end of the Arimoto–Yoshii IMF, turns into a large overproduction of Iron.

The discrepancy between data and observations for high mass clusters can be partially ascribed to simulated galactic winds, that are not enough efficient to reduce the star formation in larger objects. A different feedback mechanism, like AGN feed-

back, should reduce the excess star formation and the global metal content, bringing in better agreement also the resulting stellar mass fractions, that are too high especially for simulated massive clusters. This issue will be addressed in Chapter 4 (Section 4.3.4). Furthermore, the global metallicity content is also affected by the choice of the parameters which define the chemical evolution model. As we will see in Sec.3.3.2, the fraction of stars in binary systems that are progenitors of SNIa significantly affects the final abundances, in particular of Iron. Changing the adopted observational yields or the computed lifetime function also affects the quantity of produced metals.

■ Abundance ratios

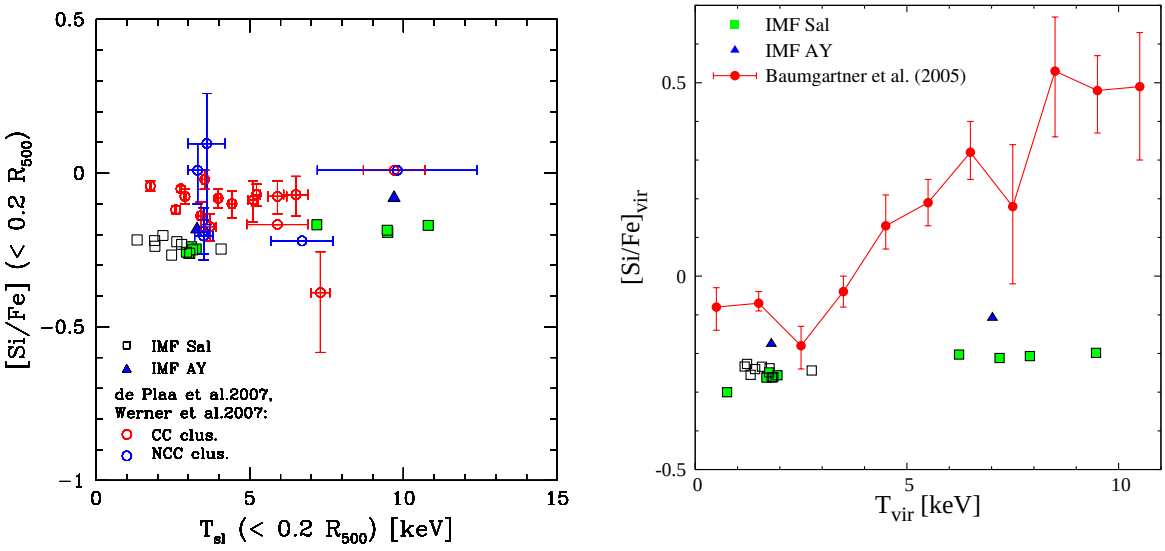

Figure 3.3: Relative abundances of [Si/Fe] with respect to cluster temperatures, both evaluated inside the $0.2R_{500}$ radius (left panel) and R_{vir} (right panel). Simulations with Salpeter IMF are represented by squares (green: main cluster; empty: satellite cluster), while simulations with Arimoto–Yoshii IMF are represented by blue triangles. Data on left panel are from a compilation of XMM-Newton observed clusters by de Plaa et al. (2007), that divide them in for cool core (CC, red empty circles) and non cool core (NCC, blue empty circles). Data on right panel are from the ASCA compilation by Baumgartner et al. (2005) (red circles).

Since different supernova types account for the production of elements in different proportions, investigating the ratio of specific elements should provide a useful diagnostic in constraining the theoretical supernova models (e.g. Werner et al., 2008, for a review). Here we will compare global abundance ratios inside clusters, however

we remark that also the radial dependence can be studied. In the latter case we can get informations on the role of both SN types at different cluster-centric distances and on gas-dynamical processes that can mix elements released on different time scales.

In Fig.3.3 and 3.4 we plot observed and simulated $[Si/Fe]$ and $[S/Fe]$ abundance ratios respectively. On both figures data on the left panel refer to the cluster set of de Plaa et al. (2007), while on right side the ASCA clusters binned in temperature are plotted.

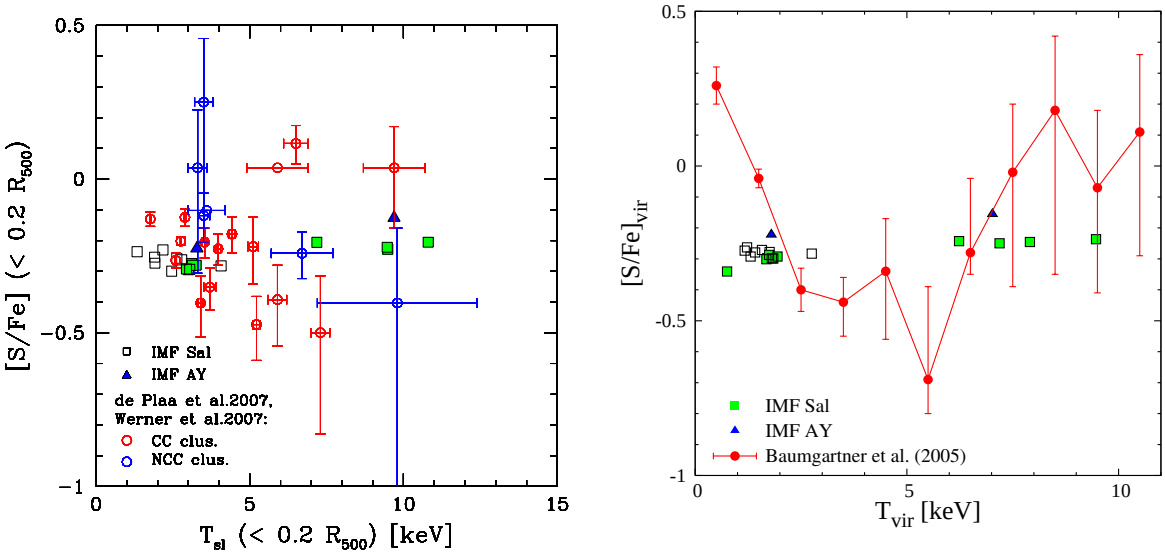

Figure 3.4: Relative abundances of [S/Fe] with respect to cluster temperatures, evaluated inside the $0.2R_{500}$ radius (left panel) and R_{vir} (right panel). Symbols for data and simulations are the same as in 3.3.

In Fig.3.3 we note the difference between the two data sets. The intrinsic scatter of the $[Si/Fe]$ ratio for the sample by de Plaa et al. (2007) is smaller than 30%, and consistent with being independent of cluster temperature. As for the ASCA clusters by Baumgartner et al. (2005), they show instead a clear increase of $[Si/Fe]$ at $T > 4$ keV. Both sets of observational data agree well on galaxy group scales, with $[Si/Fe] \sim -0.1$ dex, while our simulations on the same scale have lower abundance ratios, by about -0.2 dex. The discrepancy between simulated clusters with $T > 5$ keV and ASCA data is quite large, by about ~ 0.4 dex. Large uncertainties on data for high mass clusters can arise from a bias in the spectral fitting procedure, as described by Buote (2000). When a single-temperature fit is performed on a multi temperature ICM, the low-temperature plasma component that produces stronger Si and S emission lines determines an underestimate of the continuum level at

high energies. This in turn reduces the estimate of $Z_{\rm Fe}$ from Fe K lines. This bias is expected to be relevant for hotter clusters, thus boosting the Si/Fe and S/Fe estimates.

Despite the expected similar behaviour, since Silicon and Sulfur are predominantly released in SNII explosions, observations of the abundances for these two elements are rather different: in ASCA data $[Si/Fe]$ abundance increases with cluster temperature, while $[S/Fe]$ does not show any monotonic trend with temperature. Cluster simulations in Fig.3.4 and 3.3 predict a constant value of $[S/Fe]$ and $[Si/Fe]$ for all temperatures. Due to the large spread in observational data, we are not able to reach any firm conclusion from this comparison.

Interestingly, we find that $[Si/Fe]$ and $[S/Fe]$ abundance ratios are weakly sensitive to changes of the Initial Mass Function. While affecting the number of SNIa and SNII, results from simulations with Arimoto–Yoshii and Salpeter IMFs produce very similar values for the abundance ratios, with a slightly higher value for the Arimoto–Yoshii IMF.

3.3.2. Metallicity profiles of nearby clusters

The radial profiles of the metal abundance provide a very important record of the chemical enrichment process in galaxy clusters. Indeed, they are determined by the distribution of cluster galaxies, where most of the metals are produced, by the mechanisms responsible for their transport and diffusion from the star–forming regions (i.e., galactic ejecta, ram–pressure and viscous stripping, etc.) and by other gas–dynamical processes which redistribute them on larger scales (e.g. turbulence and sinking of enriched low–entropy gas). Here we compare the profiles of the Iron abundance of simulated galaxy clusters at $z = 0$ with the observational results from *Chandra* data of a sample of nearby relaxed clusters analysed by Vikhlinin et al. (2005).

In Figure 3.5 and 3.6 we compare the profiles of $Z_{\rm Fe}$ from our simulated clusters with the observed profiles of 8 clusters having temperature above 3 keV (see Table 1 in Vikhlinin et al., 2005). We point out that the analysis of Vikhlinin et al. (2005) provided information on the total ICM metallicity, i.e. without distinguishing the contribution from different chemical species. However, at the typical temperatures of these clusters and for the typical energy range where the spectral analysis was performed (0.6–10 keV; see Vikhlinin et al. 2005), this observed metallicity is largely dominated by Iron. We want to stress the fact that the simulated clusters are dynamically relaxed (with the last major merger undergone before $z = 0.5$) and therefore suitable for the comparison with this set of observed clusters.

As shown in the Fig.3.5, the simulations based on a Salpeter (1955) IMF produce profiles which are in reasonable agreement with observations. The scatter among the four simulated clusters is quite small, with some increase in the central regions,

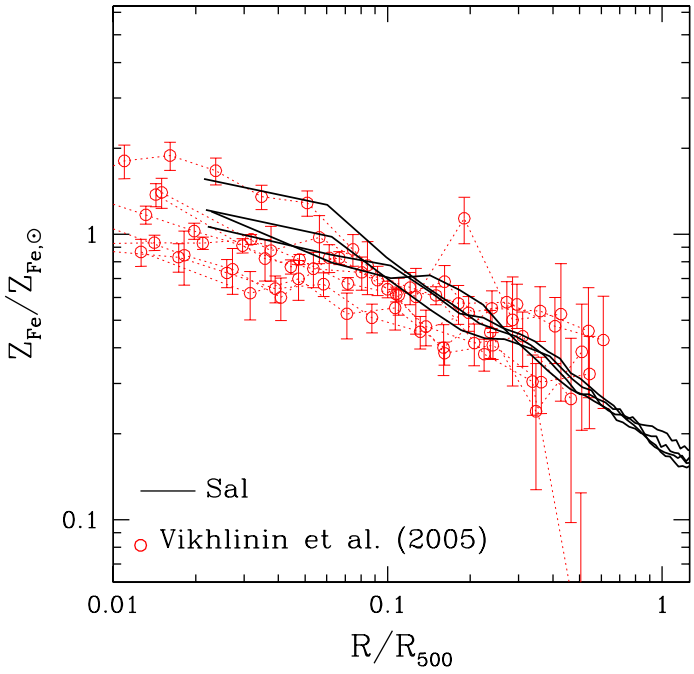

Figure 3.5: The Iron abundance profiles of simulated clusters at $z = 0$ compared to the Chandra observed profiles for 8 nearby clusters with $T > 3$ keV (Vikhlinin et al., 2005) (open circles with errorbars). In the panel the solid curves correspond to the four clusters simulated using the Salpeter (1955) IMF.

$R \lesssim 0.1\, R_{500}$. Although observations seem to have a larger scatter, it is not clear how much observational uncertainties contribute to it. Changing the IMF (Fig. 3.6) clearly turns into a change of the overall amount of the Iron abundance at all radii, with both the Kroupa and the Arimoto–Yoshii IMFs producing too high profiles. The larger amount of Iron found for these two IMFs is due to the fact that, once normalized, they both predict a larger number of supernovae contributing to the Iron production, with respect to the Salpeter one.

Besides producing more SNII, the *AY* and *Kr* IMFs also produce a larger number of SNIa, since there is a significant overlap between the mass range relevant for SNIa and the mass range where these two IMFs are higher than the Salpeter one (see Figure 2.4 on page 55).

As for the relative roles of SNIa, SNII and ILMS in the ICM enrichment, we verified that SNIa contribute for about 70 per cent of the Iron contained in the diffuse medium within R_{500} for the Salpeter IMF. This fraction decreases to about 65 per cent for the Kroupa IMF and to about 55 per cent for the Arimoto–Yoshii

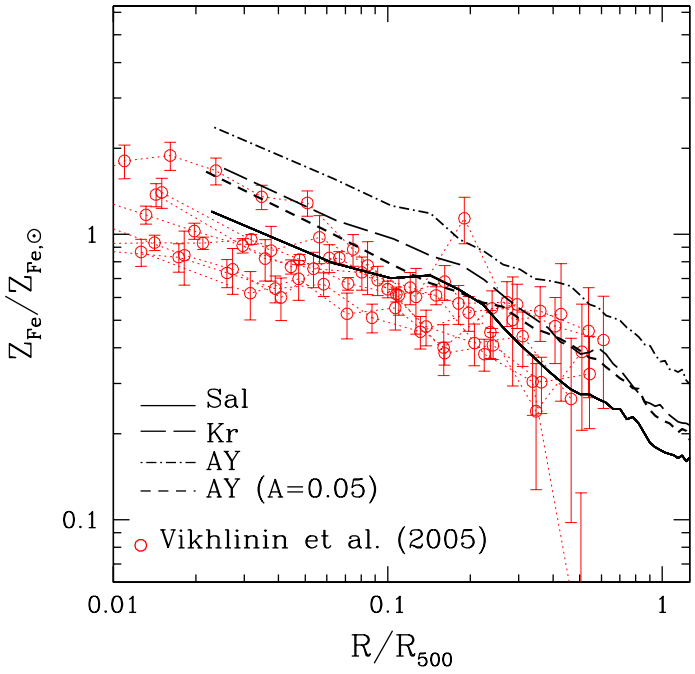

Figure 3.6: The Iron abundance profiles of simulated clusters at $z = 0$ compared to the Chandra observed profiles for 8 nearby clusters with $T > 3$ keV (Vikhlinin et al., 2005) (open circles with errorbars). The panel compares the results of the g51 cluster simulated using the IMF by Salpeter (1955) (solid), by Arimoto & Yoshii (1987) with two different values for the fraction of binary stars ($A = 0.1$: dot-dashed; $A = 0.05$: short dashed) and by Kroupa (2001) (long dashed).

IMF. Since SNIa provide a major contribution to the Iron production, our results are quite sensitive to the choice of the fraction A of stars in binary systems. As a matter of fact, this fraction can be considered as a free parameter in a model of chemical evolution. Following a phenomenological approach, for each choice of the IMF its value is determined by the requirement of reproducing some observational data. In our case, we note that decreasing A from 0.1 to 0.05 induces a significant decrease of the $Z_{\rm Fe}$ profile. This sort of degeneracy between the IMF shape and the fraction of binary stars can be broken by looking at the relative abundance of α elements with respect to Iron. For instance, since Oxygen is essentially produced by SNII, we expect a top–heavier IMF to provide values of O/Fe higher than for a top–lighter IMF. If we suppress the number of SNIa for the top–heavier IMF, by decreasing the value of A, we further increase the O/Fe ratio, thus allowing to distinguish this case from that of a top–lighter IMF with a higher A. The same argument can be

used for other elements synthetized only by SNII. However observing metal lines, in particular Oxygen, especially for high temperature clusters is intrinsically difficult and relative abundances for nearby clusters, as pointed out before, have still large observational uncertainties.

The runs with the Salpeter IMF provide results in closer agreement with the Chandra data, although in all cases the profiles of the simulated clusters are somewhat steeper than the observed ones, with negative gradients extending at least out R_{500} and beyond. This result is at variance with the recent claim by Snowden et al. (2008) who found no evidence for the presence of metallicity gradients at scales $\gtrsim 0.1R_{500}$ from the analysis of a catalog of 70 clusters observed with XMM–Newton. In the next section we will compare simulated and observed results on the evolution of the ICM metallicity at small radii, where the simulated and the observed metallicity gradients are in reasonable agreement. If confirmed by independent analyses, the lack of abundance gradients at relatively large radii will provide a non–trivial constraint for chemo–dynamical models of the ICM enrichment (this issue will be addressed in Chapter 4).

Limited numerical resolution could lead to an underestimate of high–redshift enrichment from a pristine population of relatively small under–resolved galaxies. This high–z enrichment should be rather uniform and, therefore, should soften the metallicity gradients. Indeed, T07 found that increasing resolution provides progressively shallower metallicity profiles. However, the effect is visible only at radii $\gtrsim 0.5R_{500}$, while being negligible at smaller radii, which are dominated by the star formation associated to the BCG. Another possibility to soften metallicity profiles can be provided by AGN feedback. For instance, Bhattacharya et al. (2008) analysed cosmological simulations of galaxy groups, which include the effect of energy feedback from gas accretion onto black holes. They found that the effect of this feedback is to redistribute the hot gas, driving it from the inner regions, where it should be more enriched, to the outer part of the halo, and to lower the star formation in the inner region. Sijacki & Springel (2006a) used a similar feedback scheme, in which energy is used to trigger the formation of high entropy bubbles. These bubbles rise buoyantly in the ICM, giving rise to a redistribution of the central metal–enriched gas (see also Roediger et al., 2007). Clearly, in this case the request is that the redistribution of metals should not be so efficient as to destroy the metallicity gradients in the central cluster regions (e.g., Böhringer et al., 2004).

3.3.3. Evolution of the ICM metallicity

In this Section we compare the simulation predictions on the evolution of the ICM metallicity with the observational results by Balestra et al. (2007). These authors analysed *Chandra* observations of 56 clusters at $z > 0.3$ (with the addition of XMM–Newton observations for clusters at $z > 1$) having temperatures above 3 keV. They

measured the metallicity in the central regions, with a typical extraction radius of 0.15–0.3 R_{180}, chosen object-by-object so as to maximize the signal-to-noise ratio (see also Maughan et al. 2008, for a similar analysis). For the low–redshift reference value, Balestra et al. (2007) combined this set of distant clusters with a mix of cool-core and non cool-core clusters at lower redshift. They also pointed out that the observed decrease of $Z_{\rm Fe}$ with redshift is not induced by a decrease of the fraction of cool–core clusters in the past. Therefore, we expect that no significant bias is introduced when comparing the observed evolution with that traced by our set of relaxed simulated clusters. Since it is quite difficult to define a common extraction radius for the observed clusters, we decided to adopt a value of $0.2R_{180}$ in the analysis of the simulated clusters. We verified that our conclusions are left unchanged by varying this radius in the range 0.15–0.3 R_{180}.

In the Fig. 3.7 we compare the observational results by Balestra et al. (2007) with the predictions of our simulations for different choices of the IMF. Observations and simulations are compared here by using the emission–weighted definition of metallicity, with emissivity of each gas particle computed in the 0.5–10 keV energy band. In principle, this comparison would require extracting synthetic spectra from the simulated clusters and then measure the metallicity by fitting these spectra to a single–temperature and single–metallicity plasma models, as done in the analysis of observational data. An analysis of this type has been recently presented by Rasia et al. (2008) and showed that, at least for Iron, the emission–weighted estimator gives results quite close (within about 10 per cent) to those obtained from the spectral–fitting analysis.

Interestingly, we note in all simulations a significant increase of metallicity in the cluster central regions below redshift unity. The runs based on the *Sal* IMF (the average $Z_{\rm Fe}$ of four massive clusters) provide the result closest to what observations are suggesting. On the contrary both the *Kr* and the *AY* IMFs predict too high abundances for the g51 cluster at all redshifts, with a very strong evolution at $z \gtrsim 0.5$ (we note that g51 is the cluster with the highest metallicity at $z = 0.25$ and 0.5, among the four simulated objects). This higher abundance for the *AY* and *Kr* IMFs is in line with the correspondingly higher profiles found at $z = 0$ (see Fig. 3.6). Again, decreasing the binary fraction in the *AY* run to $A = 0.05$ causes a significant decrease of the Iron abundance at all redshifts.

At lower redshifts, $z > 0.5$, g51 shows a slower evolution, even followed by an inversion below $z \simeq 0.25$. The reason for this inversion lies in the quiet accretion history of this clusters below $z = 0.5$. Since no highly enriched gas clumps, associated to major merger event, reached the central regions of g51 since $z = 0.5$, the only gas accreted there is characterized by a relatively low metal abundance. For instance, in the *Sal* run of g51 we verified that between $z = 0.25$ and $z = 0$ about $6 \times 10^{12} M_{\odot}$ of gas, having an average metallicity value $Z_{Fe} \simeq 0.64\, Z_{Fe,\odot}$, flowed out of $0.2R_{180}$. In the same redshift interval, about $10^{13} M_{\odot}$ of gas was accreted,

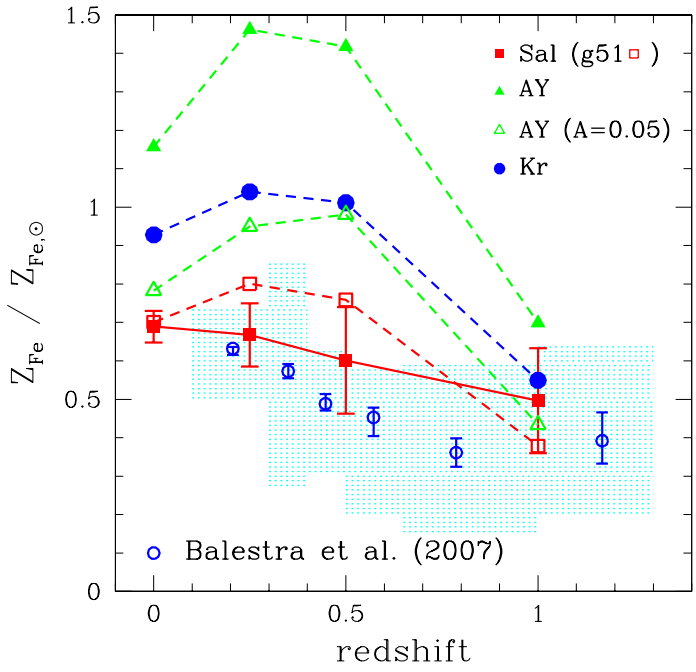

Figure 3.7: The comparison between observations and simulations for the evolution of the Iron abundance, $Z_{\rm Fe}$ the dependence of the simulation results on the stellar IMF. The filled squares show the average over the simulated clusters, assuming a Salpeter (1955) IMF (*Sal*), with errorbars indicating the r.m.s. scatter over the four objects. For the g51 cluster only, the open squares are for the run with Salpeter (1955) IMF, the filled and open triangles are for the Arimoto & Yoshii (1987) IMF (*AY*) with $A = 0.1$ and $A = 0.05$ for the binary fractions, respectively, while the filled circles are for the run with the Kroupa (2001) IMF (*Kr*). Observational results from Balestra et al. (2007) are shown with open circles, with errorbars corresponding to the 1σ uncertainty in the combined spectral fit performed for all the clusters falling within each redshift bin. The shaded area is the r.m.s. scatter among the measured metallicities within the same redshift intervals.

with an average metallicity $Z_{Fe} \simeq 0.42\, Z_{Fe,\odot}$. Therefore, in the absence of large metal–enriched clumps reaching the cluster centre, gas mixing leads to the accretion of relatively metal–poorer gas, thus turning into a decrease of $Z_{\rm Fe}$.

Although the agreement between the runs based on the Salpeter (1955) IMF and observations is rather encouraging, the question remains as to whether the positive evolution seen in the simulations is just the spurious product of the excess of star formation taking place in the central cluster regions. In order to address this question, we compare in the Fig.3.8 the evolution of $Z_{\rm Fe}$ for g51 when stopping star formation and/or metal production at low redshift. Quite remarkably, halting

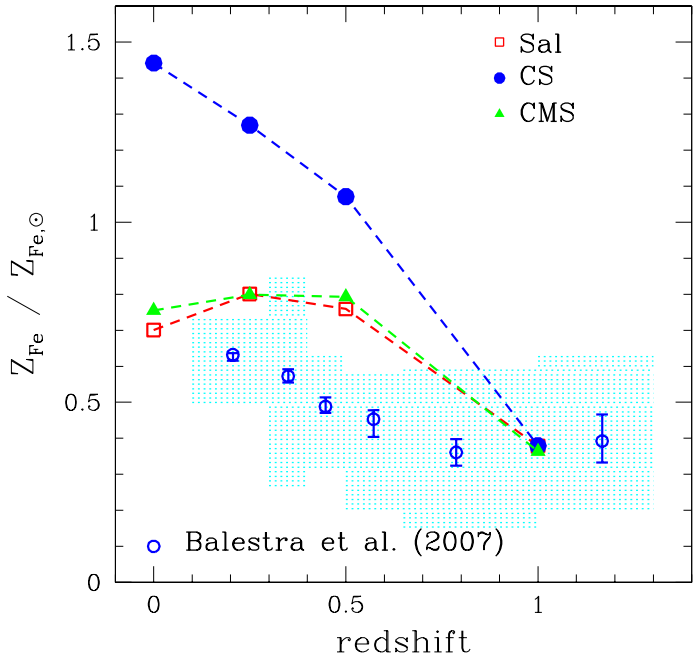

Figure 3.8: The comparison between observations and simulations for the evolution of the Iron abundance, $Z_{\rm Fe}$ the effect of stopping star formation and metal production at low redshift on the evolution of $Z_{\rm Fe}$ for the g51 cluster, using the Salpeter (1955) IMF. Results for the reference (*Sal*) run are shown with the open squares. The filled circles are for the simulation with radiative cooling and star formation stopped at $z = 1$ (CS), while the filled triangles are for the run in which also the metal production is turned off at $z = 1$ (CMS).. Observational results from Balestra et al. (2007) are shown with open circles, with errorbars corresponding to the 1σ uncertainty in the combined spectral fit performed for all the clusters falling within each redshift bin. The shaded area is the r.m.s. scatter among the measured metallicities within the same redshift intervals.

star formation below $z = 1$ while allowing already formed stars to keep releasing metals (CS run) has the effect of strongly increasing the positive evolution of $Z_{\rm Fe}$ in the central region of g51, which turns out to be over–enriched by $z = 0$. This leads to the counter-intuitive conclusion that the lack of low–z star formation should generate an increase of the enrichment of the hot gas. In order to investigate the origin of this increase, we show in Figure 3.9 the emission–weighted metallicity maps of the reference *Sal* run of g51 at $z = 0$, along with those of the CS and CMS runs. Quite apparently, the metal distribution in the CS simulation is more clumpy than in the reference run. At the cluster centre, a high $Z_{\rm Fe}$ is clearly visible, which boosts the central emission weighted metallicity shown in Fig.3.8. Indeed,

while the emission–weighted $Z_{\rm Fe}$ increases by about a factor two within $0.2R_{180}$, we verified that the mass–weighted estimate within the same radius increases only by about 10 per cent. In the reference run, the metals released in the high density clumps disappear from the hot diffuse medium due to the efficient gas cooling. As a result, the reference run has a globally higher level of diffuse enrichment, but a lower level of enrichment inside the high–density gas clumps, which dominate the emission–weighted estimate of $Z_{\rm Fe}$. These results demonstrate that the strongly positive evolution of the emission–weighted metallicity in the CMS run is driven by the accretion of highly enriched dense clumps.

■ The role of gas–dynamical processes

Inhibiting also the production of metals below redshift unity (CMS run) allows us to characterize the role played by gas–dynamical processes in redistributing metals produced at higher redshift. As shown in the bottom–left panel of Fig.3.9, metal clumps are less pronounced than in the CS run. The global enrichment level of the ICM is now significantly lower than in the reference run, although an enhancement in the innermost regions is still visible. The resulting mass–weighted metallicity within $0.2R_{180}$ at $z = 0$ decreases by ~ 60 per cent with respect to the reference run. Therefore, the stability of the emission–weighted metallicity is due to the competing effects of a more clumpy distribution of metals and of a decrease of the overall ICM metal budget.

The maps of Fig.3.9 also illustrate the role of gas–dynamical effects in redistributing highly enriched gas. Merging clumps within the cluster virial region leave behind them over–enriched tails of stripped gas, which is tempting to explain as due to ram–pressure stripping. However, a significant contribution could well be provided by viscous stripping. Since the SPH scheme is known to be generally characterized by a large numerical viscosity, this may induce an excess of gas stripping from merging halos. Sijacki & Springel (2006b) showed that the effect of including the Spitzer-Braginskii viscosity in the SPH, on the top of the numerical viscosity, is indeed that of further increasing gas stripping from merging halos. On the other hand, Dolag et al. (2005) discussed an SPH scheme of reduced viscosity. In this case, the increase of the "turbulent" stochastic gas motions should provide a more efficient diffusion of metals from star–forming regions (Rebusco et al., 2005), while making viscous stripping less efficient. Although it is beyond the aim of this work to carry out an accurate analysis of the effect of viscosity on the pattern of the ICM enrichment, there is no doubt that this aspect deserve an accurate in-depth investigation.

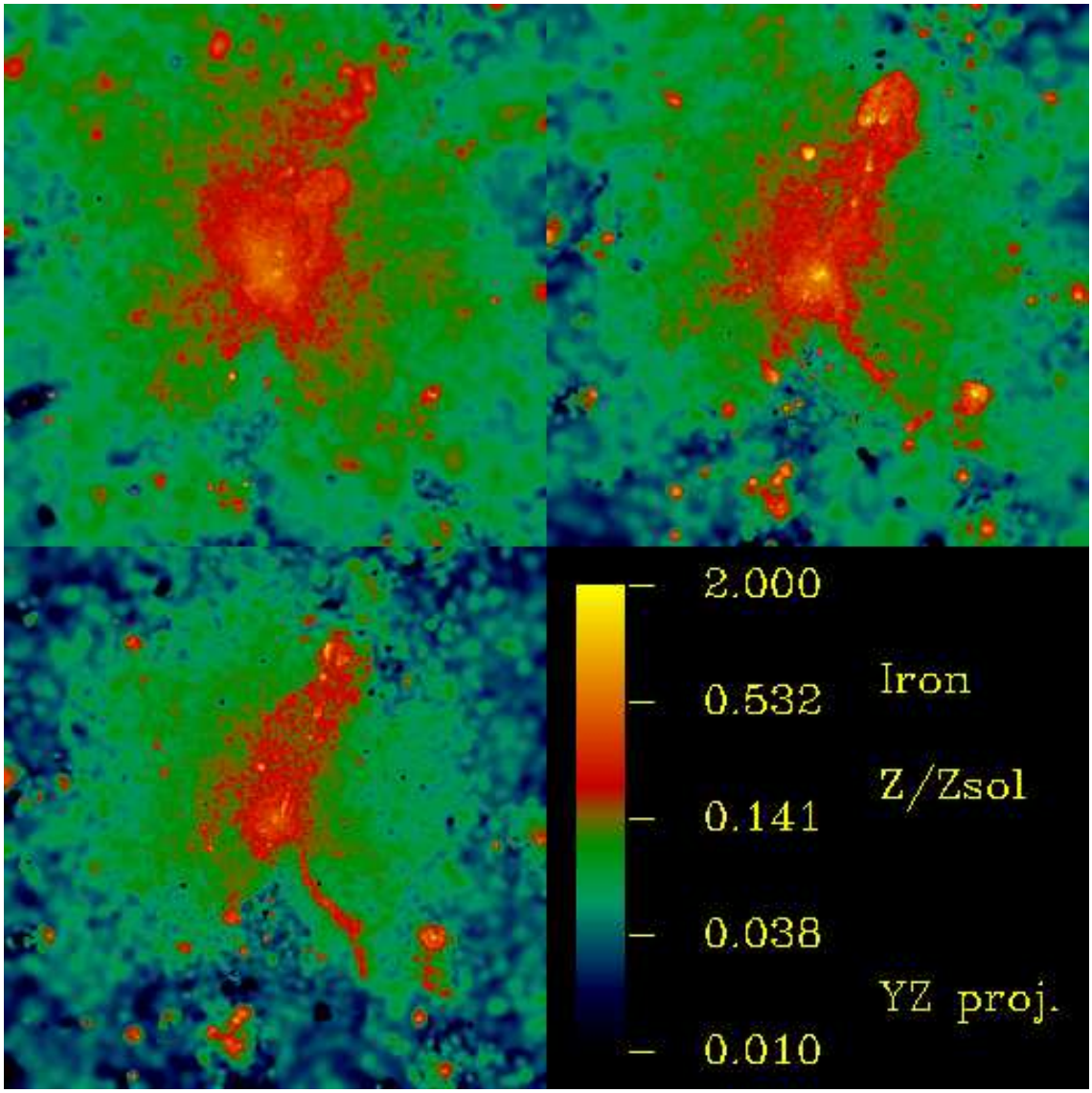

Figure 3.9: Projected maps of the emission–weighted Iron abundance for simulations of the g51 cluster, using the IMF by Salpeter (1955), for the reference run (upper left), for the run with cooling and star formation stopped at $z = 1$ (CS run; upper right) and for the run in which also the metal production is stopped at $z = 1$ (CMS run; lower left). Each map is $2R_{\rm vir}$ a side.

3.3.4. The SNIa rate

The supernova rate represents a useful diagnostic to link the observed evolution of the ICM metallicity to the past history of star formation and to shed light on the relative contribution of SNIa and SNII in releasing metals. In particular the ratio

between the SN rate and the B-band luminosity, the so–called SNU_B, can be used to distinguish the relative contribution of SNIa, which form in binary systems of stars with masses in the range (0.8–8) $M_\odot$ and the short-living massive stars that contribute substantially to the B–band luminosity of galaxies. In this section we present a comparison between the results of our simulated clusters and observational data of SNU_B in galaxy clusters from Gal-Yam et al. (2002), Mannucci et al. (2008) and Sharon et al. (2007).

The simulation analysis finalized to compute the SNU_B proceeds as follows. For each star particle we know its formation redshift and metallicity. Given the IMF and the lifetime function, this allows us to compute the rate of SNIa exploding in each such particle. Furthermore, using the spectrophotometric GALAXEV code (Bruzual & Charlot, 2003) we also compute the B–band luminosity of each star particle, which is treated as a Single Stellar Population (SSP). Once SNIa rates and luminosities are computed for all the star particles, we run the SKID substructure–finding algorithm (Stadel, 2001) on their distribution to identify galaxies as gravitationally bound groups of stars. All the star particles not bound to galaxies take part of the intracluster diffuse stellar component (e.g., Murante et al., 2007). This procedure used to identify galaxies and assign broad–band luminosities to them was defined by Saro et al. (2006) and is described in Chapter 2.

In order to reproduce the observational procedure, we compute the SNU_B values by also including the contribution of the SNIa arising from diffuse stars, while the B–band luminosity is computed by including only the contribution of the identified galaxies.

In the Figure 3.10 we compare the SNU_B values from the simulations with different IMFs with observational data. In performing this comparison one potential ambiguity arises from the definition of the extraction radius, within which luminosities and SNIa rates are measured in observations, since different authors use different aperture radii. To address this issue we computed SNU_B in the simulations within R_{vir} and verified that the results are left unchanged when using instead R_{500}.

Observational data show a declining trend at low redshift. This is generally interpreted as due to the quenching of recent star formation, which causes the number of SNIa per unit B–band luminosity to decrease after the typical lifetime of the SNIa progenitor has elapsed. On the other hand, our simulations predict a rather flat evolution of the SNU_B, independently of the choice for the IMF, which is the consequence of the excess of low–redshift star formation. The runs based on the Salpeter and on the Kroupa IMF produce very similar results. Although the Kroupa IMF produces a higher rate of SNIa, due to its higher amplitude in the (1–8) $M_\odot$ stellar mass range, this is compensated by the higher values of L_B. These two IMFs both agree with the observational data at $z \gtrsim 0.3$ within the large observational uncertainties, while they overpredict the rates measured for local clusters. Although the excess of recent star formation in the central regions of our simulated clusters pro-

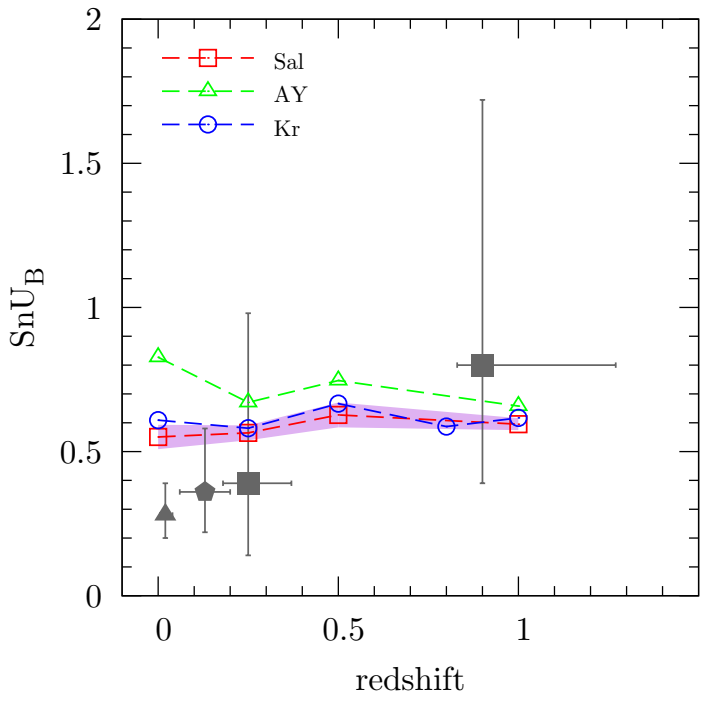

Figure 3.10: Comparison between the observed and the simulated evolution of the SNIa rate per unit B–band luminosity (SNU$_B$): the effect of changing the IMF. The open squares are for the Salpeter (1955) IMF, the open triangles are for the top–heavy IMF by Arimoto & Yoshii (1987) and the open circles for the IMF by Kroupa (2001). For the Salpeter IMF, the shaded area show the r.m.s. scatter evaluated over the four simulated clusters, while for the other two IMFs only the result for the g51 cluster is shown. Filled symbols with errorbars refer to observational data from Mannucci et al. (2008) (triangle), Gal-Yam et al. (2002) (squares) and Sharon et al. (2007) (pentagon).

duces too blue BCGs (Saro et al., 2006), the large number of SNIa associated to this star–formation overcompensate the excess of blue light.

As for the simulation with the Arimoto–Yoshii IMF, it predicts an even higher SNU$_B$ at low redshift. As shown in the Fig.3.11, decreasing the binary fraction to $A = 0.05$ decreases the value of the SNU$_B$ by more than a factor 2. While this helps in reconciling the simulation results with the low–redshift data, it introduces a tension with the data at $z \sim 1$.

Truncating star formation at $z = 1$ (Fig.3.11) has the desired effect of decreasing the value of SNU$_B$ below $z = 0.5$. Quite interesting, for $0.5 \lesssim z \lesssim 1$ the decreasing trend of the SNIa rate is compensated by the corresponding decrease of the B–band luminosity, while it is only at $z > 0.5$ that the decrease of the SNIa rate takes over

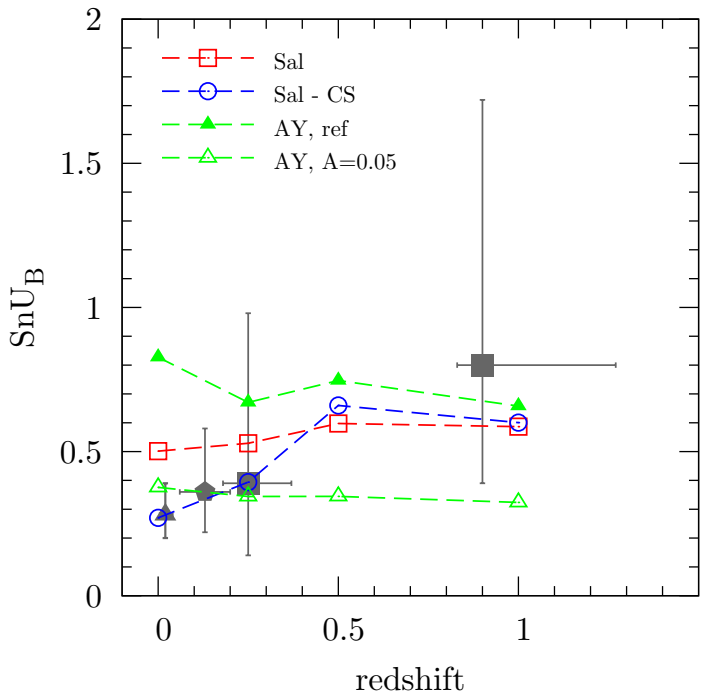

Figure 3.11: Comparison between the observed and the simulated evolution of the SNIa rate per unit B–band luminosity (SNU$_B$): the effect of suppressing low–redshift star formation and of changing the binary fraction on the SNU$_B$ evolution of the g51 cluster. The open squares and the open circles are for the reference run with Salpeter (1955) IMF and for the same run with cooling and star formation stopped at $z = 1$ (CS run), respectively. The filled and the open triangles are for the runs with Arimoto & Yoshii (1987) IMF, using $A = 0.1$ and $A = 0.05$ for the fraction of binary stars, respectively. Filled symbols with errorbars refer to observational data from Mannucci et al. (2008) (triangle), Gal-Yam et al. (2002) (squares) and Sharon et al. (2007) (pentagon).

causes the decrease of the SNU$_B$ values.

3.4 Conclusions

We have presented results from cosmological SPH hydrodynamical simulations of galaxy clusters with the purpose of characterizing the evolution of the chemical enrichment of the intra–cluster medium (ICM) out to redshift $z \simeq 1$. The simulations have been performed with a version of the GADGET-2 code (Springel, 2005), which includes a detailed model of chemical evolution (Tornatore et al., 2007a, , T07). Our simulations have been performed with the purpose of investigating the effect of

changing the chemical evolution model and the effect of suppressing star formation at $z < 1$. The main results of our analysis can be summarized as follows.

(a) The observed metallicity–temperature relation is well reproduced by our simulated cluster set based on the Salpeter (1955) IMF, at least at the scale of galaxy groups, while a top–heavy IMF overproduces Iron independently of cluster richness.

(b) The Iron abundance profiles provided by simulations based on the Salpeter (1955) IMF are in reasonable agreement with the results from Chandra observations of nearby clusters by Vikhlinin et al. (2005) at $R \lesssim 0.2 R_{500}$. Simulations based on the IMFs by Kroupa (2001) (*Kr*) and Arimoto & Yoshii (1987) (*AY*) both predict too high a normalization for these profiles. However, reducing the fraction of stars assumed to belong to binary systems suppresses the enrichment level, thus alleviating the disagreement of a top–heavy IMF with the observed $Z_{\rm Fe}$ profiles. Our simulations always predict negative metallicity gradients extending out to R_{500} and beyond, at difference with recent XMM–Newton measurements of the Iron metal abundance at relatively large radii (Snowden et al., 2008; Leccardi & Molendi, 2008a). Abundance gradients at relatively large radii can instead provide a non-trivial constraint for chemo-dynamical models of the ICM enrichment and feedback mechanism, as we will see in the next Chapter.

(c) All our simulations predict a positive evolution of the central Iron abundance, comparable to that observed by Balestra et al. (2007) (see also Maughan et al. 2008). Using a Salpeter IMF also provide an enrichment consistent with observations, while the Kroupa and Arimoto–Yoshii (*AY*) IMFs overpredict the enrichment level at all redshifts. Again, this disagreement can be alleviated by decreasing the fraction of binary systems. It is worth reminding that the observed evolution of the Iron abundance is traced by using a mix of cool–core and non cool–core clusters, while our simulated clusters are all dynamically relaxed. Clearly, a fully self–consistent comparison would require simulating a representative population of clusters, having a variety of morphologies and dynamical states.

(d) Stopping cooling and star formation at $z = 1$ (CS run) has the effect of producing a too strong positive evolution of the emission–weighted metallicity. Indeed, in the absence of star formation all the metals released at $z < 1$ by long–living stars are no longer locked back in the stellar phase. As a result, metallicity is enhanced inside high–density halos and in the central cluster region. The clumpy metal distribution boosts the emission–weighted abundance

estimate. This leads to the somewhat counter-intuitive conclusion that suppressing recent star formation has the effect of enhancing the positive evolution of the ICM metallicity.

(e) A comparison of the SNIa rate per unit B–band luminosity, SNU_B, show that our simulations are generally not able to reproduce the observed declining trend at low redshift. This result is explained by the excess of recent star formation taking place in the central regions of galaxy clusters. Indeed, excising star formation at $z < 1$ produces an evolution of SNU_B which is consistent with the observed one.

Cluster simulations which only include stellar feedback, like those presented here, are well known to be at variance with a number of observations, such as the temperature profiles in the cool core regions and an large excess of recent star formation in the BCG. Our prescription to quench recent star formation is admittedly oversimplified. A more realistic treatment would require introducing energy feedback from gas accretion onto super-massive black holes, which self–consistently follow the hierarchical build-up of the cluster (e.g., Sijacki & Springel, 2006a). Still, our results highlight that the positive evolution of the metal abundance in the central regions of simulated clusters can not be simply interpreted as a consequence of an excess of low–redshift star formation. In fact, the evolution of the metallicity pattern is driven by the combined action of the gas–dynamical processes, which redistribute already enriched gas, and of star formation, which acts both as a source and as a sink of metals.

While hydrodynamical simulations provide an important interpretative framework for observations of the history of the ICM enrichment, the numerical accuracy for the description of relevant physical processes is still missing. Nevertheless the implementation of simple model of AGN feedback described in Chapter 4 is an improvement, as we will see, and an important step in the effort of an accurate description of the relevant physics that affects the ICM.

CHAPTER 4

The IMPRINT OF FEEDBACK on the ICM PROPERTIES

This Chapter is devoted to the study of the effects that energy feedback from Active Galactic Nuclei (AGN) produce on thermodynamical and chemical properties of the IntraCluster Medium. For this study we use a large set of galaxy clusters and groups simulated within the ΛCDM cosmology with different feedback prescriptions: (i) galactic winds driven by supernovae explosions, (ii) supermassive BHs in the 'quasar mode' at high redshift, (iii) supermassive BHs powered by gas accretion in the 'radio mode', that we implemented with the simple prescription of varying the coupling efficiency of the energy with the ICM gas. The results were compared with recent observations. We found that AGNs are (i) able to quench star formation in the BCGs at $z < 4$, (ii) provide the correct temperature profile with cool cores at group scales, (iii) create a widespread enrichment in the cluster outskirts, due to a high efficiency in displacing the enriched gas to the IGM at higher redshift. The imprints left by different sources of feedback on the ICM enrichment pattern are investigated using Iron and Silicon abundances as tracers. Such imprints are found to be most notable in external regions, approaching the cluster virial boundaries.

4.1 Introduction

High quality data from the current generation of X–ray satellites (XMM-Newton, Chandra and Suzaku) have now established a number of observational facts concerning the thermo-dynamical and chemo-dynamical properties of the intra-cluster medium (ICM) for statistically representative sets of galaxy clusters: core regions of relaxed clusters show little evidence of gas cooler than about a third of the virial temperature (e.g., Peterson et al., 2001; Böhringer et al., 2002; Sanderson et al., 2006); temperature profiles have negative gradients outside core regions, a trend that extends out to the largest radii covered so far by observations (e.g., De Grandi & Molendi, 2002; Vikhlinin et al., 2005; Zhang et al., 2006; Baldi et al., 2007; Pratt et al., 2007; Leccardi & Molendi, 2008b); gas entropy is higher than expected from simple self-similar scaling properties of the ICM, not only in core regions, but also out to R_{500}[1] (e.g., Sun et al., 2009, and references therein); radial profiles of the Iron abundance show negative gradients, more pronounced for relaxed cool core (CC) clusters (see the definition in Sec.1.2.2), with central values of $Z_{\rm Fe}$ approaching solar abundance and with a global enrichment at a level of about 1/3–1/2 $Z_{Fe,\odot}$ (e.g.,De Grandi et al. 2004; Vikhlinin et al. 2005; de Plaa et al. 2006; Snowden et al. 2008; Leccardi & Molendi 2008a; see Mushotzky 2004; Werner et al. 2008 for recent reviews).

As already discussed (Sec. 1.4 and 2.3.5), the above observational properties of the ICM come from a non-trivial interplay between the underlying cosmological scenario, which shapes the large-scale structure of the Universe, and a number of astrophysical processes (e.g., star formation, energy and chemical feedback from supernovae and AGN) taking place on much smaller scales. This complexities can be described as the result of hierarchical assembly of cosmic structures as traced by cosmological simulations (e.g., Borgani & Kravtsov, 2009, for a recent review). These simulations reach nowadays a high enough resolution, while including a realistic description of the above mentioned astrophysical processes, in order to provide a coherent interpretative framework for X-ray observations. Quite remarkably, simulation predictions for the thermodynamical properties of the ICM are in good agreement with observations, at least outside the core regions: simulated profiles of gas density and temperature match the observed ones at cluster-centric distances $\gtrsim 0.1R_{500}$ (e.g., Loken et al., 2002; Borgani et al., 2004; Kay et al., 2004; Roncarelli et al., 2006; Pratt et al., 2007; Nagai et al., 2007b; Croston et al., 2008); the observed entropy level at R_{500} is well reproduced by simulations including radiative cooling and star formation (e.g., Nagai et al., 2007a; Borgani & Viel, 2009). The situation is quite different within cluster cores, where simulations including only stellar feedback generally fail at producing realistic cool cores. The two clearest manifestations of

[1] See the definition on page 83.

this failure are represented by the behaviour of temperature and entropy profiles at small radii, $\lesssim 0.1 R_{500}$. Observations of cool core clusters show that temperature profiles smoothly decline toward the centre, reaching temperatures of about 1/3–1/2 of the maximum value, while the entropy level at the smallest sampled scales is generally very low (e.g., Sun et al., 2009; Sanderson et al., 2009b). On the contrary, radiative simulations including a variety of models of stellar feedback predict steep negative temperature gradients down to the innermost resolved radii and central entropy levels much higher than observed (e.g., Valdarnini 2003; Tornatore et al. 2003; Borgani et al. 2004; Nagai et al. 2007a; cf. also Kay et al. 2007). This failure of simulations is generally interpreted as due to overcooling, which takes place in simulated clusters even when including an efficient supernova (SN) feedback, and causes an excess of star formation in the simulated brightest cluster galaxies (BCGs; Romeo et al. 2005; Saro et al. 2006).

The generally accepted solution to these shortcomings of simulations is represented by AGN feedback. Indeed, the presence of cavities in the ICM at the cluster centre is considered as the fingerprint of the conversion of mechanical energy associated to AGN jets into thermal energy (and possibly in a non–thermal content of relativistic particles) through shocks (e.g., Mazzotta et al. 2004a; Fabian et al. 2005; McNamara et al. 2006; Sanders & Fabian 2007; see McNamara & Nulsen 2007 for a review). Although analytical arguments convincingly show that the energy radiated from gas accretion onto a central super-massive black hole (BH) is enough to suppress gas cooling, it is all but clear how this energy is thermalised and distributed in the surrounding medium. A likely scenario is that bubbles of high entropy gas are created at the termination of jets. Buoyancy of these bubbles in the ICM then distributes thermal energy over larger scales (e.g., Dalla Vecchia et al., 2004; Cattaneo et al., 2007). Crucial in this process is the stability of the bubbles against gas dynamical instabilities which would tend to destroy them quite rapidly. Indeed, detailed numerical simulations have demonstrated that gas circulation associated to jets (e.g., Omma et al., 2004; Brighenti & Mathews, 2006; Heinz et al., 2006), gas viscosity, magnetic fields (e.g., Ruszkowski et al., 2007) and injection of cosmic rays (e.g., Ruszkowski et al., 2008) are all expected to cooperate in determining the evolution of buoyant bubbles. Although highly instructive, all these simulations have been performed for isolated halos and, as such, they describe neither the cosmological growth and merging of black holes, nor the hierarchical assembly of galaxy clusters.

Springel et al. (2005a) and Di Matteo et al. (2005) have presented a model that follows in a cosmological simulation the evolution of the BH population and the effect of energy feedback resulting from gas accretion onto BHs. In this model, BHs are treated as sink particles which accrete from the surrounding gas according to a Bondi accretion rate (e.g., Bondi, 1952), with an upper limit provided by the Eddington rate (see also Booth & Schaye, 2009). This model was used by

Bhattacharya et al. (2008), who run cosmological simulations to study the effect of AGN feedback on galaxy groups. They found that this feedback is effective in reducing star formation in central regions and to displace gas towards outer regions. However, the resulting entropy level within cluster cores is higher than observed. In its original version, the energy extracted from BH accretion is locally distributed to the gas around the BHs according to a SPH-kernel weighting scheme. This model has been modified by Sijacki & Springel (2006a) who included the possibility to inflate high-entropy bubbles in the ICM whenever accretion onto the central BH enters in a quiescent "radio mode". The underlying idea of injecting bubbles with this prescription was to provide a more realistic description of the effect of jet termination on the ICM, although the effect of the jet itself was not included. Puchwein et al. (2008) simulated a set of clusters and groups to show that this feedback scheme is able to reproduce the observed slope of the relation between X–ray luminosity and temperature. Sijacki et al. (2007) showed in a simulation of a single poor galaxy cluster that the injection of bubbles is quite effective in suppressing star formation in central regions. However, also in this case the temperature profile in the core regions does not match the observed slope, while more realistic temperature profiles can be produced if bubble injection is associated to the injection of a non–thermal population of relativistic particles (Pfrommer et al., 2007; Sijacki et al., 2008). Although these authors presented results concerning the effect of AGN on the ICM thermodynamics, no detailed analysis has been so far carried out to study the interplay between AGN and chemical enrichment, by including a detailed chemo-dynamical description of the ICM.

Indeed, the amount and distribution of metals in the ICM provide an important diagnostic to reconstruct the past history of star formation and the role of gas-dynamical and feedback processes in displacing metals from star forming regions (e.g., Mushotzky, 2004; Borgani et al., 2008b; Schindler & Diaferio, 2008, for reviews). Cosmological chemo-dynamical simulations of galaxy clusters generally show that the predicted profiles of Iron abundance are steeper than observed (e.g., Valdarnini, 2003; Tornatore et al., 2004; Romeo et al., 2006a; Tornatore et al., 2007a; Davé et al., 2008), with an excess of enrichment in the core regions. This is generally interpreted as due to the same excess of recent star formation in simulated BCGs. However, in Chap. 3 we show that an excess of recent star formation has also the effect of efficiently locking recently-produced metals into stars, thereby preventing a too fast increase of the metallicity of the hot diffuse medium.

All the above analyses are based on different implementations of SN energy feedback, while only much less detailed analyses of ICM metal enrichment have been so far presented by also including AGN feedback in cosmological simulations (e.g., Sijacki et al., 2007; Moll et al., 2007). For instance, Roediger et al. (2007) showed from simulations of isolated halos that buoyancy of bubbles can actually displace a large amount of the central highly enriched ICM, thus leading to a radical change

of the metallicity profiles, or even to a disruption of the metallicity gradients.

The aim of this Chapter is to present a detailed analysis of cosmological hydrodynamical simulations of galaxy clusters, which have been carried out with the GADGET-2 code (Springel, 2005), by combining the AGN feedback model described by Springel et al. (2005a) with the SPH implementation of chemo-dynamics presented by Tornatore et al. (2007a). Besides showing results on the effect of combining metallicity–dependent cooling and AGN feedback on the ICM thermodynamics, we will focus our discussion on the different effects that SNe and AGN feedback have on the chemical enrichment of the ICM. Although we will shortly discuss the effect of different feedback sources on the pattern of star formation in the BCG, the results presented in this Chapter will mainly concern the enrichment of the hot diffuse intra-cluster gas. The scheme of the Chapter is as follows. We present in Section 2 the simulated clusters, and briefly describe the implementation of the chemical evolution model in the GADGET-2 code along with the SN and AGN feedback models. In Section 3 we show our results on the thermal properties of the ICM and their comparison with observational results. Section 4 is devoted to the presentation of the results on the ICM chemical enrichment from our simulations and their comparison with the most recent observations. We discuss our results and draw our main conclusions in Section 5.

Also in this case the used solar abundances are those from Grevesse & Sauval (1998). The results presented in this Chapter were published in Fabjan et al. (2010).

4.2 The simulations

4.2.1. The set of simulated clusters

The set of simulated clusters is the same as that described in the Chapter 3 (see also Dolag et al., 2009), with the basic characteristics of each of the 18 clusters reported in Table 4.1. With respect to the previous simulations we perform the following changes:

- *the initial conditions* were prepared with periodic boundaries (while non-periodic boundaries were adopted for those used previously)
- *mass resolution* was increased by a factor of 6.5 for galaxy groups.

At the higher resolution, the mass of the DM and gas particles are $m_{DM} \simeq 1.9 \times 10^8\, h^{-1}\mathrm{M}_\odot$ and $m_{gas} = 2.8 \times 10^7\, h^{-1}\mathrm{M}_\odot$ respectively, with Plummer equivalent softening length for the computation of the gravitational force set to $\varepsilon = 2.75\, h^{-1}$kpc in physical units below $z = 2$ and to $\varepsilon = 8.25\, h^{-1}$kpc in comoving units at higher redshifts. In the lower resolution runs, these values are rescaled according to $m_{DM}^{-1/3}$.

Cluster	M_{200}	R_{200}	T_{500}	M_{BH}	
				AGN1	AGN2
g1.a	12.69	1.76	9.71	56.22	15.74
g1.b	3.64	1.16	3.39	7.96	2.52
g1.c	1.36	0.84	2.03	4.63	1.32
g1.d	1.04	0.76	1.82	1.59	0.46
g1.e	0.62	0.64	1.44	0.84	0.30
g8.a	18.51	2.00	12.82	113.50	27.73
g8.b	0.65	0.65	1.41	2.58	0.88
g8.c	0.52	0.61	1.42	1.74	0.63
g51	10.95	1.68	7.55	43.38	16.50
					$6.18^{\dagger}$
					$15.02^{\ddagger}$
g72.a	10.57	1.66	8.67	48.74	13.87
g72.b	1.48	0.86	2.18	3.79	1.34
g676	0.87	0.72	1.91	3.03	0.95
g914	0.88	0.72	2.03	2.89	1.13
g1542	0.83	0.71	1.79	2.54	0.79
g3344	0.92	0.74	2.03	3.15	1.29
g6212	0.89	0.73	2.02	2.57	0.99

Table 4.1: Characteristics of the simulated clusters. Column 1: cluster name. Column 2: mass contained within R_{200} (units of $10^{14}\,h^{-1}\mathrm{M}_{\odot}$). Column 3: value of R_{200} (units of $h^{-1}\mathrm{Mpc}$). Column 4: value of the spectroscopic-like temperature within R_{500}, T_{500}. Columns 5 and 6: mass of the central BH hosted in the BCG for the AGN1 and AGN2 runs (units of $10^{10}\,h^{-1}\mathrm{M}_{\odot}$), respectively. For the g51 cluster, the two additional values reported for the mass of the central BH refer to the AGN2(0.8) and AGN2W runs (see text) and are indicated with the † and ‡ symbol, respectively.

Only the low-mass g676 cluster was simulated at both resolutions. We provide in Table 4.2 a description of the parameters for the two different resolutions, also listing the clusters simulated at each resolution.

4.2.2. The simulation code

Our simulations were performed using the TreePM-SPH GADGET-2 code (Springel, 2005). All simulations include a metallicity-dependent radiative cooling (Sutherland & Dopita, 1993), heating from a uniform time-dependent ultraviolet background

	M_{DM}	m_{gas}	ε	Clusters
Low res.	11.0	2.03	5.00	g1, g8, g51, g72, g676
High res.	1.69	0.31	2.75	g676, g914, g1542, g3344, g6212

Table 4.2: Resolution of the different runs. Column 2-3: mass of the DM particles and initial mass of the gas particles (units of $10^8\,h^{-1}\mathrm{M}_\odot$). Column 4: value of the Plummer-equivalent gravitational force softening at $z = 0$ (units of $h^{-1}\mathrm{kpc}$). Column 5: clusters simulated at each resolution.

(Haardt & Madau, 1996) and the effective model by Springel & Hernquist (2003a) for the description of star formation. In this model, gas particles above a given density are treated as multiphase, so as to provide a sub–resolution description of the inter-stellar medium. In the following, we assume the density threshold for the onset of star formation in multiphase gas particles to be $n_H = 0.1cm^{-3}$ in terms of number density of hydrogen atoms. Our simulations also include a detailed model of chemical evolution by Tornatore et al. (2007, T07 hereafter). More details about the code and the model description can be found in Chapter 2.

Metals are produced by SNe-II, SNe-Ia and intermediate and low-mass stars in the asymptotic giant branch (AGB hereafter). We assume SNe-II to arise from stars having mass above $8M_\odot$. As for the SNe-Ia, we assume their progenitors to be binary systems, whose total mass lies in the range (3–16)$M_\odot$. Metals and energy are released by stars of different mass by properly accounting for mass–dependent lifetimes. In this work we assume the lifetime function proposed by Padovani & Matteucci (1993), while we assume the standard stellar initial mass function (IMF) by Salpeter (1955). We adopt the metallicity–dependent stellar yields by Woosley & Weaver (1995) for SNe-II, the yields by van den Hoek & Groenewegen (1997) for the AGB and by Thielemann et al. (2003) for SNe-Ia. The version of the code used for the simulations presented here allowed us to follow H, He, C, O, Mg, S, Si and Fe. Once produced by a star particle, metals are then spread to the surrounding gas particles by using the B-spline kernel with weights computed over 64 neighbours and taken to be proportional to the volume of each particle.

4.2.3. Feedback models

In the simulations presented in this Chapter we model two different sources of energy feedback. The first one is the kinetic feedback model implemented by Springel & Hernquist (2003a), in which energy released by SN-II triggers galactic winds, with mass upload rate assumed to be proportional to the star formation rate, $\dot{M}_W = \eta \dot{M}_\star$, as discussed in Chapter 2 (page 45). Therefore, fixing the parameter η and the wind velocity v_W amounts to fix the total energy carried by the winds. In the following, we assume $\eta = 2$ for the mass-upload parameter and $v_W = 500\,\mathrm{km\,s^{-1}}$ for the wind

velocity. If each SN-II releases 10^{51} ergs, the above choice of parameters corresponds to assuming that SNe-II power galactic outflows with nearly unity efficiency for a Salpeter IMF (see Springel & Hernquist, 2003a).

Furthermore, we include in our simulations the effect of feedback energy released by gas accretion onto super-massive black holes (BHs), following the scheme originally introduced by Springel et al. (2005, SDH05 hereafter; see also Di Matteo et al. 2005, 2008; Booth & Schaye 2009). We refer to SDH05 for a more detailed description. In this model, BHs are represented by collisionless sink particles of initially very small mass, that are allowed to subsequently grow via gas accretion and through mergers with other BHs during close encounters. During the growth of structures, we seed every new dark matter halo above a certain mass threshold M_{th}, identified by a run-time friends-of-friends algorithm, with a central BH of mass $10^5\,h^{-1}\mathrm{M}_\odot$, provided the halo does not contain any BH yet. For the runs at the lower resolution the value of the halo mass assumed to seed BHs is $M_{th} = 5\times10^{10}\,h^{-1}\mathrm{M}_\odot$, so that it is resolved with about 40 DM particles. At the higher resolution the halo mass threshold for BH seeding decreases to $M_{th} = 10^{10}\,h^{-1}\mathrm{M}_\odot$, so as to resolve it with approximately the same number of particles. We verified that using in the higher-resolution runs the same value of M_{th} as in the low-resolution runs causes the effect of BH accretion to be shifted toward lower redshift, since its onset has to await the formation of more massive halos, while leaving the final properties of galaxy clusters almost unaffected.

Once seeded, each BH can then grow by local gas accretion, with a rate given by

$$\dot{M}_{BH} \;=\; \min\left(\dot{M}_B, \dot{M}_{Edd}\right) \tag{4.1}$$

or by merging with other BHs. Here $\dot{M}_B$ is the accretion rate estimated with the Bondi-Hoyle-Lyttleton formula (Hoyle & Lyttleton, 1939; Bondi & Hoyle, 1944; Bondi, 1952), while $\dot{M}_{Edd}$ is the Eddington rate. The latter is inversely proportional to the radiative efficiency ϵ_r, which gives the radiated energy in units of the energy associated to the accreted mass:

$$\epsilon_r \;=\; \frac{L_r}{\dot{M}_{BH}c^2}\,. \tag{4.2}$$

Following Springel et al. (2005a), we use $\epsilon_r = 0.1$ as a reference value, which is typical for a radiatively efficient accretion onto a Schwartzschild BH (Shakura & Syunyaev, 1973). The model then assumes that a fraction ϵ_f of the radiated energy is thermally coupled to the surrounding gas, so that $\dot{E}_{\rm feed} = \epsilon_r\epsilon_f\dot{M}_{BH}c^2$ is the rate of provided energy feedback. In standard AGN feedback implementation we use $\epsilon_f = 0.05$ following Di Matteo et al. (2005), who were able with this value to reproduce the observed $M_{BH} - \sigma$ relation between bulge velocity dispersion and mass of the hosted BH (e.g., Magorrian et al., 1998). This choice was also found

to be consistent with the value required in semi-analytical models to explain the evolution of the number density of quasars (Wyithe & Loeb, 2003).

Gas swallowed by the BH is implemented in a stochastic way, by assigning to each neighbour gas particle a probability of contributing to the accretion, which is proportional to the SPH kernel weight computed at the particle position. Differently from SDH05, we assume that each selected gas particle contributes to the accretion with 1/3 of its mass, instead of being completely swallowed. In this way, a larger number of particles contribute to the accretion, which is then followed in a more continuous way. We remind that in the SDH05 scheme, this stochastic accretion is used only to increase the dynamic mass of the BHs, while their mass entering in the computation of the accretion rate is followed in a continuous way, by using the analytic expression for $\dot{M}_{BH}$. Once the amount of energy to be thermalised is computed for each BH at a given time-step, one has to distribute this energy to the surrounding gas particles. In their original formulation, SDH05 distributed this energy using the SPH kernel.

Besides following this standard implementation of the AGN feedback, we also follow an alternative prescription, which differ from the original one in two aspects.

Firstly, following Sijacki et al. (2007), we assume that a transition from a "quasar" phase to "radio" mode of the BH feedback takes place whenever the accretion rate falls below a given limit (e.g., Churazov et al., 2005, and references therein), corresponding to $\dot{M}_{BH}/\dot{M}_{Edd} < 10^{-2}$, which implies an increase of the feedback efficiency to $\epsilon_f = 0.2$. At high redshift BHs are characterised by high accretion rates and power very luminous quasars, with only a small fraction of the radiated energy being thermally coupled to the surrounding gas. On the other hand, BHs hosted within very massive halos at lower redshift are expected to accrete at a rate well below the Eddington limit, while the energy is mostly released in a kinetic form, eventually thermalised in the surrounding gas through shocks. Secondly, instead of distributing the energy using a SPH kernel, we distribute it using a top-hat kernel, having radius given by the SPH smoothing length. In order to avoid spreading the energy within a too small sphere, we assume a minimum spreading length of $2\,h^{-1}$kpc. The rationale behind the choice of the top-hat kernel is to provide a more uniform distribution of energy, thus mimicking the effect of inflating bubbles in correspondence of the termination of the AGN jets. It is well known that a number of physical processes need to be adequately included for a fully self-consistent description of bubble injection and buoyancy: gas-dynamical effects related to jets, magnetic fields, viscosity, thermal conduction, injection of relativistic particles.

In particular, a number of studies based on simulations of isolated halos (e.g., Omma et al., 2004; Brighenti & Mathews, 2006) have pointed out that gas circulation generated by jets provides an important contribution for the stabilization of cooling flows (see also Heinz et al., 2006, for a cosmological simulation of cluster formation including jets). In its current implementation, the model of BH feedback included

in our simulations neglects any kinetic feedback associated to jets. Based on an analytical model, Pope (2009) computed the typical scale of transition from kinetic to thermal feedback regime for AGN in elliptical galaxies and clusters. As a result, he found that the effect of momentum carried by jets can be neglected on scales $\gtrsim 20$ kpc, the exact value depending on the local conditions of the gas and on the injection rate of kinetic and thermal energy. In order to compare such a scale to that actually resolved in our simulations, we remind the reader that SPH hydrodynamics is numerically converged on scales about 6 times larger than the Plummer–equivalent softening scale for gravitational force (e.g., Borgani et al., 2002). Owing to the values of the gravitational softening reported in Table 2, the scales resolved in our simulations are not in the regime where kinetic feedback is expected to dominate, thus justifying the adoption of a purely thermal feedback. As a further test, we have computed the radius of the top–hat kernel within which energy is distributed around the central BHs in our simulated clusters. As a few examples, we found at $z = 0$ this radius to be 21 kpc and 23 kpc for the AGN2 runs of the g72 and g676 clusters, respectively. This implies that we are in fact distributing thermal energy over scales where kinetic feedback should not be dominant.

In view of the difficulty of self–consistently including the cooperative effect of all the physical processes we listed above, we prefer here to follow a rather simplified approach and see to what extent the final results of our simulations are sensitive to variations in the implementation of the BH feedback model.

In summary, we performed four series of runs, corresponding to as many prescription for energy feedback.

(a) No feedback (NF hereafter): neither galactic winds nor AGN feedback is included.

(b) Galactic winds (W hereafter) included by following the model by Springel & Hernquist (2003a), with $v_w = 500\,\mathrm{km\,s^{-1}}$ and $\eta = 2$ for the wind mass upload.

(c) Standard implementation of AGN feedback from BH accretion (AGN1 hereafter), using $\epsilon_f = 0.05$ for the feedback efficiency.

(d) Modified version of the AGN feedback (AGN2 hereafter), with feedback efficiency increasing from $\epsilon_f = 0.05$ to $\epsilon_f = 0.2$ when $\dot{M}_{BH}/\dot{M}_{Edd} < 10^{-2}$, and distribution of energy around the BH with a top-hat kernel.

In order to further explore the parameter space of the considered feedback models we also carried out one simulation of the g51 cluster based on the AGN2 scheme, but with the feedback efficiency increased to $\epsilon_f = 0.8$ (AGN2(0.8) hereafter). We also note that our simulations include either winds triggered by SN explosions or AGN feedback. While this choice is done with the purpose of separate the effects of these two feedback sources, we expect in realistic cases that both AGN and SN

feedback should cooperate in determining the star formation history of galaxies. In order to verify the effect of combining the two feedback sources, we carried out one simulation of the AGN2 scheme for the g51 cluster, in which also galactic winds with a velocity $v_w = 300\,\mathrm{km\,s^{-1}}$ are included (AGN2W hereafter).

Before starting the presentation of the results on the thermal and enrichment properties of the ICM, we briefly comment on the results concerning the mass of the central black holes in the simulations including AGN feedback, and the star formation rate (SFR) history of the brightest cluster galaxies (BCGs).

Looking at Table 1, we note that our simulations predict rather large masses for the super-massive BHs hosted in the central galaxies. Quite interestingly, the AGN2 runs generally produce BH masses which are smaller, by a factor 3–5, than for the AGN1 runs. This demonstrates that including the more efficient "radio mode" for the feedback and distributing the energy in a more uniform way has a significant effect in regulating gas accretion. Although BCGs are known to host BHs which are more massive than expected for normal early type galaxies of comparable mass (e.g., Lauer et al., 2007), the BH masses from our simulations seem exceedingly large, also for the AGN2 model. For instance, the BH mass hosted by M87, within the relatively poor Virgo cluster, is $m_{BH} \simeq (3-4) \times 10^9 M_\odot$ (e.g., Rafferty et al., 2006). This is about a factor 3–5 smaller than found in our AGN2 runs for clusters of comparable mass, $M_{200} \simeq 2 \times 10^{14}\,h^{-1}\mathrm{M}_\odot$. We note that increasing the radio-mode feedback efficiency from $\epsilon_f = 0.2$ to 0.8 (AGN2(0.8) run) reduces the mass of the central black hole in the g51 cluster from $m_{BH} \simeq 16.5 \times 10^9 M_\odot$ to $\simeq 6.2 \times 10^9 M_\odot$ (see Table 1). This suggests that a highly efficient thermalization of the energy extracted from the BH is required to regulate gas accretion to the observed level. Quite interestingly, we also note that adding the effect of galactic winds in the AGN2 scheme (AGN2W run) only provides a marginal reduction of the final mass of the central BH. Therefore, although galactic winds can play a significant role in regulating star formation within relatively small galaxies, they are not efficient in decreasing gas density around the largest BHs, so as to suppress their accretion rate.

As for the comparison with previous analyses, Sijacki et al. (2007) performed a simulation of the same g676 cluster included in our simulation set at the lower resolution, for their feedback scheme based on the injection of AGN driven bubbles. They found that the final mass of the central BH is $m_{BH} \simeq 6 \times 10^9\,h^{-1}\mathrm{M}_\odot$. This value is about 30 per cent lower than what we find for the AGN2 runs of g676. In order to compare more closely with the result by Sijacki et al. (2007), we repeated the run of the g676 cluster by switching off the metallicity-dependence of the cooling function. As a result, BH accretion proceeds in a less efficient way, and the resulting central BH mass in this case drops to $\simeq 3.5 \times 10^9\,h^{-1}\mathrm{M}_\odot$.

As for the SFR history of the BCG, this is estimated by identifying first all the stars belonging to the BCG at $z = 0$. This has been done by running the SKID group-finding algorithm (Stadel, 2001), using the same procedure described

by Saro et al. (2006). After tagging all the star particles belonging to the BCG, we reconstruct the SFR history by using the information on the redshift at which each star particle has been spawned by a parent gas particle, according to the stochastic algorithm of star formation implemented in the effective model by Springel & Hernquist (2003a). The resulting SFR histories for the BCG of the g51 clusters are shown in the left panel of Figure 4.1.

As expected, the run with no efficient feedback (NF) produces the highest star formation at all epochs: SFR has a peak at $z \simeq 4$ and then drops as a consequence of the exhaustion of gas with short cooling time. Despite this fast reduction of the SFR, its level at $z = 0$ is still rather large, $\simeq 400\,h^{-1}\mathrm{M}_{\odot}$ yr^{-1}. As for the run with winds, it has a reduced SFR since the very beginning, owing to the efficiency of this feedback scheme in suppressing star formation within small galaxies which form already at high redshift. Also in this case, the peak of star formation takes place at $z \sim 4$, but with an amplitude which is about 40 per cent lower than for the NF runs and with a more gentle decline afterwards. As for the runs with AGN feedback, their SFR history is quite similar to that of the W run down to $z \simeq 5$. Star formation is then suddenly quenched at $z \lesssim 4$. We note in general that SFR for the AGN1 model lies slightly below that of the AGN2 model, as a consequence of both the different way of distributing energy and, at low redshift, of the inclusion of the radio mode assumed in the quiescent BH accretion phase. Suppression of the SF at relatively low redshift is exactly the welcome effect of AGN feedback. At $z = 0$, the resulting SFR is of about $70 M_{\odot}\mathrm{yr}^{-1}$ for both models, a value which is closer to, although still higher than the typical values of SFR observed in the BCGs of clusters of comparable mass. (e.g., Rafferty et al., 2006). Quite interestingly, increasing the feedback efficiency to $\epsilon_f = 0.8$ in the AGN2(0.8) run does not significantly affect the level of low-redshift star formation, while it suppresses star formation by only ~ 10 per cent around the peak of efficiency. Therefore, while a higher efficiency is indeed effective in suppressing gas accretion onto the central BH, a further reduction of star formation associated to the BCG should require a different way of thermalizing the radiated energy. As for the AGN2W run, its SFR at high redshift is lower than for the AGN2 run, due to the effect of winds, while no significant change is observed at $z \lesssim 3$.

In the right panel of Fig.4.1 we plot the stellar mass found in the BCG at $z = 0$ that is formed before a given redshift. According to this definition, this quantity is the integral of the SFR plotted in the right panel, computed from a given redshift z to infinity. This plot clearly shows the different effect that winds and AGN feedback have in making the BGC stellar population older. In the NF and W runs, the redshift at which 50 per cent of the BCG stellar mass was already in place is $z_{50} \simeq 2$. This indicates that even an efficient SN feedback is not able to make the stellar population of the BCG older. On the contrary, the effect of AGN feedback takes place mostly at relatively low redshift. As a consequence the age of the BGC stellar population

increases, with $z_{50} \simeq 3.0-3.6$, almost independent of the detail of the AGN feedback scheme.

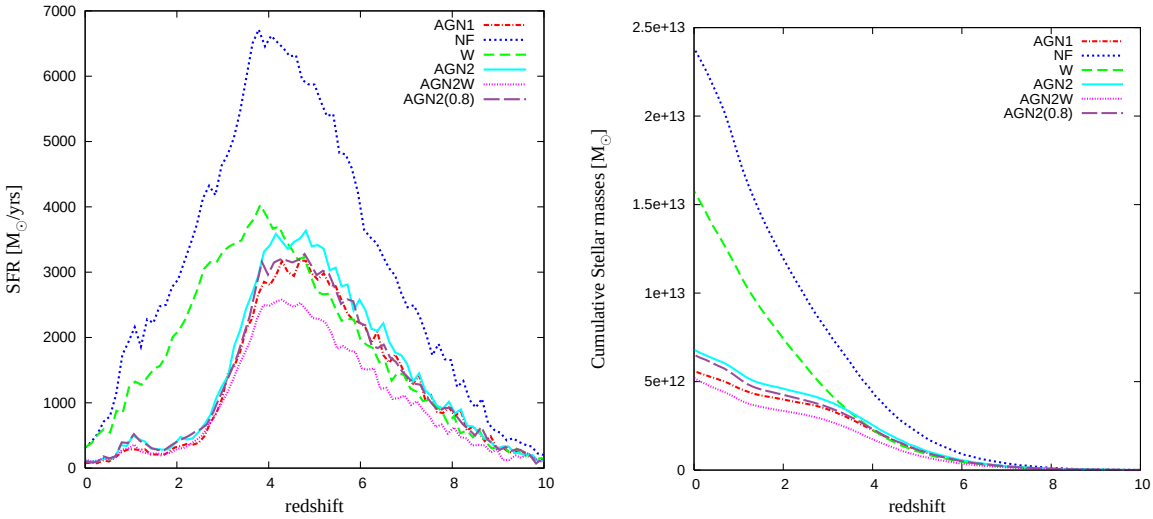

Figure 4.1: Left panel: the history of star formation rate of the brightest cluster galaxy (BCG) in the g51 cluster for the runs with no feedback (NF, blue short-dashed), with galactic winds (W, green dashed), with standard AGN feedback (AGN1, red dot-dashed) and with modified AGN feedback (AGN2, light-blue solid). Also shown are the results for the AGN2 run with higher radio-mode BH feedback efficiency (AGN2(0.8), purple long-dashed) and for the AGN2 run also including galactic winds (AGN2W, magenta dotted). **Right panel:** the cumulative stellar mass at different redshifts for the star particles that belong to the BCG at $z = 0$.

4.3 The effect of feedback on the ICM thermal properties

Galaxy clusters are identified in each simulation box by running first a friends-of-friends (FOF) algorithm over the high resolution DM particles, using a linking length of 0.15 in terms of the mean inter-particle separation. Within each FOF group, we identify the DM particle having the minimum value of the gravitational potential and take its position to correspond to the centre of the cluster. All profiles are then computed starting from this centre. The smallest radius that we use to compute profiles encompasses a minimum number of 100 SPH particles, a criterion that gives numerically converged results for profiles of gas density and temperature in non–radiative simulations (e.g., Borgani et al., 2002). As we shall see in the following, profiles computed with this criterion will extend to smaller radii for those runs which

have a higher gas density at the centre, while stopping at relatively larger radii for the runs including AGN feedback, which are characterised by a lower central gas density.

4.3.1. The luminosity-temperature relation

The relation between bolometric X–ray luminosity, L_X and ICM temperature, T, provided one of the first evidences that non–gravitational effects determine the thermo-dynamical properties of the ICM (e.g., Voit, 2005b, for a review). Its slope at the scale of clusters is observed to be $L_X \propto T^{\alpha}$ with $\alpha \simeq 2.5$–3 (e.g., Horner, 2001; Pratt et al., 2009), and possibly even steeper or with a larger scatter at the scale of galaxy groups (e.g., Osmond & Ponman, 2004). These results are at variance with respect to the prediction, $\alpha = 2$, of self-similar models based only on the effect of gravitational gas accretion (e.g., Kaiser, 1986). Attempts to reproduce the observed L_X–T relation with hydrodynamic simulations of clusters have been pursued by several groups (see Borgani et al., 2008a, for a recent review). Simulations of galaxy clusters including the effect of star formation and SN feedback in the form of energy–driven galactic winds produce results which are close to observations at the scale of clusters, while generally producing too luminous galaxy groups (e.g., Borgani et al., 2004). Although a closer agreement with observations at the scale of groups can be obtained by using SN–triggered momentum–driven winds (Davé et al., 2008), there is a general consensus that stellar feedback can not reproduce at the same time both the observed L_X–T relation and the low star formation rate observed in central cluster galaxies. Puchwein et al. (2008) presented results on the L_X–T relation for simulations of galaxy clusters which included the bubble–driven AGN feedback scheme introduced by Sijacki et al. (2007). They concluded that, while simulations not including any efficient feedback (in fact, quite similar to our NF runs) produce overluminous objects, their mechanism for AGN feedback is efficient in suppressing the X–ray luminosity of clusters and groups at the observed level.

We present here our results on the L_X–T relation, keeping in mind that our simulations differ from those by Puchwein et al. (2008) both in the details of the implementation of the AGN feedback scheme and in the treatment of the metallicity dependence of the cooling function. In the left panel of Figure 4.2 we show the results for our runs based on SN galactic winds (W runs) and for the runs not including any efficient feedback (NF runs). Filled symbols refer to the main halo of each simulated Lagrangian region, while open circles are for the "satellites". Although we find several satellites having a temperature comparable to those of the low-mass main halos (see also Table 1), we remind that these satellites are described with a mass resolution six times lower than that of the low-mass main halos. We note that the NF runs provide a L_X–T relation which is not far from the observed one,

especially at the scale of groups. The reason for this closer agreement, with respect to the result by Puchwein et al. (2008) lies in the fact that these authors adopted a cooling function computed for zero metallicity. Including the contribution of metal lines to the radiative losses increases cooling efficiency and, therefore, gas removal from the hot X–ray emitting phase. However, the price to pay for this reduction of X–ray luminosity is that a far too large baryon fraction is converted into stars within clusters (see below). Quite paradoxically, we also note than including an efficient feedback in the form of galactic winds turns into an increase of X–ray luminosity. This is due to the fact that this feedback prevents a substantial amount of gas from cooling, without displacing it from the central cluster regions, thus increasing the amount of X-ray emitting ICM.

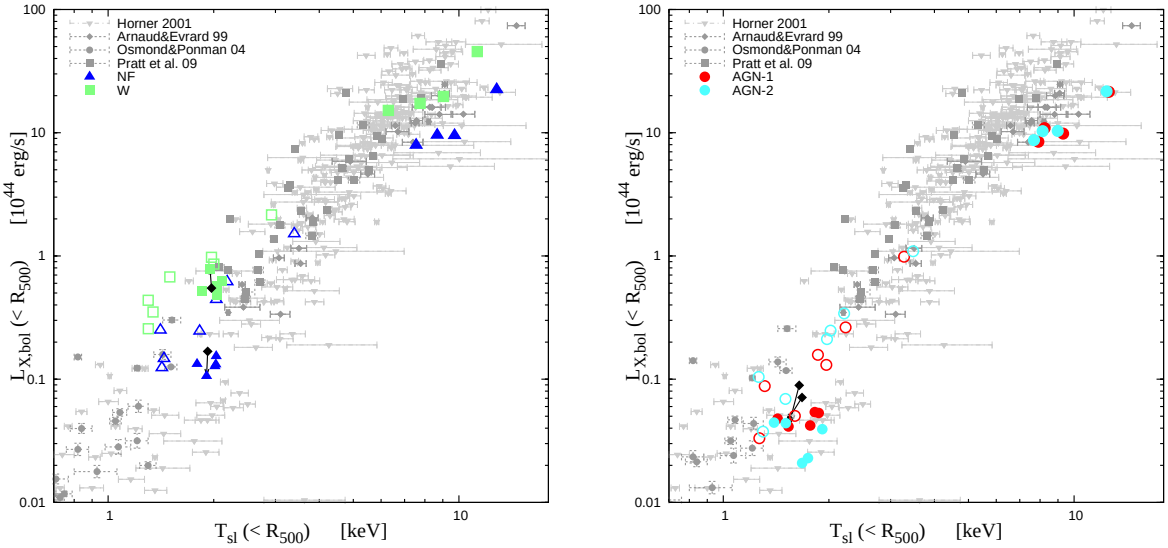

Figure 4.2: Relation between X–ray luminosity and temperature for simulated (coloured symbols) and observed (grey points with errorbars) clusters and groups. Observational data points are from Arnaud & Evrard (1999) (grey diamonds) and Pratt et al. (2009) (grey squares) for clusters, from Osmond & Ponman (2004) (grey circles) for groups and from Horner (2001) (grey triangles). Data from simulations were computed inside R_{500}. **Left panel:** results for the no feedback case (NF, blue triangles) and for the case with galactic winds (W, green squares). **Right panel:** results for the runs with standard AGN feedback (AGN1, red circles) and with the modified AGN feedback scheme, where also a radio-mode regime is included (see text, AGN2; cyan circles). For each series of runs, filled and open symbols refer to the main halo within each resimulated Lagrangian region and to "satellite" halos respectively. Black diamonds refer to the runs at $1\times$ resolution, with arrows pointing to results at $6\times$ higher resolution for the g676 cluster.

In order to asses the effect of the different resolution used for large and small clusters, we carried out runs of g676 at the same lower resolution of the massive

clusters. The results are shown in Fig. 4.2 with black diamonds connected with arrows to the corresponding higher resolution result. We note that resolution effects go in opposite directions for the NF and W runs. In fact, in the absence of winds, the runaway of cooling with resolution removes from the hot phase a larger amount of gas, thus decreasing X–ray luminosity. On the contrary, higher resolution allows a more accurate description of kinetic feedback, which starts heating gas at higher redshift. As a consequence, radiative losses are compensated at higher resolution for a larger amount of diffuse baryons, which remain in the hot phase, thereby increasing the X–ray luminosity.

As for the runs with AGN feedback, it is quite efficient in decreasing X–ray luminosity at the scale of galaxy groups, thus well recovering the observed L_X–T relation. This conclusion holds for both implementations of the AGN feedback, which have rather small differences. Therefore, although the AGN2 scheme is more efficient in regulating the growth of the central BHs hosted within the BCGs, it has a marginal effect on the X–ray luminosity. These results are in line with those found by Puchwein et al. (2008), who however used the injection of heated bubbles to distribute the energy extracted from the BH accretion. This witnesses that the feedback energy associated to gas accretion onto super-massive BHs is indeed able to produce a realistic L_X–T relation, almost independent of the detail of how the energy is thermalised in the surrounding medium.

4.3.2. The entropy of the ICM

Entropy level in central regions of clusters and groups is considered another fingerprint of the mechanisms which determine the thermodynamical history of the ICM. Early observational results on the presence of entropy cores (e.g., Ponman et al., 1999) have been more recently revised, in the light of higher quality data from Chandra (e.g., Cavagnolo et al., 2009) and XMM–Newton (e.g., Johnson et al., 2009) observations. These more recent analyses show that entropy level of clusters and groups at R_{500} is higher than predicted by non–radiative simulations, with entropy profiles for relaxed systems continuously decreasing down to the smallest resolved radii (see also Sun et al., 2009).

While radiative simulations of galaxy clusters have been generally shown to reproduce observational results at R_{500} (e.g., Nagai et al., 2007a; Davé et al., 2008), they generally predict too low entropy levels at smaller radii. For instance, Borgani & Viel (2009) have shown that the entropy at R_{2500} can be reproduced by resorting to a fairly strong pre-heating at $z = 4$. However, this pre-heating must target only relatively overdense regions, to prevent the creation of too large voids in the structure of the Lyman-α forest at $z \sim 2$ (see also Shang et al., 2007).

In the following we use the standard definition of entropy, which is usually

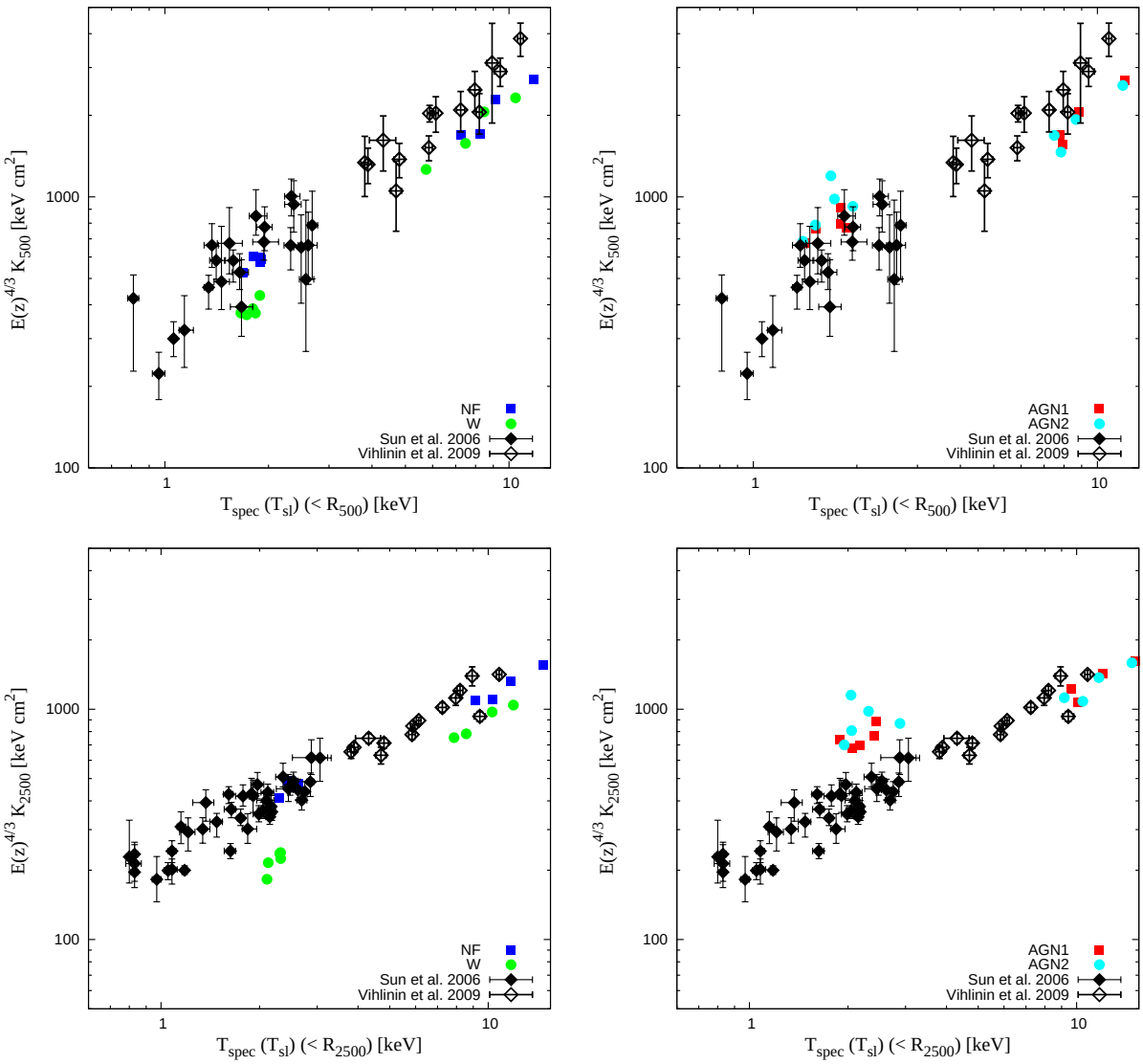

Figure 4.3: Relation between entropy and temperature for our simulated clusters (coloured circles and squares) and for the observational data points at R_{500} (upper panels) and R_{2500} (lower panels) from Sun et al. (2009) (black filled diamonds) and Vikhlinin et al. (2009) (black open diamonds). Left and right panels show results for the nine central clusters for the runs without (NF: blue squares; W: green circles) and with AGN feedback (AGN1: red squares; AGN2: cyan circles), respectively. For a fair comparison with observations, spectroscopic-like temperatures of the simulated clusters are computed by excluding the regions within $0.15R_{500}$.

adopted in X–ray studies of galaxy clusters (e.g., Sun et al., 2009):

$$K_\Delta = \frac{T_\Delta}{n_{e,\Delta}^{2/3}}, \tag{4.3}$$

where T_Δ and $n_{e,\Delta}$ are the values of gas temperature and electron number density computed at R_Δ. As for the temperature, it is computed by following the prescription of spectroscopic like temperature introduced by Mazzotta et al. (2004b). This definition of temperature has been shown to accurately reproduce, within few percents, the actual spectroscopic temperature obtained by fitting spectra of simulated clusters with a single–temperature plasma model, within the typical energy bands where detectors on-board of present X–ray satellites are typically sensitive.

We show in Figure 4.3 the comparison between our simulations and observational data on groups (Sun et al., 2009) and on clusters (Vikhlinin et al., 2009) for the relation between entropy and temperature at R_{500} and R_{2500} (upper and lower panels, respectively). In order to reproduce the procedure adopted by Sun et al. (2009), we compute the spectroscopic–like temperature of simulated clusters by excluding the core regions within $0.15R_{500}$. As for the runs with no efficient feedback (NF) we note that they produce entropy levels, at both R_{500} and R_{2500}, which are close to the observed ones. This result can be explained in the same way as that found for the L_X–T relation: overcooling, not balanced by an efficient feedback mechanism, removes a large amount of gas from the X–ray emitting phase, while leaving in this hot phase only relatively high entropy gas, which flows in from larger radii as a consequence of lack of central pressure support.

Including winds (W runs) has the effect of increasing the amount of low-entropy gas, which is now allowed to remain in the hot phase despite its formally short cooling time, thanks to the continuous heating provided by winds. As a result, entropy decreases at both radii, for the same reason for which X–ray luminosity increases. As for the runs with AGN feedback, its effect is almost negligible for massive clusters. On the other hand, AGN feedback provides a significant increase of the entropy level in poor systems, an effect which is larger at smaller clustercentric radii. The resulting entropy is higher than indicated by observational data. Together with the result on the L_X–T relation, this result shows that a rather tuned energy injection is required, which must be able to suppress X–ray luminosity by decreasing gas density, while at the same time reproducing the low entropy level measured at small radii.

4.3.3. Temperature profiles

A number of comparisons between observed and simulated temperature profiles of galaxy clusters have clearly demonstrated that a remarkable agreement exists at

relatively large radii, $R \gtrsim 0.2 R_{180}$, where the effect of cooling is relatively unimportant. While this result, which holds almost independently of the physical processes included in the simulations (e.g., Loken et al., 2002; Borgani et al., 2004; Kay et al., 2007; Pratt et al., 2007; Nagai et al., 2007a), should be regarded as a success of cosmological simulations of galaxy clusters, the same simulations have much harder time to predict realistic profiles within cool-core regions (e.g., Borgani et al., 2008a, for a recent review). In this regime, radiative simulations systematically produce steep negative temperature profiles, at variance with observations, as a consequence of the lack of pressure support caused by overcooling. This further demonstrates that a suitable feedback mechanisms is required to pressurise the gas, so as to prevent overcooling and turning the temperature gradients from negative to positive in the core regions. While feedback associated to SNe has been proved not to be successful, AGN feedback is generally considered as a likely solution for simulations to produce realistic cool cores. Based on simulations of one relatively low–mass cluster, Sijacki et al. (2008) found that AGN feedback can provide reasonable temperature profiles only if a population of relativistic particles is injected along with thermal energy in inflated bubbles.

We present in Figure 4.4 the comparison between simulated and observed temperature profiles for galaxy clusters with $T \gtrsim 3$ keV (left panel) and for poorer clusters and groups with $T \lesssim 3$ keV (right panel). Observational results are taken from Leccardi & Molendi (2008b) and Sun et al. (2009) for rich and poor systems, respectively. As for rich clusters, none of the implemented feedback scheme is capable to prevent the temperature spike at small radii, while all models provide a temperature profile quite similar to the observed one at $R \gtrsim 0.3 R_{180}$. The situation is different for groups. In this case, both schemes of AGN feedback provide results which go in the right direction. While galactic winds are not able to significantly change the steep negative temperature gradients, the AGN1 and the AGN2 feedback schemes pressurise the ICM in the central regions, thus preventing adiabatic compression in inflowing gas. From the one hand, this result confirms that a feedback scheme not related to star formation goes indeed in the right direction of regulating the thermal properties of the ICM in cool core regions. On the other hand, it also demonstrates that the schemes of AGN feedback implemented in our simulations do an excellent job at the scale of galaxy groups, while they are not efficient enough at the scale of massive clusters.

4.3.4. The gas and star mass fractions

The inventory of baryons within galaxy clusters represents an important test to understand both the efficiency of star formation and how the gas content is affected by feedback mechanisms. In general, the difficulty of regulating gas cooling in cluster simulations causes a too large stellar mass fraction (e.g., Borgani et al., 2004; Kay

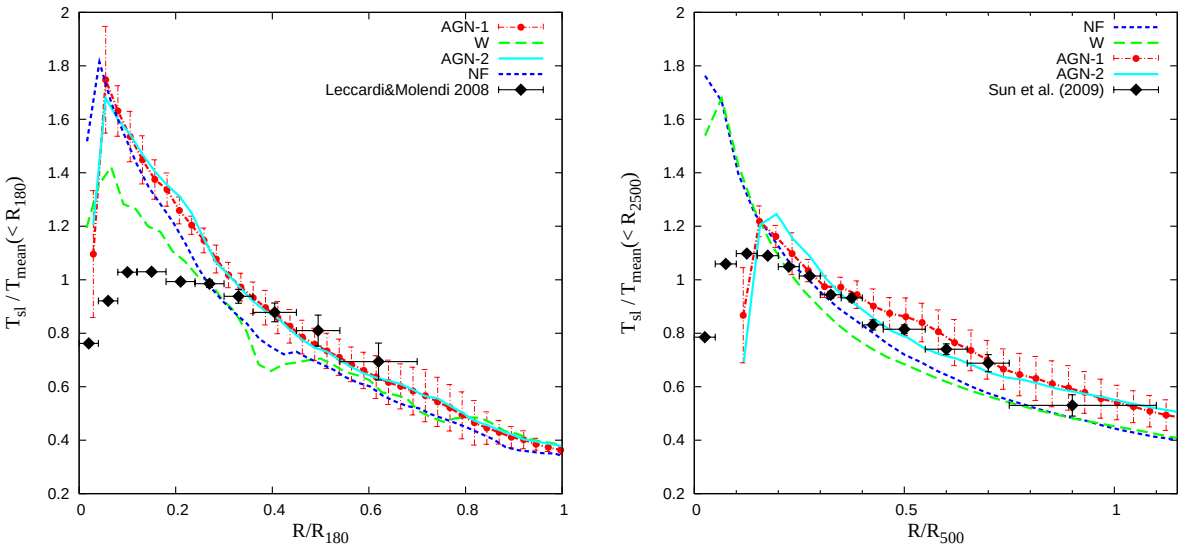

Figure 4.4: Comparison between the temperature profiles for simulated and observed clusters with $T \gtrsim 3$ keV (left panel) and for groups with $T \lesssim 3$ keV (right panel). In each panel, different lines corresponds to the average simulated profiles computed over the four main massive clusters in the left panel and over the five main low-mass clusters in the right panel, for the different sets of runs: no feedback (NF, blue short dashed), galactic winds (W, green long dashed), standard AGN feedback (AGN1, red dot-dashed), modified AGN feedback (AGN2, cyan solid). For reasons of clarity, we show with errorbars the r.m.s. scatter over the ensemble of simulated clusters only for the AGN1 runs. Observational data points for clusters in the left panel are taken from Leccardi & Molendi (2008b), while those for groups in the right panel are from Sun et al. (2009).

et al., 2007; Nagai et al., 2007a; Davé et al., 2008), which in turn should correspond to a too low fraction of gas in the diffuse ICM.

We show in Figure 4.5 the comparison between simulation results and observational data on the mass fraction of hot gas as a function of temperature from Vikhlinin et al. (2006). Gas in simulated clusters is assigned to the hot phase if it is not associated to multi-phase gas particles and if its temperature exceeds 3×10^4K. A comparison between the runs with no feedback (NF) and with galactic winds (W) shows that the latter are characterised in general by larger f_{gas} values. This is in line with the results on the L_X–T relation and confirms that winds are effective in suppressing cooling, thus increasing the hot baryon fraction. While there is a reasonable agreement at the scale of poor clusters, simulations show a weak trend with temperature, with f_{gas} for the hotter systems having values well below the observed ones. As for AGN feedback, it has the effect of increasing f_{gas} for the most massive clusters, although the resulting gas fraction is still below the observational level by about 30 per cent. On the contrary, at the scale of poor clusters the effect of AGN

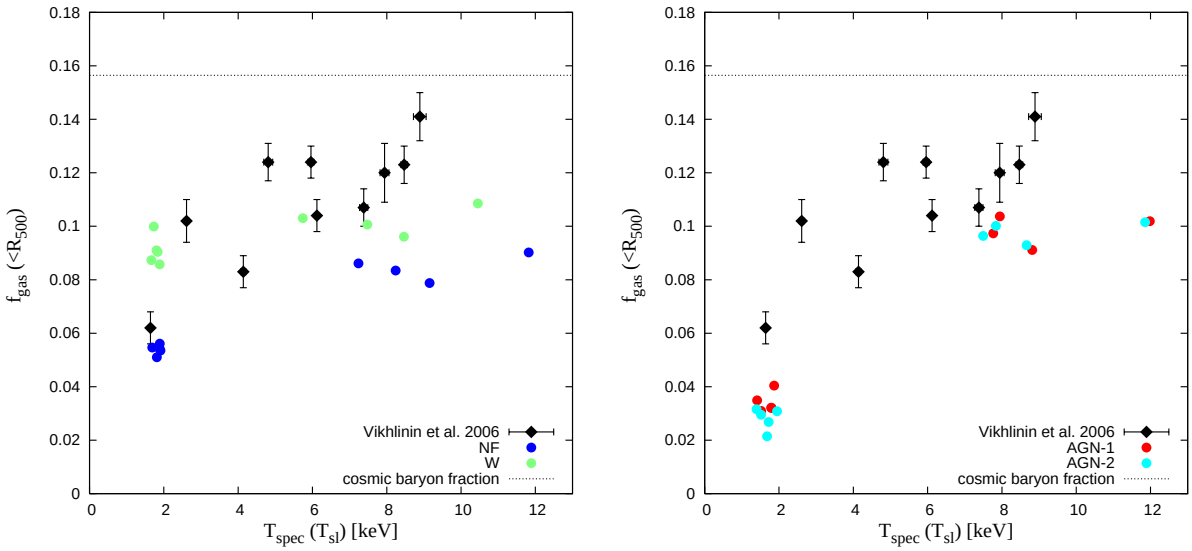

Figure 4.5: Comparison of the gas fraction within R_{500} in simulations (coloured circles) and observational data from Chandra data (diamonds with errorbars) analysed by Vikhlinin et al. (2006). **Left panel:** results for the no feedback (NF) runs (dark blue) and for the runs with galactic winds (W, light green). **Right panel:** results for the runs with the standard AGN feedback (AGN1, dark red) and with modified AGN feedback (AGN2, light cyan). The horizontal dotted line marks the cosmic baryon fraction assumed in the simulations.

feedback is that of decreasing f_{gas} below the observational limit. Indeed, while in rich systems the effect of AGN feedback is that of reducing overcooling, thereby leaving a larger amount of gas in the hot phase, in poor systems it is so efficient as to displace a large amount of gas outside the cluster potential wells.

Our result on the low value of f_{gas} at the scale of rich clusters, even in the presence of AGN feedback, is in line with the somewhat low value of L_X seen in Fig. 4.2. However, this result is in disagreement with that presented by Puchwein et al. (2008), who showed instead a good agreement at all temperatures between their simulations including AGN feedback and observational data. There may be two reasons for this difference. Firstly, the scheme to inject AGN-driven high-entropy bubbles used by Puchwein et al. (2008) could provide a more efficient means of stopping cooling in central cluster regions, at the same time preventing excessive gas removal in low-mass systems. Secondly, unlike Puchwein et al. (2008) we include the dependence of metallicity in the cooling function. As already discussed, this significantly enhances cooling efficiency and, therefore, the removal of gas from the hot phase. In order to verify the impact of this effect, we repeated the AGN2 run of g51, by assuming zero metallicity in the computation of the cooling function. As a result, we find that f_{gas} increases from 0.09 to 010. From the one hand, this result implies that the more

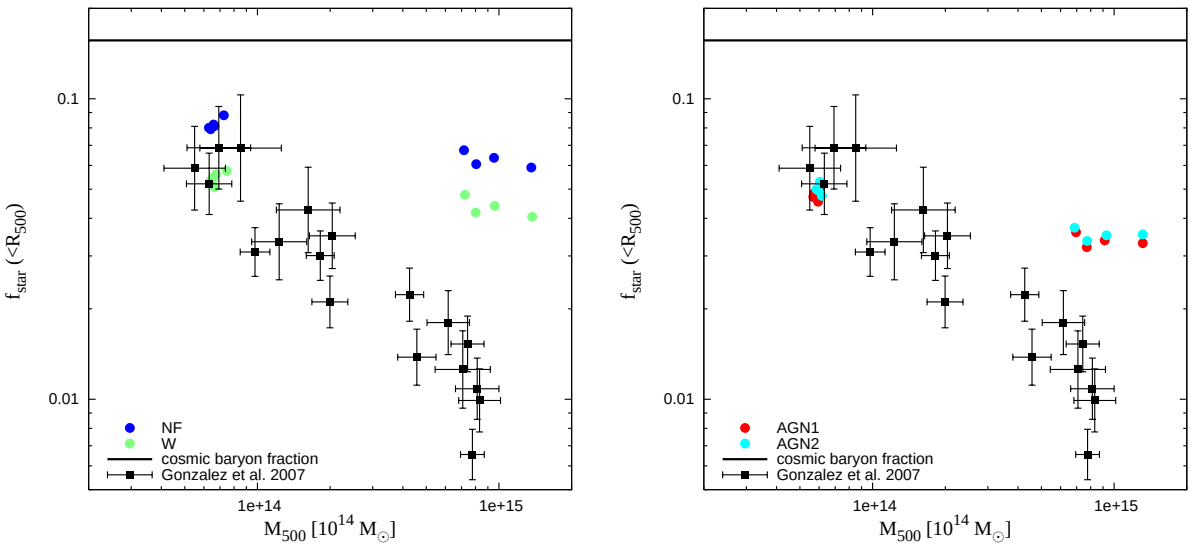

Figure 4.6: Comparison of the star fraction within R_{500} in simulations (coloured circles) and observations (squares with errorbars). **Left panel:** results for the no feedback (NF) runs (dark blue) and for the runs with galactic winds (W, light green). **Right panel:** results for the runs with the standard AGN feedback (AGN1, dark red) and with modified AGN feedback (AGN2, light cyan). Observational points are from Gonzalez et al. (2007) where stellar mass includes the brightest cluster galaxy (BCG), intra-cluster light (ICL) and galaxies within R_{500}.

efficient gas accretion onto BHs, due to metal-cooling, provides a stronger energy feedback which, in turn, balances the higher cooling efficiency. On the other hand, it also implies that the main reason for the difference with respect to Puchwein et al. (2008) should be rather ascribed to the different way in which energy associated to BH accretion is thermalised in the surrounding medium.

As for the behaviour of the mass fraction in stars, we show in Figure 4.6 the comparison between our simulations and observational results from Gonzalez et al. (2007), who also included in the stellar budget the contribution from diffuse intra-cluster stars (see also Giodini et al., 2009). These results confirm that none of our simulations are able to reproduce the observed decrease of f_{star} with increasing temperature. Overcooling is indeed partially prevented in the presence of winds and, even more, with AGN feedback. However, while simulation results for poor clusters are rather close to observations, overcooling in massive clusters is only partially alleviated by AGN feedback, with values of f_{star} which are larger than the observed ones by a factor 2–3.

In summary, the results presented in this section demonstrated that AGN feedback has indeed a significant effect in bringing the L_X–T relation and the entropy level of the ICM closer to observational results, while regulating cooling in the cen-

tral regions. However, the effect is not yet large enough to produce the correct temperature structure in the cool core of massive clusters and, correspondingly, the correct share of baryons between the stellar and the hot gas phase.

4.4 The effect of feedback on the ICM metal enrichment

The X-ray spectroscopic studies of the content and distribution of metals in the intra-cluster plasma provides important information on the connection between the process of star formation, taking place on small scales within galaxies, and the processes which determine the thermal properties of the ICM. The former affects the quantity of metals that are produced by different stellar populations, while the latter gives us insights on gas-dynamical processes, related both to the gravitational assembly of clusters and to the feedback mechanisms that displace metal-enriched gas from star forming regions.

The detailed model of chemical evolution included in the GADGET-2 code by T07 allows us to follow the production of heavy elements and to study how their distribution is affected by the adopted feedback schemes. The analysis presented in this section is aimed at quantifying the different effects that galactic outflows triggered by SN explosions and AGN feedback have on the enrichment pattern of the ICM. We present results on the Fe distribution and the corresponding abundance profiles, the enrichment age within clusters and groups, the relation between global metallicity and ICM temperature, and the relative abundance of Si with respect to Fe. Results from simulations will be compared to the most recent observational data from the Chandra, XMM-Newton and Suzaku satellites. All the abundance values will be scaled to the the solar abundances provided by Grevesse & Sauval (1998).

To qualitatively appreciate the effect of different feedback mechanisms on the ICM enrichment pattern, we show in Figure 4.7 the maps of the emission–weighted Fe abundance for the different runs of the g51 massive cluster. Here and in the following, we will rely on emission–weighted estimates of metal abundances. Rasia et al. (2008) have shown that this emission–weighted estimator actually reproduces quite closely the values obtained by fitting the X–ray spectra of simulated clusters, for both Iron and Silicon. As for Oxygen, the emission–weighted estimator has been shown to seriously overestimate the corresponding abundance, especially for hot ($T \gtrsim 3$ keV) systems.

In the run with no AGN feedback (upper panels of Fig.4.7), we clearly note that including galactic winds produces a level of enrichment which is lower than that in the NF run outside the core region, as a consequence of the lower level of star formation. Therefore, although galactic ejecta are known to be rather efficient in spreading metals in the intergalactic medium at high redshift ($z \gtrsim 2$; e.g., Oppen-

heimer & Davé 2008; Tescari et al. 2009; Tornatore et al. 2009), their effect is not strong enough to compensate the reduction of star formation within cluster regions. In the NF run we note the presence of highly enriched gas clumps which coincide with the halos of galaxies where intense star formation takes place.

A rather different enrichment pattern is provided by AGN feedback (lower panels of Fig.4.7). Despite the total amount of stars produced in these two runs is smaller than for the run including galactic winds, AGN feedback is highly efficient in spreading metals at high redshift, mostly in correspondence of the peak of BH accretion activity. This demonstrates that AGN feedback provides a rather high level of diffuse enrichment in the outskirts of galaxy clusters and in the inter-galactic medium surrounding them at low redshift.

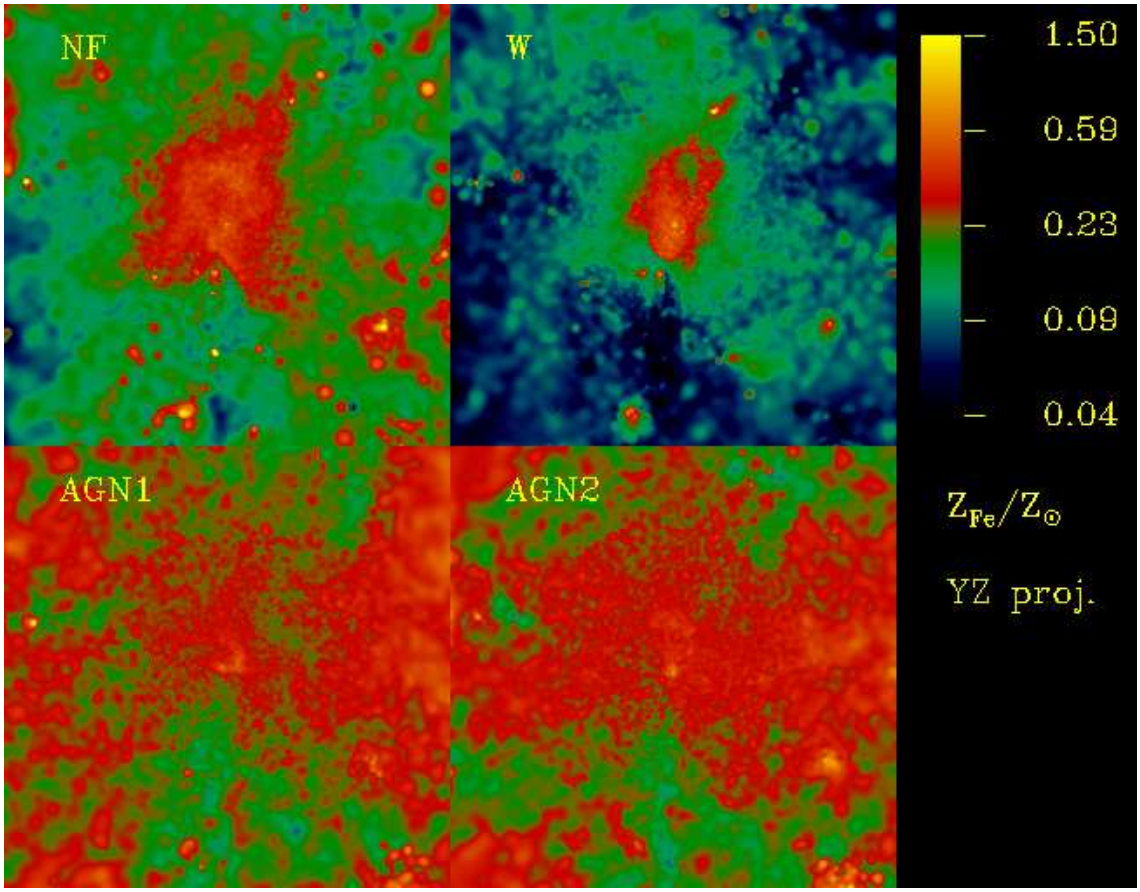

Figure 4.7: Maps of emission weighted Fe abundance in the g51 cluster for the runs without feedback (NF, top left), with winds (W, top right) and with AGNs (AGN1 and AGN2, bottom left and bottom right, respectively). Each map has a side of $2R_{vir}$. Abundance values are expressed in units of the solar value, as reported by Grevesse & Sauval (1998), with color coding specified in the right bar.

4.4.1. Profiles of Iron abundance

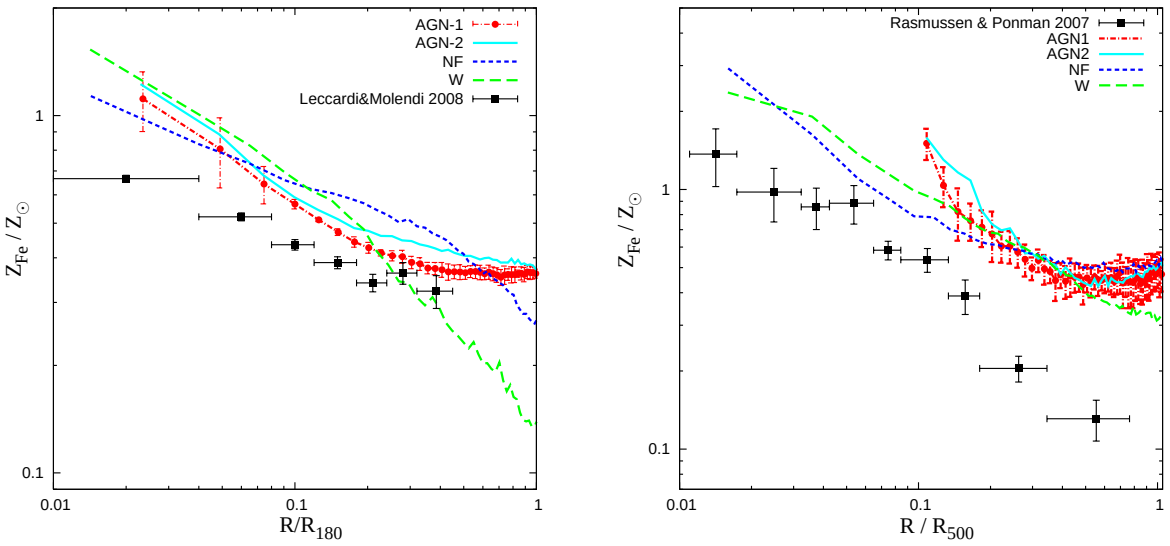

Figure 4.8: Comparison between the observed and the simulated profiles of emission-weighted Iron metallicity. **Left panel:** average $Z_{\rm Fe}$ profiles for galaxy clusters with $T_{500} > 3$ keV. Observational data points are taken from Leccardi & Molendi (2008a). **Right panel:** average $Z_{\rm Fe}$ profiles for the five simulated galaxy groups with $T_{500} < 3$ keV. Observational data points are taken from Rasmussen & Ponman (2007). In both panels different lines correspond to the average profiles computed for the different runs: no feedback (NF, blue short dashed), galactic winds (W, green long dashed), standard AGN feedback (AGN1, red dot-dashed), modified AGN feedback (AGN2, cyan solid). For reasons of clarity, we show with 1σ errorbars over the ensemble of simulated clusters only for the AGN1 runs.

We show in Figure 4.8 the emission-weighted Iron abundance profiles obtained by averaging over the four simulated clusters with $T_{sl} > 3$ keV (left panel) and the five galaxy groups with $T_{sl} < 3$ keV (right panel), compared with observational results. Each panel reports the results for the four adopted feedback schemes. For reasons of clarity we report the 1σ scatter computed over the ensemble of simulated clusters only for the AGN1 runs.

As for rich clusters, simulation predictions are compared with the observational results by Leccardi & Molendi (2008a). These authors analysed about 50 clusters with $T \gtrsim 3$ keV, that were selected from the XMM-Newton archive in the redshift range $0.1 \leq z \leq 0.3$. After carrying out a detailed modelling of the background emission, they recovered metallicity profiles out to $\simeq 0.4 R_{180}$. The results of this analysis show a central peak of Z_{Fe}, followed by a decline out to $0.2 R_{180}$, while beyond that radius profiles are consistent with being flat, with $Z_{Fe} \simeq 0.3 Z_{Fe,\odot}$ using the solar abundance value by Grevesse & Sauval (1998) ($\simeq 0.2$ in units of the

solar abundance by Anders & Grevesse (1989), as reported by Leccardi & Molendi 2008a).

All our simulations predict the presence of abundance gradients in the central regions, whose shape is in reasonable agreement with the observed one, at least for $R \lesssim 0.1 R_{180}$. The lowest enrichment level is actually found for the NF run, despite the fact that this model produces the most massive BCGs. The reason for this lies in the highly efficient cooling that selectively removes the most enriched gas, which has the shortest cooling time, thus leaving metal poorer gas in the diffuse phase. Runs with galactic winds (W) and AGN feedback (AGN1 and AGN2) are instead able to better regulate gas cooling in central region, thus allowing more metal-rich gas to survive in the hot phase. For this reason, W and AGN runs predict profiles of $Z_{\rm Fe}$ which are steeper than for the NF runs in the central regions, $\lesssim 0.1 R_{180}$. Quite interestingly, the effect that different feedback mechanisms have in displacing enriched gas and regulating star formation almost balance each other in the central cluster regions, thus producing similar profiles. However, the different nature of SN-powered winds and AGN feedback leaves a clear imprint at larger radii.

As for the runs with no feedback (NF), they produce a rather high level of enrichment out to $\sim 0.3 R_{180}$, while rapidly declining at larger radii. In this model, the high level of star formation provides a strong enrichment of the gas in the halo of galaxies which will merge in the clusters. During merging, this gas is ram–pressure stripped, thus contributing to enhance the enrichment level of the ICM. The situation is different for the runs with winds. As already mentioned, galactic outflows are efficient in displacing gas from galactic halos at relatively high redshift, $z \gtrsim 2$, when they provide an important contribution to the enrichment of the inter-galactic medium (IGM; e.g., Oppenheimer & Davé 2008). At the same time, this feedback is not efficient to quench cooling of enriched gas at low redshift. As a consequence, no much enriched gas is left to be stripped by the hot cluster atmosphere from the halos of merging galaxies, thus explaining the lower enrichment level beyond $0.1 R_{180}$.

As for the runs with AGN feedback, they produce a shape on the abundance profiles quite close to the observed ones, with a flattening beyond $\simeq 0.2 R_{180}$. In this case, the effect of AGN feedback is that of displacing large amounts of enriched gas from star forming regions at high redshift (see also Bhattacharya et al., 2008) and, at the same time, to efficiently suppress cooling at low redshift. The fact that the level of Z_{Fe} is almost constant out to R_{180} and beyond, witnesses that the main mechanism responsible for enrichment in this case is not ram–pressure stripping, whose efficiency should decline with cluster-centric radius. Instead, enrichment is this case is dominated by the diffuse accretion of pre-enriched IGM. We note that the AGN2 scheme tends to predict slightly higher Z_{Fe} values that AGN1. This is due to the effect of the more efficient radio-mode feedback, included in the former scheme, which provides a more efficient removal of gas from the halos of massive galaxies.

Although models with AGN feedback produce the correct shape of the Iron abundance profiles, their normalisation is generally higher than for the observed ones. This overproduction of Iron could be due to the uncertain knowledge of a number of ingredients entering in the chemical evolution model implemented in the simulation code. For instance, differences between different sets of stellar yields turn into significant differences in the resulting enrichment level (e.g., Tornatore et al., 2007a; Wiersma et al., 2009). Furthermore, a reduction of the Iron abundance can also be achieved by decreasing the fraction of binary systems, which are the progenitors of SNe-Ia (see Chapter 3). For these reasons, we believe that the shape of the abundance profiles, instead of their amplitude, should be considered as the relevant observational information to be used to study the impact that different feedback mechanisms have on the ICM enrichment pattern.

In the right panel of Fig. 4.8 we compare the average $Z_{\rm Fe}$ profiles of the five simulated galaxy groups with observational results from the analysis of 15 nearby galaxy groups observed with Chandra (Rasmussen & Ponman, 2007). Also in this case, the profiles from simulations have a slope quite similar to the observed one out to $R \simeq 0.3R_{500}$, although with a higher normalisation. At larger radii, the effect of AGN feedback is again that of providing rather flat profiles. This result is at variance with the observed profiles in the outermost radii. Indeed, differently from rich clusters, galaxy groups apparently show a negative gradient of Iron abundance out to the largest radii covered by observations, with no evidence of flattening. This result further demonstrates the relevance of pushing observational determinations of the ICM enrichment out to the large radii, which it is mostly sensitive to the nature of the feedback mechanism. If confirmed by future observations, this result may indicate that AGN feedback needs to be mitigated at the scale of galaxy groups, for it not to displace too large amounts of enriched gas.

As pointed out by Rebusco et al. (2005), the central Z_{Fe} peak in cool-core (CC) clusters (see also De Grandi et al. 2004) should be closely related to the star (light) distribution of the BCG. On the other hand, differences between the stellar mass profile and the metal abundance profile should be the signature of dynamic processes which mix and transport metals outside the BCG. In this way, Rebusco et al. (2005) derived the amount of diffusion, to be ascribed to stochastic gas motions, which is required to explain the shallower profiles of Z_{Fe} with respect to the BCG luminosity profiles. Roediger et al. (2007) carried out simulations of isolated cluster–sized halos in which bubbles of high-entropy gas are injected to mimic the effect of AGN feedback. They showed that the gas diffusion associated to the buoyancy of such bubbles is indeed able to considerably soften an initially steep metallicity profile.

In order to verify to what extent gas dynamical processes, associated either to the hierarchical cluster build-up or to feedback energy release, are able to diffuse metals, we compare in Figure 4.9 the average $Z_{\rm Fe}$ profiles and the stellar mass profiles for the massive clusters. As for the NF and W runs, we clearly see a central peak

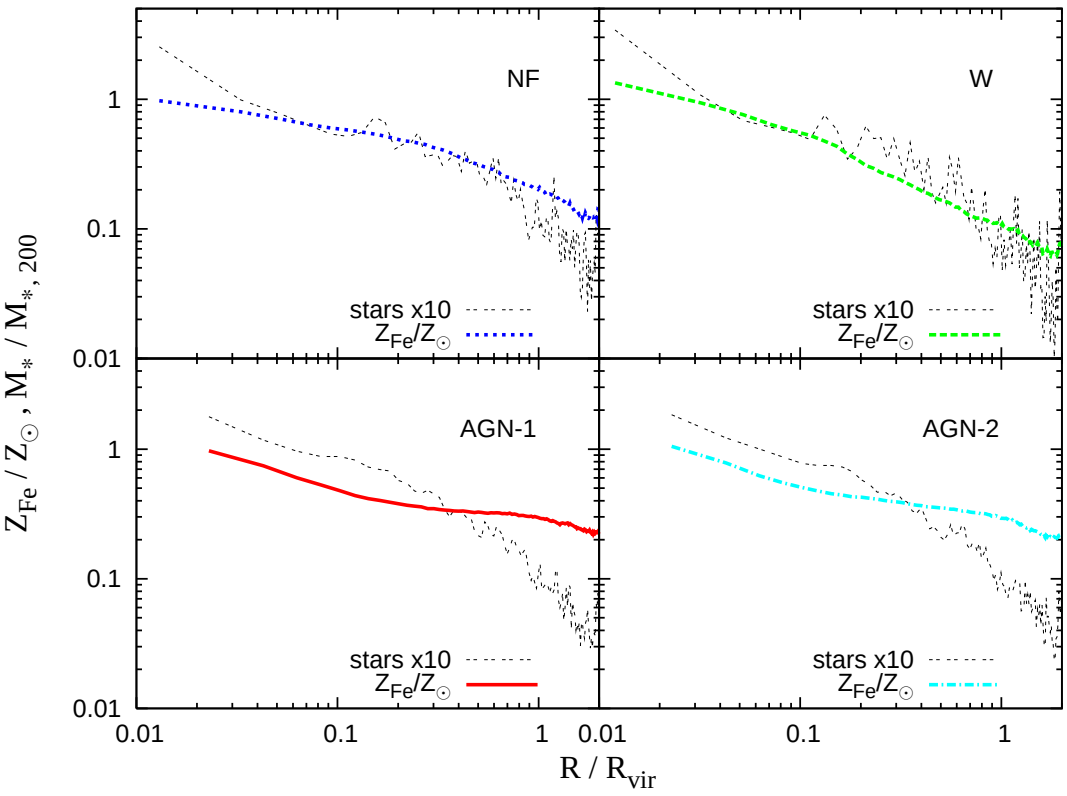

Figure 4.9: Comparison between the stellar mass density profiles, normalised to the corresponding value computed within R_{200} (black short dashed lines), and the Iron abundance profiles (coloured lines). For reasons of clarity stellar profiles are shifted by a factor 10. All curves refer to the average profiles computed over the four massive clusters. From top left to bottom right panels we show results for the runs with no feedback (NF, blue short dashed), with galactic winds (W, green long dashed), with standard AGN feedback (AGN1, red solid) and modified AGN feedback (AGN2, cyan dot-dashed).

in the stellar mass density profile, related to the BCG, followed by a more gentle decline, which traces a diffuse halo of intra-cluster stars surrounding the BCG (e.g., Murante et al., 2007). Quite clearly, the $Z_{\rm Fe}$ profiles are flatter than the distribution of stars at $R \lesssim 0.1 R_{vir}$. Since no feedback processes are at work in the NF runs, the flatter $Z_{\rm Fe}$ profile is due to the effect of selective cooling of highly enriched gas, rather than to stochastic gas motions. The same argument can be applied also to the runs including galactic winds (W), for which the kinetic energy provided galactic ejecta is not enough to fully regulate star formation in central cluster regions (see also Fig. 4.5). At intermediate radii, $R \simeq (0.1 - 0.5) R_{vir}$, profiles of Iron abundance

and stellar mass have quite similar slopes in both the NF and W runs. At even larger radii, instead, the $Z_{\rm Fe}$ profile becomes again shallower than the stellar mass profile, a trend which persists even beyond the virial radius. At such large radii the shallower slope of $Z_{\rm Fe}$ can not be explained by the effect of gas cooling. It is rather due to the effect of gas dynamical processes which help mixing the enriched gas.

As for AGN feedback, its effect is instead that of providing a similar slope for $Z_{\rm Fe}$ and stellar mass profiles at $R \lesssim 0.2 R_{vir}$. This similarity is due to two concurrent effects. The first one is the suppression of star formation, which allows now central enriched gas to be pressurised by the AGN feedback, so as to leave a relatively larger amount of metal-enriched gas in the hot phase. The second one is the shape of the stellar mass profile, which is less concentrated in the presence of AGN feedback. While the two profiles are similar in the central regions, the $Z_{\rm Fe}$ profile is instead much shallower at larger radii, $R \gtrsim 0.3 R_{vir}$. Even an efficient AGN feedback can not be able to displace at low redshift significant amounts of enriched gas from the central regions of massive clusters beyond R_{vir}. Therefore, the flatter abundance profiles in the outskirts of rich clusters can only be justified by the action played by AGN feedback at high redshift. In fact, at $Z \gtrsim 2$ AGN efficiently removed enriched gas from galaxies and quenched star formation, thus preventing metals from being locked back in the stellar phase.

4.4.2. When was the ICM enriched?

In this section we discuss how the different feedback mechanisms change the cosmic epoch at which ICM was enriched. To this purpose, we define the average age of enrichment of a gas particle at redshift z as

$$\bar{t}(z) \, = \, \frac{\sum_i \Delta m_{Z,i} t_i}{m_Z(z)} \, , \tag{4.4}$$

where the sum is taken over all time-steps performed by the simulation until redshift z, $\Delta m_{Z,i}$ is the mass in metals received by the particle at the i-th time-step, t_i is the cosmic time of that time-step and $m_Z(z)$ is the total metal mass received by the particle before z. According to this definition, a large value of enrichment age, at a given redshift, corresponds to more recent enrichment, while smaller values of $\bar{t}(z)$ indicate more pristine enrichment. In the limit in which all the metals are received by a particle at the considered redshift z, then the enrichment age coincides with the cosmic age at z. Once computed for each gas particle, we then compute the mass-weighted mean of these ages of enrichment taken over all the particles having non–vanishing metallicity.

Figure 4.10 shows how the enrichment age of the ICM changes with the cluster-centric distance for the different feedback models, for both rich clusters (top panel) and for poor clusters (bottom panel). In all cases, we note a decline towards small

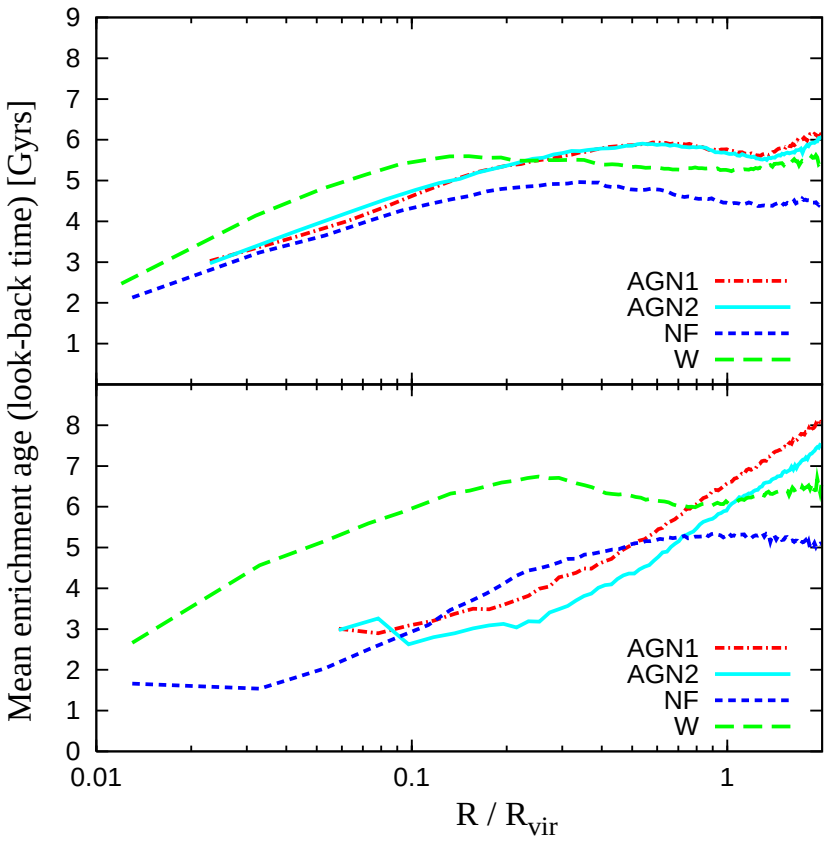

Figure 4.10: Average age of enrichment as a function of the cluster-centric distance. The y-axis is for the look-back time at which the ICM was enriched (in Gyr). The top panel is for the four massive clusters with $M_{200} > 10^{15}\,h^{-1}\mathrm{M}_{\odot}$, while the bottom panel is for the five galaxy groups with $M_{200} \simeq 10^{14}\,h^{-1}\mathrm{M}_{\odot}$. Different lines corresponds to the average age of enrichment computed within the set of simulated cluster: no feedback (NF, short dashed), galactic winds (W, long dashed), standard AGN feedback (AGN1, dot-dashed), modified AGN feedback (AGN2, solid).

radii, although with different slopes. This demonstrates that gas in central regions has been generally enriched more recently than in the outskirts. In the innermost regions, the typical age of enrichment correspond to a look-back time of about 2–3 Gyr, while increasing to 5–8 Gyr around the virial radius. This confirms that metal enrichment in the central cluster regions receives a relatively larger contribution by star formation taking place in the BCG, and by stripping of enriched gas from infalling galaxies, whose star formation has been "strangulated" only recently by the action of the hot cluster atmosphere. On the contrary, enrichment in the outskirts

has a relatively larger contribution from high–z star formation, which provides a more widespread IGM enrichment.

As for massive clusters, we note that the effect of galactic winds (W runs) is that of providing an earlier enrichment with respect to the model with no efficient feedback (NF runs), with a difference of about 1 Gyr, at all radii. This is quite expected, owing to the efficient action that winds play in displacing metals from star forming regions at high redshift. The difference between W and NF runs is larger for the less massive clusters, consistent with the expectation that winds are more efficient in transporting metals outside shallower potential wells.

Quite interestingly, AGN feedback provides a steeper radial dependence of the enrichment age, with rather similar results for the two alternative schemes of implementation (AGN1 and AGN2). In the central regions it is comparable to that of the NF runs, while becoming larger than that of the W runs for $R \gtrsim 0.3 R_{vir}$ ($\gtrsim 0.6 R_{vir}$) for rich (poor) clusters. The relatively recent enrichment age in central regions may look like a paradox, owing to the effect that AGN feedback has in suppressing low redshift star formation within the BCG (see Fig.4.1). However, we should remind that an aside effect of suppressing star formation is also that of preventing recently enriched gas from being locked back in stars. Therefore, although metal production in central regions is suppressed in the presence of AGN feedback, this effect is compensated by the suppression of cooling of recently enriched gas. The effect of AGN feedback in providing a more pristine metal enrichment becomes apparent in the outskirts of clusters. Indeed, the IGM in these regions has been efficiently enriched at high redshift, $z \simeq 3$–4, when BH accretion reached its maximum activity level and displaced enriched gas from star forming galaxies. After this epoch, little enrichment took place as a consequence of the rapidly declining star formation, thus justifying the older enrichment age. Consistently with this picture, we also note that the increase of enrichment age with radius is more apparent for poorer clusters, where AGN feedback acted in a more efficient way.

4.4.3. The metallicity - temperature relation

In Figure 4.11 we present results on the abundance of Iron as a function of cluster temperature, by comparing simulation results for the different feedback schemes with observational results from the analysis of the ASCA Cluster Catalogue (ACC; Horner 2001) carried out by Baumgartner et al. (2005). Due to the relatively poor angular resolution of the ASCA satellite, the extraction region for each cluster was selected to contain as much flux as possible. Since a unique extraction radius is not defined for the observed catalogue, we adopt R_{500} as a common extraction radius to compute Iron abundances and temperatures of simulated clusters. We verified that adopting instead a larger extraction radius (e.g. R_{vir}) slightly lowers the spectroscopic-like temperatures without changing substantially the results on $Z_{\rm Fe}$.

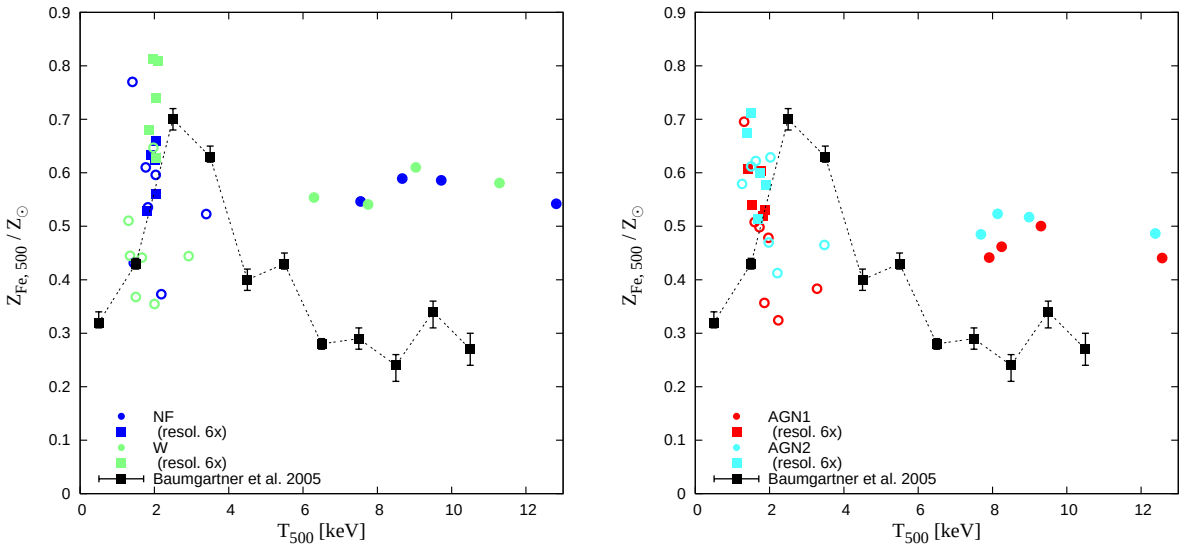

Figure 4.11: Comparison between observed (solid squares with errorbars) and simulated (coloured symbols) relation between global Iron abundance and temperature. The left panel shows the results for the NF (dark blue) and W (light green) runs, while the right panel shows the results for the AGN1 (dark red) and AGN2 (light cyan) runs. In all cases, filled and open circles refer to the main halos of the resimulated Lagrangian regions with massive clusters and to the satellites, respectively. The main-halo galaxy groups are instead plotted with filled squares. Emission–weighted Iron abundance and spectroscopic–like temperature for simulations are both computed within R_{500}. Observational results refer to the sample of clusters observed with ASCA and analysed by Baumgartner et al. (2005).

In their analysis, Baumgartner et al. (2005) partitioned their large sample of clusters in temperature bins. Then, a global value of $Z_{\rm Fe}$ was computed by combining all the clusters belonging to the same temperature bin. In this way, errorbars associated to the observational data points shown in Fig. 4.11 only account for the statistical uncertainties in the spectral fitting procedure after combining all clusters belonging to the same temperature bin, while they do not include any intrinsic scatter (i.e., cluster-by-cluster variation) in the $Z_{\rm Fe}$–T relation. This has to be taken in mind when comparing them to simulation results, for which we did not make any binning in temperature.

In both panels we see that simulations of hot ($T > 6$ keV) systems produce values of $Z_{\rm Fe}$ which are above the enrichment level found in observations, $\sim 0.3 Z_\odot$. This result is consistent with the fact that $Z_{\rm Fe}$ profiles for simulated clusters have a larger normalisation than the observed ones (see Fig. 4.8). NF and W runs predict $Z_{Fe} \simeq (0.5 - 0.6) Z_{Fe,\odot}$, with a slightly lower value, $Z_{Fe} \simeq (0.4 - 0.5) Z_{Fe,\odot}$ for the runs with AGN feedback.

As for the simulations of the poorer systems, with $T \simeq (1-3)$ keV, they have in-

stead a larger scatter. This indicates more diversity in the impact that gas-dynamical and feedback processes have in determining the enrichment pattern within smaller systems. The effect of AGN feedback for these systems is that of decreasing the value of $Z_{\rm Fe}$ by about $0.1 Z_{Fe,\odot}$. The rather large spread of abundance values and the limited number of simulated systems do not allow to establish whether simulations reproduce the increase of $Z_{\rm Fe}$ with ICM temperature for systems in the range $T \simeq (1-3)$ keV.

Observations suggests that $Z_{\rm Fe}$ is almost independent of temperature above 6 keV, a trend which is in fact reproduced by simulation results. However, between 3 and 6 keV observed clusters show a drop in metallicity by about a factor two. Although simulations predict somewhat higher metallicity values at low temperatures, still it is not clear whether they reproduce the decrease, by more than a factor 2, suggested by observations. A potential complications in comparing observational and simulation results for systems with $T \sim 3$ keV is that the spectroscopic value of $Z_{\rm Fe}$ for these systems is contributed by both K and L lines. As originally noted by Buote (2000) in the analysis of ASCA data, fitting with a single-temperature model a plasma characterised by a multi-temperature structure, with the colder component below 1 keV, leads to an underestimate of the Iron abundance (the so-called iron-bias; see also Molendi & Gastaldello, 2001; Buote et al., 2003). In this case, a simple emission–weighted definition of $Z_{\rm Fe}$ from simulations may not be fully adequate. A correct procedure would require extracting a mock X–ray spectrum from simulated clusters, to be fitted with a multi–temperature (and multi–metallicity) plasma model (e.g., Rasia et al., 2008). Finally, one should also note that more recent determinations of the $Z_{\rm Fe}$–T relation from XMM–Newton data, although based on a much smaller number of clusters, suggests a less pronounced decrease for systems hotter than 3 keV (e.g., Werner et al., 2008). There is no doubt that a systematic analysis of nearby clusters within the Chandra and XMM-Newton archives would help to confirm or disprove the metallicity–temperature relation based on ASCA observations.

4.4.4. The $Z_{\rm Si}/Z_{\rm Fe}$ relative abundance

The relative abundance of elements produced in different proportions by different SN types is directly related to the shape and possible evolution of the initial mass function. Furthermore, studying how relative abundances change with cluster-centric distance provides insights on the different timing of enrichment and on how different metals, produced over different time-scales, are mixed by gas-dynamical processes. ASCA data analysed by Loewenstein & Mushotzky (1996), Fukazawa et al. (1998) and Finoguenov et al. (2000) originally suggested that cluster outskirts are predominantly enriched by SNe-II. A similar result was found more recently also by Rasmussen & Ponman (2007), who analysed XMM data for poor clusters with

$T \lesssim 3$ keV. On the other hand, Suzaku observations of low temperature clusters and groups (Sato et al. 2008, 2009ba, 2009ab) show instead a rather flat profile of Z_{Si}/Z_{Fe} out to large radii, $\simeq 0.3R_{vir}$, thus implying that SNe-Ia and SNe-II should contribute in similar proportions to the enrichment at different radii.

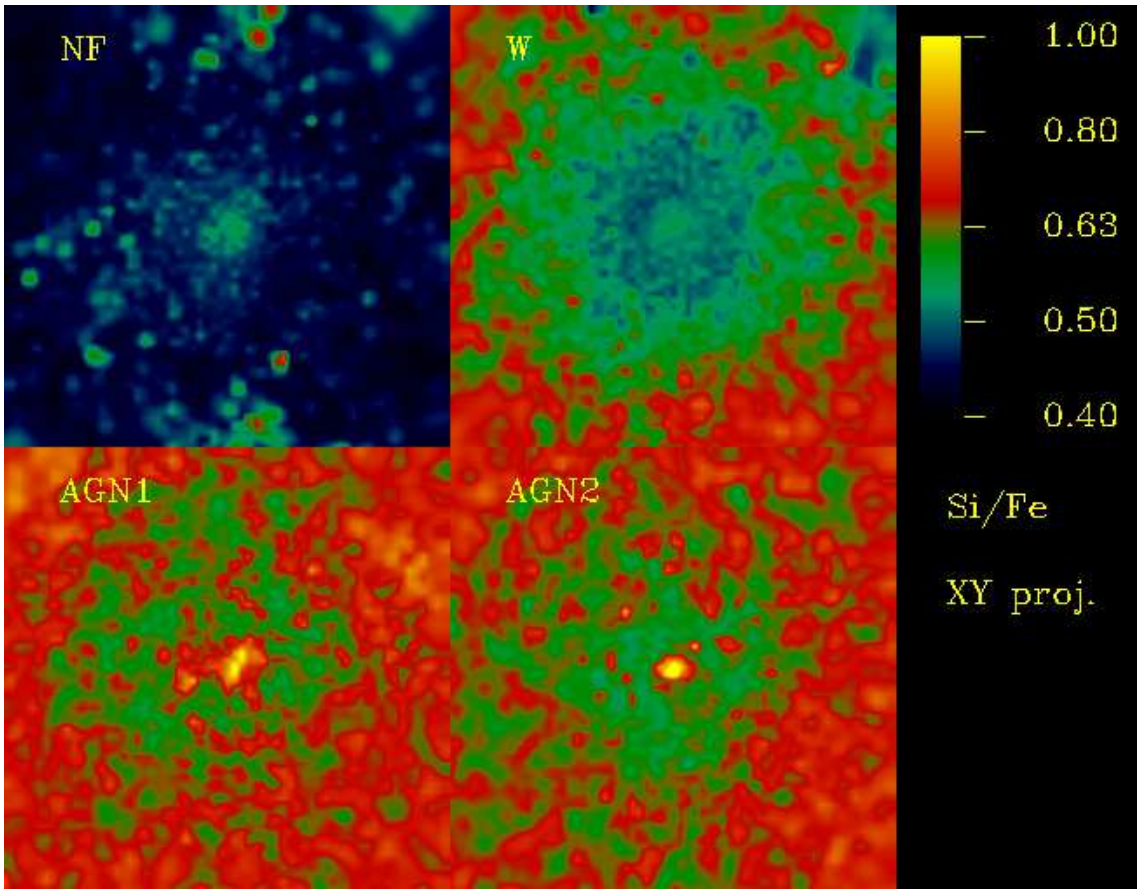

Figure 4.12: Maps of the emission–weighted $Z_{\rm Si}/Z_{\rm Fe}$ distribution for the runs of the g676 cluster without feedback (NF, top left), with winds (W, top right), with AGNs (AGN1 and AGN2, bottom left and right, respectively). The side of each map is $2R_{vir}$. Abundance values are expressed in units of the solar value, as reported by Grevesse & Sauval (1998), with color coding specified in the right bar.

In this section, we focus our attention on the $Z_{\rm Si}/Z_{\rm Fe}$ ratio for low temperature clusters. We show in Figure 4.12 the emission-weighted map of the $Z_{\rm Si}/Z_{\rm Fe}$ ratio for the four different feedback schemes applied to the g676 cluster. For the run with no feedback (NF), we note that $Z_{\rm Si}/Z_{\rm Fe}$ is generally quite patchy. It reaches higher values in correspondence of high–density star forming regions, a feature which is also shared in different proportions by the other runs. Indeed, the products of SNe-II are released over a short time scale, since they are synthesised by massive stars. As a

result, their distribution tends to trace preferentially the distribution of star-forming regions. On the other hand, SNe-Ia release metals over a longer time-scale. In fact, these stars have time to leave star forming regions, as a consequence of the same dynamical effects which generate a population of inter-galactic stars (e.g., Murante et al., 2007; Zibetti et al., 2005), thereby providing a more widespread enrichment pattern. Therefore, our simulations predict that diffuse intra-cluster stars provide a significant contribution to the enrichment of the intra-cluster medium (see also Tornatore et al., 2007a).

A comparison of the maps for the NF and W runs shows that they have comparable levels of $Z_{\rm Si}/Z_{\rm Fe}$ within the central regions. In these regions we expect that ram–pressure stripping is the dominant process in removing gas from merging galaxies (see also Kapferer et al., 2007b) and, therefore, in efficiently mixing in the ICM the nucleosynthetic products of different stellar populations. On the contrary, in the cluster outskirts winds have been much more efficient in removing freshly produced metals from galaxies during the cluster assembly, therefore providing a relatively more widespread Si distribution, with respect to the NF case in which no galactic outflows are included.

The runs with AGN feedback exhibit a behaviour in the cluster outskirts which is qualitatively similar to that of the W run, although with slightly higher values of $Z_{\rm Si}/Z_{\rm Fe}$. This indicates that AGN feedback has a higher efficiency in mixing SN-Ia and SN-II products. As for the central regions, the truncation of recent star formation by AGN feedback would lead to the naive expectation that a relatively higher value of Iron abundance with respect to Silicon should be found. The results shown in the bottom panels of Fig.4.12 lead in fact to the opposite conclusion, with a marked increase of $Z_{\rm Si}/Z_{\rm Fe}$ in the core regions. The reason for this lies again in the effect of selective removal of metal-enriched gas associated to cooling. Total metallicity of the gas around the BCG is dominated by SNe-II products. Therefore, gas more enriched by SNe-II has a relatively shorter cooling time. As a consequence, suppression of cooling in the core regions by AGN feedback tends to increase the amount of SN-II products in the ICM, thereby justifying the increase of $Z_{\rm Si}/Z_{\rm Fe}$ with respect to the runs not including AGN.

This qualitative picture is also confirmed by the profiles of $Z_{\rm Si}/Z_{\rm Fe}$, that are plotted in Figure 4.13. In each panel, simulation results show the average profile, computed over the 5 main relatively poor clusters, for each feedback model. In the left panel simulation results are compared with observational results by Rasmussen & Ponman (2007) from the analysis of 15 nearby galaxy groups observed with Chandra. Also shown with the two horizontal lines are the values of $Z_{\rm Si}/Z_{\rm Fe}$ produced by SNe-Ia and SNe-II for a simple stellar population of initial solar metallicity, having a Salpeter IMF, using the same sets of yields adopted in our simulations.

Observational data show a rather flat profile of $Z_{\rm Si}/Z_{\rm Fe}$ with a value close to solar at small radii, followed by a sudden increase beyond $\simeq 0.2R_{500}$. Taken at face value,

this result would imply that at $\sim 0.5R_{500}$ the enrichment is mostly contributed by SNe-II, while a mix of different stellar populations is required in the cluster centre. Although this result is qualitatively similar to that suggested by the visual inspection of the $Z_{\rm Si}/Z_{\rm Fe}$ maps of Fig.4.12, simulation results are quantitatively different from those by Rasmussen & Ponman (2007). Indeed, in no case simulations predict an increase of Z_{Si}/Z_{Fe} beyond $0.2R_{500}$. While the maps suggest that such an increase is also expected in simulations, it takes place only for $R > R_{500}$, with the largest values reaching at most the solar one. Within the radial range covered by Chandra observations, both NF and W runs show rather flat profiles. Also in this case, we are more interested in the slope of the $Z_{\rm Si}/Z_{\rm Fe}$ profile, rather than in its normalisation. Indeed, too low values of Z_{Si}/Z_{Fe} in simulations by about 0.3 (in solar units) can be be either due to the choice of the IMF or to adopted stellar yields.

As for the runs with AGN feedback the profiles of Z_{Si}/Z_{Fe} confirm the expectation gained from the maps of Fig.4.12 for a relative increase of the Si abundance in the central regions. As for the behaviour at large radii, $R \gtrsim 0.2R_{500}$, also AGN feedback does not predict the pronounced increase see in the Chandra data by Rasmussen & Ponman (2007).

As already mentioned, this observational evidence for an enhancement of SN-II products in the outskirts of groups is not confirmed by Suzaku data (Sato et al. 2008, 2009ba,2009ab) and XMM-Newton (Silvano Molendi, private communication). As shown in the left panel of Fig.4.12, Suzaku observations of Abell 262, NGC 507 and AWM 7 indicate a profile of $Z_{\rm Si}/Z_{\rm Fe}$ which is consistent with being flat out to $0.3R_{vir}$ (corresponding to about $0.5R_{500}$). While it is not the purpose of this work to address the reason for the different results coming from different satellites, we want to stress the great relevance of tracing the pattern of ICM enrichment out to the largest possible radii. Indeed, this is the regime where gas-dynamical processes related to the cosmological build-up of clusters, past history of star formation and nature of feedback processes regulating star formation, all play a role in determining the distribution of metals.

In summary, the analysis of chemical enrichment in our simulations of galaxy clusters confirms that the resulting metallicity distribution in the ICM is given by the interplay between gas cooling, which tends to preferentially remove more enriched gas from the hot phase, feedback processes, which displace gas from star forming regions and regulate star formation, and gas dynamical processes associated to the hierarchical build-up of galaxy clusters. In particular, feedback implemented through the action of galactic winds powered by SN explosions or through energy extracted from gas accretion onto super-massive BHs, leave distinct features on the resulting pattern and timing of ICM enrichment.

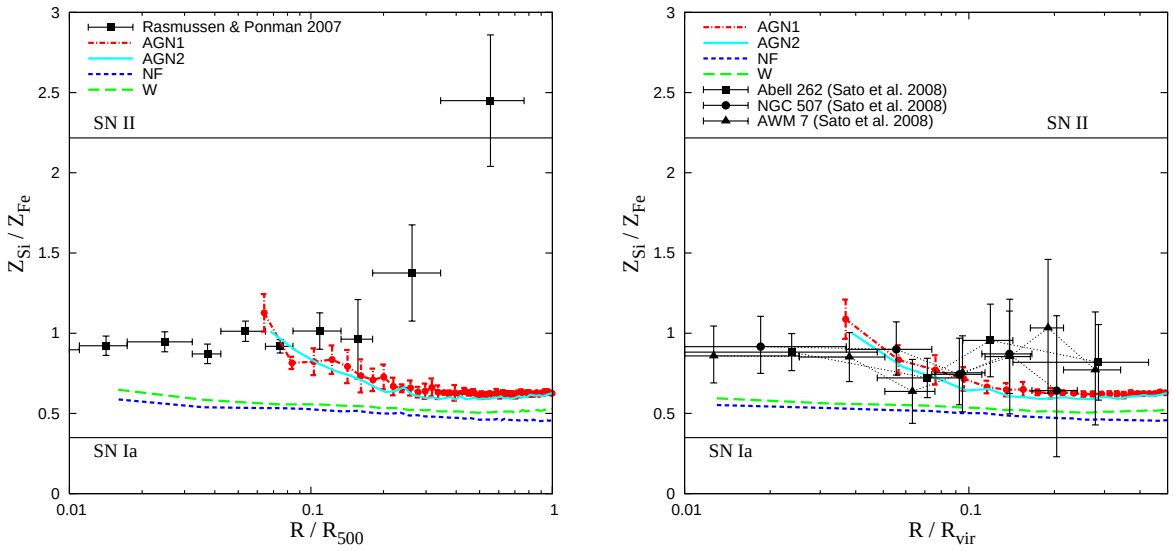

Figure 4.13: Comparison between observed and the simulated profiles of Silicon abundance relative to Iron, $Z_{\rm Si}/Z_{\rm Fe}$. In each panel, different lines correspond to the average profiles computed over clusters having $T_{500} < 3$ keV for the different sets of runs: no feedback (NF, blue short dashed), galactic winds (W, green long dashed), standard AGN feedback (AGN1, red dot-dashed), modified AGN feedback (AGN2, cyan solid). For reasons of clarity, we show with errorbars the r.m.s. scatter over the ensemble of simulated clusters only for the AGN1 runs. Observational points refer to the Chandra data analysed by Rasmussen & Ponman (2007) (left panel) and to the Suzaku data analysed by Sato et al. (2008, 2009a,b) (right panel). The two horizontal lines show the relative abundance from SNe-Ia and SNe-II, computed for a simple stellar population (SSP) having solar initial metallicity and based on the same Salpeter IMF and set of yields as used in our simulations.

4.5 Conclusions

We presented the analysis of an extended set of cosmological hydrodynamical simulations of galaxy clusters aimed at studying the different effects that stellar and AGN feedback have on the thermal and chemo-dynamical properties of the intra-cluster medium (ICM). Using a version of the Tree-SPH GADGET-2 code (Springel, 2005), which also includes a detailed description of chemical enrichment (Tornatore et al., 2007a), we carried out simulations of 16 clusters identified within 9 Lagrangian regions extracted from a lower-resolution parent cosmological box (Dolag et al., 2009). All cluster simulations of this set have been run using different prescriptions for the feedback: without including any efficient feedback (NF runs), including only the effect of galactic winds powered by supernova (SN) feedback (W runs), and including two different prescriptions of AGN feedback (AGN1 and AGN2) based on modelling gas accretion on super-massive black holes (BHs) hosted within resolved

galaxy halos (Springel et al., 2005a; Di Matteo et al., 2005). The AGN1 scheme exactly reproduces the original model by (Springel et al., 2005a) for the choice of the parameters determining the feedback efficiency and the way in which energy is distributed. As for the AGN2 scheme, it assumes the presence of a radiatively efficient "radio mode" phase when BH accretion is in a quiescent stage (e.g., Sijacki et al., 2007), also distributing energy to the gas particles surrounding BHs in a more uniform way.

The main results of our analysis can be summarised as follows.

(a) AGN feedback significantly quenches star formation rate (SFR) associated to the brightest cluster galaxies (BCGs) at $z \lesssim 4$. At $z = 0$ the SFR in the AGN1 and AGN2 models is reduced by about a factor six. For a massive cluster with $M_{200} \simeq 10^{15}\, h^{-1}\mathrm{M}_{\odot}$ we find $SFR(z = 0) \simeq 70 M_{\odot}\mathrm{yr}^{-1}$, thus not far from current observational estimates (e.g. Rafferty et al., 2006). Although the two variants of AGN feedback produce similar results on the star formation rate, the AGN2 model is more efficient is reducing gas accretion onto BHs. For this scheme, the resulting masses of the BHs sitting at the centre of the BCGs at $z = 0$ are reduced by a factor 3–5 with respect to the AGN1 scheme. Furthermore, increasing the radio-mode feedback efficiency from $\epsilon_f = 0.2$ to 0.8 further reduces the mass of the central BH by about a factor 2.5, while leaving the level of low-z star formation rate almost unaffected.

(b) AGN feedback brings the L_X–T relation in closer agreement with observational results at the scale of poor clusters and groups, thus confirming results from previous simulations based on AGN feedback (Puchwein et al., 2008). However, this is obtained at the expense of increasing the ICM entropy in central regions of groups above the level indicated by observational results (e.g., Sun et al., 2009; Sanderson et al., 2009a). This entropy excess generated in central group regions corresponds in turn to a too low value of the gas fraction.

(c) AGN feedback reduces by 30–50 per cent the fraction of baryons converted into stars, f_{star}, within R_{500}. Simulation results agree well with the observed value of f_{star} at the scale of groups. However, for rich clusters the fraction of stars within R_{500} from simulation ($\simeq$ 30–40 per cent) is larger than the observed one ($\simeq$ 10 per cent).

(d) AGN feedback is quite efficient in pressurising gas in the central regions of galaxy groups, thereby generating temperature profiles which are in reasonable agreement with the observed ones. Despite this success at the scale of groups, temperature profiles in the core regions of massive clusters are still too steep, even after including AGN feedback.

(e) The presence of AGN feedback generates a rather uniform and widespread pattern of metal enrichment in the outskirts of clusters. This is the consequence of the improved efficiency, with respect to the runs without BH feedback, to extract at high redshift highly enriched gas from star forming regions, and, therefore, to enhance metal circulation in the inter-galactic medium.

(f) Radial profiles of Fe abundance are predicted to be too steep at $R \gtrsim 0.1 R_{180}$ in runs including stellar feedback. Their shape is in much better agreement with the observed ones when including AGN feedback. The overall emission–weighted level of enrichment within massive clusters is $Z_{Fe} \simeq 0.5$ and 0.6 for runs with and without AGN feedback, respectively. Such values are generally larger than those, $Z_{Fe} \simeq 0.3$, reported from ASCA observations (Baumgartner et al., 2005).

(g) The distribution of elements mostly produced by SNe-II over a relatively short time-scale is more clumpy than the Iron distribution, which has a larger contribution from SNe-Ia, that release metals over a long time-scale. This is interpreted as due to the effect of enrichment from stars belonging to a diffuse intra-cluster population. Therefore, simulations predict that a sizable fraction of the ICM enrichment is produced by intra-cluster stars, in line with observational evidences (Sivanandam et al., 2009).

(h) The runs with no feedback (NF) and with galactic winds (W) predict similar patterns of $Z_{\rm Si}/Z_{\rm Fe}$ within R_{500}. Silicon abundance is enhanced in the outer regions by the action of galactic winds, thanks to their efficiency in transporting gas enriched by α elements from star forming regions. AGN feedback has the effect of increasing $Z_{\rm Si}/Z_{\rm Fe}$ as a consequence of the suppression of star formation, which would lock back in stars gas surrounding star forming regions, and of the efficient removal of enriched gas from galactic halos.

(i) In no case we find that profiles of $Z_{\rm Si}/Z_{\rm Fe}$ have a rising trend beyond $\simeq 0.2 R_{500}$. No strong conclusion can be drawn from a comparison with data, owing to discrepant indications from different observational results on the radial dependence of $Z_{\rm Si}/Z_{\rm Fe}$. Suppression of star formation with AGN feedback causes $Z_{\rm Si}/Z_{\rm Fe}$ to increase at small radii, $\lesssim 0.1 R_{500}$, a feature which is not seen in observational data. This suggests that the implementation of AGN feedback in our simulations may not provide enough gas mixing the central regions of clusters and groups.

Our analysis lend further support to the idea that a feedback source associated to gas accretion onto super-massive BHs is required by the observational properties of the ICM (e.g. McNamara & Nulsen, 2007). However, our results also show that a number of discrepancies between observations and predictions of simulations

still exist, especially within the core regions of massive clusters. This requires that a more efficient way of extracting and/or thermalising energy released by AGN should be introduced in richer systems. A number of observational evidences exists that AGN should represent the engine which regulates the structure of core regions of clusters and groups. However, observations also provide circumstantial evidences that a number of complex physical processes, such as injection of relativistic particles and of turbulence associated to jets, buoyancy of bubbles stabilised by magnetic fields, viscous dissipation of their mechanical energy, thermal conduction, should all cooperate to make AGN feedback a self-regulated process. In view of this complexity, we consider it as quite encouraging that the relatively simple prescriptions for energy thermalization adopted in our simulations provide a significant improvement in reconciling numerical and observational results on the ICM thermo- and chemo-dynamical properties.

Clearly, increasing numerical resolution thanks to the ever increasing supercomputing power would require including a proper description of the above processes. For instance, the current implementation of AGN feedback neglects the effect of kinetic energy associated to jets. The typical scales of ~ 20 kpc at which kinetic feedback is expected to dominate within clusters (e.g. Pope, 2009) are only marginally resolved by hydrodynamics in our simulations, thus making the assumption of a purely thermal feedback a reasonable one. However, the improved numerical resolution expected to be reached in simulations of the next generation needs to be accompanied by a suitable description of injection of jets, for them to provide a physically meaningful description of the interplay between BH accretion and ICM properties.

The results presented in this Chapter further demonstrate that different astrophysical feedback sources leave distinct signatures on the pattern of chemical enrichment of the ICM. These differences are much more evident in the outskirts of galaxy clusters, which retain memory of the past efficiency that energy feedback had in displacing enriched gas from star-forming regions and in regulating star formation itself. However, characterisation of thermal and chemical properties in cluster external regions requires X–ray telescopes with large collecting area and an excellent control of the background.

While Chandra, XMM and Suzaku will be pushed to their limits in these studies in the next few years, there is no doubt that a detailed knowledge of the ICM out the cluster virial boundaries has to await for the advent of the next generation of X–ray telescopes (e.g., Giacconi et al., 2009; Arnaud et al., 2009).

CHAPTER 5

TESTING the ROBUSTNESS of CLUSTER MASS PROXIES

In this Chapter we study the relations between the galaxy cluster mass, that is dominated by the dark matter component, and X–ray observable properties of the IntraCluster Medium, such as the spectroscopic temperature and the gas mass. By means of simulated galaxy clusters we verify to what extend mass proxies depend on the physical processes included in the simulations, in particular when conduction, viscosity, galactic winds or feedback from Active Galactic Nuclei are at work.

5.1 Introduction

Galaxy clusters are the most massive objects in the Universe and can be easily observed up to large redshifts with surveys in different wavelengths, from optical to millimetre and X–rays. Furthermore, galaxy clusters are important probes for cosmology. Their baryonic mass fraction and the evolution of their number density with redshift can constrain the Dark Matter and Dark Energy content of the Universe as well as the dark energy equation of state (e.g. Allen et al., 2004; Vikhlinin et al., 2009). In particular the evolution of the cluster mass function gives powerful constraints on current cosmological models (e.g. Voit, 2005b, for a complete review). Moreover, these constraints are complementary to the large–scale structure measurements and to the results from the cosmic microwave background (e.g. Komatsu et al., 2009). To constrain the Dark Energy and Matter Density content and

the Dark Energy equation of state one needs very detailed understanding of cluster formation and evolution.

To obtain the total cluster mass several cluster observables are used, depending on the wavelength of the observation: galaxy velocities in the optical light, X–ray data from the IntraCluster Medium (ICM), the thermal Sunyaev–Zeldovich (tZS) effect and the gravitational lensing data. Most of the methods used to extract physical quantities from observations assume that clusters are relaxed structures with a spherical geometry and in virial equilibrium. This is not the case for all the clusters. For example at low redshift the fraction of substructured and disturbed clusters is of the order of $40\% - 70\%$ (e.g. Mohr et al., 1995; Kolokotronis et al., 2001). At the same time clusters are even more disturbed and deviate from the equilibrium at higher redshifts (e.g. Jeltema et al., 2005; Maughan et al., 2008).

Many of the X–ray global integrated or averaged properties like temperature, X–ray luminosity and gas mass obey to relatively simple and well defined power–law scalings with total cluster mass and they can be measured up to very high redshift (e.g. Vikhlinin et al., 2009). The most common choice of a mass proxy are the X–ray temperature T_X (e.g. Henry & Arnaud, 1991; Markevitch, 1998; Ikebe et al., 2002; Pierpaoli et al., 2003) or the cluster gas mass M_{gas} (e.g. Vikhlinin et al., 2003; Voevodkin & Vikhlinin, 2004). For the T_X–M_{tot} relation the results of models and simulations differ at a level of $\sim 10\%$ (e.g. Vikhlinin et al., 2006). The scatter of the T_X–M_{tot} is however quite sensitive to the ICM substructure and to cluster mergers (O'Hara et al., 2006). The gas mass has the advantage that it can be measured from the X–ray imaging alone, unlike temperature, that requires deeper observations with X–ray spectroscopy. Assuming clusters as closed boxes and a fair representation of the Universe the M_{tot}–M_{gas} relation can be calibrated from the CMB measurements of the baryon density parameter. The gas mass is expected also to be less sensitive to cluster mergers, with a smaller scatter in the observable–mass relation. There is however a caveat, since the dependence of gas mass with cluster mass and possibly also with the redshift evolution are still not completely understood.

Recently Kravtsov et al. (2006) introduced the X–ray equivalent of the integrated SZ flux, the Y_X parameter, defined as the product of the gas mass with the cluster temperature. From their simulated galaxy clusters the authors found it to be a low–scatter (5-8%) mass proxy, since the error estimates on the temperature and the gas mass anticorrelate, and independent on the redshift evolution, with a closely self–similar relation. The recovered relation is also insensitive to cluster mergers, a result that was independently verified by Poole et al. (2007) with their simulated cluster set. Several recent works used the Y_X proxy when studying the X–ray luminosity scaling relations within cluster surveys obtained with Chandra (Maughan, 2007) and XMM–Newton telescopes (Pratt et al., 2009).

In general it is found that the evolution of the scaling relations follows the self–similar predictions (e.g. Vikhlinin et al., 2002; Maughan et al., 2006). For galaxy

clusters to be used as tools for precision cosmology, the required relation that links an observable quantity to the total cluster mass should have low intrinsic scatter, be insensitive to mergers of clusters and/or substructure and finally be described by a single power–law (close to the self–similar one) with the smallest number of parameters. An additional requirement is that of a low intrinsic scatter. As pointed out by Maughan (2007) the scatter in the scaling relations must be understood to account for effect of bias in samples defined basing on an observable property that has some finite intrinsic scatter with mass. The scatter is dominated by cluster cores, mergers and their (combined) different redshift dependences (e.g. Maughan et al., 2006; Pratt et al., 2009).

In this situation resorting to galaxy cluster simulation and combine them with an observational analysis (e.g. Rasia et al., 2005; Nagai et al., 2007b) is a good way to understand the processes that affect the systematics. Recent works based on a such combined approach reveal that the mass computed under the assumption of hydrostatic equilibrium is systematically smaller, by $\sim 10\%$, than the true mass (Kay et al., 2004; Rasia et al., 2005; Nagai et al., 2007b; Piffaretti & Valdarnini, 2008; Ameglio et al., 2009). The deviation of the hydrostatic mass from the true cluster mass in this simulations is due to the non–thermal pressure support from turbulent and bulk gas motions (e.g. Rasia et al., 2004; Kay et al., 2004; Rasia et al., 2006; Dolag et al., 2005; Nagai et al., 2007a; Piffaretti & Valdarnini, 2008; Ameglio et al., 2009). In addition, the deviation from the real mass is higher for unrelaxed clusters (Nagai et al., 2007b; Jeltema et al., 2008). As suggested by Jeltema et al. (2008), that found a correlation between the deviation from hydrostatic equilibrium and the cluster structure, this can be used as a diagnostic for the sources of non–thermal pressure support in clusters.

The calibration of the mass versus one of the proxies derived from X–ray observations can provide a powerful tool for cosmology when combined with weak lensing analysis (e.g. Sheldon et al., 2001) and the Sunyaev–Zel'dovich data (e.g. Mahdavi et al., 2007). Such data are now becoming available thanks to recent works (e.g. Hoekstra, 2007; Mahdavi et al., 2008; Zhang et al., 2008). Recently the same analysis was performed on simulated clusters by Meneghetti et al. (2009), by comparing the strong and weak lensing results with X–ray observed mass. Although both measurements (lensing and X–ray) are biased due to triaxiality and substructures of the individual systems, using them together on a larger cluster sample can give informations about the gas physics as well as contribute to calibrate the X–ray scaling relations. In a recent work Ameglio et al. (2009) used the combined SZ imaging and X–ray surface brightness data to recover cluster masses within cosmological simulations. Applying simultaneously the two techniques they were able to characterize better the cluster outskirts and to improve the analysis of cluster properties at high redshift, where X–ray spectroscopic data are difficult to obtain. However, observing the tSZ effect with a good spatial resolution requires a future generation of SZ

telescopes, as well as X–ray satellites with high sensitivity and good background characterization.

Within this Chapter we analyse a set of galaxy clusters extracted from high–resolution cosmological simulations to study the effect of different physics on the mass–observable scaling relations and their evolution with redshift. In particular we focused on the relation between the galaxy cluster mass and two observables, the gas mass and the new Y_X proxy. Differently from the analysis by Kravtsov et al. (2006), where the informations were extracted from simulated clusters mimicking an observers approach, we test the robustness of two relations, M_{gas}–M_{tot} and Y_X–M_{tot}, in different simulations before including any observational effect. The galaxy cluster set was simulated with the GADGET-2 code (Springel et al., 2001; Springel, 2005) adopting seven different prescriptions to describe the physics of the ICM. Four of them were previously studied by Dolag et al. (2005) to explore the effect of thermal conduction and artificial viscosity in the ICM plasma. The clusters analysed in the previous Chapter 4 were used to explore the effects on the mass–observable relations when galactic winds are active or when the feedback is powered by low and high accretion of gas onto the blackholes.

This Chapter is structured as follows. We present (in Section 5.2) the simulated clusters, with a brief description of the thermal conduction and artificial viscosity schemes adopted in GADGET-2 , and the analysis applied to the simulations. In Section 5.4.1 we present the results that concern the redshift evolution of the relations that link total cluster mass to the gas mass and to the Y_X, respectively. In Section 5.4.2 we explore the dependence of these relations on the different physics adopted in simulations and we describe the evolution of the relation when a fixed self–similar slope is adopted. Finally (in Section 5.5) we summarize our conclusions. The results presented in this Chapter will be published in Fabjan et al. (in preparation).

5.2 The simulations

5.2.1. The set of simulated clusters

In this Chapter we used a large set of galaxy clusters that were simulated for previous studies. In particular, we focused on the effect that

(i) thermal conduction,

(ii) numerical viscosity and

(iii) different feedback schemes

have on the ICM properties.

The clusters analysed in this study are extracted from 9 resimulated Lagrangian regions selected from a parent Dark Matter only simulation with a box size of $479h^{-1}$ Mpc (Yoshida et al., 2001). The clusters were already presented in Chapter 3 (pag.77). The cosmological model assumed is ΛCDM with $\Omega_m = 0.3$ for the matter density parameter, $h = 0.7$ for the Hubble parameter, $f_{bar} = 0.13$ for the baryon fraction and $\sigma_8 = 0.9$ for the normalization of the power spectrum. The adopted value of σ_8 and Ω_m is somewhat higher than the best-fitting values obtained from the analysis of the 5-year Wilkinson Microwave Anisotropy Probe data (Dunkley et al., 2009), but still consistent with current cosmological constraints.

The simulations were carried out with the TREE–PM SPH code GADGET-2 (Springel et al., 2001; Springel, 2005), which makes use of the entropy-conserving formulation of SPH (Springel & Hernquist, 2003a). If enabled, the radiative cooling and heating by a uniform, redshift–dependent UV background (Haardt & Madau, 1996) are included. The star formation prescription is based on the subresolution model, described in Chapter 2, that accounts for the multiphase structure of the ISM, where the cold ISM phase acts as a reservoir for forming stars (Springel & Hernquist, 2003a). Energy feedback supplied by supernovae heats the hot ISM phase and provides energy to evaporate cold clouds. This circle leads to a self–regulation of star formation and an effective equation of state that describes its dynamics.

To study the heat conduction in cluster plasma we compare two 'archival' cluster sets simulated by Dolag et al. (2005). In the following we will refer to them as the TC (thermal conduction) set. To study the effects of the parametrization of artificial viscosity on the scaling relations we resort to two sets of non–radiative simulations (Dolag et al., 2005). We will refer to them as the AV (artificial viscosity) set. Both TC and AV sets of simulated clusters were used in other works (see Dolag et al. 2009 for the complete list of papers where these simulations have been analysed). Finally, to study the effect of different feedback schemes we used the simulations presented in the previous Chapter 4. We named the set FDB (feedback) although we include also the no–feedback simulations, that we will use as a reference run. In Table 5.1 we summarize the main features for the TC, AV and FDB sets of simulations.

Springel & Hernquist (2003a) also include a simple fenomenological model for galactic winds that are triggered by SN-II (see Chapter 3, Section 3.2.3). The wind velocity scales with a fraction of the energy provided by SN II, that are massive stars with $M > 8M_\odot$ from a Salpeter (1955) initial mass function (IMF) and with each SN releasing 10^{51} ergs of energy. In simulations with galactic winds the constant of proportionality of the mass upload in winds, η, is fixed to 0.5 in CSF and CSFC runs yielding to a wind velocity $v_w = 340$ km s^{-1}, and to $\eta = 2$ in W run with $v_w = 500$ km s^{-1}.

The chemo–dynamical model implemented by Tornatore et al. (2007a) (see Chapter 3, Section 3.2.3 for a description) is included in the FDB simulations that were studied in the previous Chapters, NF, W and AGN2. The model is described in Sec-

THERMAL CONDUCTION - TC set

CSF	clusters were simulated with cooling and star formation, including weak winds with velocity fixed at 340 km/h
CSFC	the physics included is the same as for the CSF run with the addition of heat conduction.

ARTIFICIAL VISCOSITY - AV set

OVISC	with the usual parametrization of the SPH artificial viscosity
LVISC	with a time–varying, low–artificial viscosity scheme

FEEDBACK - FDB set

NF	clusters simulated with radiative cooling and star formation
W	clusters simulated with the galactic winds triggered by SN-II, fixing the wind velocity at 500km/s (described in Sec.3.2.3)
AGN2	clusters simulated with the 'quasar' and 'radio' mode feedback from accreting blackholes (more details in Sec.4.2.1)

Table 5.1: Description of the three sets of simulations, TC (thermal conduction), AV (artificial viscosity) and FDB (feedback schemes) sets. For each set we list the name of the simulation and a brief description.

tion 3.2.2 (page 81). TC runs include chemical enrichment only by SN-II. Here we remind that the FDB runs include beside SN-II chemical enrichment also the enrichment by SN-Ia and AGB stars by properly account for their mass–dependent lifetimes. FDB runs include also metal–dependent stellar yields and metal–dependent cooling.

As for the AGN feedback included in the AGN2 run the main features of this model are described in Chapter 4, Section 4.2.3. Based on the work of (Springel et al., 2005a) we include beside the blackhole feedback in the quasar mode regime also the radio mode regime. In these simulations the radiative efficiency is fixed to $\varepsilon_r = 0.1$ and the feedback efficiency changes from $\varepsilon_f = 0.05$ to 0.2 when $\dot{M}_{BH}/\dot{M}_{Edd} < 10^{-2}$. In this case the energy around the BH is distributed isotropically with a top–hat kernel.

Among the three sets reported in table 5.1 above there are three main differences:

- for TC and AV runs the *initial conditions* were prepared with non–periodic boundaries, while for FDB runs the boundaries were periodic

- only the FDB runs include the chemical enrichment scheme implemented by Tornatore et al. (2007a) and a metallicity dependent cooling scheme.
- in the FDB runs the low–mass systems (g676, g914, g1542, g3344, g6212) are simulated at 6 times higher resolution.

In the following we provide a short description of the numerical implementation in GADGET-2 of thermal conduction and of the scheme of reduced viscosity, which have not been discussed in previous Chapters.

■ The thermal conduction model

Heat conduction is a process where thermal energy is transported by free electrons and depends on the temperature gradients in the conducting medium. When the mean free path of the particles is small with respect to the temperature gradient, locally the flux $\mathbf{j} = -\kappa\nabla T(\mathbf{r})$ depends on the gradient of the temperature distribution $T(\mathbf{r})$ with a coefficient κ that instead depends on the properties of the medium. The heat conductivity due to electrons for the ionized plasma was derived by Spitzer (1962). In astrophysical plasma the Spitzer conductivity has a strong dependence on temperature, namely $\kappa_{Sp} \propto T^{5/2}$ (Sarazin, 1988), and has the value $\kappa_{Sp} = 8.2 \times 10^20(kT/10\mathrm{keV})^{5/2}$ erg (cm s keV)$^{-1}$. In principle it can be strongly altered by magnetic fields and depending on the magnetic field configuration the conduction can be suppressed in certain directions or even in all directions for particular cases where tangled fields are involved.

Thermal conduction was suggested by Narayan & Medvedev (2001) as a possible heating mechanism for cluster cores. This process could transport thermal energy from the outer regions of galaxy clusters to the cooler central gas and thought to mitigate the overcooling problem (e.g. Dolag et al., 2004). Zakamska & Narayan (2003) and Voigt & Fabian (2004) were able to reproduce observational data and also the temperature profiles by assuming a local balance between radiative cooling and thermal conduction. They suggest that conduction plays a secondary role with respect to AGN feedback, but is still important since it helps to stabilize the system. Moreover, they obtain an effective isotropic conductivity with a sub-Spitzer value, while other authors report a strong suppression of conductivity with $\kappa \sim (0.1 - 0.001)\kappa_{Sp}$ (e.g. Ettori & Fabian, 2000; Vikhlinin et al., 2001; Markevitch et al., 2003).

Thermal conduction was implemented in GADGET-2 by Jubelgas et al. (2004) with a new formalism that conserves thermal energy. Since the magnetic fields and their configuration in galaxy clusters are still under debate, Jubelgas et al. (2004) assume that magnetic suppression can be described in terms of an effective isotropic conductivity, taken as a fixed fraction of the temperature–dependent Spitzer rate. For the conduction runs, namely CSFC simulations, the assumed value for the conductivity

was fixed at $\kappa = (1/3)\kappa_{Sp}$. With this scheme Dolag et al. (2004) studied a low–temperature group and a high–temperature cluster. They found that the thermal conduction is effective in the high–temperature cluster, since the strong dependence of κ on the plasma temperature. Despite creating an isothermal core and a small decrease in central entropy, thermal conduction was unable to avoid the overcooling problem, leaving an essentially unchanged baryon fraction in galaxy clusters.

■ The model of reduced viscosity

Structure and dynamics of massive cluster mergers and infalls of smaller structures play a significant role. Mergers can induce bulk motions with velocities of the order of ~ 1000 km s^{-1}. Most of the kinetic energy is then dissipated by shocks, but in some part it can provide long–lasting turbulent gas motions.

Cluster turbulence can store in massive clusters a significant fraction of the thermal energy, up to 15% (Frenk et al. 1999). Observationally a mildly supersonic turbulence was revealed by Schuecker et al. (2004) in central parts of the Coma cluster (see also Brunetti & Lazarian, 2007).

As already described in paragraph 2.3.2, one of the disadvantages of the SPH technique is the need of an 'artificial' viscosity to capture shocks. With it the small–scale velocity fluctuations are smoothed out and random gas motions are damped above the resolution limit. Dolag et al. (2005) introduced a time variable viscosity following a suggestion by Morris & Monaghan (1997) to quantify how intense the shear flow must be to drive fluid instabilities, that are able to increase the level of turbulence in the cluster. With this novel scheme the discrepancy between the SPH technique and the AMR numerical scheme, that is not affected by the same problem, is proven to be reduced (e.g. Vazza et al., 2006; Cassano & Brunetti, 2005).

Differently from the original GADGET-2 version (par. 2.3.2) in the new numerical scheme the artificial viscosity for each gas particle is a dynamical variable, that increases in the vicinity of shocks and decays after the passage trough a shock. With respect to the original formulation, Dolag et al. (2005) found a smaller numerical viscosity in regions away from strong shocks. The expected effect is thus to develop more turbulent gas motions, which turn unto an increase of non–thermal pressure support.

5.3 Linking X-ray observables to mass

In the self–similar model by Kaiser (1986), that we described in Section 1.2.3, the total cluster mass can be expressed by means of gas mass or X–ray temperature. Here we list the basic expressions as reported in Kravtsov et al. (2006).

The cluster gas mass is proportional to the total mass with the constant C_{M_g} that is independent on the cluster mass or redshift. Choosing $\delta = 500$ as the overdensity with respect to the critical density of the Universe, we can write the relation:

$$M_{tot,500} = C_{Mg} M_{gas,500} \,. \tag{5.1}$$

The total mass can be derived by using temperature and the parameter $E(z) = H(z)/H_0$ as

$$M_{tot,500} = E(z)^{-1} C_T T^{3/2} \,, \tag{5.2}$$

where C_T is a constant of normalization, indipendent of the cluster redshift.

Kravtsov et al. (2006) introduce the X–ray equivalent of the integrated Sunyaev–Zeldovich flux, the Y_X. Y_X is the product of the gas mass and the temperature,

$$Y_X = M_{gas,500} T_X$$

and is proportional to the total thermal energy of the cluster. By using the above equations the scaling of the cluster mass with the new proxy is described by:

$$M_{tot,500} \propto E(z)^{-2/3} Y_X^{3/5} \,. \tag{5.3}$$

Ideally, in the above equations, M_{tot}–T and M_{tot}–Y_X, the mass–averaged T_{mw} should be used. This is because the T_{mw} is a direct measure of the ICM thermal content and as such, is the quantity relevant for the predictions of the self–similarity model. To reproduce the observed quantities Kravtsov et al. (2006) used the T_{sl} but excising the core region. This should in principle make the spectral temperature closer to the gas mass-weighted T_{mw} estimate.

5.3.1. Simulation analysis

The analysis of the simulations was performed as described in Chapter 3 (page 3.2.4). With respect to the previous analysis we include also clusters extracted at redshifts $z = 0.25, 0.5, 0.8$ and 1. We include in the analysis all the clusters with $\mathrm{M}_{vir} > 5 \times 10^{13}$ $\mathrm{M}_\odot$. All the quantities in the following analysis, in particular total cluster mass, gas mass and ICM temperature, were extracted within the R_{500} radius (see Chapter 3 for the definition).

The power–law relation used to fit the scaling relation between total mass, M_{tot}, and a given observable X, has the same form as that adopted by Kravtsov et al. (2006),

$$M_{tot} = C \left(\frac{X}{X_0} \right)^{\alpha} \,.$$

For the two observables, M_{gas} and Y_X, the power–law fit was performed with the X_0 value fixed at 2×10^{13} $\mathrm{M}_\odot$ and 4×10^{13} keV $\mathrm{M}_\odot$, respectively. We perform the fits

also with the slopes fixed at the self–similar value, 1.0 and 0.6 for $M_{tot,500}$–$M_{gas,500}$ and $M_{tot,500}$–$Y_{X,500}$ relations respectively.

The fits were performed on the log–log relation by using the least-squares Marquardt-Levenberg algorithm. The algorithm calculates at each iteration the sum of the squared differences with a new set of parameter values. The Marquardt-Levenberg algorithm selects the parameter values for the next iteration. The process continues until a preset criterium is met, either the fit has converged (the relative change in the residuals is less than 10^{-6}) or it reaches a preset iteration count limit.

The intrinsic scattering was computed as the quadratic difference between the single cluster data and the relation fitted on the whole cluster set.

To compute the Y_X parameter we resort to the mass-weighted temperature T_{mw}, that we already define in Chapter 3.2.4 (see page 83). Since the Y_X parameter is defined by analogy with the Y_{SZ}, it should be constructed adopting the mass-weighted temperature estimate, that measures the thermal content of the galaxy cluster. To compare with the results from Kravtsov et al. (2006) and to provide a more "observationally oriented" relation we computed the Y_X parameter also using the spectroscopic–like temperature T_{sl}. For this purpose we implemented in the analysis code the extension of the spectroscopic–like temperature to low–temperature systems proposed by Vikhlinin (2006). In fact the T_{sl} analytic formula introduced by Mazzotta et al. (2004b) is not accurate for clusters with temperatures < 3 keV. We use the algorithm proposed by Vikhlinin (2006) that resorts to precomputed tables of some parameters for the observed spectra as a function of the temperature. Tables were generated with the Fortran code by Vikhlinin (2006) that is publicly available at `http://hea-www.harvard.edu/~alexey/mixT`. The table was created by fixing the parameters of the galactic hydrogen density $N_H = 5 \times 10^{20}$, the abundances to Grevesse & Sauval (1998), the ACIS-S CCD on Chandra and the Energy range to $0.7 - 10$ keV.

We evaluate the ICM temperature with the radius $(0.15 - 1)\ R_{500}$, as done by Kravtsov et al. (2006). The exclusion of the central regions in cluster when computing the temperature is desiderable since observed cluster temperature profiles show a grater degree of similarity outside the core (Vikhlinin et al., 2006).

5.4 Results on mass-observable relations

5.4.1. Evolution with redshift

■ The M-M_{gas} relation

The relation between the total cluster mass and the gas mass is in principle very simple. In an ideal case when all cluster baryons are in the ICM, the ICM follows

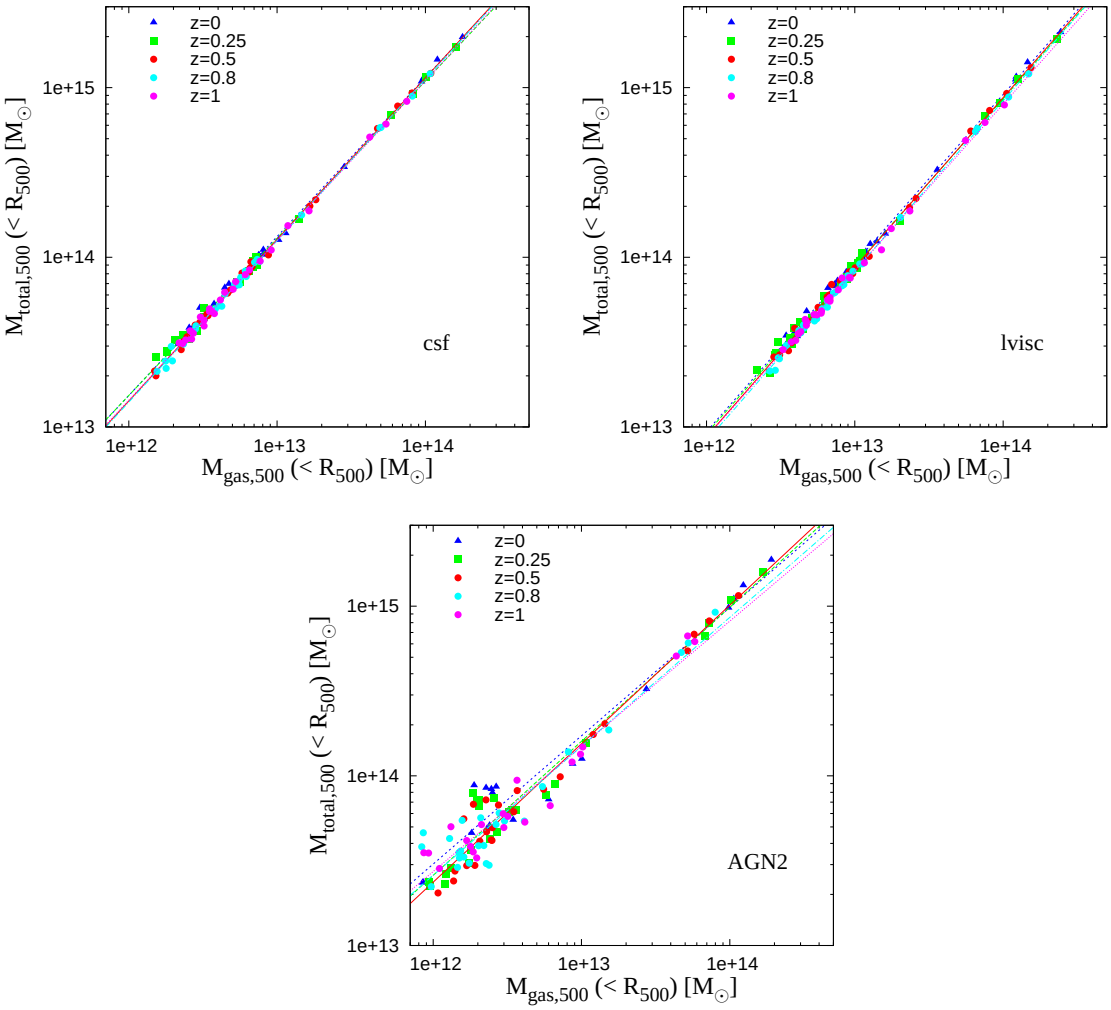

Figure 5.1: The relation between galaxy cluster total mass $M_{tot,500}$ and the gas mass $M_{gas,500}$, both of them computed inside R_{500}. Cluster values and the best–fit power law are reported at $z = 0$ (blue triangles; short dashed line), $z = 0.25$ (green squares; long–dashed line), $z = 0.5$ (red circles; continuous line), $z = 0.8$ (cyan circles; dot–dashed line) and $z = 1$ (magenta circles; dotted line). **Top left panel:** the evolution of the $M_{tot,500}$–$M_{gas,500}$ relation for the CSF simulated clusters. **Top right panel:** the relation at different redshifts for LVISC simulations of galaxy clusters. **Bottom panel:** the $M_{tot,500}$–$M_{gas,500}$ relation at different redshifts for clusters from the AGN2 run.

strictly the distribution of the Dark Matter and the content of the cluster is exactly the cosmic mix of baryonic and non–baryonic matter (e.g. Voevodkin & Vikhlinin, 2004). In this case the proportionality constant C_{M_g} is simply the inverse of the gas mass fraction, f_{gas}.

We report in Figure 5.1 three panels with the evolution of the M_{tot}–M_{gas} relation for three of the simulated sets: CSF, LVISC and AGN2. From a visual inspection we notice how the for the CSF and LVISC simulations the relation is not significantly evolving below $z = 1$. For the AGN2 run we clearly observe a large spread in M_{gas} for clusters with masses $M_{500} < 10^{14}$ $M_{\odot}$. As we reported in the previous Section 5.2 the five low–mass isolated systems in the FDB runs are simulated with 6 times higher mass resolution. For a fixed cluster mass these systems have systematically lower gas masses, as can be noticed in the bottom panel of Figure 5.1. As reported in Chapter 4 the AGN feedback in poor systems is very efficient in displacing large amount of gas outside the cluster potential well. When the ICM structure is better resolved the effect of the feedback is higher and leads to lower gas masses. The low–mass clusters that have values consistent with the fitted slope are instead satellite clusters extracted from regions centred on the massive ones. As a final result, the scatter for AGN2 groups is larger than for CSF and LVISC clusters.

sim	z = 0	z = 0.25	z=0.50	z = 0.80	z = 1
csf	14.404 ± 0.006	14.391 ± 0.007	14.392 ± 0.004	14.385 ± 0.006	14.382 ± 0.007
	0.937 ± 0.009	0.927 ± 0.010	0.952 ± 0.006	0.952 ± 0.008	0.941 ± 0.010
	0.024	0.028	0.016	0.020	0.021
csfc	14.411 ± 0.006	14.392 ± 0.008	14.392 ± 0.005	14.383 ± 0.005	14.377 ± 0.006
	0.933 ± 0.009	0.921 ± 0.011	0.948 ± 0.007	0.941 ± 0.007	0.934 ± 0.009
	0.024	0.029	0.017	0.017	0.019
lvisc	14.265 ± 0.005	14.246 ± 0.006	14.242 ± 0.005	14.222 ± 0.004	14.216 ± 0.006
	0.994 ± 0.009	0.987 ± 0.010	1.000 ± 0.009	1.003 ± 0.007	0.981 ± 0.010
	0.022	0.028	0.022	0.018	0.021
ovisc	14.257 ± 0.005	14.239 ± 0.007	14.235 ± 0.005	14.218 ± 0.004	14.215 ± 0.006
	0.978 ± 0.009	0.982 ± 0.011	0.993 ± 0.009	0.999 ± 0.007	0.985 ± 0.011
	0.023	0.029	0.022	0.017	0.023
NF	14.467 ± 0.013	14.450 ± 0.012	14.449 ± 0.012	14.432 ± 0.021	14.405 ± 0.023
	0.838 ± 0.016	0.831 ± 0.014	0.880 ± 0.015	0.866 ± 0.026	0.836 ± 0.030
	0.048	0.043	0.041	0.059	0.067
W	14.351 ± 0.009	14.334 ± 0.009	14.334 ± 0.006	14.325 ± 0.005	14.315 ± 0.008
	0.895 ± 0.014	0.885 ± 0.013	0.924 ± 0.009	0.922 ± 0.008	0.915 ± 0.013
	0.039	0.036	0.024	0.017	0.027
AGN2	14.464 ± 0.034	14.441 ± 0.034	14.435 ± 0.029	14.403 ± 0.044	14.396 ± 0.038
	0.756 ± 0.039	0.790 ± 0.036	0.816 ± 0.034	0.760 ± 0.046	0.738 ± 0.043
	0.122	0.113	0.096	0.122	0.116

Table 5.2: The table reports the fit of the $M_{tot,500}$–$M_{gas,500}$ relation for all clusters. Column 1: name of the simulated cluster set. Column 2-6: values of normalization $\log C$, slope α and scatter $\sigma_{logM_{tot}}$ of the simulated data at redshifts $z = 0, 0.25, 0.5, 0.8$ and 1. Errors on $\log C$ and α are reported with their errors from the fit.

We can further inspect the results from simulations by looking at Table 5.2, where we report the simultaneous fit of the power–law relation described in 5.3.1

to all clusters in each simulation. The data from fits are confirming our previous conclusions: both CSF and LVISC simulations show a very mild evolution of the $\log C$ normalization with redshift, although with the different values, $\log C \sim 14.39$ and $\log C \sim 14.24$ respectively. Moreover we can see that the effect of conduction (TC set) and viscosity (AV set) are negligible on the $M_{tot,500}$–$M_{gas,500}$ relation. There is however a difference with respect to the slope, that is nearly autosimilar ($\alpha = 1$) only for the non–radiative runs of the AV set. This is not surprising, since we stated above that self–similar scaling holds under the assumption that only gravity affects the evolution of the ICM. This is in fact the case of non–radiative simulations of the AV set. A slightly lower slope is instead obtained with the TC set of clusters. This reflects the effect of cooling, since some of the baryons are present in the cold phase (stars and cold gas) that are not accounted for in the M_{gas} estimate. Both AV and TC sets have very low scatter on the data extracted from simulations, on average $\sigma_{logM_{tot}} \sim 2.3\%$. For the FDB set of simulations there is a very mild evolution in the normalization of the relation. For all three simulated set the slopes differ from the self–similarity, reaching the highest value at $z = 0.5$. The least self–similar one is the slope for the AGN2 run with $\alpha \sim 0.74-0.82$, that shows however the largest scatter in the data, of about $\sim 12\%$. Interestingly the scatter for every simulated set is almost constant with redshift and does not show an increasing trend with redshift. The gas mass–total mass relation seems indeed not to be affected by secondary effects as mergers and ICM substructure, that are relevant at higher redshifts (O'Hara et al., 2006).

The dependence of gas fraction was found to be $f_{gas} \propto M^{\beta}_{tot,500}$ with $\beta = 0.2-0.25$ both in simulations (Kravtsov et al., 2005) and observations (Vikhlinin et al., 2006). The difference between non–radiative and radiative simulations is a consequence of the trends in gas fraction with cluster mass, once cooling is included. In fact, Kravtsov et al. (2005) demonstrate with simulations based on the Eulerian code ART, that including cooling and star formation has a strong effect on the total baryon fraction in the central cluster regions, where in the case of non–radiative runs it is even larger than the cosmic value. This is also relevant when metallicity dependent cooling is included, since it is even more effective in removing gas from the hot X–ray emitting phase with respect to the zero–metallicity cooling scheme. If we compare the two simulations with galactic winds, CSF and W, we observe a different slope that can be translated in the gas fraction relation with $\beta = 0.06$ and 0.12, as a combined effect of metal–dependent cooling and slightly higher wind velocity in the W simulation. Moreover, for the three simulations of the FDB set, NF, W and AGN2, the respective slope of the f_{gas}–M_{tot} relation at $z = 0$ is $\beta = 0.2, 0.17$ and 0.32 and reflects the f_{gas}–T_X relation discussed in Chapter 4 (see Figure 5.5).

The mild evolution of the normalization with redshift is in agreement with the result of Kravtsov et al. (2006) and reflects the slow evolution of the gas fraction with time (Kravtsov et al., 2005). The normalization $\log C$ differs for the different

simulation sets: ~ 14.4 for the TC set, ~ 14.25 for the AV set, ~ 14.35 for W and ~ 14.45 for NF and AGN2 runs. Kravtsov et al. (2006) obtain at $z = 0$ a value of $\log C = 14.37$ for their simulated clusters and the slope $\alpha = 0.917$. These values are close to that we obtained with similar simulations, where cooling and galactic winds are included: for the CSF run the values are 14.40 and 0.937 while the W simulations have values of 14.35 and 0.895. We remind here that the difference between those two simulations lies in the implementation of the cooling, that is metal dependent in W (as in the Kravtsov et al., 2006, simulated set), and in the strength of the galactic wind.

sim	z = 0	z = 0.25	z=0.50	z = 0.80	z = 1
csf	14.324 ± 0.007	14.315 ± 0.007	14.320 ± 0.006	14.317 ± 0.008	14.318 ± 0.008
	0.587 ± 0.007	0.585 ± 0.006	0.598 ± 0.006	0.606 ± 0.008	0.592 ± 0.009
	0.036	0.049	0.089	0.115	0.149
csfc	14.312 ± 0.006	14.302 ± 0.006	14.305 ± 0.006	14.303 ± 0.007	14.297 ± 0.006
	0.581 ± 0.007	0.583 ± 0.006	0.594 ± 0.006	0.596 ± 0.008	0.580 ± 0.007
	0.029	0.040	0.067	0.100	0.130
lvisc	14.261 ± 0.006	14.249 ± 0.010	14.257 ± 0.007	14.242 ± 0.008	14.241 ± 0.008
	0.598 ± 0.006	0.604 ± 0.010	0.601 ± 0.008	0.611 ± 0.009	0.586 ± 0.010
	0.048	0.061	0.059	0.072	0.102
ovisc	14.254 ± 0.005	14.244 ± 0.010	14.254 ± 0.007	14.242 ± 0.008	14.240 ± 0.009
	0.595 ± 0.005	0.600 ± 0.010	0.596 ± 0.008	0.606 ± 0.009	0.592 ± 0.012
	0.049	0.066	0.077	0.094	0.126
NF	14.334 ± 0.009	14.332 ± 0.007	14.330 ± 0.009	14.326 ± 0.010	14.308 ± 0.014
	0.560 ± 0.008	0.561 ± 0.006	0.585 ± 0.009	0.576 ± 0.010	0.559 ± 0.016
	0.038	0.039	0.069	0.094	0.116
W	14.279 ± 0.006	14.273 ± 0.006	14.276 ± 0.008	14.274 ± 0.006	14.263 ± 0.010
	0.578 ± 0.006	0.577 ± 0.006	0.597 ± 0.009	0.590 ± 0.007	0.582 ± 0.012
	0.027	0.039	0.070	0.096	0.115
AGN2	14.324 ± 0.022	14.313 ± 0.019	14.306 ± 0.018	14.306 ± 0.026	14.299 ± 0.024
	0.534 ± 0.019	0.554 ± 0.017	0.567 ± 0.018	0.540 ± 0.023	0.509 ± 0.024
	0.094	0.095	0.122	0.165	0.185

Table 5.3: Values of the fit of the $M_{tot,500}$–Y_X relation for all clusters, where the mass–weighted temperature T_{mw} is used to estimate the Y_X mass proxy. Column 1: name of the simulated cluster set. Column 2-6: values of normalization $\log C$, slope α and scatter $\sigma_{logM_{tot}}$ of the simulated data at redshifts $z = 0, 0.25, 0.5, 0.8$ and 1. Errors on $\log C$ and α are reported from the fit.

■ The M_{tot}–Y_X relation

The X–ray mass estimator Y_X we introduce previously is claimed to be the most robust mass estimator (e.g. Kravtsov et al., 2006; Vikhlinin et al., 2009). As found by Nagai et al. (2007a) the M_{tot}–Y_X scaling appears to have a small scatter and not to

be sensitive to the effects of gas cooling, star formation and energy feedback. These effects do not affect the power slope or the evolution, but slightly the normalization. The stability of the Y_X estimate is explained as due to the opposite trends in gas mass and temperature (see also Kravtsov et al., 2006).

Also for the Y_X parameter we plot the results with the evolution of CSF, LVISC and AGN2 simulations in Figure 5.2. From these we note that the scatter in the relation is slightly higher than for the M_{tot}–M_{gas} relation. The scatter in simulations reaches the lower level of $\sim 3\%$ and maximum values of about $\sim 10 - 18\%$ for the AGN2 simulations. The highest scatter obtained for this relation with respect to the gas mass proxy is the contrary of what was obtained in simulations by Kravtsov et al. (2006) and in the observations by Arnaud et al. (2007). No relevant evolution in the $M_{tot,500}$–Y_X relation is observed for CSF, LVISC and AGN2 runs.

sim	z = 0	z = 0.25	z=0.50	z = 0.80	z = 1
csf	14.343 ± 0.013	14.335 ± 0.013	14.365 ± 0.012	14.363 ± 0.015	14.379 ± 0.021
	0.600 ± 0.014	0.595 ± 0.012	0.612 ± 0.013	0.610 ± 0.015	0.606 ± 0.022
	0.055	0.058	0.068	0.089	0.116
csfc	14.310 ± 0.011	14.310 ± 0.011	14.323 ± 0.011	14.328 ± 0.016	14.327 ± 0.018
	0.587 ± 0.011	0.589 ± 0.011	0.596 ± 0.011	0.590 ± 0.015	0.572 ± 0.019
	0.046	0.053	0.065	0.091	0.114
lvisc	14.274 ± 0.009	14.265 ± 0.011	14.268 ± 0.010	14.250 ± 0.011	14.263 ± 0.014
	0.642 ± 0.011	0.650 ± 0.012	0.644 ± 0.012	0.652 ± 0.013	0.631 ± 0.018
	0.040	0.056	0.064	0.082	0.108
ovisc	14.279 ± 0.009	14.273 ± 0.011	14.287 ± 0.010	14.278 ± 0.011	14.285 ± 0.016
	0.640 ± 0.010	0.649 ± 0.011	0.645 ± 0.012	0.652 ± 0.013	0.643 ± 0.021
	0.040	0.053	0.064	0.082	0.112
NF	14.338 ± 0.006	14.340 ± 0.008	14.340 ± 0.009	14.338 ± 0.010	14.318 ± 0.015
	0.559 ± 0.006	0.564 ± 0.007	0.585 ± 0.009	0.584 ± 0.010	0.574 ± 0.017
	0.027	0.039	0.060	0.087	0.114
W	14.281 ± 0.009	14.280 ± 0.010	14.292 ± 0.010	14.292 ± 0.010	14.280 ± 0.011
	0.586 ± 0.009	0.580 ± 0.010	0.604 ± 0.011	0.600 ± 0.011	0.604 ± 0.014
	0.039	0.047	0.064	0.087	0.110
AGN2	14.346 ± 0.023	14.343 ± 0.021	14.348 ± 0.021	14.356 ± 0.026	14.350 ± 0.026
	0.519 ± 0.020	0.545 ± 0.017	0.556 ± 0.019	0.529 ± 0.022	0.494 ± 0.023
	0.088	0.083	0.094	0.116	0.132

Table 5.4: Values of the fitting parameters of the $M_{tot,500}$–Y_X relation for all clusters, where Y_X parameter is estimated from the spectroscopic–like temperature within $0.15 - 1$ R_{500}. Column 1: name of the simulated cluster set. Column 2-6: values of normalization $\log C$, slope α and scatter $\sigma_{logM_{tot}}$ of the simulated data at redshifts $z = 0, 0.25, 0.5, 0.8$ and 1. Errors on $\log C$ and α are reported from the fit.

The detailed results of each fit for all simulations are reported in Table 5.3. The normalization of the relation lies in the range of $14.27 - 14.34$ for all redshifts and simulations. Our W simulations have normalization and slope at $z = 0$ of 14.28

and 0.586 respectively, resulting in agreement within errors with the values of the fit reported by Kravtsov et al. (2006), 14.27 and 0.583. The results are slightly different at higher redshift ($z = 0.5$), where for the W runs we obtain values of (14.29, 0.60), with respect to the values (14.27, 0.57) at $z = 0.6$ reported by Kravtsov et al. (2006). Here we emphasize the fact that we are using the spectroscopic–like temperature to estimate the Y_X parameter, Kravtsov et al. (2006) derived their temperature estimate from X–ray imaging of simulated clusters.

Non–radiative runs with different implementation of viscosity, LVISC and OVISC show a normalization close to that reported by Kravtsov et al. (2006), while the slope is quite close to the self–similar prediction. This is not the case if the spectroscopic–like temperature is computed directly from simulations. In this case, as reported in Table 5.4, while the normalization has no strong change, the slope is 0.64, higher than expected for the self–similar relation. This means that there is a non–trivial bias when the spectroscopic–like temperature is used to estimate the Y_X parameter.

With respect to the AV set the cooling included in both the TC and FDB leads to a flatter relation. This effect on the slope reflects again the change in f_{gas} with respect to the physics implemented in simulations.

The evolution with redshift is not appreciable in AV and TC runs for both the normalization and the slope. There is however a mild increase in the normalization for the FDB runs, while the slope steepens below $z < 1$, reaching its maximum value at $z = 0.5$ and then decreasing. The highest scatter in the M_{tot}–Y_X relation is obtained in all the studied runs at the highest redshift. Since the scatter increases with increasing redshift while this is not the case when the gas mass proxy is used, we conclude that it depends mildly on ICM substructure and mergers (O'Hara et al., 2006; Jeltema et al., 2008). This is however at variance with what reported by Kravtsov et al. (2006) and Vikhlinin et al. (2009).

5.4.2. The effect of different physics on the scaling relations

■ The effect of thermal conduction

To estimate the effect of thermal conduction we compare the simulations with cooling and star formation, CSF, to the simulations where the new formalism of conduction was implemented by Jubelgas et al. (2004). The conductivity was fixed at one third of the Spitzer value. As reported by Dolag et al. (2004) the effect of this conduction is visible in the temperature profiles of hot clusters, where an isothermal core is formed. However we recall here that we excise the central core $< 0.15\ R_{500}$ in clusters when computing the mass-weighted temperature.

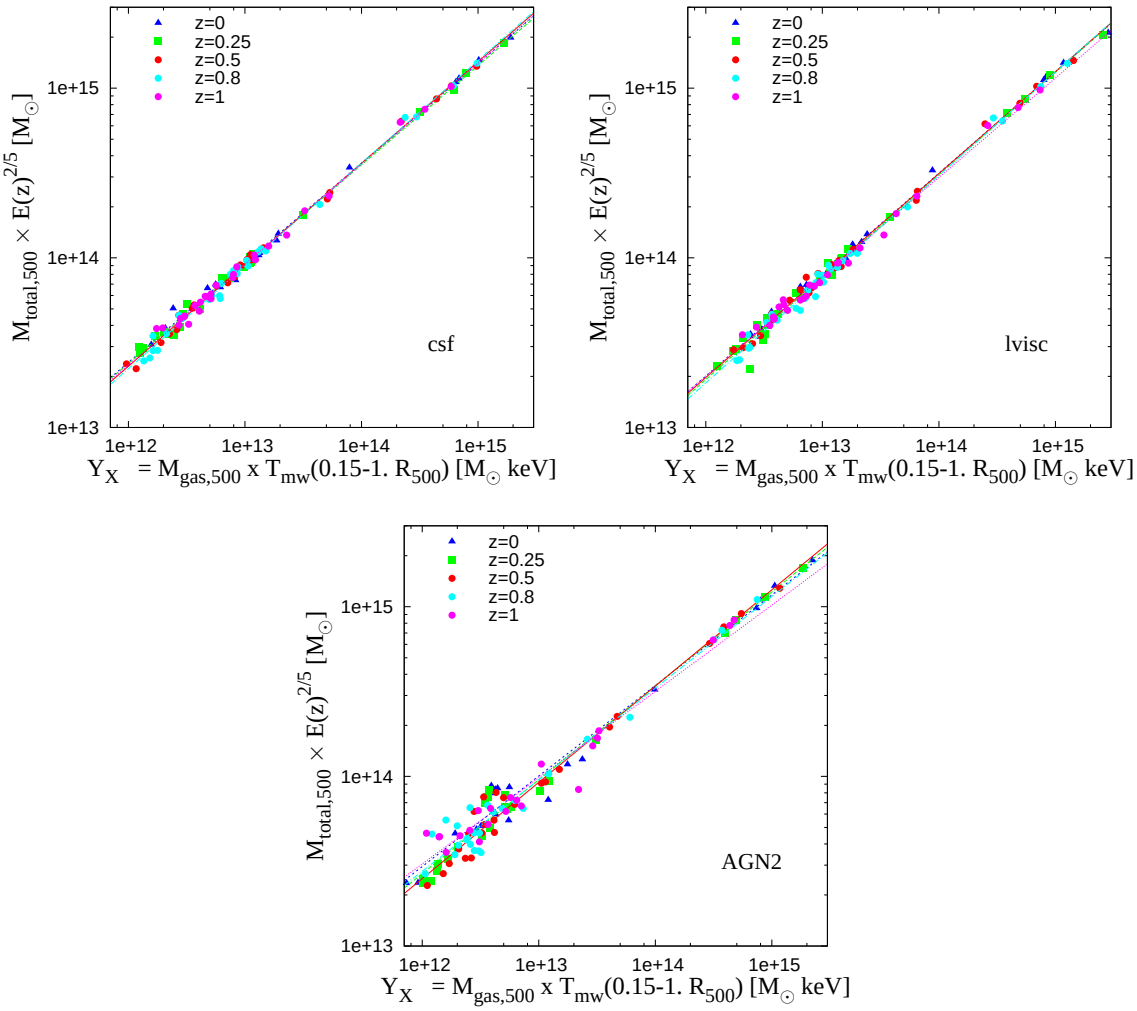

Figure 5.2: The relation between total cluster mass, computed within R_{500} and scaled by $E(z)^{2/5}$, and the Y_X parameter, estimated using the gas mass within the same radius and the spectroscopic–like temperature T_{sl} computed in the annulus $(0.1-1)\times R_{500}$. The three panels show the single cluster data at each redshift: blue triangles ($z=0$), green squares ($z=0.25$), red circles ($z=0.50$), cyan circles ($z=0.8$) and magenta circles ($z=1$). For each redshift the best fit power law is plotted with blue short dashed ($z=0$), green long dashed ($z=0.25$), red continues line ($z=0.5$), cyan dot-dashed ($z=0.8$) and magenta dotted line ($z=1$). **Top left panel:** galaxy cluster data from the CSF simulation that includes cooling, star formation and weak galactic winds. **Top right panel:** data extracted from the LVISC simulation with the scheme of a time–varying low artificial viscosity. **Bottom panel:** galaxy clusters simulated with AGN feedback (AGN2) that include both low and high–accretion modes.

The effect of relevant physical processes such as viscosity, feedback strength and thermal conduction on the baryon fraction was studied by Ettori et al. (2006) using the four high–mass systems of the TC and AV sets. The results of their analysis demonstrated that the baryon fraction is generally stable but only at rather large radii, $> R_{500}$. They also showed that changing the description of the relevant ICM physical processes changes the extrapolation of the baryon fraction from the central regions, relevant for X–ray measurements, while also slightly affecting the redshift evolution. For the CSF and CSFC simulations they obtain at R_{500} the parameter Y_{gas}, defined as the ratio of gas fraction f_{gas} to the cosmic value $\Omega_b/\Omega_m = 0.13$, of 0.658 and 0.655 respectively. These results are in partial agreement with the observations of 36 luminous clusters by Ettori & Fabian (1999). At R_{500} Ettori et al. (2006) found a sizeable underestimate of the hot baryon budget when extra physics is added to the action of gravitational heating. They found also a mild increase of the gas fraction from ~ 0.62 to ~ 0.66 below $z < 1$ for both CSF and CSFC.

Considering these results, we do not expect any relevant effect of thermal conduction on both the M_{tot}–M_{gas} and M_{tot}–Y_X relation. The effect on M_{gas} is observed in Figure 5.3, where the mass–gas mass relation is reported for CSF clusters (blue triangles) and CSFC clusters (green squares) for the local Universe ($z = 0$, left panel) and at $z = 1$ (right panel). In both cases the relation is tight, with a very low scatter around 2%, with the two fits virtually undistinguishable from each other.

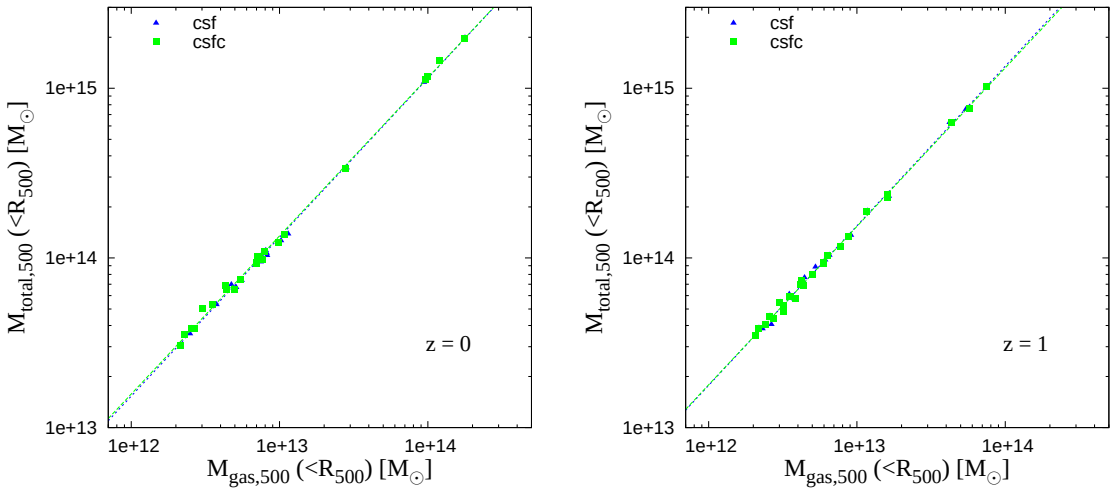

Figure 5.3: Total cluster mass plotted versus the gas mass for CSF and CSFC simulated galaxy clusters. Single clusters are plotted with: blue triangles for the CSF run and green squares for the CSFC run, where conduction is included. Lines refer to the best fit power–law relations: blue short–dashed line for the CSF run and green long–dashed for the CSFC run. **Left panel:** comparison between CSF and CSFC galaxy clusters at redshift $z = 0$. **Right panel:** comparison between CSF and CSFC simulations but for clusters at $z = 1$.

The relation between mass and Y_X in Figure 5.4 shows a slightly larger scatter, $\sim 3\%$ at $z = 0$ and $\sim 13\%$ at $z = 1$. The two fits are very close, despite the little difference on massive cluster scales, where at a fixed cluster mass Y_X is slightly larger in the CSFC clusters. The difference should be enhanced if the Y_X parameter is evaluated including the cluster core of massive clusters, where the effect of thermal conduction on the temperature profile is manifest (Dolag et al., 2005). In particular, gas in the cluster centre is made more isothermal, since conduction is able to smooth out the temperature substructure of the ICM.

As we already emphasize, using different definitions of temperature can lead to different results. In fact, when comparing the emission–weighted, mass–weighted and spectroscopic–like temperatures for a fixed cluster mass, Ameglio et al. (2006) found that T_{ew} and T_{sl} definitions provided values that differ from T_{mw}. T_{ew} weights mostly the central regions of galaxy clusters, that are characterized by higher temperatures, since the weighting scheme in this definition depends on both the cooling function and the electron density squared. T_{sl} is instead biased toward colder thermal components, while T_{mw} is directly proportional to the thermal content of the cluster. We expect that using the T_{sl} temperature to estimate Y_X, which should more closely follow the observational procedure, leads to larger discrepancies between CSF and CSFC runs. In fact, this is true especially for hot clusters both at $z = 0$ and $z = 1$, as can be seen in Table 5.4. The M_{tot}–Y_X relation is steeper for the CSF run, since in this case the colder components are not smoothed out by conduction and the temperature is then lower than in Figure 5.4, where Y_X is evaluated by means of T_{mw}.

■ The effect of artificial viscosity

In Figure 5.5 we compare the results for the mass–gas mass relation for LVISC (blue triangles) and OVISC (green squares) simulations at $z = 0$ (left panel) and at $z = 1$ (right panel). We do not notice any relevant difference between the fits for the two non–radiative runs at both redshifts in Figure 5.5. Ettori et al. (2006) showed, as mentioned before, that gas fraction f_{gas} in LVISC and OVISC are very close to each other for massive galaxy clusters. They found a slight decrease of Y_{gas} with values decreasing from 0.912 (LVISC) and 0.947 (OVISC) at $z = 1$ to 0.818 and 0.874 at $z = 0$. Slightly higher mean values, with no evident evolution, were found by Kravtsov et al. (2005) by simulating 10 clusters with the Eulerian code ART. They also compare the ART and GADGET-2 code to study the systematic uncertainties in the baryon fraction. They found a systematic difference in the gas fraction in non–radiative runs, which is 5% higher in the ART simulations than in GADGET-2 within $< 0.4\ R_{vir}$, and of about $3 - 5\%$ at larger radii. A negligible evolution of the gas fraction with redshift was found in simulations also by Eke et al. (1998).

In Figure 5.6 we report in the two panels the relation between the cluster mass

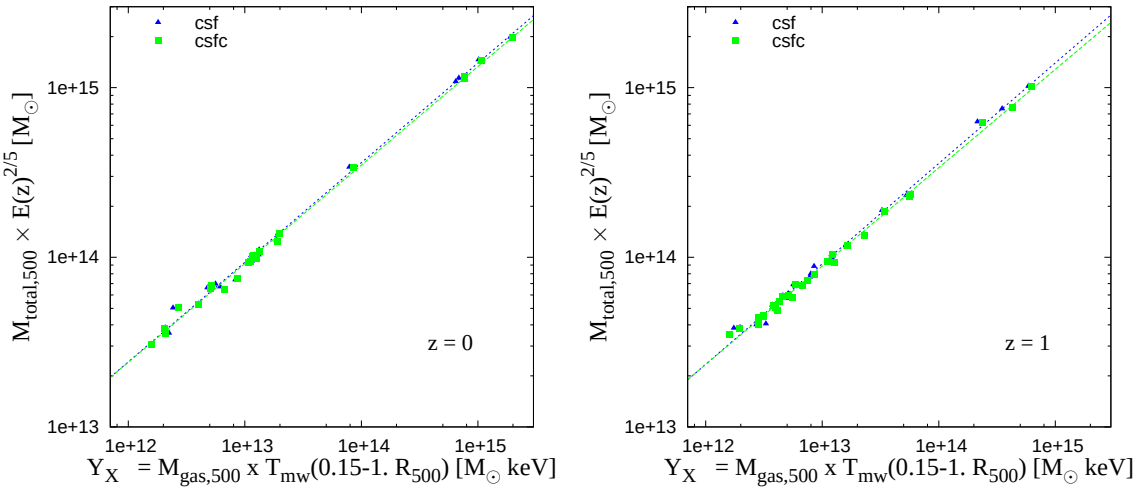

Figure 5.4: Total cluster mass (scaled by the cosmological factor $E(z)^{2/5}$) plotted versus the Y_X parameter for CSF and CSFC simulated galaxy clusters. Symbols are plotted for single clusters: blue triangles for the CSF run and green squares for the CSFC run where conduction is included. Lines refer to the best fit power–law relations: blue short–dashed line for the CSF run and green long–dashed for the CSFC run. **Left panel:** comparison between CSF and CSFC galaxy clusters at redshift 0. **Right panel:** comparison between CSF and CSFC simulations but for clusters at $z = 1.0$.

and Y_X for LVISC and OVISC simulations at $z = 0$ (left panel) and $z = 1$ (right panel). Also in this case we do not find differences in the relation for the two adopted viscosity implementations, although the low–viscosity scheme LVISC should increase the non–thermal support in the cluster. As found by Dolag et al. (2005), the low viscosity scheme in fact does not change T_{mw} in clusters, therefore we do not expect relevant differences in the results from the two schemes. Moreover, Dolag et al. (2005) found that turbulent motions are important only in the inner 0.1 R_{vir} part of the cluster, excluded from our Y_X analysis, where a significant gas density drop is observed together with a very mild trend of increasing temperature.

■ The effect of feedback

The most relevant difference among simulations is found when the FDB runs are compared. In Figure 5.7 we compare the M_{tot}–M_{gas} relation for NF (blue triangles), W (green squares) and AGN2 (red circles) simulations at $z = 0$ (left panel) and $z = 1$ (right panel). We observe a clear trend in the gas mass for low–mass systems: groups simulated with AGN feedback are depleted of gas, while groups from simulations with galactic winds contain far more gas than in the NF scheme. An intermediate position is achieved by the no feedback scheme, where only cooling and star forma-

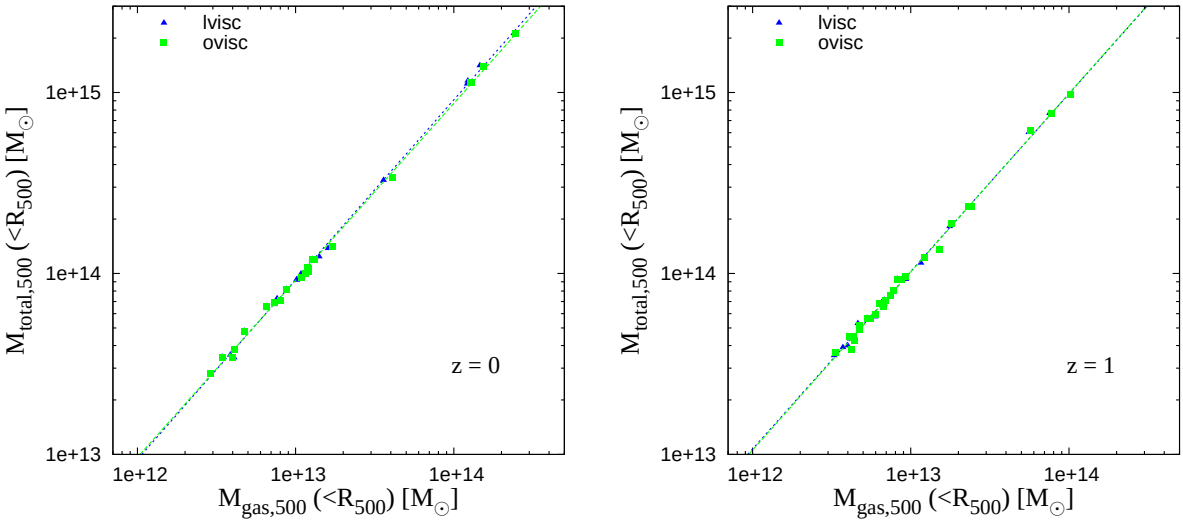

Figure 5.5: Total cluster mass plotted versus the gas mass for LVISC and OVISC simulated galaxy clusters. Clusters are plotted with blue triangles for the LVISC run and green squares for the OVISC run. Lines refer to the best fit power–law relations: blue short–dashed line for the LVISC run and green long–dashed for the OVISC run. **Left panel:** comparison between LVISC and OVISC galaxy clusters at redshift $z = 0$. **Right panel:** comparison between LVISC and OVISC simulations but for clusters at $z = 1$.

tion are at work. The low quantity of gas in AGN2 runs is the result of an effective heating by the AGN that is efficient in displacing the gas outside the potential well especially for galaxy groups. On the other hand in NF simulations a large amount of gas is cooling and fuelling the repository of cold baryons. The galactic winds in W runs, that start acting at high redshift, are instead able to bring energy to the ICM and maintain a large amount of gas in the X–ray emitting phase. A similar effect, although not so strong as in low temperature systems, can be observed for massive clusters.

For both W and NF runs we observe a small scatter in the data, around $\sim 4-5\%$ as reported in Table 5.2. The scatter is much larger for AGN2 simulations, of about $\sim 12\%$ at low redshifts. This is partially due to the groups simulated with higher mass resolution, that flatten the fitted relation with respect to what found for $z = 1$.

A smaller spread in the FDB simulated data is observed in Figure 5.8 where similar panels for $z = 0$ and 1 are reported but for the M-Y_X relation. The scatter is indeed lower, about $\sim 2-3\%$ for NF and W runs and three times higher in the AGN2 case ($\sim 9\%$). The fitting parameters are less sensitive to the variation of the feedback scheme with respect to the parameters for the M_{gas} proxy. In this sense, the Y_X parameter is more robust, or feedback independent, than the gas mass M_{gas}.

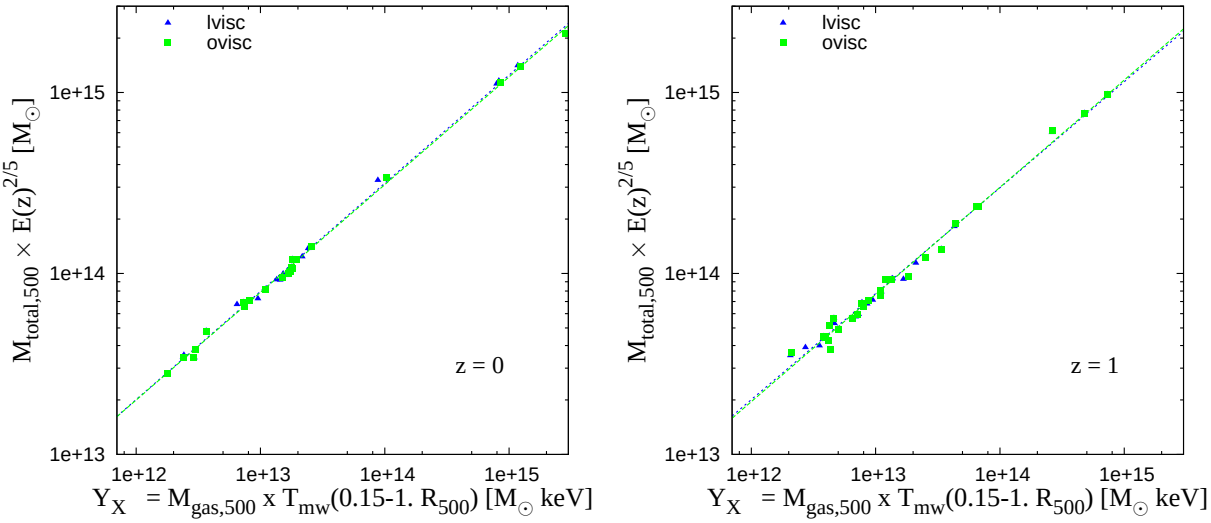

Figure 5.6: Total cluster mass (scaled by the cosmological factor $E(z)^{2/5}$) plotted versus the Y_X parameter for simulations with different artificial viscosity schemes. The LVISC simulations are plotted with blue triangles with the best fit power–law blue short–dashed line. The OVISC simulations are plotted with green squares and fitted with a power–law relation (green long–dashed line). **Left panel:** comparison between LVISC and OVISC galaxy clusters at redshift 0. **Right panel:** comparison between LVISC and OVISC simulations but for clusters at $z = 1$.

■ The evolution with the fixed self–similar slope

Following the work by Kravtsov et al. (2006), we provide in Tables 5.6 and 5.5 the best–fit normalization for the two relations, M_{tot}–M_{gas} and M_{tot}–Y_X respectively, when fitted with the slopes fixed to the self–similar value.

The evolution of the $\log C$ normalization is plotted in Figure 5.9 when the cluster data for all simulations are fitted with the slope of the M_{tot}–M_{gas} relation at the fixed self–similar value of 1.0. Non–radiative runs have the lowest normalization $\log C$, in agreement with the value obtained when performing the fit with slope left as a free parameter. The normalization is higher for runs with galactic winds W, CSF and CSFC, where the scatter is around $3-5\%$. The largest normalization and hence the more distant from a self–similar predicted slope is obtained for NF and AGN2 runs. When radiative cooling is included in simulations the M_{tot}–M_{gas} departs from self–similarity. The larger difference is obtained when AGN feedback is included in simulations. Moreover, in both figures we clearly see that when the slope is fixed there is no evident evolution of the normalization.

In Figure 5.10 we plot the normalization $\log C$ for all simulations fitted with a fixed self–similar slope of 0.6, as expected for the Y_X–M_{tot} relation. The values of

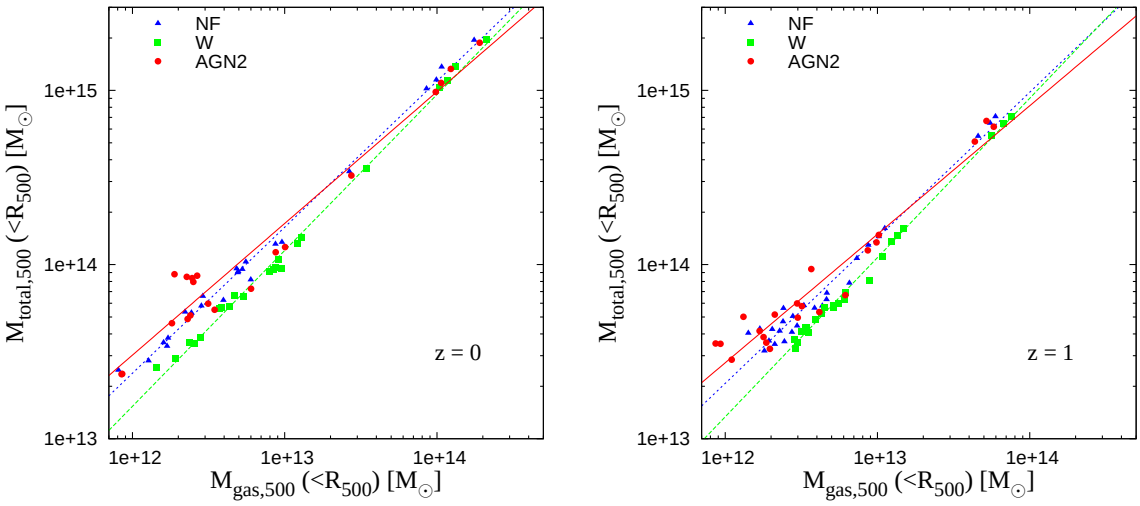

Figure 5.7: Total cluster mass with respect to the gas mass for galaxy clusters simulated with different feedback prescriptions. Symbols refer to the clusters from the no–feedback runs (NF blue triangles), runs with galactic winds (W green squares) and runs with the AGN feedback (AGN2 red circles). For all of them the best fit power–law is plotted: with blue short–dashed line (NF), green long–dashed line (W) and red continuous line (AGN2). **Left panel:** comparison between NF, W and AGN2 simulations of galaxy clusters at redshift 0. **Right panel:** comparison between NF, W and AGN2 simulations but for clusters at $z = 1$.

the fits are reported on tables 5.6 and 5.5.

In this case the range of normalizations obtained from the fit is quite smaller, from 14.25 to 14.35. Once the slope is fixed the lowest normalization and scatter are obtained for the non–radiative runs LVISC and OVISC, a slightly higher values for runs with cooling, star formation and winds CSF, CSFC and W, while AGN2 and NF runs obtain the highest values. Also in this case we find a decrease of the scatter at lower redshift for all simulations but those with AGN feedback.

Also in this case, where we fixed the slope of the power–law relation to fit the galaxy cluster data, we find that the Y_X proxy is less sensitive to the included feedback scheme. It should be noted that in the M_{tot}–Y_X case the normalization lies in the range $14.25 - 14.35$, while for the M_{tot}–M_{gas} the range is much larger, $14.25 - 14.65$. The reason for this stability of the Y_X mass proxy is that it is by definition a measure of the thermal pressure support in the ICM. Therefore, we expect its value to be robust against the introduction of any physical process, which does not lead to a significant violation of the condition of hydrostatic equilibrium.

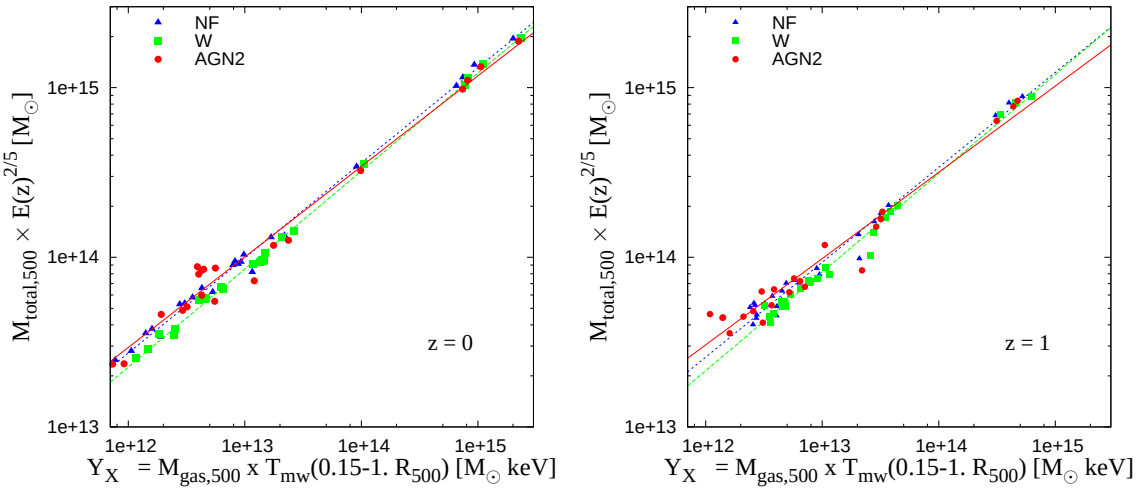

Figure 5.8: Total cluster mass (scaled by the cosmological factor $E(z)^{2/5}$) with respect to the Y_X parameter for galaxy clusters simulated with different feedback prescriptions. Symbols refer to the cluster data from the no–feedback runs (NF; blue triangles), runs with galactic winds (W; green squares) and runs with the AGN feedback (AGN2; red circles). For all of them the best fit power–law is plotted: with blue short–dashed line (NF), green long–dashed line (W) and red continuous line (AGN2). **Left panel:** comparison between NF, W and AGN2 simulations of galaxy clusters at redshift 0. **Right panel:** comparison between NF, W and AGN2 simulations but for clusters at $z = 1$.

5.5 Conclusions

Galaxy clusters are used in cosmological studies, since with the evolution of their mass function one can constrain the normalization of the power spectrum, the density parameter of Dark Matter and Dark Energy as well as the Dark Energy equation of state. Thanks to their high emissivity, clusters can be detected in X–ray band up to high redshifts, $z \sim 1.4$. It is therefore necessary to deeply understand the relation between X–ray observables and the total galaxy cluster mass.

In this Chapter we focused on a study of the effect that different physical mechanism have on the mass–observable relations. We focused on the M_{gas} and Y_X mass proxies for the total cluster mass. For this study we used galaxy clusters and groups simulated with the GADGET-2 code and with seven different physics schemes from where we study the effect of: (i) thermal conduction, (ii) artificial viscosity, (iii) cooling and star formation, (iv) galactic winds and (v) AGN feedback.

The main results of our analysis can be summarised as follows:

- the relation between gas mass and cluster total mass closely follows the self–similar relation only in non–radiative runs, while cooling and star formation

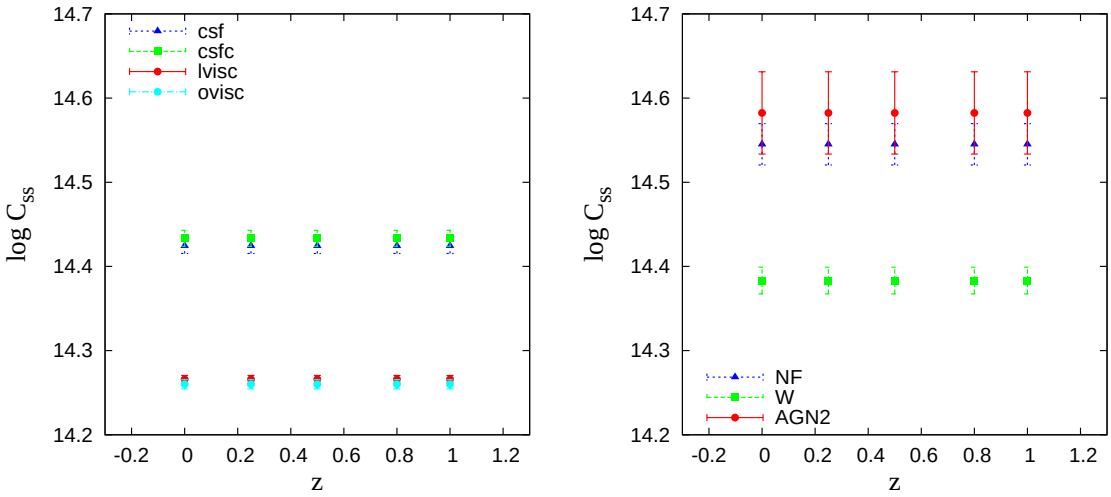

Figure 5.9: The redshift evolution of the normalization of the M_{tot} –M_{gas} relation when fitted by a power–law with the self–similar slope of 0.6. The $\log C_{ss}$ parameter and its error are reported in 5.6. **Left panel:** The best fit normalizations for the simulations CSF (blue triangles) and CSFC (green squares), where the thermal conduction is accounted for and for simulations with different viscosity scheme, namely the LVISC (red circles) and OVISC runs (cyan circles). **Right panel:** The best fit normalization for simulations with different feedback schemes: no–feedback (NF; blue triangles), galactic winds (W; green squares) and BH feedback (AGN2; red circles).

make the slope of the relation shallower.

- the scatter in the M_{tot}–M_{gas} relation does not significantly evolve with redshift for each simulation, with values from $\sim 2\%$ to 10%.

- the scatter in the M_{tot}–Y_X relation ranges from 2% to 16%, depending on the physics included in the simulations; we find an increase of the scatter with redshift, that is a consequence of mergers and substructure in the ICM, which lead to deviations from the condition of pressure equilibrium.

- both relations do not show any strong evolution with redshift for any of the simulated physics.

- when the effect of feedback is stronger the Y_X proxy has less scatter with respect to the gas mass proxy; since Y_X is by definition a measure of the thermal pressure support in the ICM, the relation M_{tot}–Y_X results more stable than the M_{tot}–M_{gas} relation against the changing of the physical processes included in the simulations.

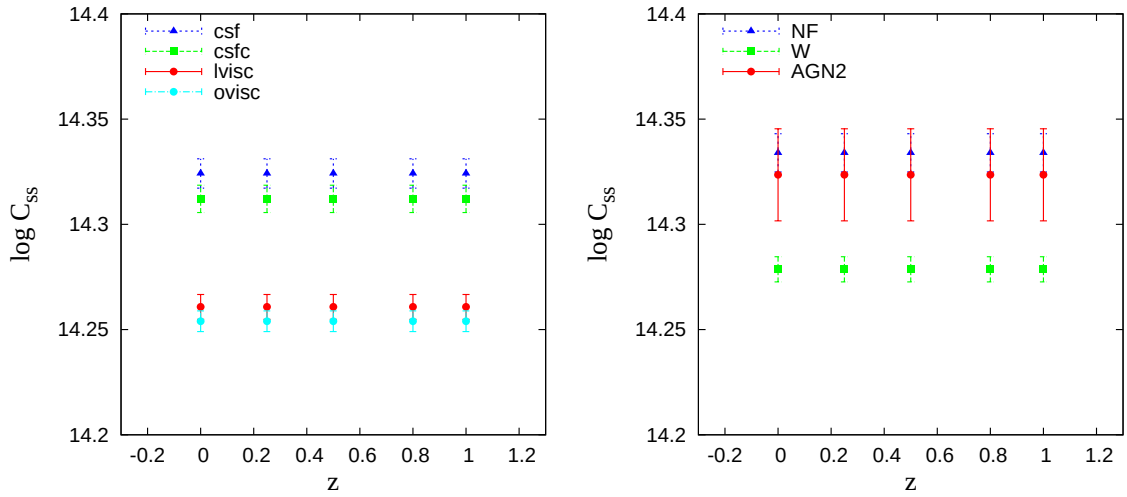

Figure 5.10: The redshift evolution of the normalization of the M_{tot}–Y_X relation when fitted by a power–law with the self–similar slope of 0.6. The $\log C_{ss}$ parameter and its error are reported in Figure 5.6. **Left panel:** The best fit normalizations for simulations CSF (blue triangles), CSFC (green squares), LVISC (red circles) and OVISC (cyan circles). **Right panel:** The best fit normalization of simulations with different feedback schemes: no–feedback (NF; blue triangles), galactic winds (W; green squares) and BH feedback (AGN2; red circles).

sim	z = 0	z = 0.25	z=0.50	z = 0.80	z = 1
csf	14.424 ± 0.009 0.043	14.426 ± 0.010 0.050	14.414 ± 0.006 0.029	14.410 ± 0.006 0.031	14.415 ± 0.006 0.032
csfc	14.433 ± 0.010 0.046	14.431 ± 0.010 0.053	14.417 ± 0.006 0.031	14.415 ± 0.006 0.034	14.412 ± 0.006 0.034
lvisc	14.266 ± 0.005 0.022	14.250 ± 0.005 0.029	14.243 ± 0.004 0.022	14.221 ± 0.003 0.018	14.223 ± 0.004 0.022
ovisc	14.260 ± 0.005 0.026	14.246 ± 0.006 0.030	14.237 ± 0.004 0.022	14.218 ± 0.003 0.017	14.220 ± 0.005 0.024
NF	14.545 ± 0.025 0.118	14.556 ± 0.023 0.115	14.518 ± 0.015 0.078	14.522 ± 0.017 0.087	14.509 ± 0.020 0.101
W	14.383 ± 0.016 0.076	14.385 ± 0.015 0.076	14.367 ± 0.009 0.045	14.365 ± 0.008 0.039	14.355 ± 0.009 0.045
AGN2	14.582 ± 0.049 0.219	14.581 ± 0.037 0.180	14.553 ± 0.029 0.146	14.594 ± 0.035 0.179	14.576 ± 0.039 0.202

Table 5.5: Values of the fitting parameters of the M_{tot}–M_{gas} relation when the slope is fixed at the self–similar value $\alpha = 1$. Column 1: name of the simulated cluster set. Column 2-6: values of normalization $\log C_{ss}$ and scatter $\sigma_{logM_{tot}}$ of the simulated data at redshifts $z = 0, 0.25, 0.5, 0.8$ and 1. Errors on $\log C_{ss}$ are reported from the fit.

A deeper inspection of the relations we measured from our simulated cluster sets

sim	z = 0	z = 0.25	z=0.50	z = 0.80	z = 1
csf	14.324 ± 0.007 0.059	14.315 ± 0.007 0.052	14.320 ± 0.006 0.051	14.317 ± 0.008 0.065	14.318 ± 0.008 0.078
csfc	14.312 ± 0.006 0.048	14.302 ± 0.006 0.049	14.305 ± 0.006 0.052	14.303 ± 0.007 0.071	14.297 ± 0.006 0.082
lvisc	14.261 ± 0.006 0.054	14.249 ± 0.010 0.073	14.257 ± 0.007 0.077	14.242 ± 0.008 0.103	14.241 ± 0.008 0.105
ovisc	14.254 ± 0.005 0.054	14.244 ± 0.010 0.064	14.254 ± 0.007 0.064	14.242 ± 0.008 0.082	14.240 ± 0.009 0.096
NF	14.334 ± 0.009 0.055	14.332 ± 0.007 0.048	14.330 ± 0.009 0.048	14.326 ± 0.010 0.067	14.308 ± 0.014 0.093
W	14.279 ± 0.006 0.042	14.273 ± 0.006 0.045	14.276 ± 0.008 0.054	14.274 ± 0.006 0.071	14.263 ± 0.010 0.096
AGN2	14.324 ± 0.022 0.136	14.313 ± 0.019 0.109	14.306 ± 0.018 0.093	14.306 ± 0.026 0.108	14.299 ± 0.024 0.127

Table 5.6: Values of the fitting parameters for M_{tot}–Y_X relation when the slope is fixed at the self–similar value $\alpha = 0.6$. The Y_X parameter is computed with the mass–weighted temperature estimate. Column 1: name of the simulated cluster set. Column 2-6: values of normalization $\log C_{ss}$ and scatter $\sigma_{logM_{tot}}$ of the simulated data at redshifts $z = 0, 0.25, 0.5, 0.8$ and 1. Errors on $\log C_{ss}$ are reported from the fit.

will require the use of a suitable software, like X–ray Map Simulator X–MAS (Gardini et al., 2004; Rasia et al., 2005, 2008), that is able to extract mock images from simulations and to reduce data using the same procedure followed for observational data. This would allow us to verify the impact of different effects, as for example projection effects, on the observed scaling relations.

CONCLUSIONS

The aim of this Thesis was to study the X–ray properties of the IntraCluster Medium (ICM) in a cosmological context resorting to high resolution hydrodynamical simulations. The thermodynamical and chemical properties of the ICM were inspected and studied within a set of galaxy clusters, described in **Chapter 3**, that were simulated with the TREE–SPH GADGET-2 code (Springel, 2005). This code, described in **Chapter 2** included a detailed model of chemical evolution (Tornatore et al., 2007a) as well as prescriptions for different physical processes: star formation, galactic winds and AGN feedback. We use this large set of simulated galaxy clusters with a twofold aim. First, we study the effect of different sources of feedback on the ICM observable properties, in particular on its metal enrichment (**Chapter 3**) and on thermo and chemo–dynamical properties when AGN feedback is at work (**Chapter 4**). Second, we test the robustness of cluster mass proxies against the different physical processes included in the simulations (**Chapter 5**).

Here we briefly summarize the results obtained in this Thesis.

■ Metal enrichment of the ICM and its evolution

In **Chapter 3** we presented a characterisation of the evolution of the chemical enrichment of the ICM out to redshift $z \simeq 1$. We run different simulations starting from the same set of initial conditions with the purpose of investigating: (i) the effect of changing the chemical evolution model and (ii) the effect of suppressing star formation at $z < 1$.

(a) We simulated the entire cluster set with the three stellar Initial Mass Functions (IMFs), namely Salpeter (1955), Kroupa (2001) and Arimoto & Yoshii (1987) IMFs, to study the *effect of changing the chemical evolution model*. Simulations based on the Kroupa and Arimoto–Yoshii IMFs predict a too high normalization for the metallicity profiles, as compared with Chandra observations of nearby clusters. We found instead that the Salpeter IMF predicts a normalization of the profiles in quantitative agreement with observations.

However, this result should be interpreted with some caution, because of the presence of a degeneracy between the IMF shape and the fraction of binary

systems that lead to a supernova type Ia explosion. In fact, reducing the fraction of stars that belong to binary systems suppresses the enrichment level and alleviates the disagreement of, for example, a top–heavy IMF with the observed $Z_{\rm Fe}$ profiles.

Our simulations predict a negative metallicity gradients out of R_{500} and beyond, at variance with recent XMM–Newton measurements of metal abundance at larger radii (e.g. Snowden et al., 2008; Leccardi & Molendi, 2008a). We should emphasize here that the simulations we used in this first part of the Thesis were performed by including galactic wind feedback triggered by supernovae explosions, without accounting for the effect of AGN feedback.

(b) We found that our simulations predict the *positive evolution of the central Iron abundance*, independently of the adopted IMF and comparable to that observed by Balestra et al. (2007). The Salpeter IMF simulations were found to provide an enrichment consistent with observations, while the Kroupa and Arimoto–Yoshii (AY) IMFs overpredict the enrichment level at all redshifts. Again, this disagreement can be alleviated by decreasing the fraction of binary systems.

(c) The positive evolution of the Iron abundance could be in principle driven by the excess of *recent star formation* that is present in our simulations. We decided therefore to run a simulation where cooling and star formation were arbitrarily stopped at $z = 1$, thus mimicking the quenching of star formation expected from the action of Active Galactic Nuclei (AGN). The net, counter-intuitive effect is that a too strong positive evolution of the emission–weighted metallicity is produced. The explanation lies in the fact that in the absence of star formation all the metals released at $z < 1$ by long–living stars are no longer locked back in the stellar phase. As a result, high–density halos contain more metals and the clumpy metal distribution boosts the emission–weighted abundance estimate. The conclusion is that suppressing recent star formation has the effect of enhancing the positive evolution of the ICM metallicity.

The effect of the excess recent star formation was inspected by comparing the observed SNIa rate per unit B–band luminosity, SNU_B, in galaxy clusters to the simulation predictions. We were only able to reproduce consistently the observed declining trend of SNU_B at low redshift only when the star formation is excised at $z < 1$.

In summary, we found that among different prescriptions for the IMF, the best results on Iron abundance profiles and global Iron evolution are found when applying the Salpeter IMF. We also found that the positive evolution of the metal abundance in the central regions of simulated clusters can not be simply interpreted as a consequence of an excess of low–redshift star formation. Instead the evolution of the

metallicity pattern is driven by the combined action of gas–dynamical processes, which redistribute already enriched gas, and of star formation, which acts both as a source and as a sink of metals.

■ The imprint of feedback on the ICM properties

Cluster simulations which only include stellar feedback, like those presented in **Chapter 3**, have been demonstrated to be at variance with observations of the temperature profiles in the cool core regions and of the much suppressed star formation in the BCGs. We chose to address such problems by adding the effect of the energy feedback from gas accretion onto super-massive black holes.

In **Chapter 4** we presented the analysis of an extended set of cosmological hydrodynamical simulations of galaxy clusters aimed at studying the different effects that stellar and AGN feedback have on the thermal and chemo-dynamical properties of the ICM. The different feedback prescriptions adopted were: (i) galactic winds driven by supernova (SN) explosions, (ii) AGN feedback by gas accretion onto supermassive blackholes (BHs) in an active stage ('quasar mode') (Springel et al., 2005a; Di Matteo et al., 2005) and (iii) AGN feedback where BHs accrete gas quiescent in a radiatively efficient mode ('radio mode'). The quasar mode scheme reproduces the original model by Springel et al. (2005a) for the choice of the parameters determining the feedback efficiency and the way in which energy is distributed. The radio mode scheme assumes beside the quasar mode phase also the presence of a radiatively efficient phase, where BH accretion takes place in a quiescent stage (e.g., Sijacki et al., 2007) and a higher fraction of the released energy is thermalized in the gas surrounding the BHs.

The results of this analysis can be summarized as follows:

(a) As for the effect on the *star formation of the BCGs* we found that with AGN feedback we predict a much lower star formation rate at low redshift. Furthermore, feedback with radio mode AGN is more efficient in reducing gas accretion onto BHs, thus providing BH masses in closer agreement with observations.

(b) Concerning the *thermo–dynamical properties of the ICM* we found that AGN feedback brings the L_X–T relation in closer agreement with observations, especially on the scale of poor clusters and groups. Despite this, the ICM entropy in central regions of groups has a higher level with respect to observational results (e.g., Sun et al., 2009; Sanderson et al., 2009a) and corresponds in turn to a too low value of the gas fraction for galaxy groups. Moreover, feedback by AGNs reduces the fraction of baryons converted into stars by about 30–50 per cent. However, for rich clusters the fraction of stars within R_{500} from simulations is still larger than the observed one ($\simeq 10$ per cent).

The most relevant result beside the recovering of the $L_X - T$ relation is that AGN feedback is efficient in pressurizing gas in the central regions of galaxy groups, thereby generating temperature profiles which are in reasonable agreement with the observed ones. Despite this success, the core regions of massive clusters are still characterized by too steep temperature profiles.

(c) As for the *metallicity content of the ICM*, we found a rather uniform and widespread pattern of metal enrichment in the outskirts of galaxy clusters simulated with the AGN feedback. Indeed, the effect of BHs feedback is that of displacing highly enriched gas from star forming regions at high redshift, so as to improve the metal circulation in the inter–galactic medium.

This more widespread enrichment produces at low redshift Iron abundance profiles with a plateau in the cluster outskirts, at variance with simulations including only stellar feedback or galactic winds, and in much better agreement with observational results.

Comparing the distribution of elements produced by SNe-II, that are released over a short timescale and are more clumpy, and elements released by SN-Ia, released over a longer time–scale, we found that simulations predict that a sizable fraction of the ICM enrichment is produced by intra-cluster stars, in line with observational indications (Sivanandam et al., 2009).

Finally, we find flat $Z_{\rm Si}/Z_{\rm Fe}$ profiles in simulations. Understanding the reason for the discrepant results on the observed radial dependence of $Z_{\rm Si}/Z_{\rm Fe}$ by Chandra and Suzaku requires future generation X–ray telescopes able to detect with more accuracy and with low background the chemical composition of the ICM in the outskirts of clusters. Moreover, we find that the suppression of star formation with AGN feedback causes $Z_{\rm Si}/Z_{\rm Fe}$ to increase at small radii, $\lesssim 0.1 R_{500}$, a feature which is not seen in observations and suggests that the AGN feedback implementation may not provide enough gas mixing within the central regions of clusters and groups.

Our analysis lend further support to the idea that a feedback source associated to gas accretion onto super-massive BHs is required by the observational properties of the ICM (e.g. McNamara & Nulsen, 2007). However, our results also show that there are still a number of discrepancies between observations and the predictions made by simulations. This is especially true within the core regions of massive clusters, where a more efficient way of extracting and/or thermalising energy released by AGN is required.

The results presented in this Chapter further demonstrate that different astrophysical feedback sources leave distinct signatures on the pattern of chemical enrichment of the ICM. These differences are much more evident in the outskirts of galaxy clusters, which retain memory of the past efficiency that energy feedback had

in displacing enriched gas from star-forming regions and in regulating star formation itself. The characterization of thermal and chemical properties in cluster external regions requires X–ray telescopes with large collecting area and an excellent control of the background, characteristics which should be eventually met by a future generation of X–ray satellites.

■ Testing the robustness of cluster mass proxies

In **Chapter 5** we studied the effect that different physical processes included in the simulations have on the mass–observable scaling relations and their evolution with redshift. We focused on two cluster mass proxies, the gas mass M_{gas} and a new Y_X proxy defined by Kravtsov et al. (2006), that is the product of gas mass and cluster temperature. In their work Kravtsov et al. (2006) studied the scaling relations by extracting information from simulated clusters mimicking an observers approach. We prefer instead to take a step backward and test the robustness of the two relations, M_{tot}–M_{gas} and M_{tot}–Y_X, in simulations before including any observational effect. We test the relations against the change of prescription for the physics that describes the ICM, such as viscosity, thermal conduction, star formation, galactic winds and AGN feedback.

The results of this Chapter can be summarized as follows:

(a) The M_{gas}–M_{tot} relation between gas mass and cluster total mass follows closely the self–similar relation only in non–radiative runs, while cooling and star formation, that reduce the amount of hot gas in clusters, make the slope of the relation shallower. A similar trend was observed also for the Y_X relation.

(b) The scatter in both relations, M_{tot}–M_{gas} and M_{tot}–Y_X, depends on the physics included in the simulation: (i) the scatter in the M_{tot}–M_{gas} relation does not significantly evolve with redshift, with values from $\sim$ 2% to 10%, while (ii) the M_{tot}–Y_X scatter ranges from 2% to 16% with an increase with redshift as a consequence of mergers and substructure, which led to deviations from the condition of pressure equilibrium.

(c) The evolutions of both relations do not show any significant deviation from the predictions of the simple self–similar model. However we found that the Y_X proxy is less sensitive to the change of physical processes included in simulations. Y_X is by definition a measure of the thermal pressure support in the ICM. Therefore, with respect to M_{tot}–M_{gas}, once the central cluster region is excised, the relation M_{tot}–Y_X is more stable then the M_{tot}–M_{gas} relation changing the physical processes included in the simulations.

Including in detail observational effects as the relations measured from our simulated clusters requires the use of a suitable software (e.g. X-ray Map Simulator,

Gardini et al. 2004, Rasia et al. 2006, Rasia et al. 2008) that provides X–ray mock observations to be analysed by following the same procedures adopted for observational data.

■ Future perspectives

While hydrodynamical simulations probably provide the most complete interpretative framework for observations of the ICM physical properties, they have still to improve in the numerical accuracy for the description of relevant physical processes.

In the future, the improved numerical resolution expected to be reached in simulations of the next generation needs to be accompanied by a suitable description of the subresolution physics, both concerning the star formation physics and and the AGN feedback. Within the latter, the inclusion of the jet injection by AGN would of course provide a physically meaningful description of the interplay between BH accretion and ICM properties. Moreover for a fully self–consistent comparison between data and observations of a representative population of clusters is required, having a variety of morphologies and dynamical states. A simulated cluster set with these properties is at the moment still missing.

Another important issue concerns understanding the possible observational biases which complicate any direct comparison between data and model predictions (e.g. Rasia et al., 2008). In this respect, simulations provide a potentially ideal tool to understand these biases. Mock X–ray observations of simulated clusters, which include the effect of instrumental response, can be analysed exactly in the same way as real observational data. The resulting observed properties can be then compared with the true ones to calibrate out possible systematics. There is no doubt that observations and simulations should go hand in hand in order to fully exploit the wealth of information provided by X–ray telescopes.

While Chandra, XMM and Suzaku will be pushed to their limits in these studies in the next few years, there is no doubt that a detailed knowledge of the ICM out the cluster virial boundaries and reaching very high redshift has to await for the advent of the next generation of X–ray telescopes (e.g., Giacconi et al., 2009; Arnaud et al., 2009).

APPENDIX

Cosmology studies the structure, origin and evolution of the Universe. The fundamental assumption of the modern cosmology is known as the *cosmological principle*, introduced by Einstein and Milne (e.g. Milne, 1935). It states that the Universe is spatially homogeneous and isotropic when large enough scales are considered and with a uniformly expanding mass distribution. Spatial homogeneity is a natural extension of the Copernican principle, which asserts that our viewpoint is not special. If the Universe is isotropic around every point, then it is necessarily homogeneous. The cosmological principle is the starting point for most theoretical models. Both isotropy and homogeneity were confirmed by observations of the spatial distribution of galaxies and radio sources as well as by the observed cosmic microwave background radiation.

Clearly, the Universe appears irregular on small scales. This difference with respect to the stated principle is due to small primeval perturbations of the density field, superimposed on a large–scale homogeneous density distribution. Tiny inhomogeneities left by the cosmic inflation were amplified under the action of gravitation, dominated by the *cold dark matter* component. In this epoch, the linear growth of the density inhomogeneities is described by a simple linear differential equation.

At some point the linear approximation begins to break down and a more detailed treatment becomes necessary. Aside from the background expansion of the Universe, which is due to general relativity, evolution on these comparatively small scales is usually well approximated by the Newtonian theory. The non–linear growth of structures formed galaxy clusters and galaxy haloes. Also in this regime only gravitational forces are significant because dark matter is still the dominant player.

This Appendix wants to provide a brief introduction to modern cosmology. The relevant concepts and equations are presented in Section 5.5. The linear evolution and the non–linear growth of cosmic structures are presented in Sections 5.5 and 5.5. For a more complete and extended treatment of these arguments, please refer to Bertschinger (2001); Longair (1996); Coles & Lucchin (2002b); Peacock & Murdin (2002); Padmanabhan (2002, 2006); Borgani (2006).

The expanding Universe

We assume that gravitation governs the evolution of the Universe on large scales through the Einstein's General Relativity and that the geometry of the space–time is described by the Friedman–Robertson–Walker metric (e.g. Weinberg, 1972):

$$ds^2 = dt^2 - a(t)^2 \left[\frac{dr^2}{1-kr^2} + r^2(d\theta^2 + \sin^2\theta d\psi^2) \right]$$

written in comoving spherical coordinates (r, θ, ϕ) [1]. The parameter k describes the *curvature* of the space, while the temporal dependence of the metric is included in the *expansion factor* $a(t)$. All separations between objects in the Universe scale with time in proportion to this scale factor.

The standard convention (Peebles, 1980) sets $a(t) = 1$ at the present day value $t = t_0$. The cosmic scale factor is related to the *redshift*, since a radiation source emitting radiation at $t < t_0$ has redshift $\lambda/\lambda_0 = z = -1 + a^{-1}$, where λ_0 is the rest frame wavelength.

The position of each galaxy relative to some origin may be written as $\mathbf{r} = a(t)\mathbf{x}$, where $\mathbf{x}$ is a constant position vector for that galaxy. The Hubble law, the velocity of recession of this galaxy, can be then expressed as

$$\mathbf{v} = \frac{d\mathbf{r}}{dt} = H\,\mathbf{r}$$

where the present day value $H_0 = H(t = 0)$ is called the *Hubble constant* and more generally H is defined as a time dependent function

$$H(t) = \frac{d\log a(t)}{dt}.$$

$H(t)$ is commonly parametrized with $H(t) = 100h$ km s^{-1} Mpc^{-1}, where the most recent estimate of from the cosmic microwave background (5–year WMAP data, Komatsu et al., 2009) gives $h = 0.705 \pm 0.013$.

The Einstein's field equation relates the energy content of the Universe, described by the stress–energy tensor $T_{\alpha\beta}$, with the geometry of the Universe represented by the metric tensor $g_{\alpha\beta}$,

$$R_{\alpha\beta} - \frac{1}{2}Rg_{\alpha\beta} = \frac{8\pi G}{c^4}T_{\alpha\beta}\,,$$

where $R_{\alpha\beta}$ and R are derived from the curvature tensor $R^{\gamma}_{\alpha\beta\delta}$ and G is the universal gravitational constant. For a perfect fluid with density ρ, pressure p and four–velocity u_α the stress–energy tensor is defined as

$$T_{\alpha\beta} = (p + \rho c^2)u_\alpha u_\beta - p g_{\alpha\beta}\,.$$

[1] The *comoving coordinates* assign constant spatial coordinate values to observers who perceive the Universe as isotropic. The distance $\mathbf{r}$ between two objects can be written as a product of the *comoving distance* $\mathbf{x}$ and the time–varying scale factor $a(t)$, $\mathbf{r} = a(t)\mathbf{x}$.

The Einstein's equation dictates how the space–time curvature (left hand side of the equation) is related to the mass–energy content of the Universe (right hand side). The pressure p and density ρ of the fluid are related by the equation of state $p = p(\rho) = w\rho c^2$. The form of this equation depends on the fluid component, in particular. $w = 1/3$ for the relativistic matter, $w = 0$ for the non–relativistic matter, $w = -1$ for the vacuum energy and $w = -1/3$ for the curvature.

Using the Friedman–Robertson–Walker metric in the Einstein's equation for a perfect fluid one obtains the Friedman equations for the expanding Universe (Friedman, 1999), one from the time–time component

$$\frac{\ddot{a}}{a} = -\frac{4\pi}{3} G \left(\rho + 3\frac{p}{c^2}\right) , \tag{4}$$

and the other from the space–space components

$$a\ddot{a} + 2\dot{a}^2 + 2kc^2 = 4\pi G \left(\rho - \frac{p}{c^2}\right) a^2 ,$$

that, eliminating $\ddot{a}$, results in

$$\frac{\dot{a}^2}{a^2} + \frac{kc^2}{a^2} = \frac{8}{3}\pi G\rho . \tag{5}$$

The first Friedman equation relates the geometry of space to the mean mass density. In this framework it is useful to define the *critical density* ρ_c as

$$\rho_c(t) = \frac{3H^2(t)}{8\pi G} ,$$

where the value at $z = 0$ is $\rho_c(0) \simeq 1.9 \times 10^{-29}$ g cm^{-3} h^2. The density of each component X, ρ_X, can be expressed by the dimensionless density parameter

$$\Omega_X = \rho_X/\rho_c .$$

The space–space Friedman equation 5 can be written in terms of spatial curvature

$$k = \frac{a^2}{c^2} H^2(\Omega_{tot} - 1) ,$$

that depends on the mean density of the Universe, since in Ω_{tot} we include the contribution to the density from radiation, matter and the cosmological constant. This density parameter determines the curvature k of the Universe, that can be *closed*, *flat* or *open* when the density is smaller, equal or larger than the critical density.

The last equation can be rewritten as

$$\frac{H^2(t)}{H_0^2} = \left[\frac{\Omega_R}{a^4} + \frac{\Omega_M}{a^3} + \frac{\Omega_k}{a^2} + \Omega_\Lambda\right] ,$$

or simply as $H(z) = H_0 E(z)$, where

$$E(z) = [\Omega_{R,0}(1+z)^4 + \Omega_{M,0}(1+z)^3 + \Omega_{\Lambda,0} + (1-\Omega_{tot,0})(1+z)^2]^{1/2}\,.$$

Here $\Omega_{R,0}$ is the density from the radiation field, $\Omega_{M,0}$ is the matter density contributed by both baryonic and dark matter and $\Omega_{\Lambda,0}$ is due to the cosmological constant Λ.

The linear growth of structures

Among the four known fundamental forces, gravity would seem to be the most likely agent responsible for the formation of cosmic structure. The purely attractive and long-range nature of gravity causes it to be more important on large scales with respect to other forces. To test whether gravity might create structure it is useful to consider the evolution of small-amplitude perturbations of a homogeneous medium.

The basic equations for the linear evolution of the perturbation come from fluidodynamics, where density ρ, pressure p, velocity $\mathbf{v}$ and entropy s are the characteristics of the fluid and are described by the continuity equation

$$\frac{\partial \rho}{\partial t} + \nabla \cdot (\rho \mathbf{v}) = 0\,,$$

the Euler equation

$$\frac{\partial \mathbf{v}}{\partial t} + (\mathbf{v}\cdot\nabla)\mathbf{v} = -\frac{1}{\rho}\nabla p - \nabla\Phi\,,$$

the Poisson equation

$$\nabla^2\Phi = 4\pi G\rho\,,$$

and the entropy conservation

$$\frac{\partial s}{\partial t} + \mathbf{v}\cdot\nabla s = 0\,.$$

To explain the perturbation theory we need to introduce the *relative density contrast* δ. At the position $\mathbf{x}$ the density contrast is defined as the difference between the density $\rho(\mathbf{x})$ and the mean density averaged on a large volume of the Universe, $\bar{\rho}$, with the final result scaled to the mean density:

$$\delta(\mathbf{x}) = \frac{\rho(\mathbf{x}) - \bar{\rho}}{\bar{\rho}}.$$

By definition $\bar{\delta} = 0$ and $\delta(\mathbf{x}) \geq -1$.

The set of equations can be written in comoving coordinates, with the position vector $\mathbf{r} = a(t)\mathbf{x}$:

$$\frac{\partial \delta}{\partial t} + \nabla[(1+\delta)\mathbf{u}] = 0\,,$$
$$\frac{\partial \mathbf{u}}{\partial t} + 2H\mathbf{u} + (\mathbf{u}\cdot\nabla)\mathbf{u} = -\frac{1}{\bar{\rho}a^2}\nabla\delta p - \frac{\nabla\delta\Phi}{a^2}\,,$$
$$\nabla^2\delta\Phi = 4\pi G a^2\bar{\rho}\delta\,.$$

The terms $\delta\Phi$, δp and $\delta\mathbf{v} = a(t)\mathbf{u}$ represent respectively the perturbation of the gravitational potential, pressure and velocity.

To solve the above equations we consider the propagation of waves in a uniform background, with relative density fluctuation $\delta \propto \exp[i(\mathbf{k}\cdot\mathbf{x} - \omega t)]$, where $\mathbf{k}$ is the wavenumber. From the above equations one obtains the dispersion relation

$$\omega^2 = k^2 c_s^2 - 4\pi G\bar{\rho} = c_s^2(k^2 - k_J^2)\,,$$

where c_s is the sound speed and k_J is the Jeans wavenumber, $k_J = \sqrt{4\pi G\bar{\rho}}/c_s$. The solution depends on the value of ω^2: if $\omega^2 > 0$ the pressure is large enough to balance gravity and the perturbation oscillates, if instead $\omega^2 < 0$ the perturbation is allowed to grow exponentially. The critical value is given by the Jeans length scale, that represents the the minimum dimension for which the perturbation can collapse and is defined as

$$\lambda_J = \frac{2\pi}{k_J} = c_s\sqrt{\frac{\pi}{G\rho_0}}\,.$$

As was first pointed out by Jeans (Jeans, 1902), this means that pressure forces cannot prevent the gravitational collapse of a perturbation with proper length $\lambda > \lambda_J$ (that corresponds to $k < k_J$), when the sound crossing time λ/c_s is larger than the gravitational dynamical time $(G\bar{\rho})^{1/2}$.

In fact, the growth is exponential only for a static medium with $H = 0$ and constant $\bar{\rho}$. In an expanding universe the equation becomes:

$$\ddot{\delta} + 2\,\frac{\dot{a}}{a}\,\dot{\delta} = \frac{c_s^2}{a^2}\nabla^2\delta + 4\pi G\bar{\rho}\delta\,,$$

where spatial derivatives are done with respect to $\mathbf{x}$. The second term on the left side of the above equation acts as a viscosity term, slowing down the perturbation growth. In this case the linear growth of perturbations is proportional to a power of t rather than being exponential. The solution can be casted in the form

$$\delta(\mathbf{x},t) = \delta_+(\mathbf{x},t)D_+(t) + \delta_-(\mathbf{x},t)D_-(t)\,,$$

where the growing and decaying modes are described by D_+ and D_- respectively. In case of the Einstein–de Sitter universe with $\Omega_M = 1$ and $\Omega_\Lambda = 0$, $D_+(t) = (t/t_i)^{2/3}$ and $D_-(t) = (t/t_i)^{-1}$.

The power spectrum

The initial fluctuations of the field can be expressed as a superposition of plain waves. The advantage is that they evolve independently as long as the fluctuations are still linear. In the Fourier space we can describe the fluctuation field as

$$\hat{\delta}(\mathbf{k}) = \frac{1}{(2\pi)^3} \int d^3x \delta(\mathbf{x}) \exp(-i\mathbf{k} \cdot \mathbf{x}) \, .$$

If the density field is a isotropic Gaussian random field, then its statistic is entirely described by the *power spectrum* $P(k) = \langle |\delta_k^2| \rangle$. The fact that the universe is isotropic is expressed by $P(\mathbf{k}) = P(k)$.

The primordial fluctuations are thought to be produced during the inflation epoch and many versions of the inflationary scenario for the very early Universe produce a power–law initial fluctuation spectrum

$$P(k) \propto k^n \, ,$$

where n is the spectral index, that can be not constant over the entire range of wave numbers. The values for n are physically limited by $n > -3$ for $k \leftarrow 0$ to $n < -3$ for $k \leftarrow \infty$. The favoured value for the exponent is $n = 1$ that leads to the scale–invariant spectrum proposed independently by Harrison and Zel'dovich (Harrison, 1970; Zeldovich, 1972).

The most important statistical property of the density perturbation field is the variance

$$\sigma^2 = \langle |\delta^2(\mathbf{x})| \rangle = \frac{1}{(2\pi)^3} \int P(\mathbf{k}) d^3k \, ,$$

that describes the amplitude of different waves and is independent of the position.

Other physical properties besides gravitation affect the growth of initial perturbations and are accounted for by the *transfer function* $T(k)$. The final power spectrum is then $P(k) = P_0(k) \times T(k)^2$, where $P_0(k)$ is the original post–inflationary perturbation spectrum.

More extensive discussion can be found in Peebles (1980).

Non-linear evolution

When the perturbations have grown sufficiently, a small region might become substantially denser than the mean density of the universe. At this point, the physics involved becomes more complicated and overdensities with $\delta \gg 1$ evolve in a strongly non–linear regime.

The spherical Top-Hat collapse

The simplest approach is to consider a spherical perturbation with constant density inside, that at the initial time t_i has an amplitude $\delta_i > 0$ and $\delta_i \ll 1$. Within the simplest Einstein–de Sitter model for the Universe and assuming that pressure gradients are negligible, the spherical perturbation evolves like a Friedman model with the initial density parameter $\Omega_p(t_i) = \Omega(t_i)(1+\delta_i)$, where the suffix $_p$ determines the quantities related to the perturbation.

At time t_m the spherical region will cease to expand with the background Universe and will start to collapse. At this turn–around point the perturbation overdensity will be

$$\delta_+(t_m) = \frac{\rho_p(t_m)}{\rho(t_m)} - 1 \simeq 4.6$$

while the extrapolation from the linear theory significantly underestimates the overdensity at t_m, resulting in

$$\delta_+(t_m) = \delta(t_i) \left(\frac{t_m}{t_i}\right)^{2/3} \simeq 1.07\,.$$

The spherical perturbation after the turn–around point will collapse, reaching the virial equilibrium at time t_{vir}. Since at the turn around the kinetical energy is null, the total energy results to be

$$E_m = -\frac{3}{5}\frac{GM^2}{R_m}\,,$$

while at the virialization the total energy is estimated from the virial theorem as

$$E_{vir} = \frac{U}{2} = -\frac{1}{2}\frac{3}{5}\frac{GM^2}{R_{vir}}\,.$$

Ignoring the energy loss from the system we obtain the relation $R_m = 2R_{vir}$ between the two radii at turn–around and at virial equilibrium. The overdensity at t_{vir} will then be

$$\frac{\rho_p(t_{vir})}{\rho(t_{vir})} = \left(\frac{t_{vir}}{t_m}\right)^2 \left(\frac{R_m}{R_{vir}}\right)^3 \frac{\rho_p(t_m)}{\rho(t_m)} \simeq 178\,,$$

while the extrapolation from the linear theory predicts $\delta(t_{vir}) \simeq 1.67$. An overdensity of about 200 is usually considered as typical for a dark matter halo in virial equilibrium. It is worth to remind here that the above derivation is valid for a flat cosmology of the Einstein–de Sitter model. More general derivation can be found in Eke et al. (1996).

The Zel'dovich approximation

The spherical top–hat model is limited to the situations where a spherical perturbation has negligible pressure and dissipation during its collapse. To study the development of perturbations a clever approximation devised by Zel'Dovich (1970) is used for small amplitude perturbations when the Universe is dominated by the matter component (and the gas pressure is zero).

A set of particles uniformly distributed in space have initial Lagrangian coordinates $\mathbf{q}$ for their unperturbed position. Each particle is then subjected to a displacement, that corresponds to a density perturbation. The Eulerian coordinate of the particle at time t becomes

$$\mathbf{r}(\mathbf{q},t) = a(t)[\mathbf{q} - b(t)s(\mathbf{q})]\,.$$

Here $a(t)$ is the cosmological expansion factor, $b(t)$ is the growth rate of the linear density fluctuations in the expanding Universe and $s(\mathbf{q})$ represents the spatial perturbation and is expressed as the gradient of the potential, $s(\mathbf{q}) = \nabla_{\mathbf{q}}\Phi(\mathbf{q})$. The first term on the right, $a(t)\mathbf{q}$, is the unperturbed position of the particle.

Starting from mass conservation, $\rho(\mathbf{r},t)d\mathbf{r} = \rho_0 d\mathbf{q}$, one can derive the density and the density contrast. The approximation within the linear stage recovers the solution

$$\delta(\mathbf{x},t)\bar{\rho} = -b(t)\nabla_{\mathbf{q}}s(\mathbf{q})\,,$$

that resembles the growing mode of the linear solution. More in general for a collisionless medium Shandarin & Zeldovich (1989) found the solution

$$\rho(\mathbf{q},t) = \frac{\rho_0}{[1-b(t)\alpha_1(\mathbf{q})][1-b(t)\alpha_2(\mathbf{q})][1-b(t)\alpha_3(\mathbf{q})]}\,,$$

where α, β and γ are the eigenvalues of the deformation tensor $s(\mathbf{q})$. The above equation indicates that the density becomes formally infinite at some time t_{sc} when $b((t_{sc}) = 1/\alpha_j$, with $j = 1, 2$ or 3. This singularity is called *shell crossing* and corresponds to the situation when two points with different Lagrangian coordinates end up in the same Eulerian coordinate. One, two or three dimensional collapse of the structure leads to the formation of sheet–like (or "pancake") structures, filaments or points. However the Zel'dovich approximation is only kinematic and does not account for the short–range gravitational interaction, that will pull back the particles in pancakes before they could escape. To treat strongly nonlinear regime as well as the formation of shocks one should therefore resort to N–body simulations.

However, the Zel'dovich approximation is still used in cosmology to generate accurate initial conditions for N–body simulations (e.g. Dolag et al., 2008a). For every point in the k-space

$$\hat{\delta_{\mathbf{k}}} = \sqrt{-2P(|\mathbf{k}|)ln(A)}e^{i2\pi\varphi}$$

one has to generate a set of complex numbers within the interval $]0, 1]$ with a randomly distributed phase φ and with amplitude normally distributed with a variance given by the desired spectrum. To obtain the perturbation field from this distribution the potential $\phi(\mathbf{q})$ is generated on a grid $\mathbf{q}$ in real space via a Fourier transform. With the Zel'dovich approximation one can find the initial positions $\mathbf{x} = \mathbf{q} - D^+(z)\phi(\mathbf{q})$ and velocities $\mathbf{v} = \dot{D}^+(z)\nabla\phi(\mathbf{q})$ of the particles, where $D^+(z)$ is the cosmological linear growth factor at the initial redshift z (see also Efstathiou et al., 1985).

Bibliography

Abell, G. O.: 1958, The Distribution of Rich Clusters of Galaxies., ApJS, 3, 211–+

Allen, S. W., Dunn, R. J. H., Fabian, A. C., Taylor, G. B., & Reynolds, C. S.: 2006, The relation between accretion rate and jet power in X-ray luminous elliptical galaxies, MNRAS, 372, 21–30

Allen, S. W., Schmidt, R. W., Ebeling, H., Fabian, A. C., & van Speybroeck, L.: 2004, Constraints on dark energy from Chandra observations of the largest relaxed galaxy clusters, MNRAS, 353, 457–467

Allen, S. W., Schmidt, R. W., & Fabian, A. C.: 2001, The X-ray virial relations for relaxed lensing clusters observed with Chandra, MNRAS, 328, L37–L41

Ameglio, S., Borgani, S., Diaferio, A., & Dolag, K.: 2006, Angular-diameter distance estimates from the Sunyaev-Zeldovich effect in hydrodynamical cluster simulations, MNRAS, 369, 1459–1468

Ameglio, S., Borgani, S., Pierpaoli, E., Dolag, K., Ettori, S., & Morandi, A.: 2009, Reconstructing mass profiles of simulated galaxy clusters by combining Sunyaev-Zeldovich and X-ray images, MNRAS, 394, 479–490

Anders, E. & Grevesse, N.: 1989, Abundances of the elements - Meteoritic and solar, GeCoA, 53, 197–214

Anderson, M. E., Bregman, J. N., Butler, S. C., & Mullis, C. R.: 2009, Redshift Evolution in the Iron Abundance of the Intracluster Medium, ApJ, 698, 317–323

Arimoto, N. & Yoshii, Y.: 1987, Chemical and photometric properties of a galactic wind model for elliptical galaxies, A&A, 173, 23–38

Arnaud, M., Bohringer, H., Jones, C., McNamara, B., Ohashi, T., Patnaude, D., Arnaud, K., Bautz, M., & et al.: 2009, Galaxy Clusters Across Cosmic Time, Astro2010: The Astronomy and Astrophysics Decadal Survey Science White Papers, no. 4–+

Arnaud, M. & Evrard, A. E.: 1999, The L_X-T relation and intracluster gas fractions of X-ray clusters, MNRAS, 305, 631–640

Arnaud, M., Pointecouteau, E., & Pratt, G. W.: 2007, Calibration of the galaxy cluster M_{500}-Y_X relation with XMM-Newton, A&A, 474, L37–L40

Asplund, M., Grevesse, N., & Sauval, A. J.: 2005, The Solar Chemical Composition, in T. G. Barnes III & F. N. Bash (ed.), Cosmic Abundances as Records of Stellar Evolution and Nucleosynthesis, Vol. 336 of Astronomical Society of the Pacific Conference Series, pp 25–+

Böhringer, H., Matsushita, K., Churazov, E., Ikebe, Y., & Chen, Y.: 2002, The new emerging model for the structure of cooling cores in clusters of galaxies, A&A, 382, 804–820

Bagla, J. S.: 2002, TreePM: A Code for Cosmological N-Body Simulations, Journal of Astrophysics and Astronomy 23, 185–196

Bagla, J. S. & Ray, S.: 2003, Performance characteristics of TreePM codes, New Astronomy 8, 665–677

Bagla, J. S. & Ray, S.: 2005, Comments on the size of the simulation box in cosmological N-body simulations, MNRAS, 358, 1076–1082

Baldi, A., Ettori, S., Mazzotta, P., Tozzi, P., & Borgani, S.: 2007, A Chandra Archival Study of the Temperature and Metal Abundance Profiles in Hot Galaxy Clusters at 0.1 L_X–T ˜ z L_X–T ˜ 0.3, ApJ, 666, 835–845

Balestra, I., Tozzi, P., Ettori, S., Rosati, P., Borgani, S., Norman, V. M. C., & Viola, M.: 2007, Tracing the evolution in the iron content of the intra-cluster medium, A&A, 462, 429–442

Balogh, M. L., Pearce, F. R., Bower, R. G., & Kay, S. T.: 2001, Revisiting the cosmic cooling crisis, MNRAS, 326, 1228–1234

Barger, A. J., Cowie, L. L., Mushotzky, R. F., Yang, Y., Wang, W., Steffen, A. T., & Capak, P.: 2005, The Cosmic Evolution of Hard X-Ray-selected Active Galactic Nuclei, AJ, 129, 578–609

Barnes, J. & Hut, P.: 1986, A hierarchical O(N log N) force-calculation algorithm, Nature, 324, 446–449

Bartelmann, M.: 2003, Numerical Methods in Gravitational Lensing, ArXiv Astrophysics e-prints

Baugh, C. M.: 2006, A primer on hierarchical galaxy formation: the semi-analytical approach, Reports on Progress in Physics 69, 3101–3156

Baumgartner, W. H., Loewenstein, M., Horner, D. J., & Mushotzky, R. F.: 2005, Intermediate-Element Abundances in Galaxy Clusters, ApJ, 620, 680–696

Begelman, M. C., Volonteri, M., & Rees, M. J.: 2006, Formation of supermassive black holes by direct collapse in pre-galactic haloes, MNRAS, 370, 289–298

Bertelli, G., Bressan, A., Chiosi, C., Fagotto, F., & Nasi, E.: 1994, Theoretical isochrones from models with new radiative opacities, A&AS, 106, 275–302

Bertschinger, E.: 2001, Cosmological Perturbation Theory and Structure Formation, ArXiv Astrophysics e-prints

Bhattacharya, S., di Matteo, T., & Kosowsky, A.: 2008, Effects of quasar feedback in galaxy groups, MNRAS, 389, 34–44

Bignamini, A., Tozzi, P., Borgani, S., Ettori, S., & Rosati, P.: 2008, Intra cluster medium properties and AGN distribution in high-z RCS clusters, A&A, 489, 967–979

Binney, J. & Tabor, G.: 1995, Evolving Cooling Flows, MNRAS, 276, 663–+

Bîrzan, L., Rafferty, D. A., McNamara, B. R., Wise, M. W., & Nulsen, P. E. J.: 2004, A Systematic Study of Radio-induced X-Ray Cavities in Clusters, Groups, and Galaxies, ApJ, 607, 800–809

Biviano, A.: 2000, From Messier to Abell: 200 Years of Science with Galaxy Clusters, in Constructing the Universe with Clusters of Galaxies

Bode, P., Ostriker, J. P., & Xu, G.: 2000, The Tree Particle-Mesh N-Body Gravity Solver, ApJS, 128, 561–569

Boehringer, H. & Hensler, G.: 1989, Metallicity-dependence of radiative cooling in optically thin, hot plasmas, A&A, 215, 147–149

Boehringer, H. & Werner, N.: 2009, X-ray Spectroscopy of Galaxy Clusters, ArXiv e-prints

Böhringer, H., Belsole, E., Kennea, J., Matsushita, K., Molendi, S., Worrall, D. M., Mushotzky, R. F., Ehle, M., Guainazzi, M., Sakelliou, I., Stewart, G., Vestrand, W. T., & Dos Santos, S.: 2001, XMM-Newton observations of M 87 and its X-ray halo, A&A, 365, L181–L187

Böhringer, H., Matsushita, K., Churazov, E., Finoguenov, A., & Ikebe, Y.: 2004, Implications of the central metal abundance peak in cooling core clusters of galaxies, A&A, 416, L21–L25

Bondi, H.: 1952, On spherically symmetrical accretion, MNRAS, 112, 195–+

Bondi, H. & Hoyle, F.: 1944, On the mechanism of accretion by stars, MNRAS, 104, 273–+

Bonnell, I. A., Clarke, C. J., & Bate, M. R.: 2006, The Jeans mass and the origin of the knee in the IMF, MNRAS, 368, 1296–1300

Booth, C. M. & Schaye, J.: 2009, Cosmological simulations of the growth of supermassive black holes and feedback from active galactic nuclei: method and tests, ArXiv e-prints, MNRAS, in press

Borgani, S.: 2006, Cosmology with clusters of galaxies, ArXiv Astrophysics e-prints

Borgani, S., Diaferio, A., Dolag, K., & Schindler, S.: 2008a, Thermodynamical Properties of the ICM from Hydrodynamical Simulations, Space Science Reviews 134, 269–293

Borgani, S., Dolag, K., Murante, G., Cheng, L.-M., Springel, V., Diaferio, A., Moscardini, L., Tormen, G., Tornatore, L., & Tozzi, P.: 2006, Hot and

cooled baryons in smoothed particle hydrodynamic simulations of galaxy clusters: physics and numerics, MNRAS, 367, 1641–1654

Borgani, S., Fabjan, D., Tornatore, L., Schindler, S., Dolag, K., & Diaferio, A.: 2008b, The Chemical Enrichment of the ICM from Hydrodynamical Simulations, Space Science Reviews 134, 379–403

Borgani, S., Governato, F., Wadsley, J., Menci, N., Tozzi, P., Quinn, T., Stadel, J., & Lake, G.: 2002, The effect of non-gravitational gas heating in groups and clusters of galaxies, MNRAS, 336, 409–424

Borgani, S. & Kravtsov, A.: 2009, Cosmological simulations of galaxy clusters, ArXiv e-prints, ASL, in press

Borgani, S., Murante, G., Springel, V., Diaferio, A., Dolag, K., Moscardini, L., Tormen, G., Tornatore, L., & Tozzi, P.: 2004, X-ray properties of galaxy clusters and groups from a cosmological hydrodynamical simulation, MNRAS, 348, 1078–1096

Borgani, S. & Viel, M.: 2009, The evolution of a pre-heated intergalactic medium, MNRAS, 392, L26–L30

Bower, R. G., Benson, A. J., Malbon, R., Helly, J. C., Frenk, C. S., Baugh, C. M., Cole, S., & Lacey, C. G.: 2006, Breaking the hierarchy of galaxy formation, MNRAS, 370, 645–655

Bower, R. G., McCarthy, I. G., & Benson, A. J.: 2008, The flip side of galaxy formation: a combined model of galaxy formation and cluster heating, MNRAS, 390, 1399–1410

Branchesi, M., Gioia, I. M., Fanti, C., & Fanti, R.: 2007, High redshift X-ray galaxy clusters. II. The $L_X - T$ relationship revisited, A&A, 472, 739–748

Brighenti, F. & Mathews, W. G.: 2003, Feedback Heating in Cluster and Galactic Cooling Flows, ApJ, 587, 580–588

Brighenti, F. & Mathews, W. G.: 2006, Stopping Cooling Flows with Jets, ApJ, 643, 120–127

Brunetti, G. & Lazarian, A.: 2007, Compressible turbulence in galaxy clusters: physics and stochastic particle re-acceleration, MNRAS, 378, 245–275

Bruzual, G. & Charlot, S.: 2003, Stellar population synthesis at the resolution of 2003, MNRAS, 344, 1000–1028

Bryan, G. L.: 2000, Explaining the Entropy Excess in Clusters and Groups of Galaxies without Additional Heating, ApJL, 544, L1–L5

Buote, D. A.: 2000, X-ray evidence for multiphase hot gas with nearly solar Fe abundances in the brightest groups of galaxies, MNRAS, 311, 176–200

Buote, D. A., Lewis, A. D., Brighenti, F., & Mathews, W. G.: 2003, XMM-Newton and Chandra Observations of the Galaxy Group NGC 5044. II. Metal Abundances

and Supernova Fraction, ApJ, 595, 151–166

Burns, J. O.: 1990, The radio properties of cD galaxies in Abell clusters. I - an X-ray selected sample, AJ, 99, 14–30

Calura, F., Matteucci, F., & Tozzi, P.: 2007, On the evolution of the Fe abundance and of the Type Ia supernova rate in clusters of galaxies, MNRAS, 378, L11–L15

Canizares, C. R., Clark, G. W., Jernigan, J. G., & Markert, T. H.: 1982, X-ray spectroscopy of the galaxy M87 - Radiative accretion of the hot plasma halo, ApJ, 262, 33–43

Canizares, C. R., Clark, G. W., Markert, T. H., Berg, C., Smedira, M., Bardas, D., Schnopper, H., & Kalata, K.: 1979, High-resolution X-ray spectroscopy of M87 with the Einstein observatory - The detection of an O VIII emission line, ApJL, 234, L33–L37

Carlstrom, J. E., Holder, G. P., & Reese, E. D.: 2002, Cosmology with the Sunyaev-Zel'dovich Effect, ARA&A, 40, 643–680

Cassano, R. & Brunetti, G.: 2005, Cluster mergers and non-thermal phenomena: a statistical magneto-turbulent model, MNRAS, 357, 1313–1329

Cattaneo, A., Blaizot, J., Weinberg, D. H., Kereš, D., Colombi, S., Davé, R., Devriendt, J., Guiderdoni, B., & Katz, N.: 2007, Accretion, feedback and galaxy bimodality: a comparison of the GalICS semi-analytic model and cosmological SPH simulations, MNRAS, 377, 63–76

Cavagnolo, K. W., Donahue, M., Voit, G. M., & Sun, M.: 2009, Intracluster Medium Entropy Profiles for a Chandra Archival Sample of Galaxy Clusters, ApJS, 182, 12–32

Cavaliere, A. & Fusco-Femiano, R.: 1976, X-rays from hot plasma in clusters of galaxies, A&A, 49, 137–144

Cavaliere, A., Menci, N., & Tozzi, P.: 1998, Diffuse Baryons in Groups and Clusters of Galaxies, ApJ, 501, 493–+

Chabrier, G.: 2003, Galactic Stellar and Substellar Initial Mass Function, PASP, 115, 763–795

Chen, Y., Reiprich, T. H., Böhringer, H., Ikebe, Y., & Zhang, Y.: 2007, Statistics of X-ray observables for the cooling-core and non-cooling core galaxy clusters, A&A, 466, 805–812

Chiappini, C., Matteucci, F., & Gratton, R.: 1997, The Chemical Evolution of the Galaxy: The Two-Infall Model, ApJ, 477, 765–+

Chieffi, A. & Limongi, M.: 2004, Explosive Yields of Massive Stars from $Z = 0$ to $Z = Z_{solar}$, ApJ, 608, 405–410

Chung, A., van Gorkom, J. H., Kenney, J. D. P., & Vollmer, B.: 2007, Virgo Galaxies with Long One-sided H I Tails, ApJL, 659, L115–L119

Churazov, E., Brüggen, M., Kaiser, C. R., Böhringer, H., & Forman, W.: 2001, Evolution of Buoyant Bubbles in M87, ApJ, 554, 261–273

Churazov, E., Sazonov, S., Sunyaev, R., Forman, W., Jones, C., & Böhringer, H.: 2005, Supermassive black holes in elliptical galaxies: switching from very bright to very dim, MNRAS, 363, L91–L95

Coles, P. & Lucchin, F.: 2002a, Cosmology: The Origin and Evolution of Cosmic Structure, Second Edition, Cosmology: The Origin and Evolution of Cosmic Structure, Second Edition, by Peter Coles, Francesco Lucchin, pp. 512. ISBN 0-471-48909-3. Wiley-VCH , July 2002.

Coles, P. & Lucchin, F.: 2002b, Cosmology: The Origin and Evolution of Cosmic Structure, Second Edition

Cora, S. A.: 2006, Metal enrichment of the intracluster medium: a three-dimensional picture of chemical and dynamical properties, MNRAS, 368, 1540–1560

Cora, S. A., Tornatore, L., Tozzi, P., & Dolag, K.: 2008, On the Dynamical Origin of the ICM Metallicity Evolution, ArXiv e-prints 802

Couchman, H. M. P.: 1991, Mesh-refined P3M - A fast adaptive N-body algorithm, ApJL, 368, L23–L26

Cowie, L. L.: 1981, Theoretical models of X-ray emission from rich clusters of galaxies, in R. Giacconi (ed.), X-ray Astronomy with the Einstein Satellite, Vol. 87 of Astrophysics and Space Science Library, pp 227–240

Cowie, L. L. & Binney, J.: 1977, Radiative regulation of gas flow within clusters of galaxies - A model for cluster X-ray sources, ApJ, 215, 723–732

Cowie, L. L., Fabian, A. C., & Nulsen, P. E. J.: 1980, NGC 1275 and the Perseus cluster - The formation of optical filaments in cooling gas in X-ray clusters, MNRAS, 191, 399–410

Croston, J. H., Pratt, G. W., Böhringer, H., Arnaud, M., Pointecouteau, E., Ponman, T. J., Sanderson, A. J. R., Temple, R. F., Bower, R. G., & Donahue, M.: 2008, Galaxy-cluster gas-density distributions of the representative XMM-Newton cluster structure survey (REXCESS), A&A, 487, 431–443

Croton, D. J., Springel, V., White, S. D. M., De Lucia, G., Frenk, C. S., Gao, L., Jenkins, A., Kauffmann, G., Navarro, J. F., & Yoshida, N.: 2006, The many lives of active galactic nuclei: cooling flows, black holes and the luminosities and colours of galaxies, MNRAS, 365, 11–28

Dahlem, M., Weaver, K. A., & Heckman, T. M.: 1998, An X-Ray Minisurvey of Nearby Edge-on Starburst Galaxies. I. The Data, ApJS, 118, 401–453

Dalla Bontà, E., Ferrarese, L., Corsini, E. M., Miralda-Escudé, J., Coccato, L., Sarzi, M., Pizzella, A., & Beifiori, A.: 2009, The High-Mass End of the Black Hole Mass Function: Mass Estimates in Brightest Cluster Galaxies, ApJ, 690,

537–559

Dalla Vecchia, C., Bower, R. G., Theuns, T., Balogh, M. L., Mazzotta, P., & Frenk, C. S.: 2004, Quenching cluster cooling flows with recurrent hot plasma bubbles, MNRAS, 355, 995–1004

Dalla Vecchia, C. & Schaye, J.: 2008, Simulating galactic outflows with kinetic supernova feedback, MNRAS, 387, 1431–1444

Davé, R. & Oppenheimer, B. D.: 2007, The enrichment history of baryons in the Universe, MNRAS, 374, 427–435

Davé, R., Oppenheimer, B. D., & Sivanandam, S.: 2008, Enrichment and preheating in intragroup gas from galactic outflows, MNRAS, 391, 110–123

David, L. P., Nulsen, P. E. J., McNamara, B. R., Forman, W., Jones, C., Ponman, T., Robertson, B., & Wise, M.: 2001, A High-Resolution Study of the Hydra A Cluster with Chandra: Comparison of the Core Mass Distribution with Theoretical Predictions and Evidence for Feedback in the Cooling Flow, ApJ, 557, 546–559

De Grandi, S., Ettori, S., Longhetti, M., & Molendi, S.: 2004, On the iron content in rich nearby clusters of galaxies, A&A, 419, 7–18

De Grandi, S. & Molendi, S.: 2002, Temperature Profiles of Nearby Clusters of Galaxies, ApJ, 567, 163–177

de Grandi, S. & Molendi, S.: 2009, Metal abundances in the cool cores of galaxy clusters, A&A, 508, 565–574

De Lucia, G., Kauffmann, G., & White, S. D. M.: 2004, Chemical enrichment of the intracluster and intergalactic medium in a hierarchical galaxy formation model, MNRAS, 349, 1101–1116

de Plaa, J., Werner, N., Bleeker, J. A. M., Vink, J., Kaastra, J. S., & Méndez, M.: 2007, Constraining supernova models using the hot gas in clusters of galaxies, A&A, 465, 345–355

de Plaa, J., Werner, N., Bykov, A. M., Kaastra, J. S., Méndez, M., Vink, J., Bleeker, J. A. M., Bonamente, M., & Peterson, J. R.: 2006, Chemical evolution in Sérsic 159-03 observed with XMM-Newton, A&A, 452, 397–412

Di Matteo, T., Colberg, J., Springel, V., Hernquist, L., & Sijacki, D.: 2008, Direct Cosmological Simulations of the Growth of Black Holes and Galaxies, ApJ, 676, 33–53

Di Matteo, T., Springel, V., & Hernquist, L.: 2005, Energy input from quasars regulates the growth and activity of black holes and their host galaxies, Nature, 433, 604–607

Dolag, K., Borgani, S., Murante, G., & Springel, V.: 2009, Substructures in hydrodynamical cluster simulations, MNRAS, 399, 497–514

Dolag, K., Borgani, S., Schindler, S., Diaferio, A., & Bykov, A. M.: 2008a, Simulation Techniques for Cosmological Simulations, Space Science Reviews 134, 229–268

Dolag, K., Jubelgas, M., Springel, V., Borgani, S., & Rasia, E.: 2004, Thermal Conduction in Simulated Galaxy Clusters, ApJL, 606, L97–L100

Dolag, K., Reinecke, M., Gheller, C., & Imboden, S.: 2008b, Splotch: visualizing cosmological simulations, New Journal of Physics 10(12), 125006–+

Dolag, K., Vazza, F., Brunetti, G., & Tormen, G.: 2005, Turbulent gas motions in galaxy cluster simulations: the role of smoothed particle hydrodynamics viscosity, MNRAS, 364, 753–772

Domainko, W., Mair, M., Kapferer, W., van Kampen, E., Kronberger, T., Schindler, S., Kimeswenger, S., Ruffert, M., & Mangete, O. E.: 2006, Enrichment of the ICM of galaxy clusters due to ram-pressure stripping, A&A, 452, 795–802

Donahue, M., Horner, D. J., Cavagnolo, K. W., & Voit, G. M.: 2006, Entropy Profiles in the Cores of Cooling Flow Clusters of Galaxies, ApJ, 643, 730–750

Donahue, M. & Voit, G. M.: 2004, Cool Gas in Clusters of Galaxies, in J. S. Mulchaey, A. Dressler, & A. Oemler (ed.), Clusters of Galaxies: Probes of Cosmological Structure and Galaxy Evolution, pp 143–+

Donahue, M., Voit, G. M., Scharf, C. A., Gioia, I. M., Mullis, C. R., Hughes, J. P., & Stocke, J. T.: 1999, The Second Most Distant Cluster of Galaxies in the Extended Medium Sensitivity Survey, ApJ, 527, 525–534

Dunkley, J., Komatsu, E., Nolta, M. R., Spergel, D. N., Larson, D., Hinshaw, G., Page, L., Bennett, C. L., Gold, B., Jarosik, N., Weiland, J. L., Halpern, M., Hill, R. S., Kogut, A., Limon, M., Meyer, S. S., Tucker, G. S., Wollack, E., & Wright, E. L.: 2009, Five-Year Wilkinson Microwave Anisotropy Probe Observations: Likelihoods and Parameters from the WMAP Data, ApJS, 180, 306–329

Edge, A. C. & Frayer, D. T.: 2003, Resolving Molecular gas in the Central Galaxies of Cooling Flow Clusters, ApJL, 594, L13–L17

Efstathiou, G., Davis, M., White, S. D. M., & Frenk, C. S.: 1985, Numerical techniques for large cosmological N-body simulations, ApJS, 57, 241–260

Eke, V. R., Cole, S., & Frenk, C. S.: 1996, Cluster evolution as a diagnostic for Omega, MNRAS, 282, 263–280

Eke, V. R., Navarro, J. F., & Frenk, C. S.: 1998, The Evolution of X-Ray Clusters in a Low-Density Universe, ApJ, 503, 569–+

El-Zant, A. A.: 2006, Two-body relaxation in simulated cosmological haloes, MNRAS, 370, 1247–1256

Ettori, S.: 2005, Brief history of metal accumulation in the intracluster medium, MNRAS, 362, 110–116

Ettori, S., Dolag, K., Borgani, S., & Murante, G.: 2006, The baryon fraction in hydrodynamical simulations of galaxy clusters, MNRAS, 365, 1021–1030

Ettori, S. & Fabian, A. C.: 1999, ROSAT PSPC observations of 36 high-luminosity clusters of galaxies: constraints on the gas fraction, MNRAS, 305, 834–848

Ettori, S. & Fabian, A. C.: 2000, Chandra constraints on the thermal conduction in the intracluster plasma of A2142, MNRAS, 317, L57–L59

Ettori, S., Morandi, A., Tozzi, P., Balestra, I., Borgani, S., Rosati, P., Lovisari, L., & Terenziani, F.: 2009, The cluster gas mass fraction as a cosmological probe: a revised study, A&A, 501, 61–73

Ettori, S., Tozzi, P., Borgani, S., & Rosati, P.: 2004, Scaling laws in X-ray galaxy clusters at redshift between 0.4 and 1.3, A&A, 417, 13–27

Evrard, A. E. & Henry, J. P.: 1991a, Expectations for X-ray cluster observations by the ROSAT satellite, ApJ, 383, 95–103

Evrard, A. E. & Henry, J. P.: 1991b, Expectations for X-ray cluster observations by the ROSAT satellite, ApJ, 383, 95–103

Fabian, A. C.: 1994, Cooling Flows in Clusters of Galaxies, ARA&A, 32, 277–318

Fabian, A. C. & Nulsen, P. E. J.: 1977, Subsonic accretion of cooling gas in clusters of galaxies, MNRAS, 180, 479–484

Fabian, A. C., Sanders, J. S., Allen, S. W., Crawford, C. S., Iwasawa, K., Johnstone, R. M., Schmidt, R. W., & Taylor, G. B.: 2003, A deep Chandra observation of the Perseus cluster: shocks and ripples, MNRAS, 344, L43–L47

Fabian, A. C., Sanders, J. S., Ettori, S., Taylor, G. B., Allen, S. W., Crawford, C. S., Iwasawa, K., Johnstone, R. M., & Ogle, P. M.: 2000, Chandra imaging of the complex X-ray core of the Perseus cluster, MNRAS, 318, L65–L68

Fabian, A. C., Sanders, J. S., Taylor, G. B., & Allen, S. W.: 2005, A deep Chandra observation of the Centaurus cluster: bubbles, filaments and edges, MNRAS, 360, L20–L24

Fabjan, D., Borgani, S., Tornatore, L., Saro, A., Murante, G., & Dolag, K.: 2010, Simulating the effect of active galactic nuclei feedback on the metal enrichment of galaxy clusters, MNRAS, 401, 1670–1690

Fabjan, D., Tornatore, L., Borgani, S., Saro, A., & Dolag, K.: 2008, Evolution of the metal content of the intracluster medium with hydrodynamical simulations, MNRAS, 386, 1265–1273

Fan, X., Narayanan, V. K., Lupton, R. H., Strauss, M. A., Knapp, G. R., Becker, R. H., White, R. L., Pentericci, L., Leggett, S. K., Haiman, Z., Gunn, J. E., Ivezić, Ž., Schneider, D. P., Anderson, S. F., Brinkmann, J., Bahcall, N. A., Connolly, A. J., Csabai, I., Doi, M., Fukugita, M., Geballe, T., Grebel, E. K., Harbeck, D., Hennessy, G., Lamb, D. Q., Miknaitis, G., Munn, J. A., Nichol, R., Okamura, S.,

Pier, J. R., Prada, F., Richards, G. T., Szalay, A., & York, D. G.: 2001, A Survey of $z > 5.8$ Quasars in the Sloan Digital Sky Survey. I. Discovery of Three New Quasars and the Spatial Density of Luminous Quasars at z˜6, AJ, 122, 2833–2849

Ferrarese, L. & Ford, H.: 2005, Supermassive Black Holes in Galactic Nuclei: Past, Present and Future Research, Space Science Reviews 116, 523–624

Ferrarese, L. & Merritt, D.: 2000, A Fundamental Relation between Supermassive Black Holes and Their Host Galaxies, ApJL, 539, L9–L12

Finoguenov, A., Burkert, A., & Böhringer, H.: 2003, Role of Clusters of Galaxies in the Evolution of the Metal Budget in the Universe, ApJ, 594, 136–143

Finoguenov, A., David, L. P., & Ponman, T. J.: 2000, An ASCA Study of the Heavy-Element Distribution in Clusters of Galaxies, ApJ, 544, 188–203

Finoguenov, A., Matsushita, K., Böhringer, H., Ikebe, Y., & Arnaud, M.: 2002, X-ray evidence for spectroscopic diversity of type Ia supernovae:. XMM observation of the elemental abundance pattern in M 87, A&A, 381, 21–31

Friedman, A.: 1999, On the Curvature of Space, General Relativity and Gravitation 31, 1991–+

Fukazawa, Y., Makishima, K., Tamura, T., Ezawa, H., Xu, H., Ikebe, Y., Kikuchi, K., & Ohashi, T.: 1998, ASCA Measurements of Silicon and Iron Abundances in the Intracluster Medium, PASJ, 50, 187–193

Fukazawa, Y., Ohashi, T., Fabian, A. C., Canizares, C. R., Ikebe, Y., Makishima, K., Mushotzky, R. F., & Yamashita, K.: 1994, Metal concentration and X-ray cool spectral component in the central region of the Centaurus cluster of galaxies, PASJ, 46, L55–L58

Gal-Yam, A., Maoz, D., & Sharon, K.: 2002, Supernovae in deep Hubble Space Telescope galaxy cluster fields: cluster rates and field counts, MNRAS, 332, 37–48

Gardini, A., Rasia, E., Mazzotta, P., Tormen, G., De Grandi, S., & Moscardini, L.: 2004, Simulating Chandra observations of galaxy clusters, MNRAS, 351, 505–514

Gastaldello, F. & Molendi, S.: 2002, Abundance Gradients and the Role of Supernovae in M87, ApJ, 572, 160–168

Gebhardt, K., Bender, R., Bower, G., Dressler, A., Faber, S. M., Filippenko, A. V., Green, R., Grillmair, C., Ho, L. C., Kormendy, J., Lauer, T. R., Magorrian, J., Pinkney, J., Richstone, D., & Tremaine, S.: 2000, A Relationship between Nuclear Black Hole Mass and Galaxy Velocity Dispersion, ApJL, 539, L13–L16

Giacconi, R., Borgani, S., Rosati, P., Tozzi, P., Gilli, R., Murray, S., Paolillo, M., Pareschi, G., & et al.: 2009, Galaxy clusters and the cosmic cycle of baryons across cosmic times, Astro2010: The Astronomy and Astrophysics Decadal Survey Science White Papers, no. 90–+

Giacconi, R., Branduardi, G., Briel, U., & et al.: 1979, The Einstein /HEAO 2/ X-ray Observatory, ApJ, 230, 540–550

Gingold, R. A. & Monaghan, J. J.: 1977, Smoothed particle hydrodynamics - Theory and application to non-spherical stars, MNRAS, 181, 375–389

Giodini, S., Pierini, D., Finoguenov, A., Pratt, G. W., Boehringer, H., Leauthaud, & the COSMOS Collaboration: 2009, Stellar and Total Baryon Mass Fractions in Groups and Clusters Since Redshift 1, ApJ, 703, 982–993

Gonzalez, A. H., Zaritsky, D., & Zabludoff, A. I.: 2007, A Census of Baryons in Galaxy Clusters and Groups, ApJ, 666, 147–155

Graham, A. W.: 2007, The black hole mass - spheroid luminosity relation, MNRAS, 379, 711–722

Greggio, L.: 2005, The rates of type Ia supernovae. I. Analytical formulations, A&A, 441, 1055–1078

Greggio, L. & Renzini, A.: 1983, The binary model for type I supernovae - Theoretical rates, A&A, 118, 217–222

Grevesse, N. & Sauval, A. J.: 1998, Standard Solar Composition, Space Science Reviews 85, 161–174

Gronenschild, E. H. B. M. & Mewe, R.: 1978, Calculated X-radiation from optically thin plasmas. III - Abundance effects on continuum emission, A&AS, 32, 283–305

Gursky, H., Solinger, A., Kellogg, E. M., Murray, S., Tananbaum, H., Giacconi, R., & Cavaliere, A.: 1972, X-Ray Emission from Rich Clusters of Galaxies, ApJL, 173, L99+

Haardt, F. & Madau, P.: 1996, Radiative Transfer in a Clumpy Universe. II. The Ultraviolet Extragalactic Background, ApJ, 461, 20–+

Harrison, E. R.: 1970, Fluctuations at the Threshold of Classical Cosmology, PRD, 1, 2726–2730

Hawley, J. F., Beckwith, K., & Krolik, J. H.: 2007, General relativistic MHD simulations of black hole accretion disks and jets, Ap&SS, 311, 117–125

Heckman, T. M.: 2003, Starburst-Driven Galactic Winds, in V. Avila-Reese, C. Firmani, C. S. Frenk, & C. Allen (ed.), Revista Mexicana de Astronomia y Astrofisica Conference Series, Vol. 17 of Revista Mexicana de Astronomia y Astrofisica, vol. 27, pp 47–55

Heckman, T. M., Lehnert, M. D., Strickland, D. K., & Armus, L.: 2000, Absorption-Line Probes of Gas and Dust in Galactic Superwinds, ApJS, 129, 493–516

Heinz, S., Brüggen, M., Young, A., & Levesque, E.: 2006, The answer is blowing in the wind: simulating the interaction of jets with dynamic cluster atmospheres, MNRAS, 373, L65–L69

Henry, J. P. & Arnaud, K. A.: 1991, A measurement of the mass fluctuation

spectrum from the cluster X-ray temperature function, ApJ, 372, 410–418

Hernquist, L., Bouchet, F. R., & Suto, Y.: 1991, Application of the Ewald method to cosmological N-body simulations, ApJS, 75, 231–240

Hernquist, L. & Katz, N.: 1989, TREESPH - A unification of SPH with the hierarchical tree method, ApJS, 70, 419–446

Hoekstra, H.: 2007, A comparison of weak-lensing masses and X-ray properties of galaxy clusters, MNRAS, 379, 317–330

Hopkins, P. F., Hernquist, L., Cox, T. J., Robertson, B., & Krause, E.: 2007, An Observed Fundamental Plane Relation for Supermassive Black Holes, ApJ, 669, 67–73

Horner, D. J.: 2001, X-ray scaling laws for galaxy clusters and groups, Ph.D. thesis, University of Maryland College Park

Hoyle, F. & Lyttleton, R. A.: 1939, The effect of interstellar matter on climatic variation, in Proceedings of the Cambridge Philosophical Society, Vol. 35 of Proceedings of the Cambridge Philosophical Society, pp 405–+

Hubble, E.: 1929, A Relation between Distance and Radial Velocity among Extra-Galactic Nebulae, Proceedings of the National Academy of Science 15, 168–173

Ikebe, Y., Reiprich, T. H., Böhringer, H., Tanaka, Y., & Kitayama, T.: 2002, A new measurement of the X-ray temperature function of clusters of galaxies, A&A, 383, 773–790

Iwamoto, K., Brachwitz, F., Nomoto, K., Kishimoto, N., Umeda, H., Hix, W. R., & Thielemann, F.-K.: 1999, Nucleosynthesis in Chandrasekhar Mass Models for Type IA Supernovae and Constraints on Progenitor Systems and Burning-Front Propagation, ApJS, 125, 439–462

Jeans, J. H.: 1902, The Stability of a Spherical Nebula, Royal Society of London Philosophical Transactions Series A 199, 1–53

Jeltema, T. E., Canizares, C. R., Bautz, M. W., & Buote, D. A.: 2005, The Evolution of Structure in X-Ray Clusters of Galaxies, ApJ, 624, 606–629

Jeltema, T. E., Hallman, E. J., Burns, J. O., & Motl, P. M.: 2008, Cluster Structure in Cosmological Simulations. I. Correlation to Observables, Mass Estimates, and Evolution, ApJ, 681, 167–186

Johnson, R., Ponman, T. J., & Finoguenov, A.: 2009, A statistical analysis of the Two-Dimensional XMM-Newton Group Survey: the impact of feedback on group properties, MNRAS, pp 469–+

Jubelgas, M., Springel, V., & Dolag, K.: 2004, Thermal conduction in cosmological SPH simulations, MNRAS, 351, 423–435

Kaastra, J. S., Paerels, F. B. S., Durret, F., Schindler, S., & Richter, P.: 2008, Thermal Radiation Processes, Space Science Reviews 134, 155–190

Kaiser, N.: 1986, Evolution and clustering of rich clusters, MNRAS, 222, 323–345

Kaiser, N.: 1991, Evolution of clusters of galaxies, ApJ, 383, 104–111

Kapferer, W., Kronberger, T., Weratschnig, J., & Schindler, S.: 2007a, X-ray measured metallicities of the intra-cluster medium: a good measure for the metal mass?, A&A, 472, 757–762

Kapferer, W., Kronberger, T., Weratschnig, J., Schindler, S., Domainko, W., van Kampen, E., Kimeswenger, S., Mair, M., & Ruffert, M.: 2007b, Metal enrichment of the intra-cluster medium over a Hubble time for merging and relaxed galaxy clusters, A&A, 466, 813–821

Katz, N.: 1992, Dissipational galaxy formation. II - Effects of star formation, ApJ, 391, 502–517

Katz, N., Weinberg, D. H., & Hernquist, L.: 1996, Cosmological Simulations with TreeSPH, ApJS, 105, 19–+

Kawata, D. & Gibson, B. K.: 2003a, GCD+: a new chemodynamical approach to modelling supernovae and chemical enrichment in elliptical galaxies, MNRAS, 340, 908–922

Kawata, D. & Gibson, B. K.: 2003b, Multiwavelength cosmological simulations of elliptical galaxies, MNRAS, 346, 135–152

Kay, S. T., da Silva, A. C., Aghanim, N., Blanchard, A., Liddle, A. R., Puget, J.-L., Sadat, R., & Thomas, P. A.: 2007, The evolution of clusters in the CLEF cosmological simulation: X-ray structural and scaling properties, MNRAS, 377, 317–334

Kay, S. T., Pearce, F. R., Frenk, C. S., & Jenkins, A.: 2002, Including star formation and supernova feedback within cosmological simulations of galaxy formation, MNRAS, 330, 113–128

Kay, S. T., Thomas, P. A., Jenkins, A., & Pearce, F. R.: 2004, Cosmological simulations of the intracluster medium, MNRAS, 355, 1091–1104

King, I. R.: 1966, The structure of star clusters. III. Some simple dynamical models, AJ, 71, 64–+

Kirkpatrick, C. C., Gitti, M., Cavagnolo, K. W., McNamara, B. R., David, L. P., Nulsen, P. E. J., & Wise, M. W.: 2009, Direct Evidence for Outflow of Metal-Enriched Gas Along the Radio Jets of Hydra A, ApJL, 707, L69–L72

Kobayashi, C.: 2004, GRAPE-SPH chemodynamical simulation of elliptical galaxies - I. Evolution of metallicity gradients, MNRAS, 347, 740–758

Kolokotronis, V., Basilakos, S., Plionis, M., & Georgantopoulos, I.: 2001, Searching for cluster substructure using APM and ROSAT data, MNRAS, 320, 49–60

Komatsu, E., Dunkley, J., Nolta, M. R., Bennett, C. L., Gold, B., Hinshaw, G., Jarosik, N., Larson, D., Limon, M., Page, L., Spergel, D. N., Halpern, M., Hill,

R. S., Kogut, A., Meyer, S. S., Tucker, G. S., Weiland, J. L., Wollack, E., & Wright, E. L.: 2009, Five-Year Wilkinson Microwave Anisotropy Probe Observations: Cosmological Interpretation, ApJS, 180, 330–376

Kormendy, J. & Richstone, D.: 1995, Inward Bound—The Search For Supermassive Black Holes In Galactic Nuclei, ARA&A, 33, 581–+

Kowalski, M., Rubin, D., Aldering, G., Agostinho, R. J., Amadon, A., Amanullah, R., Balland, C., Barbary, K., Blanc, G., Challis, P. J., Conley, A., Connolly, N. V., Covarrubias, R., Dawson, K. S., Deustua, S. E., Ellis, R., Fabbro, S., Fadeyev, V., Fan, X., Farris, B., Folatelli, G., Frye, B. L., Garavini, G., Gates, E. L., Germany, L., Goldhaber, G., Goldman, B., Goobar, A., Groom, D. E., Haissinski, J., Hardin, D., Hook, I., Kent, S., Kim, A. G., Knop, R. A., Lidman, C., Linder, E. V., Mendez, J., Meyers, J., Miller, G. J., Moniez, M., Mourão, A. M., Newberg, H., Nobili, S., Nugent, P. E., Pain, R., Perdereau, O., Perlmutter, S., Phillips, M. M., Prasad, V., Quimby, R., Regnault, N., Rich, J., Rubenstein, E. P., Ruiz-Lapuente, P., Santos, F. D., Schaefer, B. E., Schommer, R. A., Smith, R. C., Soderberg, A. M., Spadafora, A. L., Strolger, L., Strovink, M., Suntzeff, N. B., Suzuki, N., Thomas, R. C., Walton, N. A., Wang, L., Wood-Vasey, W. M., & Yun, J. L.: 2008, Improved Cosmological Constraints from New, Old, and Combined Supernova Data Sets, ApJ, 686, 749–778

Kravtsov, A. V., Klypin, A. A., & Khokhlov, A. M.: 1997, Adaptive Refinement Tree: A New High-Resolution N-Body Code for Cosmological Simulations, ApJS, 111, 73–+

Kravtsov, A. V., Nagai, D., & Vikhlinin, A. A.: 2005, Effects of Cooling and Star Formation on the Baryon Fractions in Clusters, ApJ, 625, 588–598

Kravtsov, A. V., Vikhlinin, A., & Nagai, D.: 2006, A New Robust Low-Scatter X-Ray Mass Indicator for Clusters of Galaxies, ApJ, 650, 128–136

Krolik, J. H., Hawley, J. F., & Hirose, S.: 2005, Magnetically Driven Accretion Flows in the Kerr Metric. IV. Dynamical Properties of the Inner Disk, ApJ, 622, 1008–1023

Kroupa, P.: 2001, On the variation of the initial mass function, MNRAS, 322, 231–246

Kroupa, P., Tout, C. A., & Gilmore, G.: 1993, The distribution of low-mass stars in the Galactic disc, MNRAS, 262, 545–587

Laganá, T. F., Lima Neto, G. B., Andrade-Santos, F., & Cypriano, E. S.: 2008, Star formation efficiency in galaxy clusters, A&A, 485, 633–644

Larson, R. B.: 1998, Early star formation and the evolution of the stellar initial mass function in galaxies, MNRAS, 301, 569–581

Lauer, T. R., Faber, S. M., Richstone, D., Gebhardt, K., Tremaine, S., Postman, M., Dressler, A., Aller, M. C., Filippenko, A. V., Green, R., Ho, L. C., Kormendy,

J., Magorrian, J., & Pinkney, J.: 2007, The Masses of Nuclear Black Holes in Luminous Elliptical Galaxies and Implications for the Space Density of the Most Massive Black Holes, ApJ, 662, 808–834

Lea, S. M., Mushotzky, R., & Holt, S. S.: 1982, Einstein Observatory solid state spectrometer observations of M87 and the Virgo cluster, ApJ, 262, 24–32

Leccardi, A. & Molendi, S.: 2008a, Radial metallicity profiles for a large sample of galaxy clusters observed with XMM-Newton, A&A, 487, 461–466

Leccardi, A. & Molendi, S.: 2008b, Radial temperature profiles for a large sample of galaxy clusters observed with XMM-Newton, A&A, 486, 359–373

Li, Y., Hernquist, L., Robertson, B., Cox, T. J., Hopkins, P. F., Springel, V., Gao, L., Di Matteo, T., Zentner, A. R., Jenkins, A., & Yoshida, N.: 2007, Formation of z˜6 Quasars from Hierarchical Galaxy Mergers, ApJ, 665, 187–208

Lia, C., Portinari, L., & Carraro, G.: 2002, Star formation and chemical evolution in smoothed particle hydrodynamics simulations: a statistical approach, MNRAS, 330, 821–836

Lin, Y.-T., Mohr, J. J., & Stanford, S. A.: 2003, Near-Infrared Properties of Galaxy Clusters: Luminosity as a Binding Mass Predictor and the State of Cluster Baryons, ApJ, 591, 749–763

Lodders, K.: 2003, Solar System Abundances and Condensation Temperatures of the Elements, ApJ, 591, 1220–1247

Loeb, A. & Barkana, R.: 2001, The Reionization of the Universe by the First Stars and Quasars, ARA&A, 39, 19–66

Loewenstein, M.: 2006, On Iron Enrichment, Star Formation, and Type Ia Supernovae in Galaxy Clusters, ApJ, 648, 230–249

Loewenstein, M. & Mushotzky, R. F.: 1996, Measurement of the Elemental Abundances in Four Rich Clusters of Galaxies. II. The Initial Mass Function and Mass Loss in Elliptical Galaxies, Enrichment, and Energetics in the ICM, ApJ, 466, 695–+

Loken, C., Norman, M. L., Nelson, E., Burns, J., Bryan, G. L., & Motl, P.: 2002, A Universal Temperature Profile for Galaxy Clusters, ApJ, 579, 571–576

Longair, M. S.: 1996, Our evolving universe

Lucy, L. B.: 1977, A numerical approach to the testing of the fission hypothesis, AJ, 82, 1013–1024

Madau, P., Ferguson, H. C., Dickinson, M. E., Giavalisco, M., Steidel, C. C., & Fruchter, A.: 1996, High-redshift galaxies in the Hubble Deep Field: colour selection and star formation history to z˜4, MNRAS, 283, 1388–1404

Maeder, A. & Meynet, G.: 1989, Grids of evolutionary models from 0.85 to 120 solar masses - Observational tests and the mass limits, A&A, 210, 155–173

Magorrian, J., Tremaine, S., Richstone, D., Bender, R., Bower, G., Dressler, A., Faber, S. M., Gebhardt, K., Green, R., Grillmair, C., Kormendy, J., & Lauer, T.: 1998, The Demography of Massive Dark Objects in Galaxy Centers, AJ, 115, 2285–2305

Mahdavi, A., Hoekstra, H., Babul, A., & Henry, J. P.: 2008, Evidence for non-hydrostatic gas from the cluster X-ray to lensing mass ratio, MNRAS, 384, 1567–1574

Mahdavi, A., Hoekstra, H., Babul, A., Sievers, J., Myers, S. T., & Henry, J. P.: 2007, Joint Analysis of Cluster Observations. I. Mass Profile of Abell 478 from Combined X-Ray, Sunyaev-Zel'dovich, and Weak-Lensing Data, ApJ, 664, 162–180

Mannucci, F., Della Valle, M., & Panagia, N.: 2006, Two populations of progenitors for Type Ia supernovae?, MNRAS, 370, 773–783

Mannucci, F., Maoz, D., Sharon, K., Botticella, M. T., Della Valle, M., Gal-Yam, A., & Panagia, N.: 2008, The supernova rate in local galaxy clusters, MNRAS, 383, 1121–1130

Marconi, A. & Hunt, L. K.: 2003, The Relation between Black Hole Mass, Bulge Mass, and Near-Infrared Luminosity, ApJL, 589, L21–L24

Marigo, P.: 2001, Chemical yields from low- and intermediate-mass stars: Model predictions and basic observational constraints, A&A, 370, 194–217

Markevitch, M.: 1998, The L X-T Relation and Temperature Function for Nearby Clusters Revisited, ApJ, 504, 27–+

Markevitch, M., Mazzotta, P., Vikhlinin, A., Burke, D., Butt, Y., David, L., Donnelly, H., Forman, W. R., Harris, D., Kim, D., Virani, S., & Vrtilek, J.: 2003, Chandra Temperature Map of A754 and Constraints on Thermal Conduction, ApJL, 586, L19–L23

Martin, C. L.: 1999, Properties of Galactic Outflows: Measurements of the Feedback from Star Formation, ApJ, 513, 156–160

Martin, C. L.: 2005, Mapping Large-Scale Gaseous Outflows in Ultraluminous Galaxies with Keck II ESI Spectra: Variations in Outflow Velocity with Galactic Mass, ApJ, 621, 227–245

Matsumoto, H., Pierre, M., Tsuru, T. G., & Davis, D. S.: 2001, ASCA observations of massive medium-distant clusters of galaxies. II., A&A, 374, 28–35

Matsumoto, H., Tsuru, T. G., Fukazawa, Y., Hattori, M., & Davis, D. S.: 2000, Gas, Iron, and Gravitational Mass in Galaxy Clusters: The General Lack of Cluster Evolution at z L_X–T 1.0, PASJ, 52, 153–+

Matteucci, F.: 2003, The Chemical Evolution of the Galaxy, The Chemical Evolution of the Galaxy. By Francesca Matteucci, Department of Astronomy, Univer-

sity of Trieste, Italy. Astrophysics and Space Science Library Volume 253 reprint Kluwer Academic Publishers, Dordrecht

Matteucci, F. & Chiappini, C.: 2005, Interpretation of Abundance Ratios, Publications of the Astronomical Society of Australia 22, 49–55

Matteucci, F. & Gibson, B. K.: 1995, Chemical abundances in clusters of galaxies., A&A, 304, 11–+

Matteucci, F. & Greggio, L.: 1986, Relative roles of type I and II supernovae in the chemical enrichment of the interstellar gas, A&A, 154, 279–287

Matteucci, F. & Recchi, S.: 2001, On the Typical Timescale for the Chemical Enrichment from Type Ia Supernovae in Galaxies, ApJ, 558, 351–358

Maughan, B. J.: 2007, The $L_X - Y_X$ Relation: Using Galaxy Cluster X-Ray Luminosity as a Robust, Low-Scatter Mass Proxy, ApJ, 668, 772–780

Maughan, B. J., Jones, C., Forman, W., & Van Speybroeck, L.: 2008, Images, Structural Properties, and Metal Abundances of Galaxy Clusters Observed with Chandra ACIS-I at $0.1 L_X$–T zL_X–T 1.3, ApJS, 174, 117–135

Maughan, B. J., Jones, L. R., Ebeling, H., & Scharf, C.: 2006, The evolution of the cluster X-ray scaling relations in the Wide Angle ROSAT Pointed Survey sample at $0.6 < z < 1.0$, MNRAS, 365, 509–529

Mazzotta, P., Brunetti, G., Giacintucci, S., Venturi, T., & Bardelli, S.: 2004a, Heated Intracluster Gas and Radio Connections: The Singular Case of MKW 3S, Journal of Korean Astronomical Society 37, 381–385

Mazzotta, P., Rasia, E., Moscardini, L., & Tormen, G.: 2004b, Comparing the temperatures of galaxy clusters from hydrodynamical N-body simulations to Chandra and XMM-Newton observations, MNRAS, 354, 10–24

McKee, C. F. & Ostriker, E. C.: 2007, Theory of Star Formation, ARA&A, 45, 565–687

McNamara, B. R. & Nulsen, P. E. J.: 2007, Heating Hot Atmospheres with Active Galactic Nuclei, ARA&A, 45, 117–175

McNamara, B. R., Rafferty, D. A., Bîrzan, L., Steiner, J., Wise, M. W., Nulsen, P. E. J., Carilli, C. L., Ryan, R., & Sharma, M.: 2006, The Starburst in the Abell 1835 Cluster Central Galaxy: A Case Study of Galaxy Formation Regulated by an Outburst from a Supermassive Black Hole, ApJ, 648, 164–175

McNamara, B. R., Wise, M., Nulsen, P. E. J., David, L. P., Sarazin, C. L., Bautz, M., Markevitch, M., Vikhlinin, A., Forman, W. R., Jones, C., & Harris, D. E.: 2000, Chandra X-Ray Observations of the Hydra A Cluster: An Interaction between the Radio Source and the X-Ray-emitting Gas, ApJL, 534, L135–L138

Meneghetti, M., Rasia, E., Merten, J., Bellagamba, F., Ettori, S., Mazzotta, P., & Dolag, K.: 2009, Weighing simulated galaxy clusters using lensing and X-ray,

ArXiv e-prints

Merloni, A., Heinz, S., & Di Matteo, T.: 2005, A Fundamental Plane of Black Hole Activity: Pushing Forward the Unification Scheme, Ap&SS, 300, 45–53

Milne, E. A.: 1935, Relativity, gravitation and world-structure

Mitchell, R. J., Culhane, J. L., Davison, P. J. N., & Ives, J. C.: 1976, Ariel 5 observations of the X-ray spectrum of the Perseus Cluster, MNRAS, 175, 29P–34P

Mohr, J. J., Evrard, A. E., Fabricant, D. G., & Geller, M. J.: 1995, Cosmological Constraints from Observed Cluster X-Ray Morphologies, ApJ, 447, 8–+

Molendi, S. & Gastaldello, F.: 2001, On the metal abundance in the core of M 87, A&A, 375, L14–L17

Molendi, S. & Pizzolato, F.: 2001, Is the Gas in Cooling Flows Multiphase?, ApJ, 560, 194–200

Moll, R., Schindler, S., Domainko, W., Kapferer, W., Mair, M., van Kampen, E., Kronberger, T., Kimeswenger, S., & Ruffert, M.: 2007, Simulations of metal enrichment in galaxy clusters by AGN outflows, A&A, 463, 513–518

Monaghan, J. J.: 1992, Smoothed particle hydrodynamics, ARA&A, 30, 543–574

Monaghan, J. J.: 2006, Smoothed particle hydrodynamic simulations of shear flow, MNRAS, 365, 199–213

Monaghan, J. J. & Gingold, R. A.: 1983, Shock Simulation by the Particle Method SPH, Journal of Computational Physics 52, 374–+

Monaghan, J. J. & Lattanzio, J. C.: 1985, A refined particle method for astrophysical problems, A&A, 149, 135–143

Monaghan, J. J. & Price, D. J.: 2004, Toy stars in one dimension, MNRAS, 350, 1449–1456

Mosconi, M. B., Tissera, P. B., Lambas, D. G., & Cora, S. A.: 2001, Chemical evolution using smooth particle hydrodynamical cosmological simulations - I. Implementation, tests and first results, MNRAS, 325, 34–48

Murante, G., Arnaboldi, M., Gerhard, O., Borgani, S., Cheng, L. M., Diaferio, A., Dolag, K., Moscardini, L., Tormen, G., Tornatore, L., & Tozzi, P.: 2004, The Diffuse Light in Simulations of Galaxy Clusters, ApJL, 607, L83–L86

Murante, G., Giovalli, M., Gerhard, O., Arnaboldi, M., Borgani, S., & Dolag, K.: 2007, The importance of mergers for the origin of intracluster stars in cosmological simulations of galaxy clusters, MNRAS, 377, 2–16

Mushotzky, R. F.: 2004, Clusters of Galaxies: An X-ray Perspective, in J. S. Mulchaey, A. Dressler, & A. Oemler (eds.), Clusters of Galaxies: Probes of Cosmological Structure and Galaxy Evolution, pp 123–+

Mushotzky, R. F. & Loewenstein, M.: 1997, Lack of Evolution in the Iron Abundance in Clusters of Galaxies and Implications for the Global Star Formation Rate at High Redshift, ApJL, 481, L63+

Mushotzky, R. F., Serlemitsos, P. J., Boldt, E. A., Holt, S. S., & Smith, B. W.: 1978, OSO 8 X-ray spectra of clusters of galaxies. I - Observations of twenty clusters: Physical correlations, ApJ, 225, 21–39

Nagai, D., Kravtsov, A. V., & Vikhlinin, A.: 2007a, Effects of Galaxy Formation on Thermodynamics of the Intracluster Medium, ApJ, 668, 1–14

Nagai, D., Vikhlinin, A., & Kravtsov, A. V.: 2007b, Testing X-Ray Measurements of Galaxy Clusters with Cosmological Simulations, ApJ, 655, 98–108

Nagashima, M., Lacey, C. G., Baugh, C. M., Frenk, C. S., & Cole, S.: 2005, The metal enrichment of the intracluster medium in hierarchical galaxy formation models, MNRAS, 358, 1247–1266

Narayan, R. & Bartelmann, M.: 1999, Gravitational lensing, in A. Dekel & J. P. Ostriker (ed.), Formation of Structure in the Universe, pp 360–+

Narayan, R. & Medvedev, M. V.: 2001, Thermal Conduction in Clusters of Galaxies, ApJL, 562, L129–L132

Nomoto, K. & et al.: 2000, Type Ia supernova Progenitors, Environmental Effects, and Cosmic Supernova Rates, in J. C. Niemeyer & J. W. Truran (eds.), Type Ia Supernovae, Theory and Cosmology. Edited by J. C. Niemeyer and J. W. Truran. Published by Cambridge University Press, 2000., p.63, pp 63–+

Nomoto, K., Iwamoto, K., Nakasato, N., Thielemann, F.-K., Brachwitz, F., Tsujimoto, T., Kubo, Y., & Kishimoto, N.: 1997, Nucleosynthesis in type Ia supernovae, Nuclear Physics A 621, 467–476

Nulsen, P. E. J., Jones, C., Forman, W. R., David, L. P., McNamara, B. R., Rafferty, D. A., Bîrzan, L., & Wise, M. W.: 2007, AGN Heating Through Cavities and Shocks, in H. Böhringer, G. W. Pratt, A. Finoguenov, & P. Schuecker (ed.), Heating versus Cooling in Galaxies and Clusters of Galaxies, pp 210–+

O'Hara, T. B., Mohr, J. J., Bialek, J. J., & Evrard, A. E.: 2006, Effects of Mergers and Core Structure on the Bulk Properties of Nearby Galaxy Clusters, ApJ, 639, 64–80

Omma, H. & Binney, J.: 2004, Structural stability of cooling flows, MNRAS, 350, L13–L16

Omma, H., Binney, J., Bryan, G., & Slyz, A.: 2004, Heating cooling flows with jets, MNRAS, 348, 1105–1119

Oppenheimer, B. D. & Davé, R.: 2008, Mass, metal, and energy feedback in cosmological simulations, MNRAS, 387, 577–600

O'Shea, B. W., Bryan, G., Bordner, J., Norman, M. L., Abel, T., Harkness, R., &

Kritsuk, A.: 2004, Introducing Enzo, an AMR Cosmology Application, ArXiv Astrophysics e-prints

Osmond, J. P. F. & Ponman, T. J.: 2004, The GEMS project: X-ray analysis and statistical properties of the group sample, MNRAS, 350, 1511–1535

Owen, F. N., Eilek, J. A., & Kassim, N. E.: 2000, M87 at 90 Centimeters: A Different Picture, ApJ, 543, 611–619

Padmanabhan, T.: 2002, Theoretical Astrophysics - Volume 3, Galaxies and Cosmology

Padmanabhan, T.: 2006, Advanced Topics in Cosmology: A Pedagogical Introduction, in S. Daflon, J. Alcaniz, E. Telles, & R. de la Reza (ed.), Graduate School in Astronomy: X, Vol. 843 of American Institute of Physics Conference Series, pp 111–166

Padoan, P., Nordlund, Å., Kritsuk, A. G., Norman, M. L., & Li, P. S.: 2007, Two Regimes of Turbulent Fragmentation and the Stellar Initial Mass Function from Primordial to Present-Day Star Formation, ApJ, 661, 972–981

Padovani, P. & Matteucci, F.: 1993, Stellar Mass Loss in Elliptical Galaxies and the Fueling of Active Galactic Nuclei, ApJ, 416, 26–+

Peacock, J. & Murdin, P.: 2002, Cosmology: Standard Model

Peebles, P. J. E.: 1980, The large-scale structure of the universe

Peres, C. B., Fabian, A. C., Edge, A. C., Allen, S. W., Johnstone, R. M., & White, D. A.: 1998, A ROSAT study of the cores of clusters of galaxies - I. Cooling flows in an X-ray flux-limited sample, MNRAS, 298, 416–432

Peterson, J. R., Kahn, S. M., Paerels, F. B. S., Kaastra, J. S., Tamura, T., Bleeker, J. A. M., Ferrigno, C., & Jernigan, J. G.: 2003, High-Resolution X-Ray Spectroscopic Constraints on Cooling-Flow Models for Clusters of Galaxies, ApJ, 590, 207–224

Peterson, J. R., Paerels, F. B. S., Kaastra, J. S., Arnaud, M., Reiprich, T. H., Fabian, A. C., Mushotzky, R. F., Jernigan, J. G., & Sakelliou, I.: 2001, X-ray imaging-spectroscopy of Abell 1835, A&A, 365, L104–L109

Pfrommer, C., Enßlin, T. A., Springel, V., Jubelgas, M., & Dolag, K.: 2007, Simulating cosmic rays in clusters of galaxies - I. Effects on the Sunyaev-Zel'dovich effect and the X-ray emission, MNRAS, 378, 385–408

Pierpaoli, E., Borgani, S., Scott, D., & White, M.: 2003, On determining the cluster abundance normalization, MNRAS, 342, 163–175

Piffaretti, R. & Valdarnini, R.: 2008, Total mass biases in X-ray galaxy clusters, A&A, 491, 71–87

Pipino, A., Matteucci, F., Borgani, S., & Biviano, A.: 2002, SNe heating and the chemical evolution of the intra-cluster medium, New Astronomy 7, 227–247

Ponman, T. J., Cannon, D. B., & Navarro, J. F.: 1999, The thermal imprint of galaxy formation on X-ray clusters, Nature, 397, 135–137

Poole, G. B., Babul, A., McCarthy, I. G., Fardal, M. A., Bildfell, C. J., Quinn, T., & Mahdavi, A.: 2007, The impact of mergers on relaxed X-ray clusters - II. Effects on global X-ray and Sunyaev-Zel'dovich properties and their scaling relations, MNRAS, 380, 437–454

Pope, E. C. D.: 2009, Observable consequences of kinetic and thermal AGN feedback in elliptical galaxies and galaxy clusters, MNRAS, 395, 2317–2325

Portinari, L., Chiosi, C., & Bressan, A.: 1998, Galactic chemical enrichment with new metallicity dependent stellar yields, A&A, 334, 505–539

Portinari, L., Moretti, A., Chiosi, C., & Sommer-Larsen, J.: 2004, Can a "Standard" Initial Mass Function Explain the Metal Enrichment in Clusters of Galaxies?, ApJ, 604, 579–595

Pratt, G. W. & Arnaud, M.: 2003, Entropy scaling in galaxy clusters: Insights from an XMM-Newton observation of the poor cluster ¡ASTROBJ¿A1983¡/ASTROBJ¿, A&A, 408, 1–16

Pratt, G. W., Böhringer, H., Croston, J. H., Arnaud, M., Borgani, S., Finoguenov, A., & Temple, R. F.: 2007, Temperature profiles of a representative sample of nearby X-ray galaxy clusters, A&A, 461, 71–80

Pratt, G. W., Croston, J. H., Arnaud, M., & Böhringer, H.: 2009, Galaxy cluster X-ray luminosity scaling relations from a representative local sample (REXCESS), A&A, 498, 361–378

Puchwein, E., Sijacki, D., & Springel, V.: 2008, Simulations of AGN Feedback in Galaxy Clusters and Groups: Impact on Gas Fractions and the LX-T Scaling Relation, ApJL, 687, L53–L56

Rafferty, D. A., McNamara, B. R., Nulsen, P. E. J., & Wise, M. W.: 2006, The Feedback-regulated Growth of Black Holes and Bulges through Gas Accretion and Starbursts in Cluster Central Dominant Galaxies, ApJ, 652, 216–231

Raiteri, C. M., Villata, M., & Navarro, J. F.: 1996, Simulations of Galactic chemical evolution. I. O and Fe abundances in a simple collapse model., A&A, 315, 105–115

Rasia, E., Ettori, S., Moscardini, L., Mazzotta, P., Borgani, S., Dolag, K., Tormen, G., Cheng, L. M., & Diaferio, A.: 2006, Systematics in the X-ray cluster mass estimators, MNRAS, 369, 2013–2024

Rasia, E., Mazzotta, P., Borgani, S., Moscardini, L., Dolag, K., Tormen, G., Diaferio, A., & Murante, G.: 2005, Mismatch between X-Ray and Emission-weighted Temperatures in Galaxy Clusters: Cosmological Implications, ApJL, 618, L1–L4

Rasia, E., Mazzotta, P., Bourdin, H., Borgani, S., Tornatore, L., Ettori, S., Dolag, K., & Moscardini, L.: 2008, X-MAS2: Study Systematics on the ICM Metallicity

Measurements, ApJ, 674, 728–741

Rasia, E., Tormen, G., & Moscardini, L.: 2004, A dynamical model for the distribution of dark matter and gas in galaxy clusters, MNRAS, 351, 237–252

Rasmussen, J. & Ponman, T. J.: 2007, Temperature and abundance profiles of hot gas in galaxy groups - I. Results and statistical analysis, MNRAS, 380, 1554–1572

Rebusco, P., Churazov, E., Böhringer, H., & Forman, W.: 2005, Impact of stochastic gas motions on galaxy cluster abundance profiles, MNRAS, 359, 1041–1048

Renzini, A.: 1997, Iron as a Tracer in Galaxy Clusters and Groups, ApJ, 488, 35–+

Renzini, A.: 2000, What Heavy Elements in Clusters of Galaxies Tell about Clusters and Galaxies, in M. Plionis & I. Georgantopoulos (ed.), Large Scale Structure in the X-ray Universe, Proceedings of the 20-22 September 1999 Workshop, Santorini, Greece, eds. Plionis, M. and Georgantopoulos, I., Atlantisciences, Paris, France, p.103, pp 103–+

Renzini, A.: 2004, The Chemistry of Galaxy Clusters, in J. S. Mulchaey, A. Dressler, & A. Oemler (eds.), Clusters of Galaxies: Probes of Cosmological Structure and Galaxy Evolution, pp 260–+

Renzini, A. & Voli, M.: 1981, Advanced evolutionary stages of intermediate-mass stars. I - Evolution of surface compositions, A&A, 94, 175–193

Roediger, E. & Brüggen, M.: 2007, Ram pressure stripping of disc galaxies orbiting in clusters - I. Mass and radius of the remaining gas disc, MNRAS, 380, 1399–1408

Roediger, E., Brüggen, M., Rebusco, P., Böhringer, H., & Churazov, E.: 2007, Metal mixing by buoyant bubbles in galaxy clusters, MNRAS, 375, 15–28

Romano, D., Chiappini, C., Matteucci, F., & Tosi, M.: 2005, Quantifying the uncertainties of chemical evolution studies. I. Stellar lifetimes and initial mass function, A&A, 430, 491–505

Romeo, A. D., Portinari, L., & Sommer-Larsen, J.: 2005, Simulating galaxy clusters - II. Global star formation histories and the galaxy populations, MNRAS, 361, 983–996

Romeo, A. D., Sommer-Larsen, J., Portinari, L., & Antonuccio-Delogu, V.: 2006a, Simulating galaxy clusters - I. Thermal and chemical properties of the intracluster medium, MNRAS, 371, 548–568

Romeo, A. D., Sommer-Larsen, J., Portinari, L., & Antonuccio-Delogu, V.: 2006b, Simulating galaxy clusters - I. Thermal and chemical properties of the intracluster medium, MNRAS, 371, 548–568

Roncarelli, M., Ettori, S., Dolag, K., Moscardini, L., Borgani, S., & Murante, G.: 2006, Simulated X-ray galaxy clusters at the virial radius: Slopes of the gas density, temperature and surface brightness profiles, MNRAS, 373, 1339–1350

Rosati, P., Borgani, S., & Norman, C.: 2002, The Evolution of X-ray Clusters of

Galaxies, ARA&A, 40, 539–577

Rosswog, S.: 2009, Astrophysical smooth particle hydrodynamics, New Astronomy Review 53, 78–104

Ruszkowski, M. & Begelman, M. C.: 2002, Heating, Conduction, and Minimum Temperatures in Cooling Flows, ApJ, 581, 223–228

Ruszkowski, M., Enßlin, T. A., Brüggen, M., Begelman, M. C., & Churazov, E.: 2008, Cosmic ray confinement in fossil cluster bubbles, MNRAS, 383, 1359–1365

Ruszkowski, M., Enßlin, T. A., Brüggen, M., Heinz, S., & Pfrommer, C.: 2007, Impact of tangled magnetic fields on fossil radio bubbles, MNRAS, 378, 662–672

Salpeter, E. E.: 1955, The Luminosity Function and Stellar Evolution., ApJ, 121, 161–+

Sanders, J. S. & Fabian, A. C.: 2007, A deeper X-ray study of the core of the Perseus galaxy cluster: the power of sound waves and the distribution of metals and cosmic rays, MNRAS, 381, 1381–1399

Sanderson, A. J. R., O'Sullivan, E., & Ponman, T. J.: 2009a, A statistically selected Chandra sample of 20 galaxy clusters - II. Gas properties and cool core/non-cool core bimodality, MNRAS, 395, 764–776

Sanderson, A. J. R., O'Sullivan, E., & Ponman, T. J.: 2009b, A statistically selected Chandra sample of 20 galaxy clusters - II. Gas properties and cool core/non-cool core bimodality, MNRAS, pp 428–+

Sanderson, A. J. R., Ponman, T. J., & O'Sullivan, E.: 2006, A statistically selected Chandra sample of 20 galaxy clusters - I. Temperature and cooling time profiles, MNRAS, 372, 1496–1508

Santos, J. S., Rosati, P., Tozzi, P., Böhringer, H., Ettori, S., & Bignamini, A.: 2008, Searching for cool core clusters at high redshift, A&A, 483, 35–47

Sarazin, C. L.: 1988, X-ray emission from clusters of galaxies, Cambridge Astrophysics Series, Cambridge: Cambridge University Press, 1988

Sarazin, C. L.: 1988, X-ray emission from clusters of galaxies, Cambridge University Press, Cambridge

Saro, A., Borgani, S., Tornatore, L., Dolag, K., Murante, G., Biviano, A., Calura, F., & Charlot, S.: 2006, Properties of the galaxy population in hydrodynamical simulations of clusters, MNRAS, 373, 397–410

Sato, K., Matsushita, K., & Gastaldello, F.: 2009a, Temperature and Metallicity in the Intra-Cluster Medium of Abell 262 Observed with Suzaku, PASJ, 61, 365–+

Sato, K., Matsushita, K., Ishisaki, Y., Sasaki, S., Ohashi, T., Yamasaki, N. Y., & Ishida, M.: 2008, Suzaku Observations of AWM 7 Cluster of Galaxies: Temperatures, Abundances, and Bulk Motions, PASJ, 60, 333–+

Sato, K., Matsushita, K., Ishisaki, Y., Yamasaki, N. Y., Ishida, M., & Ohashi, T.:

2009b, Suzaku Observation of Group of Galaxies NGC 507: Temperature and Metal Distributions in the Intra-Cluster Medium, PASJ, 61, 353–+

Scannapieco, C., Tissera, P. B., White, S. D. M., & Springel, V.: 2005, Feedback and metal enrichment in cosmological smoothed particle hydrodynamics simulations - I. A model for chemical enrichment, MNRAS, 364, 552–564

Schindler, S. & Diaferio, A.: 2008, Metal Enrichment Processes, Space Science Reviews 134, 363–377

Schindler, S., Kapferer, W., Domainko, W., Mair, M., van Kampen, E., Kronberger, T., Kimeswenger, S., Ruffert, M., Mangete, O., & Breitschwerdt, D.: 2005, Metal enrichment processes in the intra-cluster medium, A&A, 435, L25–L28

Schmidt, M.: 1959, The Rate of Star Formation., ApJ, 129, 243–+

Schuecker, P., Finoguenov, A., Miniati, F., Böhringer, H., & Briel, U. G.: 2004, Probing turbulence in the Coma galaxy cluster, A&A, 426, 387–397

Serlemitsos, P. J., Smith, B. W., Boldt, E. A., Holt, S. S., & Swank, J. H.: 1977, X-radiation from clusters of galaxies - Spectral evidence for a hot evolved gas, ApJL, 211, L63–L66

Shakura, N. I. & Syunyaev, R. A.: 1973, Black holes in binary systems. Observational appearance., A&A, 24, 337–355

Shandarin, S. F. & Zeldovich, Y. B.: 1989, The large-scale structure of the universe: Turbulence, intermittency, structures in a self-gravitating medium, Reviews of Modern Physics 61, 185–220

Shang, C., Crotts, A., & Haiman, Z.: 2007, Constraints on the Abundance of Highly Ionized Protocluster Regions from the Absence of Large Voids in the Lyα Forest, ApJ, 671, 136–145

Sharon, K., Gal-Yam, A., Maoz, D., Filippenko, A. V., & Guhathakurta, P.: 2007, Supernovae in Low-Redshift Galaxy Clusters: The Type Ia Supernova Rate, ApJ, 660, 1165–1175

Sheldon, E. S., Annis, J., Böhringer, H., Fischer, P., Frieman, J. A., Joffre, M., Johnston, D., McKay, T. A., Miller, C., Nichol, R. C., Stebbins, A., Voges, W., Anderson, S. F., Bahcall, N. A., Brinkmann, J., Brunner, R., Csabai, I., Fukugita, M., Hennessy, G. S., Ivezić, Ž., Lupton, R. H., Munn, J. A., Pier, J. R., & York, D. G.: 2001, Weak-Lensing Measurements of 42 SDSS/RASS Galaxy Clusters, ApJ, 554, 881–887

Sijacki, D., Pfrommer, C., Springel, V., & Enßlin, T. A.: 2008, Simulations of cosmic-ray feedback by active galactic nuclei in galaxy clusters, MNRAS, 387, 1403–1415

Sijacki, D. & Springel, V.: 2006a, Hydrodynamical simulations of cluster formation with central AGN heating, MNRAS, 366, 397–416

Sijacki, D. & Springel, V.: 2006b, Physical viscosity in smoothed particle hydrodynamics simulations of galaxy clusters, MNRAS, 371, 1025–1046

Sijacki, D., Springel, V., di Matteo, T., & Hernquist, L.: 2007, A unified model for AGN feedback in cosmological simulations of structure formation, MNRAS, 380, 877–900

Simionescu, A., Werner, N., Böhringer, H., Kaastra, J. S., Finoguenov, A., Brüggen, M., & Nulsen, P. E. J.: 2009, Chemical enrichment in the cluster of galaxies Hydra A, A&A, 493, 409–424

Simionescu, A., Werner, N., Finoguenov, A., Böhringer, H., & Brüggen, M.: 2008, Metal-rich multi-phase gas in M 87. AGN-driven metal transport, magnetic-field supported multi-temperature gas, and constraints on non-thermal emission observed with XMM-Newton, A&A, 482, 97–112

Sivanandam, S., Zabludoff, A. I., Zaritsky, D., Gonzalez, A. H., & Kelson, D. D.: 2009, The Enrichment of the Intracluster Medium, ApJ, 691, 1787–1806

Smith, S.: 1936, The Mass of the Virgo Cluster, ApJ, 83, 23–+

Snowden, S. L., Mushotzky, R. F., Kuntz, K. D., & Davis, D. S.: 2008, A catalog of galaxy clusters observed by XMM-Newton, A&A, 478, 615–658

Spitzer, L.: 1962, Physics of Fully Ionized Gases

Springel, V.: 2005, The cosmological simulation code GADGET-2, MNRAS, 364, 1105–1134

Springel, V., Di Matteo, T., & Hernquist, L.: 2005a, Modelling feedback from stars and black holes in galaxy mergers, MNRAS, 361, 776–794

Springel, V. & Hernquist, L.: 2003a, Cosmological smoothed particle hydrodynamics simulations: a hybrid multiphase model for star formation, MNRAS, 339, 289–311

Springel, V. & Hernquist, L.: 2003b, The history of star formation in a Λ cold dark matter universe, MNRAS, 339, 312–334

Springel, V., White, S. D. M., Jenkins, A., Frenk, C. S., Yoshida, N., Gao, L., Navarro, J., Thacker, R., Croton, D., Helly, J., Peacock, J. A., Cole, S., Thomas, P., Couchman, H., Evrard, A., Colberg, J., & Pearce, F.: 2005b, Simulations of the formation, evolution and clustering of galaxies and quasars, Nature, 435, 629–636

Springel, V., Yoshida, N., & White, S.: 2001, Gadget: a code for collisionless and gasdynamical cosmological simulations, New Astronomy 6, 79

Springel, V., Yoshida, N., & White, S. D. M.: 2001, GADGET: a code for collisionless and gasdynamical cosmological simulations, New Astronomy 6, 79–117

Stadel, J. G.: 2001, Cosmological N-body simulations and their analysis, Ph.D. thesis, AA(University of Washington)

Sun, M.: 2009, Every BCG with a Strong Radio Agn has an X-Ray Cool Core: Is

the Cool Core-Noncool Core Dichotomy Too Simple?, ApJ, 704, 1586–1604

Sun, M., Voit, G. M., Donahue, M., Jones, C., Forman, W., & Vikhlinin, A.: 2009, Chandra Studies of the X-Ray Gas Properties of Galaxy Groups, ApJ, 693, 1142–1172

Sutherland, R. S. & Dopita, M. A.: 1993, Cooling functions for low-density astrophysical plasmas, ApJS, 88, 253–327

Tescari, E., Viel, M., Tornatore, L., & Borgani, S.: 2009, Damped Lyman α systems in high-resolution hydrodynamical simulations, MNRAS, 397, 411–430

Thielemann, F.-K., Argast, D., Brachwitz, F., Hix, W. R., Höflich, P., Liebendörfer, M., Martinez-Pinedo, G., Mezzacappa, A., Panov, I., & Rauscher, T.: 2003, Nuclear cross sections, nuclear structure and stellar nucleosynthesis, Nuclear Physics A 718, 139–146

Thorne, K. S.: 1974, Disk-Accretion onto a Black Hole. II. Evolution of the Hole, ApJ, 191, 507–520

Tinsley, B. M.: 1980, Evolution of the Stars and Gas in Galaxies, Fundamentals of Cosmic Physics 5, 287–388

Tormen, G., Bouchet, F., & White, S.: 1997, The structure and dynamical evolution of dark matter haloes, MNRAS 286, 865

Tormen, G., Bouchet, F. R., & White, S. D. M.: 1997, The structure and dynamical evolution of dark matter haloes, MNRAS, 286, 865–884

Tornatore, L., Borgani, S., Dolag, K., & Matteucci, F.: 2007a, Chemical enrichment of galaxy clusters from hydrodynamical simulations, MNRAS, 382, 1050–1072

Tornatore, L., Borgani, S., Matteucci, F., Recchi, S., & Tozzi, P.: 2004, Simulating the metal enrichment of the intracluster medium, MNRAS, 349, L19–L24

Tornatore, L., Borgani, S., Springel, V., Matteucci, F., Menci, N., & Murante, G.: 2003, Cooling and heating the intracluster medium in hydrodynamical simulations, MNRAS, 342, 1025–1040

Tornatore, L., Borgani, S., Viel, M., & Springel, V.: 2009, The impact of feedback on the low-redshift intergalactic medium, MNRAS, pp 1906–+

Tornatore, L., Ferrara, A., & Schneider, R.: 2007b, Population III stars: hidden or disappeared ?, ArXiv e-prints 707

Tozzi, P. & Norman, C.: 2001, The Evolution of X-Ray Clusters and the Entropy of the Intracluster Medium, ApJ, 546, 63–84

Tozzi, P., Rosati, P., Ettori, S., Borgani, S., Mainieri, V., & Norman, C.: 2003, Iron Abundance in the Intracluster Medium at High Redshift, ApJ, 593, 705–720

Tremaine, S., Gebhardt, K., Bender, R., Bower, G., Dressler, A., Faber, S. M., Filippenko, A. V., Green, R., Grillmair, C., Ho, L. C., Kormendy, J., Lauer, T. R., Magorrian, J., Pinkney, J., & Richstone, D.: 2002, The Slope of the Black

Hole Mass versus Velocity Dispersion Correlation, ApJ, 574, 740–753

Tutukov, A. V. & Iungelson, L. R.: 1980, Statistical investigation of spectroscopic binary stars, in M. J. Plavec, D. M. Popper, & R. K. Ulrich (eds.), IAU Symp. 88: Close Binary Stars: Observations and Interpretation, pp 15–22

Valdarnini, R.: 2003, Iron abundances and heating of the intracluster medium in hydrodynamical simulations of galaxy clusters, MNRAS, 339, 1117–1134

van den Hoek, L. B. & Groenewegen, M. A. T.: 1997, New theoretical yields of intermediate mass stars, A&AS, 123, 305–328

Vazza, F., Tormen, G., Cassano, R., Brunetti, G., & Dolag, K.: 2006, Turbulent velocity fields in smoothed particle hydrodymanics simulated galaxy clusters: scaling laws for the turbulent energy, MNRAS, 369, L14–L18

Vernaleo, J. C. & Reynolds, C. S.: 2006, AGN Feedback and Cooling Flows: Problems with Simple Hydrodynamic Models, ApJ, 645, 83–94

Vikhlinin, A.: 2006, Predicting a Single-Temperature Fit to Multicomponent Thermal Plasma Spectra, ApJ, 640, 710–715

Vikhlinin, A., Burenin, R. A., Ebeling, H., Forman, W. R., Hornstrup, A., Jones, C., Kravtsov, A. V., Murray, S. S., Nagai, D., Quintana, H., & Voevodkin, A.: 2009, Chandra Cluster Cosmology Project. II. Samples and X-Ray Data Reduction, ApJ, 692, 1033–1059

Vikhlinin, A., Kravtsov, A., Forman, W., Jones, C., Markevitch, M., Murray, S. S., & Van Speybroeck, L.: 2006, Chandra Sample of Nearby Relaxed Galaxy Clusters: Mass, Gas Fraction, and Mass-Temperature Relation, ApJ, 640, 691–709

Vikhlinin, A., Markevitch, M., & Murray, S. S.: 2001, A Moving Cold Front in the Intergalactic Medium of A3667, ApJ, 551, 160–171

Vikhlinin, A., Markevitch, M., Murray, S. S., Jones, C., Forman, W., & Van Speybroeck, L.: 2005, Chandra Temperature Profiles for a Sample of Nearby Relaxed Galaxy Clusters, ApJ, 628, 655–672

Vikhlinin, A., VanSpeybroeck, L., Markevitch, M., Forman, W. R., & Grego, L.: 2002, Evolution of the Cluster X-Ray Scaling Relations since $z > 0.4$, ApJL, 578, L107–L111

Vikhlinin, A., Voevodkin, A., Mullis, C. R., VanSpeybroeck, L., Quintana, H., McNamara, B. R., Gioia, I., Hornstrup, A., Henry, J. P., Forman, W. R., & Jones, C.: 2003, Cosmological Constraints from the Evolution of the Cluster Baryon Mass Function at z ˜ 0.5, ApJ, 590, 15–25

Voevodkin, A. & Vikhlinin, A.: 2004, Constraining Amplitude and Slope of the Mass Fluctuation Spectrum Using a Cluster Baryon Mass Function, ApJ, 601, 610–620

Voigt, L. M. & Fabian, A. C.: 2004, Thermal conduction and reduced cooling flows

in galaxy clusters, MNRAS, 347, 1130–1149

Voit, G. M.: 2004, Intracluster thermodynamics, in A. Diaferio (ed.), IAU Colloq. 195: Outskirts of Galaxy Clusters: Intense Life in the Suburbs, pp 253–259

Voit, G. M.: 2005a, Expectations for evolution of cluster scaling relations, Advances in Space Research 36, 701–705

Voit, G. M.: 2005b, Tracing cosmic evolution with clusters of galaxies, Reviews of Modern Physics 77, 207–258

Voit, G. M. & Bryan, G. L.: 2001, Regulation of the X-ray luminosity of clusters of galaxies by cooling and supernova feedback, Nature, 414, 425–427

Voit, G. M. & Donahue, M.: 2005, An Observationally Motivated Framework for AGN Heating of Cluster Cores, ApJ, 634, 955–963

Weinberg, S.: 1972, Gravitation and Cosmology: Principles and Applications of the General Theory of Relativity

Werner, N., Durret, F., Ohashi, T., Schindler, S., & Wiersma, R. P. C.: 2008, Observations of Metals in the Intra-Cluster Medium, Space Science Reviews 134, 337–362

White, D. A., Fabian, A. C., Allen, S. W., Edge, A. C., Crawford, C. S., Johnstone, R. M., Stewart, G. C., & Voges, W.: 1994, A ROSAT HRI Observation of the ABELL:478 Cluster of Galaxies, MNRAS, 269, 589–+

White, S. D. M.: 1994, Formation and Evolution of Galaxies: Les Houches Lectures, ArXiv Astrophysics e-prints

Wiersma, R. P. C., Schaye, J., Theuns, T., Dalla Vecchia, C., & Tornatore, L.: 2009, Chemical enrichment in cosmological, smoothed particle hydrodynamics simulations, ArXiv e-prints, MNRAS, in press

Wise, M. W. & McNamara, B. R.: 2001, Chandra Observations of the Massive Cluster MS2137.3-2353, in Two Years of Science with Chandra

Woosley, S. E. & Weaver, T. A.: 1995, The Evolution and Explosion of Massive Stars. II. Explosive Hydrodynamics and Nucleosynthesis, ApJS, 101, 181–+

Wyithe, J. S. B. & Loeb, A.: 2003, Self-regulated Growth of Supermassive Black Holes in Galaxies as the Origin of the Optical and X-Ray Luminosity Functions of Quasars, ApJ, 595, 614–623

Xu, G.: 1995, A New Parallel N-Body Gravity Solver: TPM, ApJS, 98, 355–+

Yoshida, N., Sheth, R. K., & Diaferio, A.: 2001, Non-Gaussian cosmic microwave background temperature fluctuations from peculiar velocities of clusters, MNRAS, 328, 669–677

Zakamska, N. L. & Narayan, R.: 2003, Models of Galaxy Clusters with Thermal Conduction, ApJ, 582, 162–169

Zel'Dovich, Y. B.: 1970, Gravitational instability: An approximate theory for large density perturbations., A&A, 5, 84–89

Zeldovich, Y. B.: 1972, A hypothesis, unifying the structure and the entropy of the Universe, MNRAS, 160, 1P–+

Zhang, Y., Finoguenov, A., Böhringer, H., Kneib, J., Smith, G. P., Kneissl, R., Okabe, N., & Dahle, H.: 2008, LoCuSS: comparison of observed X-ray and lensing galaxy cluster scaling relations with simulations, A&A, 482, 451–472

Zhang, Y.-Y., Böhringer, H., Finoguenov, A., Ikebe, Y., Matsushita, K., Schuecker, P., Guzzo, L., & Collins, C. A.: 2006, X-ray properties in massive galaxy clusters: XMM-Newton observations of the REFLEX-DXL sample, A&A, 456, 55–74

Zibetti, S., White, S. D. M., Schneider, D. P., & Brinkmann, J.: 2005, Intergalactic stars in z˜ 0.25 galaxy clusters: systematic properties from stacking of Sloan Digital Sky Survey imaging data, MNRAS, 358, 949–967

Zwicky, F.: 1937, On the Masses of Nebulae and of Clusters of Nebulae, ApJ, 86, 217–+